Evaluation of the Bonner Bridge Girders: Assessing Residual Capacity, Prestress Losses and Degradation of the 56 Year Old Members

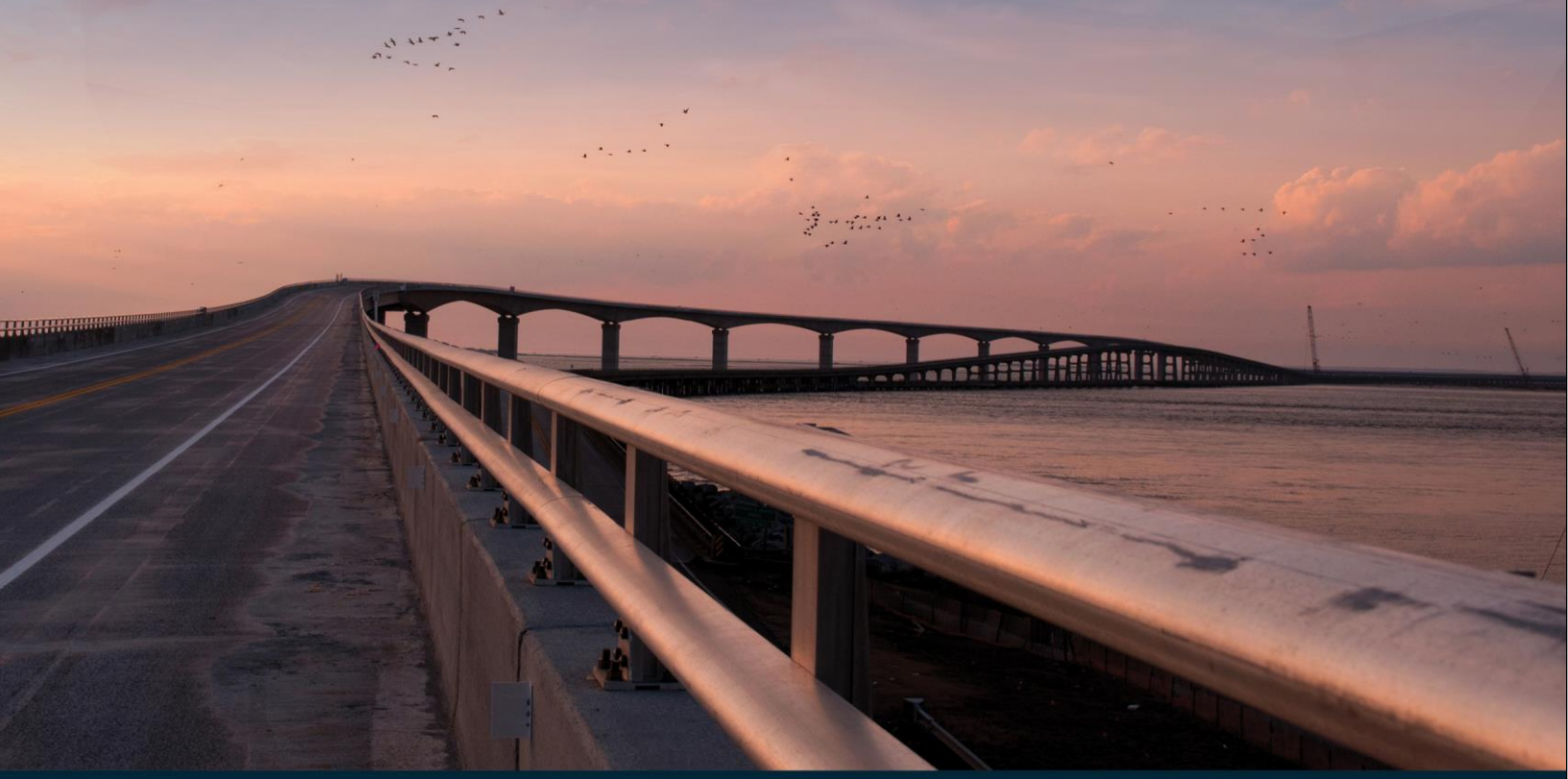

NCDOT Project 2021-09
FHWA/NC/2021-09
March 2024

Giorgio T. Proestos, Ph.D.
Rudolf Seracino, Ph.D.
Gregory Lucier, Ph.D.
Anindya Samya Saha, M.Sc.
Eric Throckmorton, M.Sc.

Department of Civil, Construction and Environmental Engineering
North Carolina State University

RESEARCH & DEVELOPMENT

Evaluation of the Bonner Bridge Girders: Assessing Residual Capacity, Prestress Losses and Degradation of the 56 Year Old Members

Principal Investigator	Dr. Giorgio T. Proestos
Other Investigator	Dr. Rudolf Seracino
Other Investigator	Dr. Gregory Lucier
Graduate Student	Anindya Samya Saha
Graduate Student	Eric Throckmorton

Department of Civil, Construction, and Environmental Engineering
North Carolina State University
Raleigh, NC

Prepared for:
North Carolina Department of Transportation
Research and Development

March 2024

Technical Report Documentation Page

1. Report No. FWHA/NC/2021-09	2. Government Accession No.	3. Recipient's Catalog No.
4. Title and Subtitle Evaluation of the Bonner Bridge Girders: Assessing Residual Capacity, Prestress Losses and Degradation of the 56 Year Old Members		5. Report Date 03/13/2024
		6. Performing Organization Code
7. Author(s) Giorgio T. Proestos, Rudolf Seracino, Gregory Lucier, Anindya Samya Saha, Eric Throckmorton		8. Performing Organization Report No.
9. Performing Organization Name and Address		10. Work Unit No. (TRAIS)
		11. Contract or Grant No.
12. Sponsoring Agency Name and Address North Carolina State University Research and Analysis Group 1 South Wilmington Street Raleigh, North Carolina 27601		13. Type of Report and Period Covered Final Report January 1. 2021 - December 31, 2023
		14. Sponsoring Agency Code 2021-09
Supplementary Notes:		

16. Abstract

Prestressed concrete bridges built in 1950s have deteriorated due to prestress loss, aging, and corrosion. If load rating criteria are not met, these bridges may be load posted or completely deconstructed. Accurate estimation of prestress loss and assessing the condition of in-service girders is vital, given the high cost of replacements. An example is North Carolina's Herbert C. Bonner Bridge, which was deconstructed after 56 years in service. Four recovered AASHTO Type III girders were tested in the lab. The results of the experiments and analyses were used to make recommendations on the performance of these girders, including discussion on prestress losses for girders with and without corroded strands, on improved prestress loss calculation methods, and on the remaining safe load carrying capacity of the selected bridge girders. Testing involved a small number of load cycles at low levels prior to montonically loading to ultimate capacity. The measured prestress losses for the four specimens were 44.3 ksi, 34.0 ksi, 35.4 ksi, and 36.0 ksi. Sectional analysis models of the girders were developed in Response-2000, which predicts the ultimate capacity and moment-curvature response with reasonable accuracy. The study has shown corrosion of strands can significantly influence effective prestress losses, and models developed in Response-2000 can capture these effects by accounting for the corroded strands. The study recommends the use of Response-2000 to model the behavior of aged prestressed concrete girders. At the time of replacement, the measured losses in the girders were such that the zero stress limit was exceeded under the service limit state according to the AASHTO LRFD Refined Method (using nominal material properties), the AASHTO LRFD Refined Method using measured material properties, Response-2000 with measured material properties and experimental measured values. In-situ material properties would ideally be used near the end of the service life to refine loss estimates, but it is not recommended at the design phase. The study recommends that the bridge girders could have operated safely under an extended service life if the zero tensile stress limit could have been relaxed under the service limit states, only at the end of the service life. The results indicated that the experimental flexural strengths far exceeded the service limit states, which is safe and conservative.

17. Key Words Prestressed Concrete Bridges, Prestressing, Design Practices, Cracking, Stiffness, Ultimate Load, Testing	18. Distribution Statement		
19. Security Classif. (of this report) Unclassified	20. Security Classif. (of this page) Unclassified	21. No. of Pages 315	22. Price

Form DOT F 1700.7 (8-72) **Reproduction of completed page authorized**

DISCLAIMER

The contents of this report reflect the views of the author(s) and not necessarily the views of the University. The author(s) are responsible for the facts and the accuracy of the data presented herein. The contents do not necessarily reflect the official views or policies of either the North Carolina Department of Transportation or the Federal Highway Administration at the time of publication. This report does not constitute a standard, specification, or regulation.

ACKNOWLEDGMENTS

The research team would like to thank the North Carolina Department of Transportation Steering and Implementation Committee who oversaw this project. The Steering and Implementation Committee included the following members:

Nick Pierce (Chair)
Brian Hanks
Gichuru Muchane
Trey Carroll
Doug Cantrell
Suzana Matta
Ashvin Patel
Aaron Earwood
Cameroon Cochran
Pablo Hernandez
Randy Midgett
Adam Venckauskas
Daniel Muller
Boyd Thrarrington
Mustan Kadibhai
Neil Mastin
Curtis T. Bradley

The research team would like to thank technician Mr. Johnathan McEntire at NC State's Constructed Facilities Laboratory (CFL) for his help with the laboratory testing.

EXECUTIVE SUMMARY

Prestressed concrete structures experience a reduction of the effective prestressing force in strands, often called the 'Prestress Loss', that occurs as a result of time-dependent effects such as creep, shrinkage and relaxation. Prestress loss is a factor in determining the lifespan of prestressed concrete bridge girders because, as the quantity of prestressing reduces, tensile stresses from service load moments can overcome the compressive stress from prestressing resulting in tensile stresses in the girders. The prestress losses as well as the condition of the in-service girders are factors used in load rating a structure. The strength or serviceability of bridge girders can be affected by the assumptions used for load rating. As a result, some transportation authorities, like the North Carolina Department of Transportation, may "load post" or limit the load allowed on the bridge if strength or serviceability criteria are not met, causing traffic disruptions. Four AASHTO Type III girders were recovered during the deconstruction of North Carolina's Herbert C. Bonner Bridge and brought to the laboratory for testing to failure. This project gives the opportunity to evaluate the losses of these four prestressed girders in varying conditions that were used in service for nearly 60 years. It also focuses on examining how the code-based methods for predicting losses and capacities perform for these aged girders. The results of the experiments and analyses were used to make recommendations on the performance of these girders, including discussion on prestress losses for girders with and without corroded strands, on improved prestress loss calculation methods, and on the remaining safe load carrying capacity of the selected bridge girders.

The four girders recovered from the laboratory for structural testing are referred to as the BTE series of experiments in this report. The BTE specimens were tested to failure at the Constructed Facilities Laboratory (CFL) at North Carolina State University, to evaluate strength and serviceability performance after 56 years of service in a corrosive environment. A small number of load cycles were performed at relatively low load levels prior to monotonically loading to ultimate capacity. The specimens were heavily instrumented to determine their deformation response throughout loading. This instrumentation included the use of high-resolution digital image correlation (DIC) equipment. The instrumentation was also used to monitor first cracking. Using the experimental data, prestressing losses at the time of testing in the laboratory were determined. Sectional analysis models of the girders were developed in Response-2000 to predict

load deformation response. Experimental results showed that BTE2, BTE3 and BTE4 had similar amount of prestress loss while BTE1 had a significantly higher loss of prestress attributed to a corroded strand near midspan. The measured prestress losses for the four specimens were 44.3 ksi, 34.0 ksi, 35.4 ksi, and 36.0 ksi for BTE1, BTE2, BTE3, and BTE4, respectively. The flexural capacities of girders BTE1, BTE2, BTE3, and BTE4 were 2831 k-ft, 2860 k-ft, 2699 k-ft and 2698 k-ft, respectively, which agrees reasonably well with the predictions given by the software program Response-2000. The loading of BTE3 and BTE4 was stopped before catastrophic failure occurred so that their end regions could be tested in shear. Response-2000 shows that the tests of these girders reached 97% and 98% of their predicted ultimate flexural capacities (2760 k-ft for BTE3 and 2780 k-ft for BTE4). The test-to-predicted ratio for the BTE series ranged from 0.971 to 1.006, with the predicted flexural capacities between 2760 and 2860 k-ft. The mean prediction was 2804 k-ft, and the results had a coefficient of variation of 1.56%. The moment-curvature response given by Response-2000 aligns well with the experimental response, including the transition in stiffness from the uncracked response to the cracked response. The study has shown corrosion of strands can significantly influence effective prestress losses, and models developed in Response-2000 can capture these effects by accounting for the corroded strands.

Current design equations for predicting short-term and long-term prestress losses are based on empirical relationships for a range of structural typologies. Material properties such as compressive strength and modulus of elasticity change with time and their estimation at a certain point in time is based on empirical relationships. Creep, shrinkage and relaxation are also a function of local environmental factors, such as humidity, temperature, and the amount of traffic. Approximate estimates are typically used in the design and evaluation of structures, but approximate methods may not reflect the exact conditions of a particular structure. Theoretical prestress losses were calculated using the methods described in the AASHTO LRFD. The methods include the AASHTO LRFD Refined Method (using nominal material properties), the AASHTO LRFD Refined Method consistent with NCDOT assumptions, the AASHTO LRFD Refined Method using measured material properties, and the Lump Sum Method. The Refined Methods give reasonable estimates of losses for BTE1 with corroded strands. For BTE2, BTE3, and BTE4, the Refined Method using nominal material properties and the Refined Method consistent with NCDOT assumptions are both conservative approaches with a mean test-to-predicted ratio of 0.76 and 0.78, respectively. Lump Sum estimates are found to be more conservative than Refined

Methods with test-to-predicted ratios between 0.66 and 0.80. The results of this study indicate that using measured material properties with the AASHTO LRFD Refined Method gives more accurate estimates of losses, as compared to laboratory measurements, with test-to-predicted ratios between 0.92 and 1.09.

The ultimate load capacity and stresses at cracking were eventually incorporated in a load rating calculation of the girders. Theoretical and experimental results indicate the rating factors exceed 1.0 under the Strength I (both inventory and operating) and Service III limit states (for an allowable stress of $6\sqrt{f'_c}$). Therefore, the structure has sufficient load carrying capacity under these limit states with the HL-93 design truck considered for estimating live loads. However, the rating factors are less than 1.0 for the zero tensile stress criteria under the Service III limit state. The results indicate the zero tensile stress limit is not near the capacity of the members and significant benefits could be achieved if this zero stress limit is relaxed in some scenarios.

The study also provides a unique opportunity to determine the shear capacity of these aged girders in certain load configurations. Shear testing was conducted to examine the shear response in scenarios where the load is applied near to a support. Both ends of BTE3 and one end of BTE4 were tested in shear. While it was not possible to catastrophically fail one end of BTE3 as the actuator capacity was reached, the end region capacity of the girders in applied shear were 287 kips and 276 kips. The corresponding applied moments were 2585 k-ft and 2447 k-ft. BTE4 failed at an applied shear of 274 kips. The applied moment in this case was 2394 k-ft. The maximum crack width observed was 2.50 mm and the failure was brittle in nature.

The study recommends the use of Response-2000 to model the behavior of aged prestressed concrete girders, as the software was shown to predict both the load-deformation response and ultimate capacity of beams with reasonable accuracy. In-situ material properties would ideally be used near the end of the service life to refine loss estimates, but it is not recommended at the design phase. The results indicated that the experimental flexural strengths far exceeded the service limit states, which is safe and conservative. The study recommends that the bridge girders could have operated safely under an extended service life if the zero tensile stress limit could have been relaxed under the service limit states, only at the end of the service life. At the time the girders were replaced, the measured losses in the girders were such that the zero stress limit was exceeded under the service limit state according to the AASHTO LRFD Refined Method (using nominal

material properties), the AASHTO LRFD Refined Method using measured material properties, Response-2000 with measured material properties and experimental measured values.

TABLE OF CONTENTS

LIST OF FIGURES

LIST OF TABLES

CHAPTER 1 – INTRODUCTION

1.1. Background

Application of prestressed concrete beams to highway bridges in the United States dates to the 1950s. One factor that contributes to the continued popularity of prestressed concrete for long-span flexural members is that these members are often capable of remaining uncracked throughout their service lives. Cracking in concrete facilitates water infiltration which leads to the progression of corrosion of the reinforcing steel, concrete spalling, and eventually a reduction in load carrying capacity of a bridge girder. This deterioration from cracking can reduce the service life and increase maintenance costs. Prestressed concrete resists flexural cracking because the prestressing steel, often referred to as strands or tendons, is tensioned to produce compressive stresses in the concrete. By adding precompression, an applied moment must first relieve the compressive stress in the girder concrete resulting from prestressing before a tensile stress can be produced. Therefore, the moments required to crack a prestressed concrete member are typically significantly higher than those required to crack a similar reinforced concrete member. Designs can be configured so that the service loads placed on a prestressed concrete member may never exceed their cracking capacity. However as prestressed concrete structures age, time dependent effects such as shrinkage and creep of concrete and relaxation of steel cause a reduction in the effective prestressing force. This loss of strand tension in the strands implies a loss of compression in the concrete. This loss of strand tension is the common definition adopted for “prestress loss” and is the definition used in this report. Thus, final prestress losses in a girder would be the difference in the initial strand tensile stress, just prior to transfer, and the effective prestress at the end of service life of the member.

As concrete forms the products of hydration after casting and any excess free water evaporates, the concrete will shrink. Unrestrained shrinkage reduces the length of members thereby resulting in a prestress loss. Creep is the long-term increase of concrete strain under constant stress. Since the tensioning of the prestressing steel produces a compressive stress in the member, creep in the concrete will result in an increasing compressive strain throughout its life, stated otherwise as a shortening of the concrete element. Like shrinkage, the reduction in total strand strain resulting from concrete creep reduces the force in the prestressing strand and

contributes to prestress losses. Finally, relaxation of the prestressing steel is the reduction in stress at a constant strain over time. In a prestressed concrete structure, the relaxation of the strands will result in reduced strand tension, and thus, reduced compressive stress in the concrete. Figure 1.1 shows a representation of creep and relaxation on the stress-strain response of the concrete and steel. While it is convenient to think of creep, shrinkage and relaxation as independent phenomena, however, they occur simultaneously and interact with one another throughout the life of the structure.

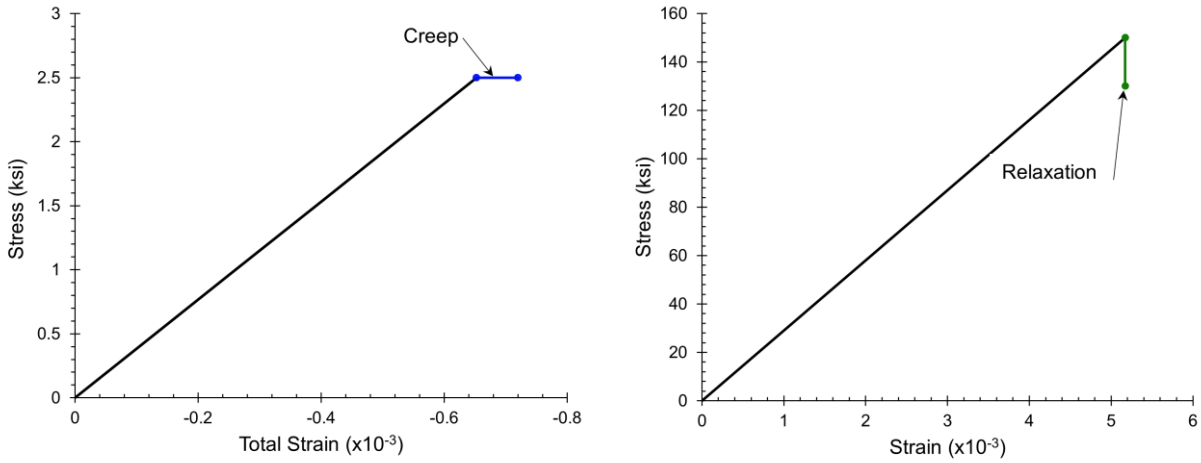

Concrete Response

Steel Response

Figure 1.1: Representation of losses from creep and relaxation.

The cumulative effect of these long-term losses reduces the effectiveness of the initial prestressing of the concrete. As the pre-compression applied to a section decreases, tensile stresses from applied moments on simply supported members can more easily overcome the compressive stress generated by prestressing, making the member more susceptible to cracking. While prestressed concrete may increase the durability of a member by reducing cracking, and thereby corrosion, the long-term loss of prestressing acts as a limit on the serviceable life of a prestressed concrete member, especially if a zero-tension limit state criterion is imposed. For bridge structures, many government agencies, including the North Carolina Department of Transportation (NCDOT) require that the service loads placed on a bridge do not cause tensile stress to any portion of concrete in any cross-section. Figure 1.2 shows the short-term moment curvature response for different levels of prestress loss to illustrate the reduction of a girder's cracking moment for increasing prestress loss. Note the ultimate strength is not significantly affected by the reduction

of prestressing, but the cracking moment decreases significantly as the losses become more severe indicating tensile stresses in the concrete begin at lower loads with increasing losses.

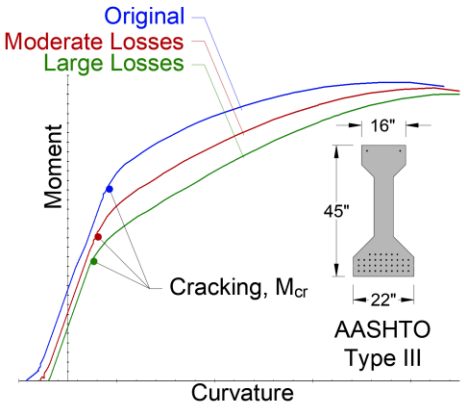

Figure 1.2: Decrease in cracking moment as prestress losses increase.

Since the serviceability and performance of prestressed concrete girders essentially depends on the existing effective prestressing force, accurate estimation of prestress losses can directly improve the accuracy of condition assessment. An over-prediction in prestress losses results in an overly conservative design for service load conditions, while an under-prediction in prestress losses, depending on the severity of the under-prediction, could result in cracking under service loads. Over the last decade, only few parametric studies investigating prestress losses in prestressed concrete girders have been conducted (Garber et al., 2015; Higgs et al., 2015; Pessiki et al., 1996; Rizkalla et al., 2010; Steinberg, 1995; Tadros et al., 1977). Estimation of prestress loss is complex in nature because of variations in initial stressing conditions, difficulty in predicting the variation of environmental conditions at the site after prestressing, estimation of material properties (e.g. concrete strength and, ultimate tensile strength of strands), factors contributing to concrete shrinkage and creep and their interdependence, varying geometry of the member, and more. Additionally, the losses are a function of load on the structure which can be estimated with accuracy that will vary based on the specific girders examined.

The Herbert C. Bonner Bridge spanned the Oregon Inlet in the North Carolina Outer Banks, and construction was completed on the bridge in the early 1960s. As a result of deterioration and other factors, the Bonner Bridge was deconstructed after the new Marc Basnight bridge was completed. The Bonner Bridge consisted of 260 spans, with a majority constructed from utilizing

AASHTO Type III prestressed concrete girders with cast-in-place concrete decks. A few of the 260 spans, particularly those crossing over the navigation channel, were founded on steel plate girders. During deconstruction, four AASHTO Type III girders, each approximately 61 feet long, were recovered as part of this research. The purpose of the research program is to determine the performance of prestressed concrete girders after 56 years in use. The girders were brought to the Constructed Facilities Laboratory (CFL) at North Carolina State University (NCSU) for structural destructive testing to determine the prestress losses and the ultimate flexural capacity. Measured prestress losses from the tests are compared to several analytical procedures currently practiced such as the AASHTO LRFD Refined Method and the AASHTO Lump Sum Method, and the AASHTO Standard Specifications. Testing of the aged girders sheds light on the load-deformation response and provides experimental data on the prestress losses after 56-years in service. In addition, tests documented the cracking loads and ultimate loads for each girder. The results are used to provide recommendations related to prestress losses for the North Carolina Department of Transportation. The research program provided the unique opportunity to also determine the shear capacity of recovered bridge girders by testing the ends of the members. The tests provide insight into the shear capacity of aged girders when loaded near their ends.

1.2. Research Significance

One of the main advantages of prestressing concrete structures is to delay the occurrence of cracks by pre-compressing the concrete. Prestress losses that occur throughout the life of bridge girders reduces the efficacy of the prestressing. Designers must consider these prestress losses at design and during the evaluation of existing structures to determine if service limits are expected to be exceeded. There have been very few large-scale tests of prestressed concrete girders recovered from service to determine long-term prestress losses. This research provides the opportunity to investigate four prestressed concrete girders that experienced 56 years of service in a corrosive environment. The four girders were brought to the CFL at NCSU and destructively tested to failure. The experiments were used to determine the full load deformation response, strength in flexure, cracking moments and amount of effective prestressing. The experiments also provide information on the stiffness of the girders, and the influence of deterioration including corrosion of strands that has occurred. The research explores how long-term effects can change service and capacity estimates. The results also informs how losses are determined for girders with and without

corrosion. The experiments were instrumented with Digital Image Correlation (DIC) to measure the displacement field response of the members so that accurate estimates of first cracking and the prestressing losses could be determined. The measured prestress losses are compared with several analytical procedures. The measured prestress loss and flexural strengths obtained from the experiments are then used to conduct load rating calculations of the bridge according to the provisions of LRFR and LFR.

1.3. Layout of the Report

The balance of this report is divided into the following chapters:

- Chapter 2 contains a review of relevant literature. It reviews the best practices for calculating prestress loss and remaining flexural capacity. Existing research and findings on prestress losses in concrete girders are discussed in Appendix A.
- Chapter 3 discusses the experimental program for testing the four prestressed concrete girders recovered from Bonner Bridge, referred to in this report as the BTE series of experiments. The chapter discusses material properties that affect prestress losses and covers the experimental program for testing of materials. It includes the specimen details, specimen condition assessment identifying existing damage or repairs. Appendix B provides additional details on the experimental program such as the detailed test setup, instrumentation, and loading protocol.
- Chapter 4 presents the experimental results from the BTE series. Results such as the load-deformation behavior, longitudinal strains, cracking moment, crack reopening moment, and ultimate flexural capacity of the members are presented. Appendix C provides additional details of the experimental results.
- Chapter 5, discusses the loss of prestress in the recovered girders. Prestress losses are measured from the results of the flexural testing of the girders. Response-2000 is used to predict the behavior of the girders along with composite deck and estimate the nominal flexural and shear resistance of the structure with the deck. In addition, theoretical prestress losses are calculated according to the AASHTO LRFD Refined Method, the AASHTO LRFD Lump Sum Method, and the AASHTO Standard Specifications, and the results are compared with measured prestress losses from the experiments.

- In Chapter 6, load rating of the bridge according to both the Load and Resistance Factor Rating (LRFR) Method and the Load Factor Rating (LFR) Method are estimated. It discusses the use of measured prestress losses and actual flexural resistance of the member to inform the load rating. The results from code based predictions and the experimentally observed response are discussed. Appendix G provides additional context and bridge load rating calculations.
- Chapter 7 summarizes the conclusions and recommendations determined from the research.
- Appendix H includes a summary of the shear testing of the girders. In includes the experimental program, shear behavior, the detailed load-displacement response and the deformation pattern of the girders throughout loading.

CHAPTER 2 – LITERATURE REVIEW

2.1 Prestress Loss Calculation Methods

The negative effects of prestress losses were understood very early in the development of prestressed concrete structures. As early as 1958, a joint American Concrete Institute (ACI) and American Society of Civil Engineers (ASCE) committee developed Tentative Recommendations for Prestressed Concrete (ACI-ASCE, 1958), a document that included methods for determining the long-term prestress losses. The committee provided two different methods for determining prestress loss. Method 1 assesses the loss of steel stress using a combination of the individual loss components, and Method 2 provides different approximate losses for pre-tensioned and post-tensioned concrete structures (ACI-ASCE, 1958). Method 1 uses Eq. 1 to estimate the change in strand stress, Δf_s, where u_s is the strain in the concrete from shrinkage, u_e is the strain in the concrete from elastic shortening, u_d is the strain in the concrete from creep, E_s is the elastic modulus of the prestressing steel, δ_1 is the ratio of loss in steel stress from relaxation, δ_2 is the ratio of loss in steel stress from friction during prestressing, and f_{si} is the initial stress in prestressing steel after seating of the strand anchors.

$$\Delta f_s = (u_s + u_e + u_d)E_s + \delta_1 f_{si} + \delta_2 f_{si} \quad (1)$$

Method 2 states that the loss in the steel not including friction loss is 35,000 psi for pretensioned structures and 25,000 psi for post-tensioned structures. The two different values for pre- and post-tensioned concrete reflects the difference in losses that result from the two forms of tensioning and different anchor sets. The ACI-ASCE joint committee's loss estimates are Lump Sum estimates of the change in strand stress from long-term losses. Lump Sum Methods are not as versatile as methodologies that account for more complex effects, such as detailed loading histories, however Lump Sum loss calculations are simple to perform and can be appropriate in certain scenarios.

The literature describes that prestress loss calculation procedures can be generally categorized into three approaches, listed in ascending order of complexity a) Lump Sum Methods b) Refined Methods, and c) Time-Step methods (Garber et al., 2015; Russel and Jayaseelan, 2007; Steinberg, 1995; AASHTO LRFD BDS, 2020). Typical lump-sum methods represent average

conditions, viable only for members with normal weight concrete (either steam or moist cured), strands with low relaxation properties or prestressed by bars, and average exposure conditions and temperatures (AASHTO LRFD BDS, 2020; NCHRP Report 496, 2003). An example of a current lump sum method is provided in the AASHTO LRFD Bridge Design Specifications as the Approximate Estimate of Time-Dependent Losses (AASHTO, 2020). The equations of the Lump Sum Method have been updated over the years, and it is believed that although it somewhat overestimates the prestress loss, the method can give reasonable results and can be appropriate in preliminary design or other scenarios where more refined estimates are not required. Many DOTs in the United States use Lump Sum methods to estimate their prestress losses. More complex methodologies such as the Refined Method and the Time-Step Method are required to model and predict prestress loss at a specific time in different stages of the life of the structure. More complex methods are sometimes needed because stresses in the concrete and in the strand are constantly interacting with one another and change over time. As steel strand relaxes, not only is the stress in the strand decreasing and reducing the rate of relaxation, but the stress in the concrete also reduces and concrete creep occurs more slowly. In addition to the interactions between loss components, structures undergo a variety of different loading conditions throughout their life that change the state of stress of the members. Figure 2.1 is reproduced from the National Cooperative Highway Research Program (NCHRP) Report 496 (Tadros et al., 2003) on Prestress Losses in Pretensioned High-Strength Concrete Bridge Girders. Figure 2.1 shows a representation of the changes in strand stress over time for pretensioned concrete structures. Both these methods calculate prestress loss by accounting for each increment in time and calculating the updated strains and stresses in each of the materials. These strains can then be related back to global response. The Refined Method is used to determine the individual loss components due to creep, shrinkage and relaxation separately, and then sums up the components to give the total prestress loss. Lump-Sum methods are a generalized form of the Refined Method, in that they approximate Refined Method calculations and provide a simplified equation to determine prestress loss.

The Refined Method is used to determine the total loss of strand stress at any stage of the life of structure by dividing the time frame into two phases. The Time-Step method is more complex since stresses and strains of the structure are updated over much shorter time intervals to give a more accurate estimation of the prestress loss, and hence, can account for the events shown in Figure 2.1 appropriately. An early example of Refined Methods for assessing prestress loss can

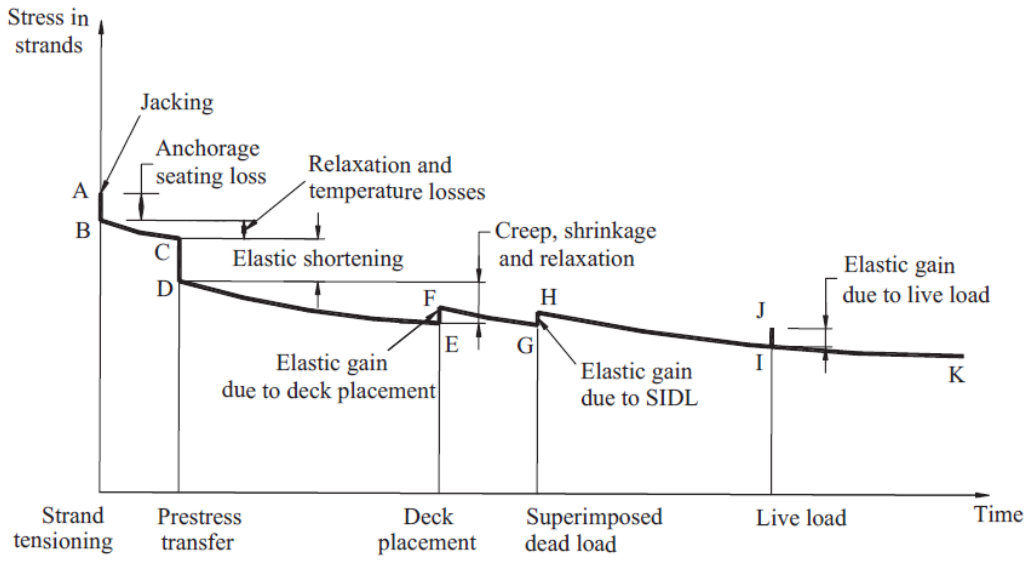

Figure 2.1: Pretensioned concrete girder strand stress over time (reproduced from Tadros et al., 2003).

be found in the eleventh edition of the AASHTO Standard Specifications for Highway Bridges published in 1973 (AASHTO, 1973). Refined Methods are desirable for the design of new construction and for the assessment of aging infrastructure because they do not require a computerized calculation processes like the even more complex Time-Step methods do. Examples of current Refined Methods of prestress loss assessment are given in the PCI Bridge Design Manual (2014) and AASHTO LRFD Bridge Design Specifications (2020). These two Refined Methods are conducive for use on bridge structures like the Herbert C. Bonner Bridge, and they are discussed in detail in sections A1.1 and A1.2 of Appendix A1. The AASHTO LRFD loss calculations are currently used by the NCDOT for the assessment of aged bridges. For this reason, combined with the prevalence of AASHTO LRFD Refined Method for assessment of bridge structures, this loss prediction method is the focus of analysis in chapter 4 of this report. The results are also compared with experimentally obtained prestress loss, Lump-Sum methods, and losses calculated using actual material properties instead of nominal properties in AASHTO LRFD equations.

Lastly, Time-Step methods are the most complex option, implemented with the equations for Refined Methods fed into a computer program, where time-dependent losses are measured in four different stages of varying time steps according to specific events occurring over the service

life of a prestressed concrete girder. The strains and stress along the girder are updated with each time increment, and the strains can be related back to the global response. The strand stress changes more frequently in the early life of a concrete structure, so the time intervals in a Time-Step analysis may start as a relatively short increments, becoming longer as the structure ages in the analysis. An example of time step loss analysis is given by Tadros et al. (1977). These methods are powerful and can account for complicating factors such as varying cross sections over time, composite action, material property changes through the depth, and varying loading over time, but the complexity of these methods precludes them from frequent use in the assessment of aging prestressed concrete infrastructure. The application of a Time-Step method also requires detailed information of loading conditions that occur throughout the time period being examined which may not be available.

Although the aforementioned methods can be used to estimate prestress loss at any stage of the life of a structure, there have been only few experiments to measure and verify the amount of losses in aged girders. The experimental research programs performed on prestressed concrete bridge girders by Tadros et al. (2003), Miller et al (2000), Pessiki et al (1996), and Russell and Burns (1996) observed that the PCI Design Handbook method, ACI 318, and AASHTO-LRFD equations all overestimated the prestress losses. Besides these studies, few have attempted to measure prestress losses in existing or deconstructed real world prestressed concrete bridges by flexural testing of the specimens. Even rarer is the evaluation of structures 50 years or older. Visual inspections of concrete and steel and the use of acoustic emission (AE) sensors and a few other non-destructive techniques are currently the only field level practices commonly used to estimate girder condition. These inspections have issues of subjectivity and complexity of determining the actual structural capacity from observed external damage. The condition assessment does not explain the performance of structures under existing loads and any measure of prestress loss from the non-destructive techniques needs further research for reliability and accuracy (Civjan et al., 1998).

Additional descriptions of methods in the literature, experimental investigations into prestress losses in concrete structures, and studies on creep, shrinkage and relaxation are discussed in Appendix A.

2.2 Evaluation of Loss Methods for Peer Departments of Transportation

As part of the research program, a survey was conducted to gather information from state agencies about practices related to prestress loss calculations in precast prestressed bridge girders. The questionnaire specifically aimed at understanding prestress loss calculation procedures currently practiced, and tried to acquire information about whether peer state departments of transportation outside North Carolina use the AASHTO LRFD Refined Method, the Lump Sum Method, or other procedures developed specific to that DOT. The survey also inquired as to the assumptions used in loss estimates, such as the use of nominal versus measured properties, the maximum allowable tensile stress under service conditions, whether to account for deterioration of a structure when updating prestress loss, and finally, the steps taken to inform load rating of these bridges at any point of their service life.

As discussed in this chapter, prestress loss consists of two components, the initial elastic loss and long-term loss due to shrinkage, creep, and relaxation. The responses from the survey indicate peer DOTs follow a range of methods and standards when it comes to assessing short-term and long-term prestress losses. The initial elastic losses are most commonly calculated according to AASHTO LRFD Eq. 5.9.3.2.3a-1. The long-term losses are most often determined according to the provisions of the AASHTO LRFD Refined Method (5.9.3.4), as some peer DOTs indicate the method gives reasonable estimates of long-term losses. In the Refined Method, different agencies make different assumptions as to the age of beam concrete at deck placement, to include 28 days, 56 days (NCHRP Report 496), 60 days, 90 days (a rule of thumb based off guidance from the PCI Bridge Design Manual), and up to as much as 180 days. Girders constructed at facilities require time for transportation to site and often there are delays to project schedules.

The DOTs often select the exact age of concrete instead of relying on standard numbers. While choosing the age of concrete at deck placement, DOTs assume that significant long-term girder deflections due to shrinkage, creep, and relaxation have already occurred so that the deck grade can be set and maintained. The final age of concrete is either taken as the exact age, or a standard value to include 27 years (used by peer DOTs), 56 years (PCI-BDM, 2014; NCHRP Report 496), or even 75 years (used by peer DOTs).

As much as the AASHTO LRFD Refined Method is used, the Lump Sum Method is also commonly used. The survey revealed DOTs also use the Lump Sum long-term loss equation from previous versions of the AASHTO LRFD Bridge Design Specifications, and may have not yet adopted the 9th Edition of the Standard. Some peer DOTs indicate that the "old" long-term Lump Sum equation in AASHTO LRFD 4th Edition generates results similar to even older prestress loss recommendations whereas the current AASHTO LRFD equations often generate significantly lower prestress loss values. Some DOTs recommend the use of "old" long–term equations for estimating prestress losses in pre-decked girder sections, as they indicate the current AASHTO equations were not developed for such structures and gives inaccurate results.

At the design phase, prestress loss calculations are carried out with nominal material properties. Generally, prestress losses are not reevaluated at any stage of service life of girder because of any kind of deterioration and practices such as core extraction from girders to determine existing material properties is not commonly conducted for this purpose. When prestressed concrete girder bridges are load rated, however, the existing condition of the bridge is taken into account through thorough inspection and identifying deterioration such as concrete spalls, corrosion, etc. The long -term effects of corrosion are not usually linked by calculation procedure to prestress loss, as corrosion is usually only accounted for in capacity calculations by removing exposed and corroded strands.

There are also some differences in how the different DOTs consider superimposed dead loads and live loads for prestress gain under service conditions in the calculation of final prestress loss. Three cases were observed: 1) Consideration of prestress gains from both superimposed dead loads and live loads in prestress loss; 2) Exclusion of live load gains in prestress loss; and 3) Exclusion of any prestress gain in the calculation of prestress loss. NCDOT considers both non-composite (girder self-weight, diaphragm, build-up/haunch, deck etc.) and composite loads (asphalt wearing surface, bridge rails, future wearing surface) in creep calculation for final time, and also in elastic gains due to deck weight and superimposed dead loads. Prestress gain also comes from the shrinkage of the deck, but some DOTs suggest losses after concrete deck curing (after the deck becomes composite section) are generally small. So, the prestress gain due to deck shrinkage in the composite section is relatively small compared to the overall prestress loss over

the entire service life, and does not significantly affect the final prestress loss. Nevertheless, the loss component is still considered in calculation of prestress losses by some DOTs.

In the case of load rating the bridge, the Load and Resistance Factor Rating (LRFR) method is generally followed. However, some DOTs prefer to rate old bridges according to their design method, which is consistent with Load Factor Rating (LFR). An important finding is that there are a wide range of stresses allowed under the service condition, ranging from 0 to $3\sqrt{f_c'}$ to even $6\sqrt{f_c'}$. The tensile limit chosen is often project specific.

Overall, the survey provided information to identify the choice of methods and assumptions used by peer DOTs to determine prestress losses. The findings inform the theoretical prestress loss calculation procedure used for the BTE test series. Prestress loss estimates are also important when determining the load rating of the bridge under service and ultimate conditions. Both prestress loss calculation and load rating determination involves accounting for a number of variables such as material properties, time intervals chosen for estimating prestress loss components, deterioration such as corrosion and its impacts, allowable tensile stress, and more. The survey provides useful information on selecting or estimating these variables to improve the accuracy of prestress loss estimation and of load rating calculations for the BTE series.

CHAPTER 3 – EXPERIMENTAL PROGRAM

To assess the amount of prestress losses in aged bridge structures and to improve methods for determining predicted prestress losses, four girders from The Herbert C. Bonner Bridge in North Carolina were recovered and tested at North Carolina State University's (NCSU) Constructed Facilities Laboratory (CFL). These four girders are labeled the BTE series, and were all in service for approximately 56 years. The BTE experimental program provides the opportunity to determine the amount of prestress losses and the influence of losses and degradation on the performance of the girder in flexure by investigating first cracking and ultimate capacities. This chapter discusses the experimental program, including specimen specifications and conditions, tested material properties, experimental setup, and instrumentation. Further details including methods of testing material properties, instrumentation and loading protocol are described in Appendix B.

3.1 Bonner Bridge Specimens

The concrete girders recovered for testing consisted of four AASHTO type III girders that utilized a composite deck during service in the field. The girders were taken from span number 142 of the Bonner Bridge and temporarily stored at a yard in Oxford, North Carolina before being transported to the CFL. The decision to select these girders was based on their condition and their availability relative to the deconstruction schedule. The condition of the selected girders was considered typical based on the 2007 site report produced by the Alpha & Omega Group, an inspection agency contracted by the NCDOT at that time. As discussed in the next section, this assessment was consistent with observations made by NCSU of the girders just prior to testing. All four recovered girders were 45 in. tall AASHTO Type III sections measuring 61 ft. long. The laboratory testing of recovered girders is discussed herein, and the exact condition of each tested girder was documented prior to instrumentation and testing at the CFL. These condition assessments contain any noted damage to the girders upon arrival to the CFL, and a measurement of camber for each simply supported girder. The condition assessment of each tested girder is discussed in the next section. In addition to condition drawing summaries, the NCDOT provided the original construction drawings for the Bonner Bridge, and from the drawings, strand layout and shear reinforcement of the girders is summarized below (see Figure 3.1 and Figure 3.2).

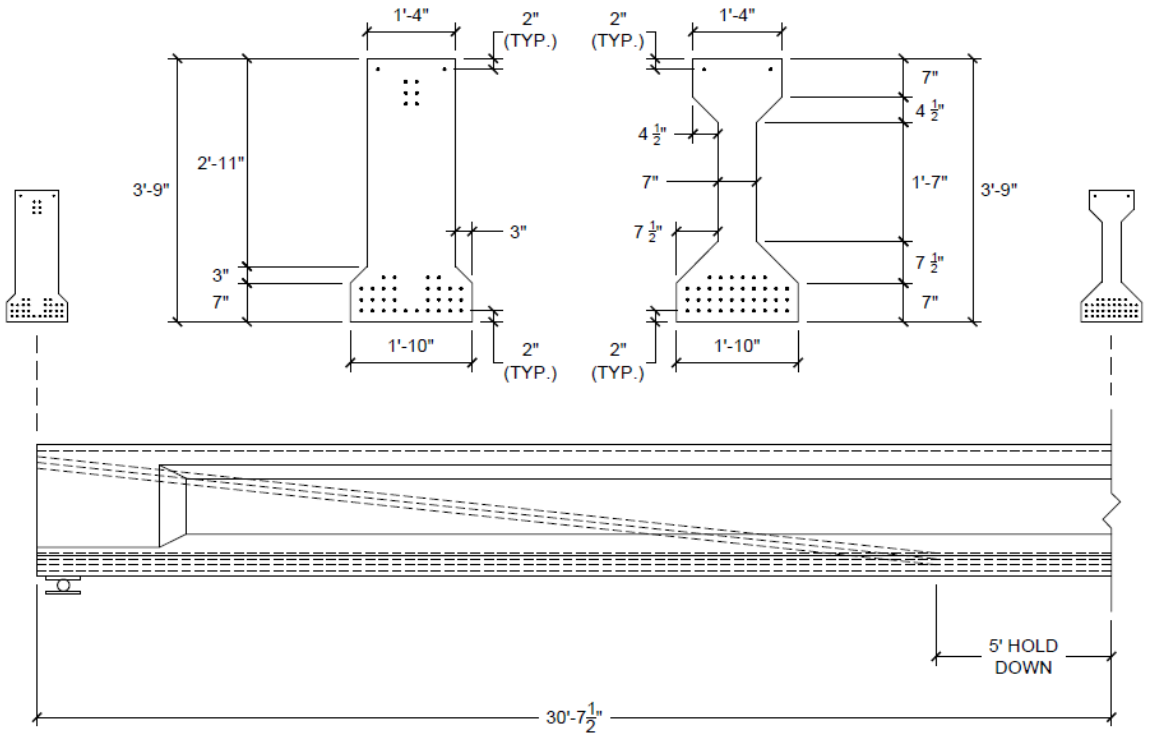

Figure 3.1: Bonner Bridge half-span elevation view strand layout (reproduced from Bonner Bridge plans originally prepared by Structural Design Unit of DOT).

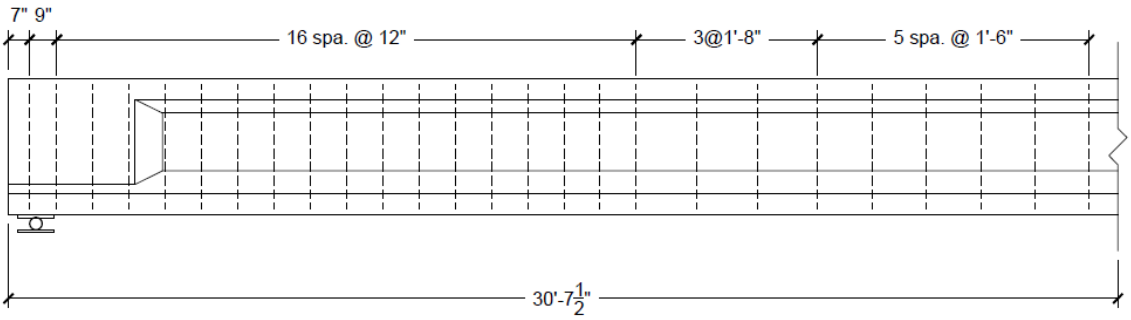

Figure 3.2: Bonner Bridge half-span elevation view stirrup layout (reproduced from original construction drawings).

Each precast girder had 38 stress-relieved 7/16 in. diameter strands: two in the flexural compression region and 36 in the flexural tension region. Six of the 36 strands in the flexural tension zone were harped with harping locations at 5 ft. on either side of midspan. As indicated in the drawings, the strands were each tensioned to 18,900 lbs prior to casting. The shear reinforcement consists of #4 vertical stirrups (1/2 in. nominal diameter). Measuring from the end

of a girder, stirrups were spaced at approximately 12″ on center through the shear span, transitioning to no more than 20″ in the midspan region (see Figure 3.2). The specified girder concrete strength was 5000 psi, and the specified cast-in-place concrete deck strength was 3000 psi. To enable transport of the girders, the concrete deck was cut off the girders during bridge deconstruction. However, to ensure no damage occurred to the girder itself when removing the concrete deck, the cut occurred approximately two inches above the top of the girder, leaving a thin residual layer of deck concrete bonded to the top of each girder.

3.1.1 Condition of BTE1

A summary of the condition of BTE1 can be seen in Figure 3.3.

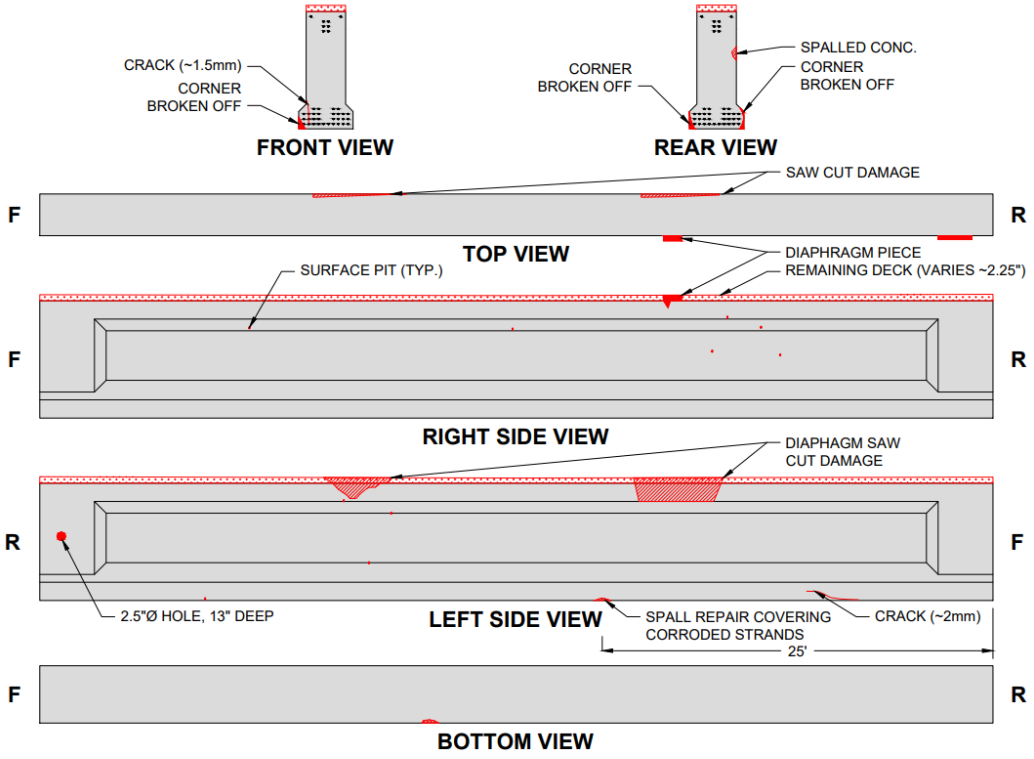

Figure 3.3: Condition of BTE1 (horizontal scale reduced).

Figure 3.4 also provides supporting photos of the condition observed in the laboratory prior to testing. BTE1 had approximately 2.25 in. of concrete deck remaining on the top of the girder. There is also some sawcut damage to the top flange near where site-cast concrete diaphragms were removed. A spall repair near the girder's midspan, as seen in Figure 3.3, covered a strand in the bottom row of strands that was nearly completely corroded. Additionally, the spall repair covered

another strand in the bottom row that was only partially corroded. Figure 3.5 shows these corroded strands after flexural failure of the girder.

Rear end core hole (left side)

Front end bottom crack (left side)

Rear end diaphragm sawcut damage (left side)

Front end diaphragm sawcut damage (left side)

Figure 3.4: Condition of BTE1 photos.

Figure 3.5: BTE1 corroded strands (visible only after testing).

With the girder simply supported, camber measurements were taken along the length of the girder by stretching a string line taught across the bottom flange of the girder and measuring from the string line to a consistent place on the section. Figure 3.6 shows the camber measurements taken along the length of the girder. The maximum measured camber was 1-7/8 in. at the midspan.

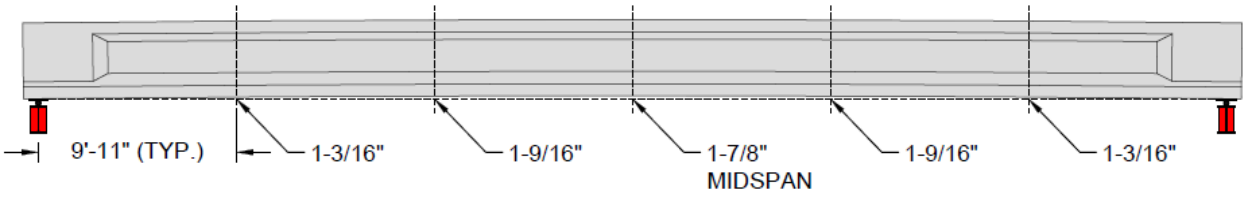

Figure 3.6: BTE1 camber measurements.

3.1.2 Condition of BTE2

A summary of the condition of BTE2 can be seen in Figure 3.7. Figure 3.8 also provides supporting photos of the condition in the laboratory. BTE2 had approximately 1.5 in. of residual concrete deck remaining after saw cutting. The specimen has some top cracking, which likely resulted from the transportation of the girder. When the specimens were inspected at the temporary storage yard, no top cracking was observed. Thus, the top cracking likely occurred during transport to the

laboratory from Oxford, NC, or was not as visible in the storage yard. The condition of BTE2 was, overall, very good. Unlike BTE1, there was no damage to the top flange from removal of the concrete deck, nor was there any evidence of repairs covering heavily corroded strands.

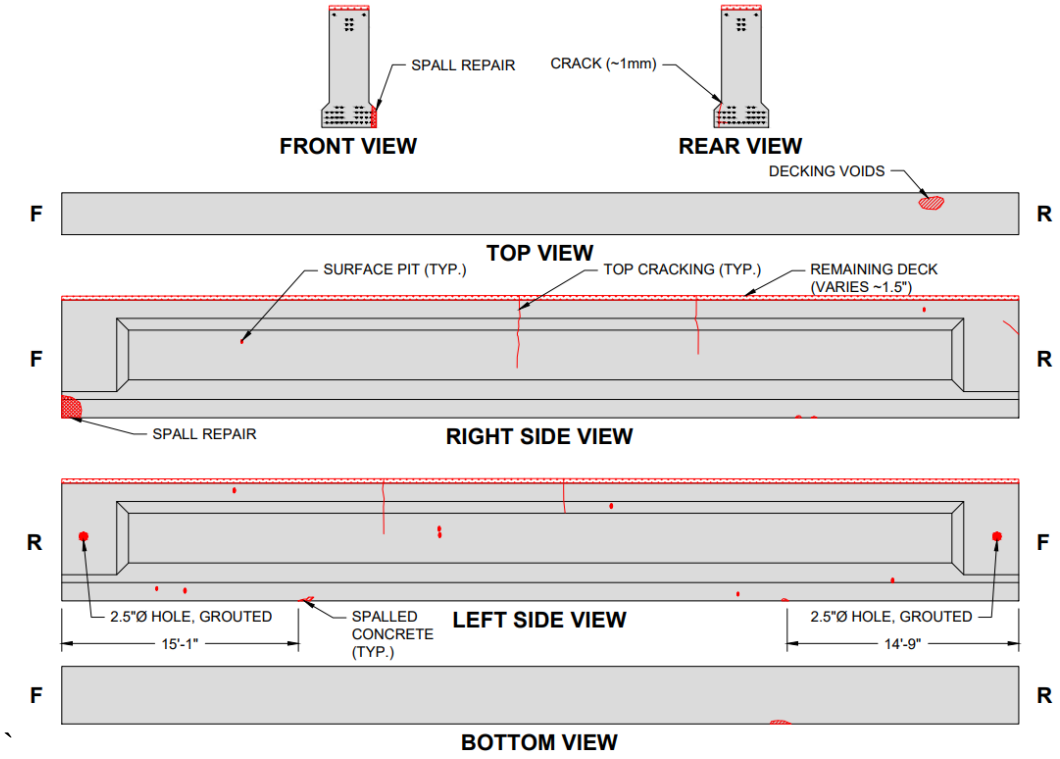

Figure 3.7: Condition of BTE2 (horizontal scale reduced).

Rear deck honeycombing (top)

Rear end grouted hole (left side)

Midspan top cracking (right side)

Front corner spall repair (right side)

Figure 3.8: Condition of BTE2 photos.

With the girder simply supported, camber measurements were taken along the length of the girder, similar to BTE1. As shown in Figure 3.9, the maximum camber measured along the length of the girder was 3/4 in. at the midspan. The measured camber of BTE2 was the least measured across the recovered girders.

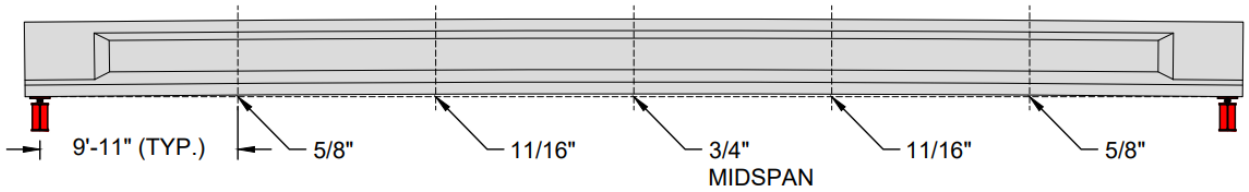

Figure 3.9: BTE2 camber measurements.

3.1.3 Condition of BTE3

A summary of the condition of BTE3 can be seen in Figure 3.10. Figure 3.11 also provides supporting pictures of the condition in the laboratory. BTE3 had 1.75 in. of residual concrete deck remaining, and like BTE2, some top cracking occurred during transport to the CFL. BTE2 and BTE3 were in similar conditions, except that BTE3 had a section of exposed strand visible near the quarter point at one end.

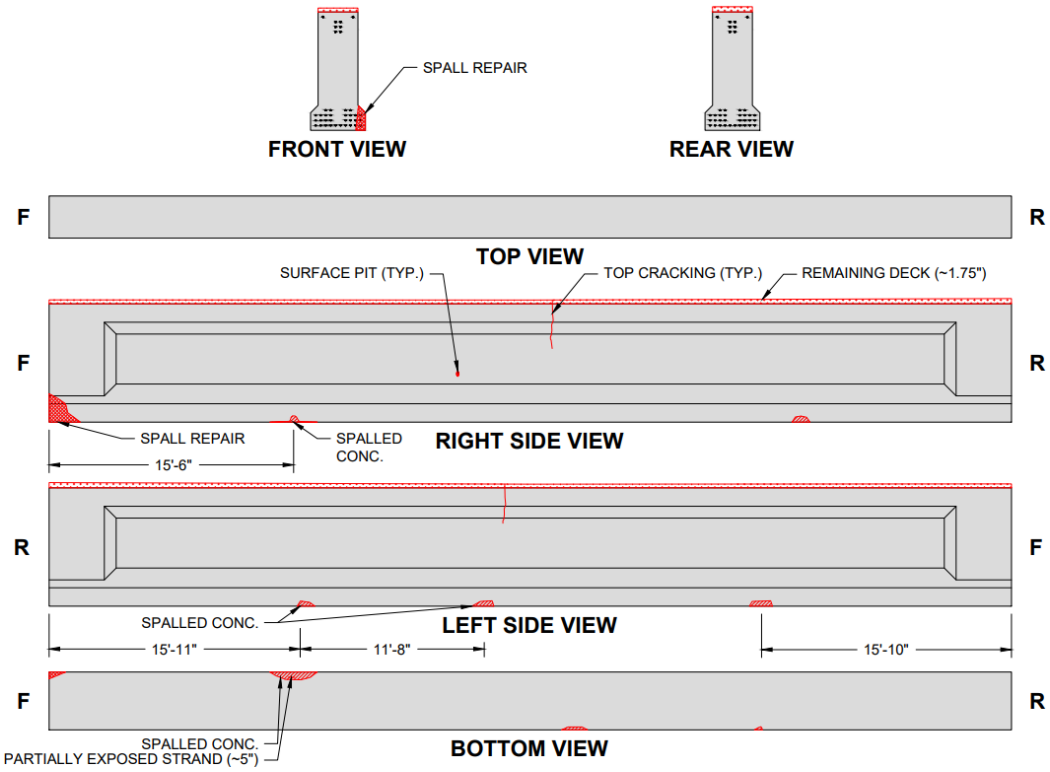

Figure 3.10: Condition of BTE3 (horizontal scale reduced).

Figure 3.11 shows this exposed strand with corrosion not severe enough to significantly reduce the total area of the strand.

Bottom flange damage (left side)


Midspan top cracking (right side)


Exposed strand from spall (bottom)

Front corner spall repair (right side)

Figure 3.11: Condition of BTE3 photos.

With the girder simply supported, camber measurements were taken along the length of the girder, as shown in Figure 3.12. The maximum camber measured was 1-3/8 in. at the midspan.

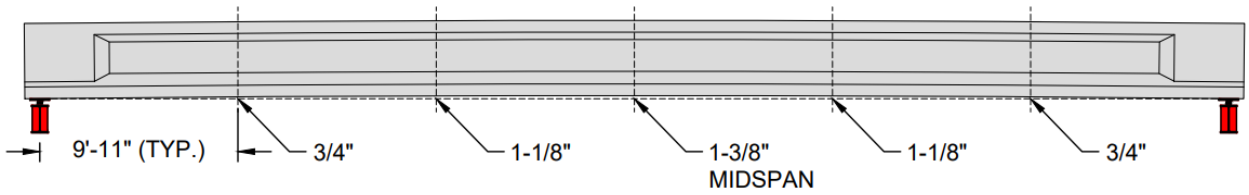

Figure 3.12: BTE3 camber measurements.

3.1.4 Condition of BTE4

A summary of the condition of BTE4 can be seen in Figure 3.13. Figure 3.14 also provides supporting photos of the condition in the laboratory. BTE4 had approximately 1.75 in. of residual concrete deck remaining after saw cutting. The overall condition of BTE2 was generally very good, and, there was no damage to the top flange from removal of the concrete deck. Concrete spalls and repairs were observed at the bottom flange.

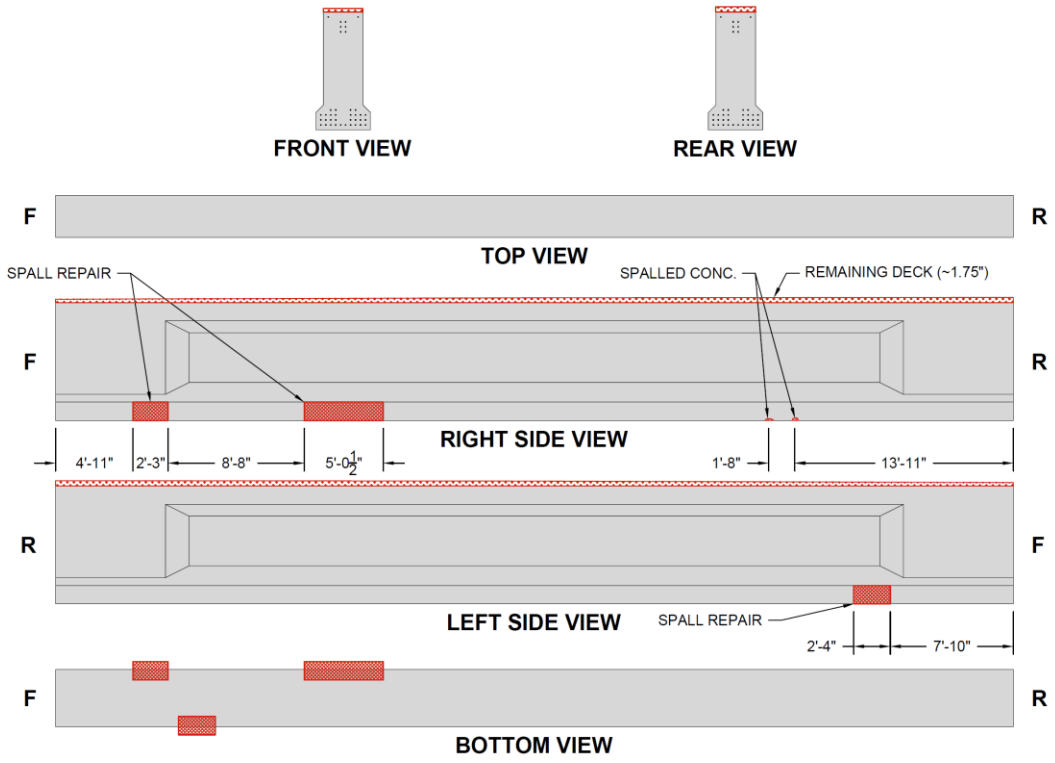

Figure 3.13: Condition of BTE4 (horizontal scale reduced).

Spall repair (left side)

Spalled concrete (right side)

Front end spall repair (right side)

Front end spall repair (right side)

Figure 3.14: Condition of BTE4 photos.

Camber measurements were taken along the length keeping the girder simply supported. Figure 3.15 shows the measured camber along the length of the girder. The maximum camber was 1-1/4 in. measured at the midspan.

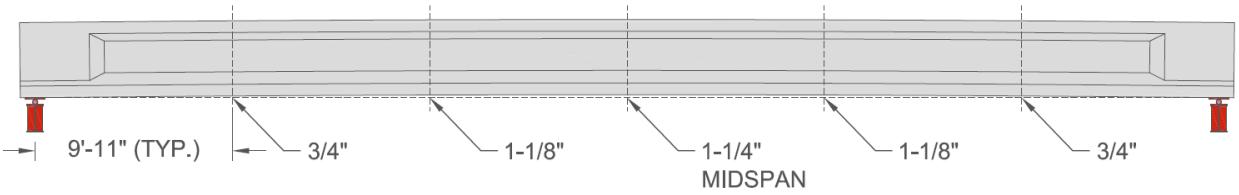

Figure 3.15: BTE4 camber measurements.

3.1.5 Condition from Inspection Documents

The NCDOT provided condition assessment drawings for the Bonner Bridge produced by the Alpha & Omega Group (2007). Figure 3.16 shows the assessment drawing for span number 142 (all girders recovered for testing came from this span).

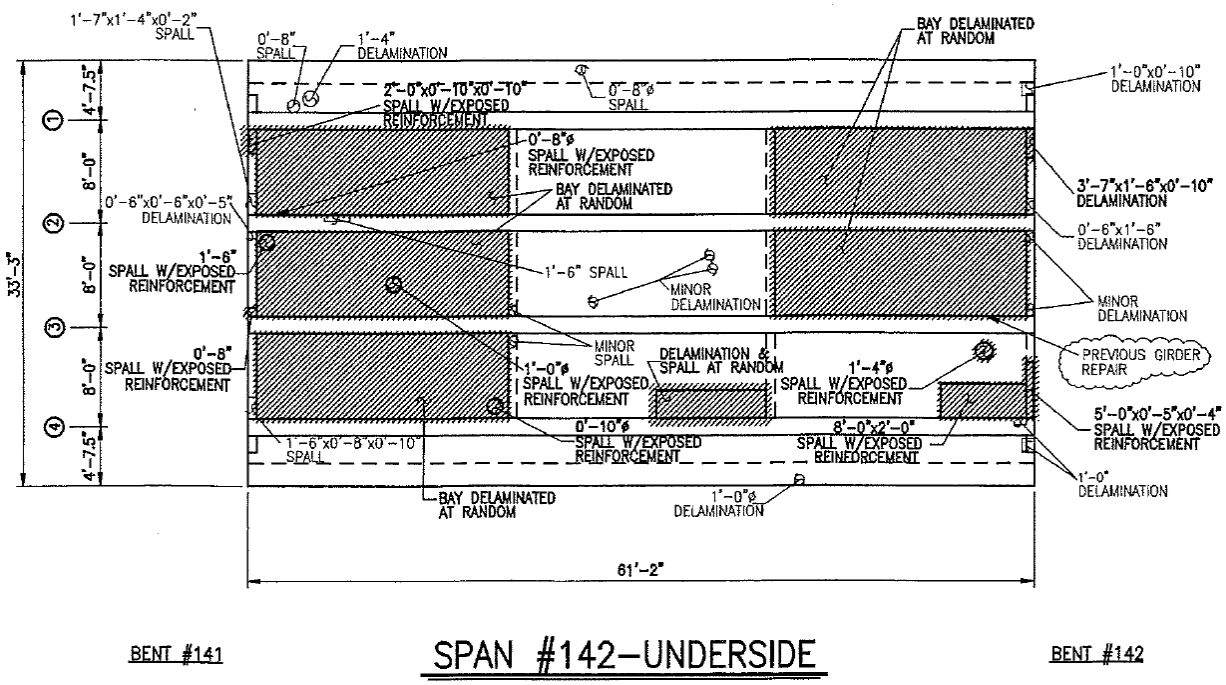

Figure 3.16: Bonner span number 142 condition drawing (Alpha & Omega, 2007).

Most of the deterioration for the span was on the underside of the concrete deck. Little deterioration was noted on the girders except for an end region repair on the second girder from the bottom (girder BTE4 in this report). Besides corrosion of strands and, spall repairs, the other damage described above was likely minor cracking and spalling by deconstructing, handling, and shipping the bridge girders. The girders have bottom flange damage consistent with reasonable

lifting points that might have been used during deconstruction, and any minor sawcut damage or limited top cracking is the result of deconstructing the girders and transporting them to the CFL.

3.2 Material Properties

The stress-strain response of the concrete for each of the four girders tested in the laboratory was determined using compression testing of cores taken from the girders at the laboratory. At least 5 cores were extracted from the top of each girder, each core having a nominal diameter of 3.75 in. and a length of around 7.50 in. The compressive strength of the deck concrete was also measured by compression testing cores with similar dimensions taken in the field by the deconstruction crews. Additionally, the stress-strain response of the prestressing strand was determined by tension testing segments of strands harvested from the recovered girders. Strands were taken from the end regions of selected beams that failed in flexure so that the harvested strand samples were not heavily damaged by the flexure testing. Details of the core testing and strand testing are discussed in Appendix B.

A summary of the material properties of the prestressing strand and the concrete (discussed in Section B.1 of Appendix B) are presented in Table 3.1.

Table 3.1: Summary of material properties.

Steel Properties			
Steel Type	f_{py} (ksi)	f_{pu} (ksi)	E_p (ksi)
7/16 in. Strand	239	271	28000
Concrete Properties			
Specimen	f'_c (psi)	E_c (ksi)	ε'_c ($x10^{-3}$)
BTE1	6150	4710	1.89
BTE2	9080	6580	1.76
BTE3	7270	5870	1.70
BTE4	7970	5050	2.09
Deck	5550	3950	2.08

3.3 Experimental Setup for Flexural Testing

To determine the prestress loss and ultimate flexural capacity of the recovered Bonner Bridge girders, the girders were first tested in four-point bending. The applied shear force and applied

moment diagram corresponding to the flexural testing of the BTE series are depicted in Figure 3.17.

For BTE1 the load plates were placed 4.5 ft. to either side of midspan. The load spacing for the four-point bending setup was placed such that the constant moment region occurred over the unharped strands to avoid the effects from the vertical component of the strand in the harped region. The strands are not harped for 5 ft. to either side of midspan. Additionally, since the shear reinforcement density reduces near midspan, the applied load points needed to be placed near midspan of the beam to increase the moment-to-shear force ratio, mitigating risk of a shear failure in end region. Wider spacing of the load points would increase the applied shear to the section for a given moment, and the relatively light shear reinforcement near the middle 50% of the girders was insufficient to provide an adequate factor of safety against a shear failure with load points spaced greater than 10 feet.

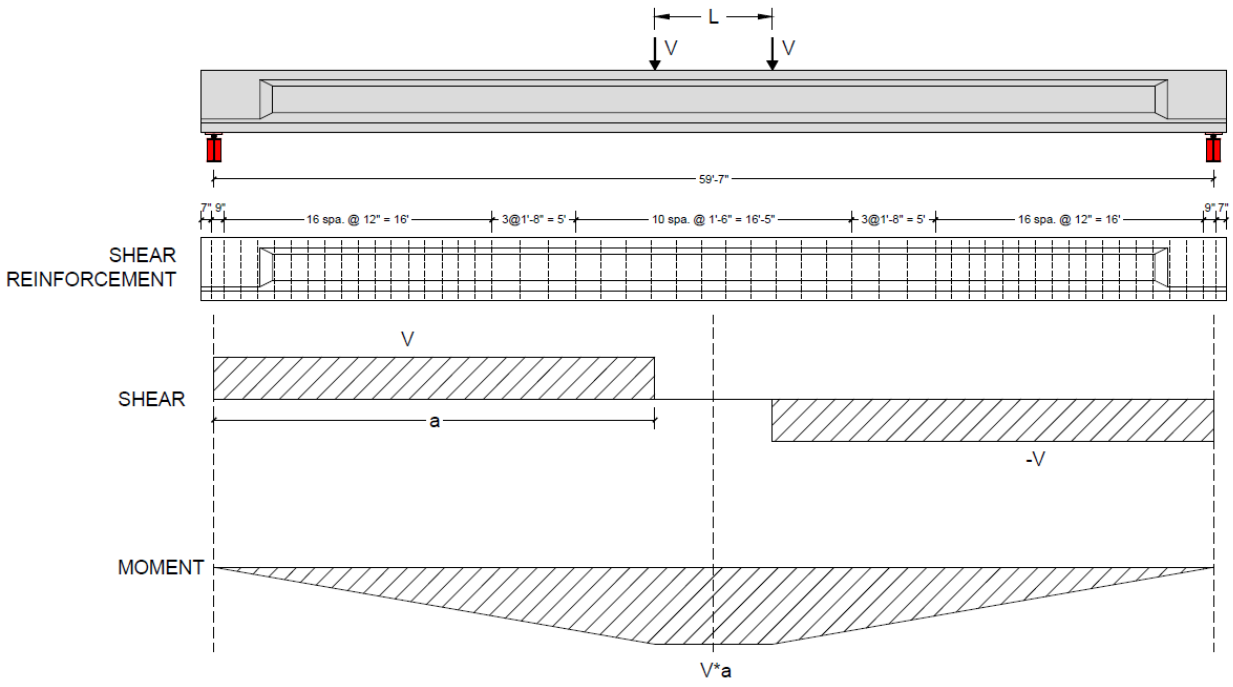

Figure 3.17: Applied shear and moment diagrams for flexural testing of the BTE series.

The applied load for BTE1 placed the load points at sections near the harping locations, and there may have been some influence on post-peak response after the flexural compression failure. Therefore, for BTE2, load points were placed 7 ft. apart about the midspan to provide more

distance between the load plates and the strand harping locations, while still providing a constant moment region for instrumentation. The load was applied to the girders using a single 440 kip actuator and a spreader beam spanning between the two 8 in. wide, 1 in. thick steel load plates. Since the sawcut on the top of the girder was not level across the flange, the load plates were leveled using grout. The girders were supported on two 6 in. wide, 1/2 in. thick steel plates with the center of the plate located 9 in. from the ends of the girder to match the specified bearing location in the original construction drawings. The support plates on both sides were grouted to the bottom surface of the girder to ensure full contact with the embedded steel bearing plates. Each support plate rested on a 3-1/2 in. diameter steel cylinder. On one side of the specimen the cylinder was tack welded to a plate to create a pin condition, and on the other side of the specimen the cylinder remained free to create a roller condition. The actuator was free to translate and rotate as the girder deformed. Both sides of the beam were supported on 15 in. tall wide flange sections to provide adequate clearance for deflection of the beam towards the strong floor. The support condition can be seen in Figure 3.18, and the side and end view of the test setup can be seen in Figure 3.19.

Figure 3.18: Support condition pin (left), pin stitch weld (center), and roller (right).

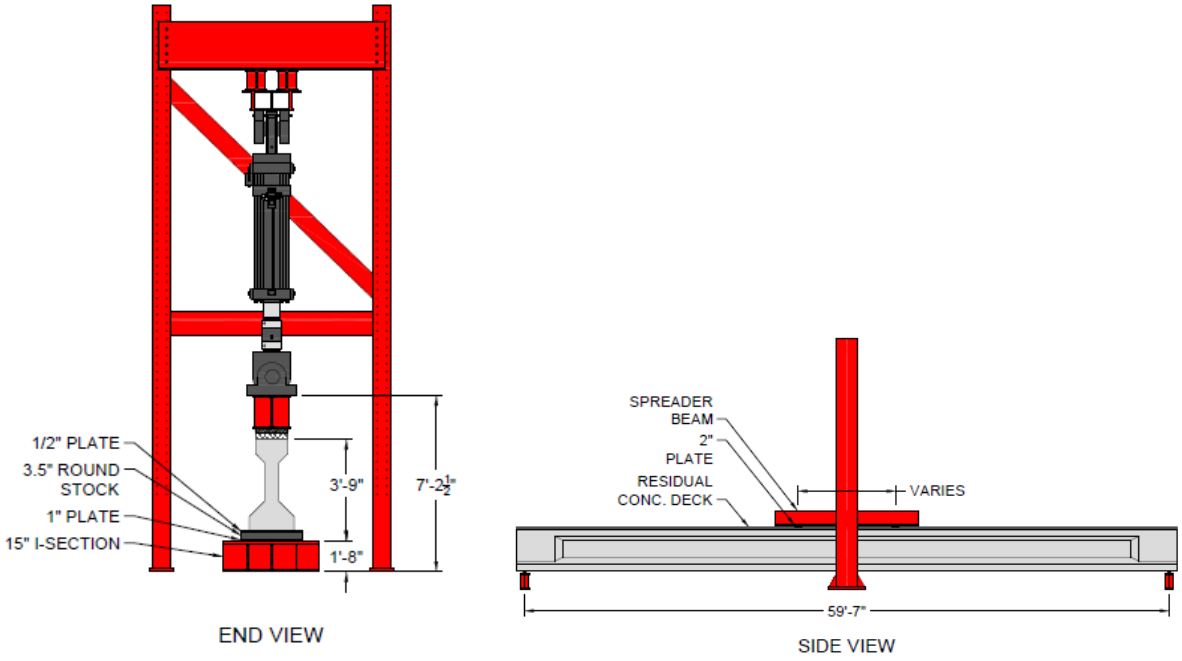

Figure 3.19: Experimental setup for flexure tests.

3.4 Instrumentation for Flexure Tests

All BTE girders were instrumented to measure the applied load, vertical displacement, and selected deformation data in the constant moment region throughout flexural testing. Load was applied by a hydraulic actuator and measured using an integrated load cell of appropriate capacity. The hydraulic actuator was also instrumented with a displacement transducer that recorded the actuator stroke as load increased. Deformation of the girder between the loading points was extensively measured using a number of systems including digital image correlation (DIC) equipment, a non-contact optical LED system (Optotrak), several strain gauges placed along the depth of girder, and traditional potentiometer displacement measurements. The DIC system recorded deformation data on the west face of specimen, whereas LED markers were placed on the east face. The strain gauges placed on the girder were used to measure strains near the top and bottom flange. The strain gauges on the bottom flange can indicate cracking by a stiffness change during loading. In addition to full field deformation data in the constant moment region, string potentiometers were used to collect vertical displacement at five locations along the length of the girder. The full instrumentation of the BTE girders can be seen in Figure 3.20.

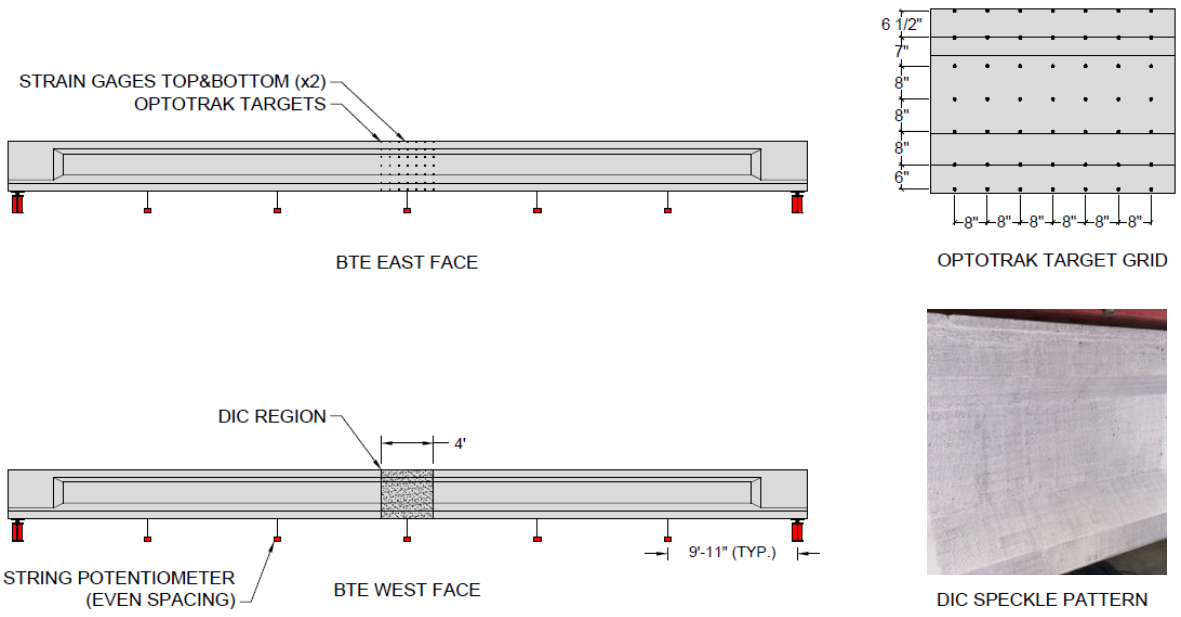

Figure 3.20: Instrumentation of BTE series girders.

As configured for testing, under self-weight, the bottom flange of a given girder is in compression from the prestressing, but as load is applied in four-point bending, tensile flexural stresses overcome the compressive stress created by prestressing. Figure 3.21 illustrates this behavior. Load and deformation data recorded by the instrumentation is used to carefully investigate this transition from compression to tension in the bottom fiber of the beam. Deformation data collected with the DIC system is used to identify opening and closing of flexural cracks which can then be carefully analyzed to calculate prestress loss. Further details on each instrumentation are discussed in the subsequent sections.

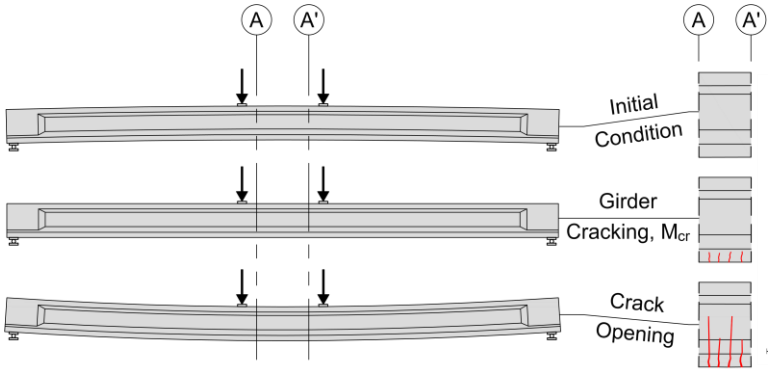

Figure 3.21: Behavior of prestressed girder in four-point bending as prestress is overcome.

CHAPTER 4 – EXPERIMENTAL OBSERVATIONS

In this chapter, the results of laboratory testing the BTE series is presented. Results such as the load-deformation, longitudinal strains, cracking moment, crack reopening moment, and ultimate flexural capacity of the members is presented. For each girder, several load cycles were conducted at low load levels. The girders were then monotonically loaded in flexure to assess their ultimate capacity along with load-deformation response among other parameters studied. The detailed analysis and results from the flexural tests along with photographs of the experimental program are provided in Appendix C. The data presented is obtained from strain gauges on the girder surface and deformation data recorded with the DIC system. For the DIC data, the strains presented are engineering strains.

4.1 Discussion of Experimental Observations from Flexure Test

This section discusses the performance of the girders in flexure. The flexural testing shows that the performance of the four girders was similar. A summary of the results from the BTE series of tests is presented in Table 4.1 below. Note that these are all applied moments, M_{max} is the maximum moment applied to the specimen, M_{cr} is the cracking moment, M_{ro} is the moment required to reopen preexisting flexural cracks, and Δ is the deflection at peak load.

Table 4.1: Summary of experimental observations.

Specimen	M_{cr} (k-ft)	M_{ro} (k-ft)	Δ (in)	M_{max} (k-ft)
BTE1	1295	905	7.85	2550
BTE2	1370	995	6.58	2580
BTE3	1335	990	5.41	2420 (95%)
BTE4	1338	995	5.64	2420 (95%)

BTE1 had the lowest peak moment of the two girders tested to failure, and BTE1 had the lowest cracking and crack reopening moment of the four girders. Testing of BTE1 revealed that one of the strands in the bottom most row of strands was corroded, and core testing of BTE1 revealed that the compressive strength of the concrete was the lowest of the four girders. Thus, it is expected that the capacity of BTE1 would be slightly lower than the other three specimens. The difference in ultimate capacity between BTE1 and BTE2 is, however, less than 1.5%. The response

near cracking and crack-reopening of BTE2, BTE3 and BTE4 are nearly identical. If BTE3 and also BTE4 were loaded further, it is likely that the ultimate moment capacity would be similar to that of BTE2, and any difference would be the result of varying concrete strengths. This is discussed in subsequent sections with corresponding modelling results.

The moment- relative curvature response of the BTE specimens is shown in Figure 4.1. Relative curvature is defined as zero when the girder is simply supported on its supports with no external loads on the member other than its self-weight. In this condition, there is negative curvature from the prestressing and self- weight combination. The relative curvature for each girder test can be determined using horizontal virtual extensometers in DIC post-processing, and these extensometers are the same as the ones used to produce the strain profiles through the height for each girder in section C.1 C.2, C.3 and C.4 in Appendix C. The curvature was determined from the average longitudinal strains at multiple sections over the height over multiple cracks.

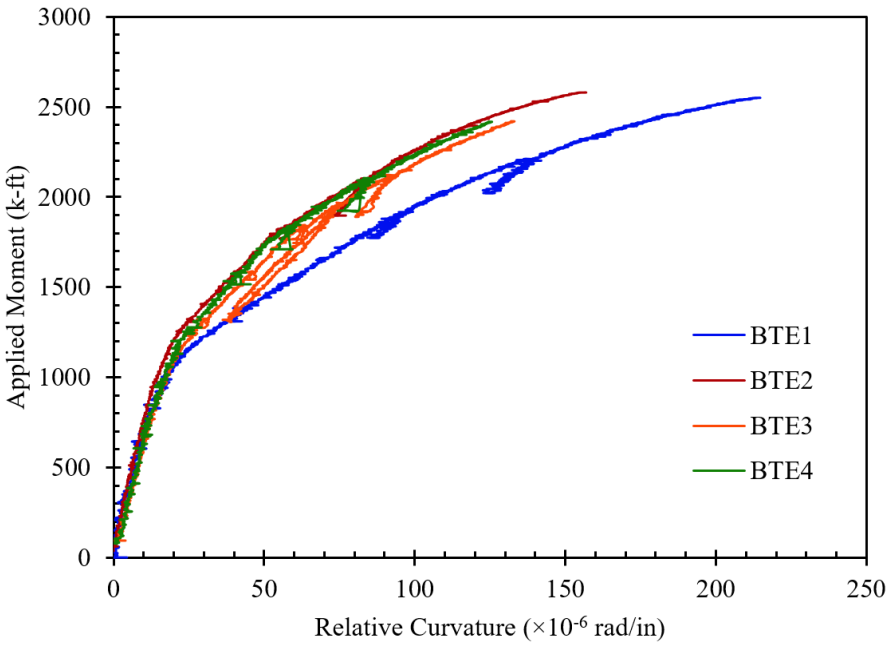

Figure 4.1: Moment-relative curvature girder comparison.

Figure 4.1 confirms that except for BTE1 (where a corroded strand was observed), all the specimens performed with a very similar response. BTE1 exhibits the same pre-cracked stiffness as the other girders, but the response is less stiff after cracking compared to BTE2, BTE3 and BTE4. The loss of a prestressing strand combined with the lower concrete strength contributes to

the reduced post-cracking stiffness of BTE1. The transition from pre-cracked stiffness to post-cracked stiffness in Figure 4.19 is an indicator of the amount of prestress loss in each of the three beams. BTE1 transitions stiffness at a lower applied moment, suggesting that it has more prestress loss compared to BTE2, BTE3 and BTE4. BTE2 transitions stiffness at the highest applied moment, suggesting that BTE2 has the least loss of the four. BTE2, BTE3, and BTE4 can be considered as control specimens with no corrosion and provides means of comparison with BTE1 which had corroded strands.

CHAPTER 5 – PRESTRESS LOSSES, RESIDUAL CAPACITY, COMPARISON OF PRESTRESS LOSSES TO ANALYTICAL MODELS AND AASHTO LRFD CODE

This chapter discusses the loss of prestress in the recovered girders from the Bonner Bridge determined from the results of the experimental testing on BTE1, BTE2, BTE3 and BTE4 and uses Response-2000 to predict the response of the girders with a composite deck. The nominal flexural of the structure is given by Response-2000. Theoretical prestress losses are also determined according to AASHTO LRFD Refined Method, AASHTO LRFD Lump Sum Method and AASHTO Standard Specifications and the results are compared with measured prestress losses. In this chapter the term "loss" in reference to prestress losses is defined as the total reduction in strand stress from the original specified jacking stress. This loss of strand stress is comprised of all possible losses from the time of jacking including: elastic shortening of the member, concrete creep, concrete shrinkage, strand relaxation, losses from thermal effects during casting, deck placement, deck removal, anchor slip.

5.1 Prestress Loss Analysis

The prestress loss in each of the girders in the BTE series was determined using the crack reopening moment determined in the cyclic flexural testing of each girder. The reopening moment is an indication of the transition from compression to tension in the bottom fiber without the effect of the tensile capacity of the concrete, and therefore the tensile capacity of the concrete does not need to be known to determine remaining prestress and the variability of concrete tensile capacity does not affect the result. The elastic equation for the stresses in the section given by Eq. 2, can be used to determine the effective prestress force, P_{eff}, in the girders from the crack reopening moment, M_{ro}, by equilibrating the bending stress applied by load to the stresses induced by prestressing less the stresses induced by dead load moment. As discussed in section A.4.2, a similar equation was used by Azizinamini *et al.* (1996), Halsey and Miller (1996), and Higgs *et al.* (2015). In these equations (Eq. 2 and Eq. 3), y is the distance from the transformed neutral axis to the point in the section of interest where y is positive for heights below the transformed neutral axis. I is the moment of inertia for the section using transformed section properties, A is the transformed section area, e is the eccentricity of the prestressing strand, and M_d is the dead load moment at the section of interest.

$$\frac{M_{ro}y}{I} = \frac{P_{eff}}{A} + \frac{P_{eff}ey}{I} - \frac{M_d y}{I} \quad (2)$$

Which can be rearranged to

$$P_{eff} = \left(\frac{M_{ro}y}{I} + \frac{M_d y}{I}\right) / \left(\frac{1}{A} + \frac{ey}{I}\right) \quad (3)$$

The crack reopening moment for the BTE series was determined using virtual extensometers in the analysis of DIC data and DIC principal strain maps which shows crack propagation. The extensometers were placed approximately 1.75 in. above the bottom fiber of the girder. As discussed in Chapter 4 and Appendix C, the crack height corresponding to the crack reopening moment is the same as extensometer location and is equal to 1.75 in. Therefore, the height into the cross section where total stress is zero is taken as 1.75 in. above the bottom fiber, and *y* in Eq. 3 is equal to the height of the transformed section neutral axis less 1.75 in. From P_{eff} for each of the girders determined by Eq. 3, the individual strand stress can be determined by dividing the total force, P_{eff}, by the total strand area. The individual strand stress at crack reopening for each of the girders is listed in Table 5.1 below. For BTE1, since one of the strands was found to be corroded, the area of 37 strands is used instead of the original 38 strands in cross-section. Corrosion is progressive and occurred over the service period. Completely disregarding one strand may not be ideal as the strand continued to provide prestress over a significant period of the life of the structure. For load rating purposes, AASHTO LRFD suggests to reduce the cross-section to include the effects of deterioration and hence calculations were done for an area of steel equal to 37 strands.

Table 5.1: Average strand stress at crack reopening for BTE series.

Specimen	$\sigma_{s,eff}$ (ksi)
BTE1 (37 strands)	131.0
BTE2	141.4
BTE3	139.6
BTE4	139.5

The strand stresses provided in Table 5.1 are slightly higher than the strand stress when only dead weight is applied because they are determined at the crack reopening moment for each girder. Therefore, to determine the average strand stress under only self-weight, the layered sectional analysis program Response-2000 (Bentz, 2000) was used. The average effective strand

stresses from Table 5.1 above were used to determine an average effective strain differential between the concrete and the strand, $\Delta\varepsilon_{p,eff}$, by dividing by the strand modulus determined by tension testing in section B.1.1 of this report. BTE1 has the lowest $\Delta\varepsilon_{p,eff}$ among all the girders. Figure 5.1 shows the cross-sections used in Response-2000. The tensile strength of the concrete was taken as zero in the Response-2000 models to simulate the crack reopening behavior of the girders. Popovics stress-strain relationship fitted to average stress-strain results from core testing of each girder and the modified Ramberg-Osgood relationship for the steel was used in Response-2000. The deck thickness was the residual concrete deck remaining after saw cutting. The midspan section was analyzed in Response-2000 to determine flexural capacity. The dead load moment includes the girders own self-weight and weight of residual deck. The unit weight of concrete in each girder is a function of compressive strength and calculated as stated in AASHTO LRFD Table 3.5.1-1.

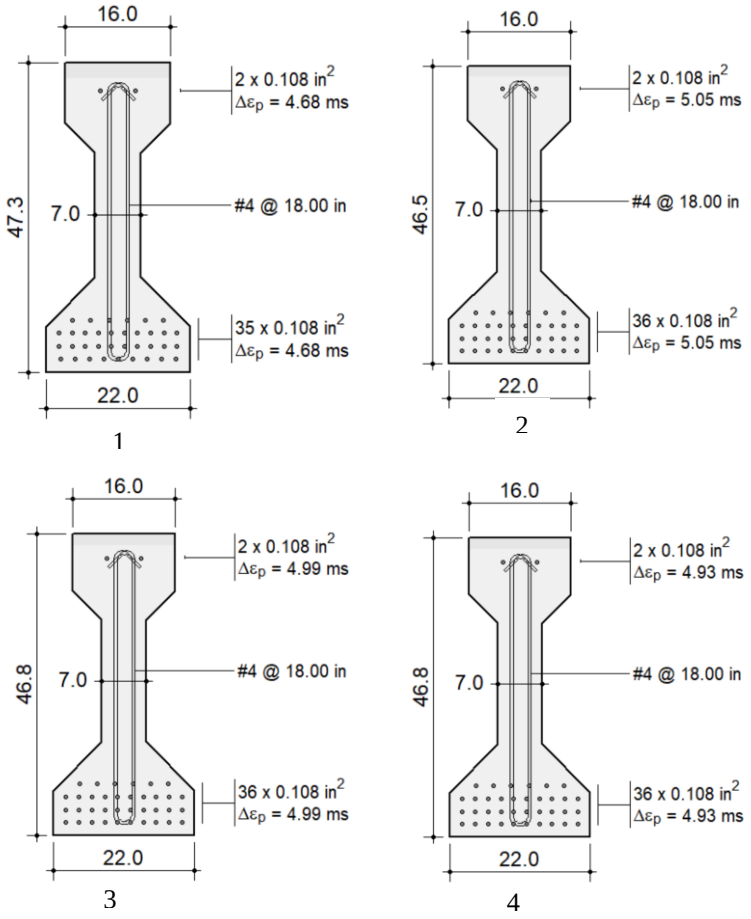

Figure 5.1: Response-2000 section for BTE series (1) BTE1 with 37 strands (2) BTE2 (3) BTE3 (4) BTE4

From these Response-2000 models the in-lab average strand stress at midspan for the girders simply supported at their design span was determined. Since the prestressing steel stress immediately before transfer is known from the original design, subtracting the in-lab average strand stress at midspan given by Response-2000 models gives a measure of prestress loss over the entire service life of the structure. If there was no prestress loss after 56 years of service, the effective prestressing force would be the same and therefore, the stress in strands would be 175 ksi. Response-2000 uses the average effective strain differential between the concrete and the strand which should be the same throughout the life of prestressed structure and other material properties as necessary inputs to predict the behavior of girder in its current state. Since it can generate the moment-curvature of the structure up to its flexural capacity, it can also give a measure of strand stress under self-weight in a simply supported condition. The measured strand stresses as determined form the laboratory experiments and with the application of Response-2000 are shown in Table 5.2 along with the total loss of prestress from the tension bed stress. The results show that prestress losses in BTE2 (34.0 ksi), BTE3 (35.4 ksi) and BTE4 (36.0 ksi) are similar. BTE1 have a much higher prestress loss, equal to 44.3 ksi which is 23.3%, 20.1% and 18.7% higher in comparison to BTE2, BTE3 and BTE4. The higher prestress loss in BTE1 can be the effect of corrosion. The condition assessments indicate that BTE2, BTE3, BTE4 had multiple concrete spall locations, exposed section of strands, and repairs but it does not appear to have affected the losses for this series of tests.

Table 5.2: Average strand stress for recovered girders determined by Response-2000.

Specimen	σ_T (ksi)	σ_s (ksi)	Loss (ksi)	Loss (%)
BTE1 (37 strands)	175	130.7	44.3	25.0%
BTE2		141.0	34.0	19.4%
BTE3		139.6	35.4	20.2%
BTE4		139.0	36.0	20.6%

* σ_T is the nominal tension bed stress.
† σ_s is the midspan average strand stress from lab testing.

Response 2000 also yields an estimate of the flexural capacity of these girders as shown in the Table 5.3.

Table 5.3: Experimental and Predicted Flexural Capacity.

Specimen	*Experiment, M_u (k-ft)	Response-2000, M_u (k-ft)	Test-to-Predicted Ratio
BTE1 (37 strands)	2831	2815	1.006
BTE2	2860	2860	1.000
BTE3	†2699	2760	0.978
BTE4	†2698	2780	0.971
Mean	2846	2804	-
COV	0.72%	1.56%	-

*Includes both self-weight and applied moment

†BTE3 and BTE4 were brought to 95% of the flexural capacity of BTE1

To further verify the accuracy of the Response-2000 models used to determine the strand stresses in the BTE series, the short-term moment-relative curvature response at midspan for the monotonic loading of each girder was compared to the predicted moment-curvature response developed in Response-2000. For this, the girders self-weight moment was subtracted from the moment-curvature response developed in Response-2000 to directly compare against the actuator applied moments. Additionally, the curvatures in the Response-2000 moment-curvature plots were adjusted so that the relative curvatures measured in the flexural testing of the BTE series could be compared. Figure 5.2 shows the measured and predicted moment-curvature response for BTE1 having 37 strands. Response-2000 models for BTE2, BTE3 and BTE4 are shown in Figures 5.3, 5.4 and 5.5. The bandwidths are $\pm$25% of the predicted moment.

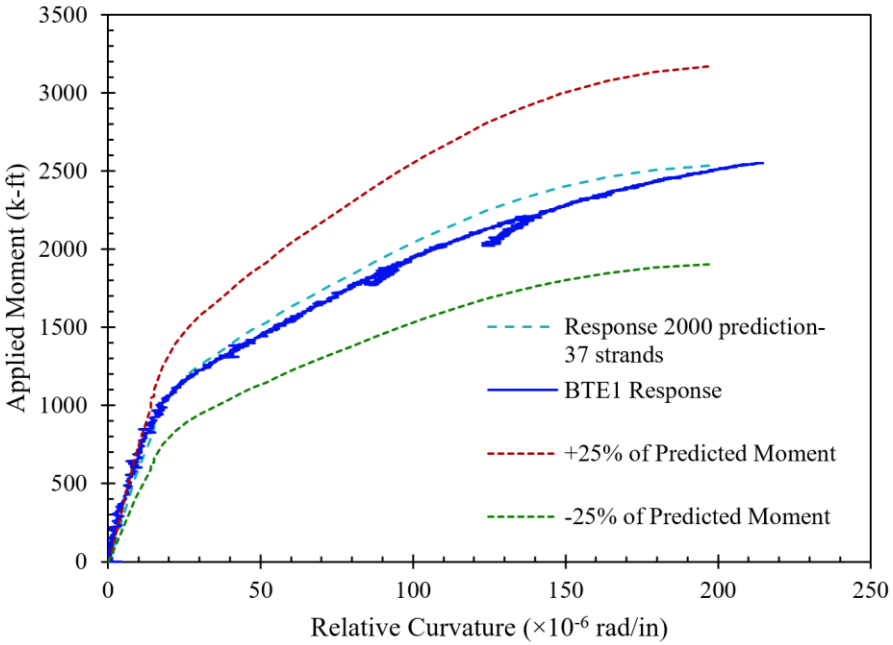

Figure 5.2: BTE1 experimental and predicted response.

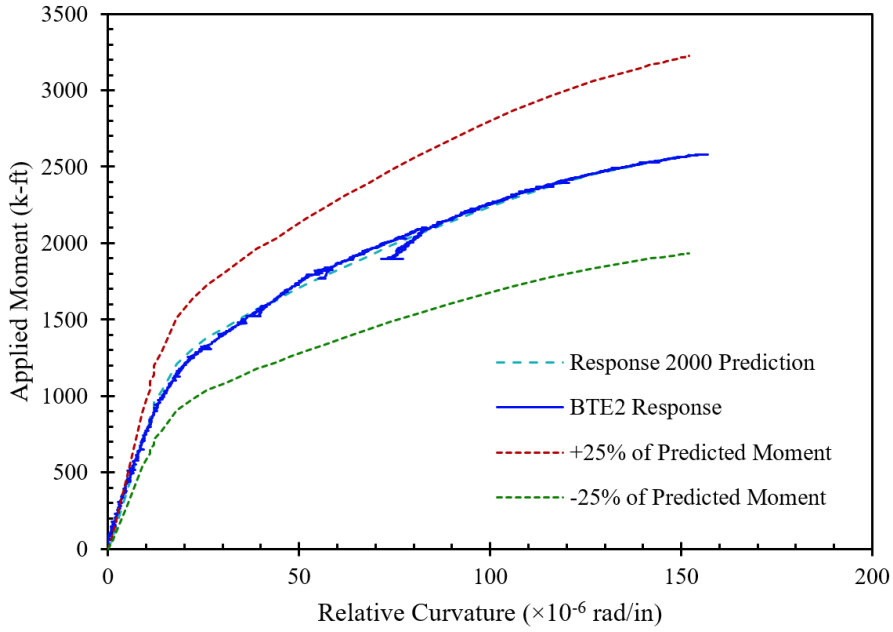

Figure 5.3: BTE2 experimental and predicted response.

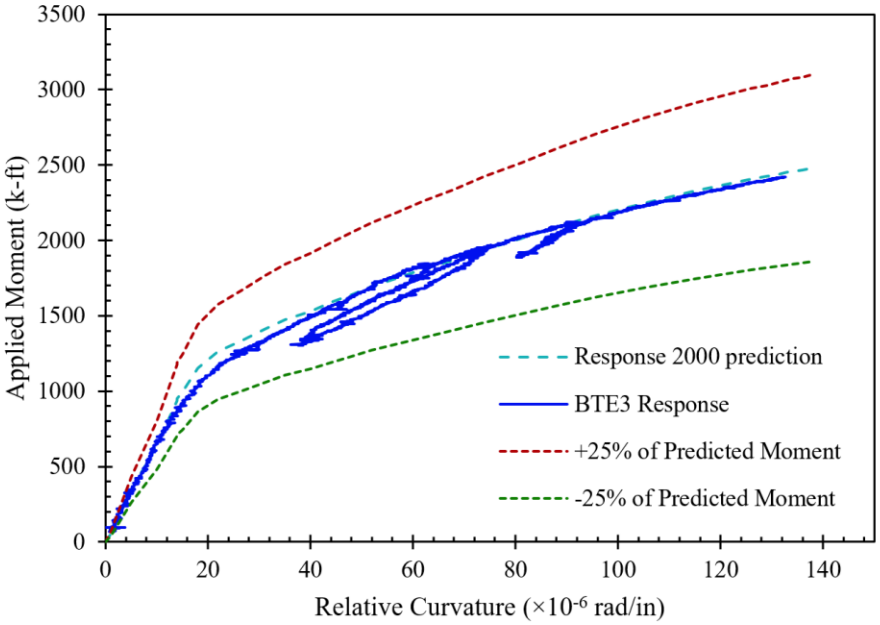

Figure 5.4: BTE3 experimental and predicted response.

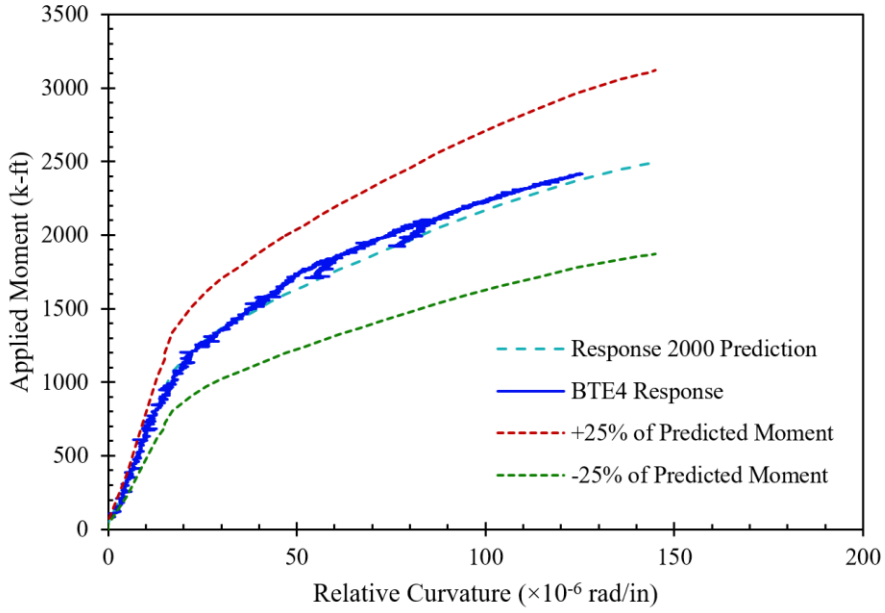

Figure 5.5: BTE4 experimental and predicted response.

The Response-2000 prediction for BTE1 with 37 strands (neglecting a strand from the original 38 strands in cross-section due to corrosion) matches the moment-curvature response from laboratory testing very well, and the model does particularly well in predicting the uncracked stiffness as well as the transition from uncracked stiffness to cracked stiffness. The transition from uncracked stiffness to cracked stiffness is directly related to the strand stress in the girder, and an accurate representation of this behavior indicates that the strand stress in the model matches the true strand stress in the specimen. In specimen BTE1, Figure 5.2 however, shows that the predicted cracked stiffness is slightly higher than the actual response of BTE1. One of the reasons can be the effect of corrosion among other variables. The moment curvature response of the BTE series determined by flexural testing shows that the pre-cracked stiffness is similar for all specimens. After transition, BTE1 had a slightly lower cracked stiffness and corrosion may be a contributing factor to the observed response.

In general, the inspection report of bridges indicate any signs of deterioration such as corrosion, but it is difficult to estimate the extent of corrosion from visual inspection. The survey of peer DOTs also indicate they do not relate corrosion to loss. Since Response-2000 can predict the moment-curvature response of the aged prestressed concrete girders without corroded strands (as can be seen in subsequent sections when modelling BTE2 and BTE3), an effort was made to incorporate the effects of corrosion in Response-2000 (HADRIAN SOFTWARE WORKS, 2023). The approaches focus on estimating the effect of corrosion through reducing cross-section (as is done for load rating purposes) and considering change in prestress along the depth of cross-section due to corrosion. However, the outcome of the approaches are limited to comparison of the moment-curvature response determined through flexural test and that given by Response-2000. The approaches for modelling BTE1 using Response-2000 are listed below:

1. Reducing the cross-section by removing any corroded strand identified through visual inspection and assuming uniform prestress loss for all strands. BTE1 had one corroded strand and therefore, a section considering 37 strands was modelled using Response-2000.
2. Considering all 38 strands in the cross-section and assuming uniform prestress loss for all strands. This may attribute to the fact that the corroded strand was in service for a longer duration and it may not be ideal to completely disregard the strand from cross-section. The corroded strand certainly affects prestress loss but may not contribute significantly.

3. Considering corrosion to affect other strands which were not visually identified and assuming uniform prestress loss in all strands. A cross-section comprising of 36 strands was modelled in Response-2000.
4. Considering corrosion to affect other strands which were not visually identified and assuming a staggered prestress loss in strands along the depth of cross-section. The loss is assumed to be higher in the bottom row of strands compared to the strands located higher in the profile where effects of corrosion has not progressed yet. A cross-section comprising of 36 strands was modelled in Response-2000.

The same crack reopening moment as determined from the experiment was used. The cross-section used in Response-2000 for approach 2, 3 and 4 are shown in Figure 5.6. The cross-section used for approach 1 can be found in Figure 5.1 shown earlier.

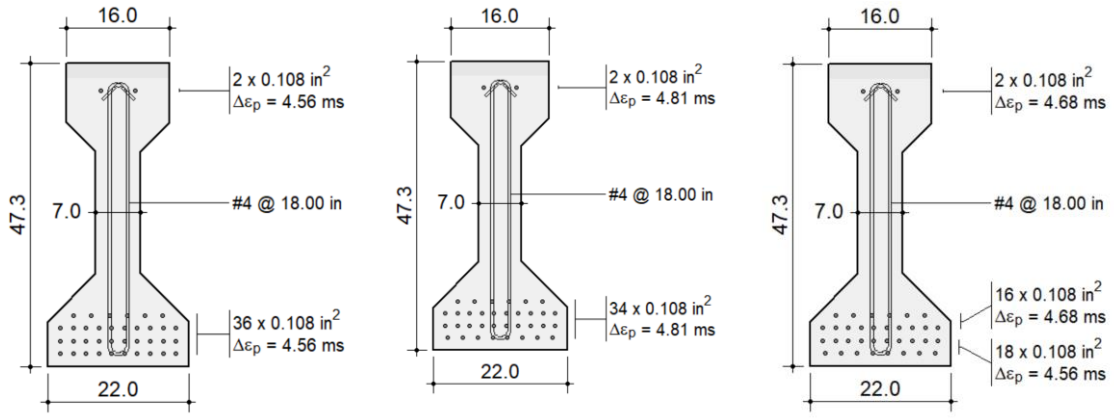

(1) (2) (3)

Figure 5.6: Response-2000 section for BTE1 (1) 38 Strands (2) 36 Strands (3) Staggered Loss with 36 strands.

In all the approaches, the same material properties determined in Chapter 3 for specimen BTE1 are used. Since the crack reopening moment remains the same regardless of the approach and was determined experimentally, Eq. 73 gives roughly the same effective prestressing force for each section. There is no significant change in the transformed area or moment of inertia when one or two strands are disregarded in the section and therefore neglected. For all the sections to have same effective prestressing force, the average strand stress in the section with 36 strands would

essentially be higher compared to sections with 38 or 37 strands in approach 1 and 2 respectively. This would give a higher average effective strain differential between the concrete and the strand which is obtained by dividing average effective strand stress by the elastic modulus as discussed previously. As before, the average strand stress are slightly higher than the strand stress when only dead weight is applied because they are determined at the crack reopening moment for each girder. Therefore, to determine the average strand stress under only self-weight, Response-2000 was used to model these sections. For the staggered loss approach, it is assumed that the prestress loss is more in the bottom rows compared to the strands above and generalizing a single value for the prestress loss of the entire may not predict the response properly. Therefore, a higher prestress loss of 44 ksi was applied to the bottom two rows of strands and a comparatively lower prestress loss of 40 ksi was selectively applied for the strands above. The results are listed below in Table 5.4. The predicted short-term moment relative curvature given by Response-2000 is shown in Figure 5.7.

Response-2000 models predict that BTE1 would fail by flexural crushing of the flange for all the approaches. The flexural capacity of BTE1 from the flexural test was found to be 2550 k-ft. The test to predicted ratio ranges from 0.97-1.02. The difference in flexural capacity occurs as strands are removed to account for corrosion. This results in a reduced cross-section which have a lower flexural capacity as the effective prestressing force is the same for all cases. Nevertheless, the predicted flexural capacities are within 4% of the test result. A close observation of the moment-relative curvature plot shows, Response-2000 can closely replicate cracked stiffness of the member in approach 4, followed by approach 3, 2 and 1 respectively in order of decreasing accuracy. This indicates approach 4 can predict the transition reasonably well compared to other

Table 5.4: Modelling BTE1 in Response-2000.

Predicted Parameters	38 strands	37 strands	36 strands	36 strands (Staggered loss)
$\sigma_{s,eff}$ (ksi)	127.3	130.7	134.3	129.9
ΔF_{pT} (ksi)	47.7	44.3	40.7	45.1
*Ultimate Applied Moment (k-ft)	2595	2535	2471	2465
Flexural Capacity (k-ft)	2876	2815	2714	2712
Test to Predicted Ratio	1.02	0.99	0.97	0.97

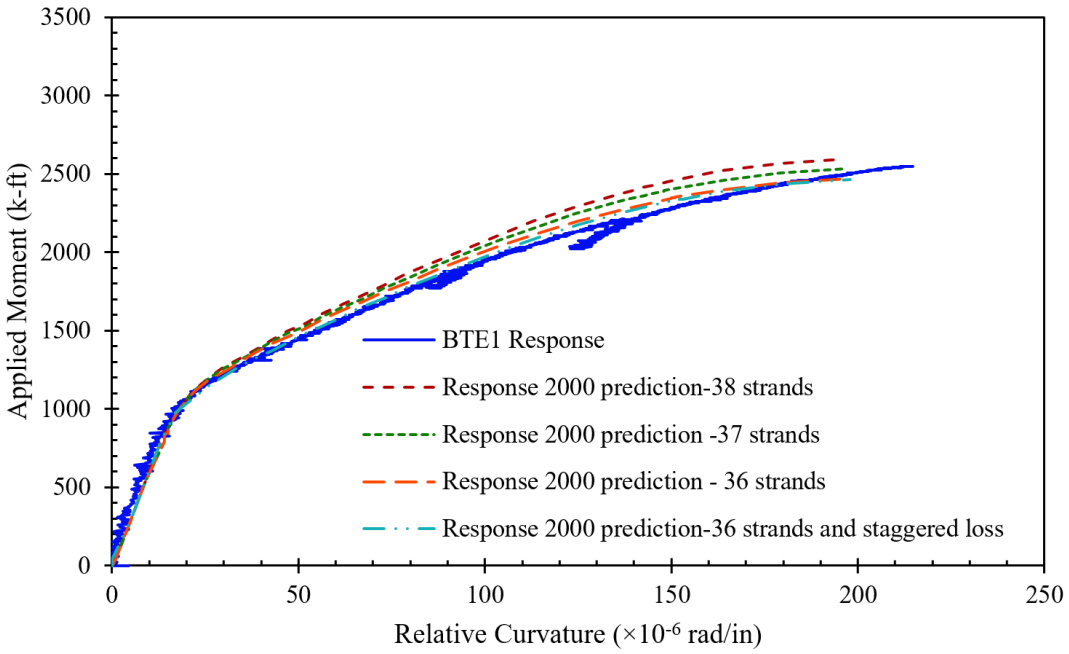

Figure 5.7: Prediction of moment-relative curvature response of corrosion affected girders.

approaches and therefore better represent the strand stress at different levels of the section. The staggered loss approach predicts a prestress loss of 45.1 ksi. Approach 2 which has considered 37 strands also give similar prestress loss predictions (44.3 ksi) and predict the transition well. The prestress loss in approach 3 is much lower (40.7 ksi) and that in approach 1 is the highest among all approaches (47.7 ksi). Although the differences in response are relatively minor, they show that if the effect of corrosion is taken into account by disregarding strands and appropriately considering prestress loss over the strand profile, Response-2000 can predict the short-term moment-relative curvature response of these aged prestressed concrete structure well. Subsequent sections regarding analysis of BTE1, the result for approach 2 is followed as visually only one strand was found to be corroded and the test-to-predicted ratio of the flexural capacity is the closest to 1. Corroded strands were only observed in case of BTE1 specimen and such analysis was not carried out for other BTE specimens.

The Response-2000 predictions for BTE2 agrees well with the moment-curvature response observed experimentally. The models do an excellent job of predicting the transition in stiffness from uncracked to cracked response. For BTE2, which was tested to failure in flexure, the Response-2000 model predicts BTE2 to have a flexural failure by crushing of the top flange at an

applied moment of 2580 k-ft. The test to predicted ratio for the BTE2 model is 1.00. Thus, the model is capable of predicting the peak capacity well. In specimen BTE3, the change in stiffness occurs at a slightly lower curvature than the actual response, but in general the prediction aligns well with the results from the experiment. BTE3 was not tested to catastrophic failure in flexure. Since the Response-2000 model matches the test behavior very well up through the peak applied moment of 2420 k-ft, it suggests that the girder was very close to a flexural compression failure with the predicted peak applied moment of 2480 k-ft. Response-2000 predicts that flexural testing of BTE3 was stopped at 98% of the peak. The model for BTE4 predicts the cracked stiffness accurately and also the transition phase. Response-2000 predicts that the test was stopped at 97% of the peak load. Since Response-2000 predicts the series well including the initial stiffness, post cracking stiffness and transitions from uncracked to cracked response it can be concluded that the strand stresses determined and losses calculated are reasonable.

A sensitivity analysis showing Response-2000 predictions for losses higher and lower than the predicted prestress loss was performed to corroborate the change in stiffness and also to assess if the observed response crosses the limits. To examine the sensitivity of response to the losses, Response-2000 predictions for 25% greater loss and 25% less loss was determined as shown in Figure 5.8 and Figure 5.9 for BTE2 and BTE3 as the girders have similar predicted response. The predicted first cracking moment (discussed in section 5.2 below) at the bottom fiber is also shown for the predicted loss and the corresponding upper and lower bound cases. Results of the sensitivity analysis shows that the observed and predicted response of BTE2 fits well within the bandwidth. In specimen BTE3, both the +25% and -25% loss curve fits well to predict the initial stiffness. At the transition, the moment-relative curvature response observed from test data aligns with +25% loss curve. The observed response fits the cracked stiffness exceedingly well and is between the $\pm$25% loss curves. So, the prediction of Response-2000 using the measured prestress loss is fairly close to the observed response of the specimens and losses calculated are accurate.

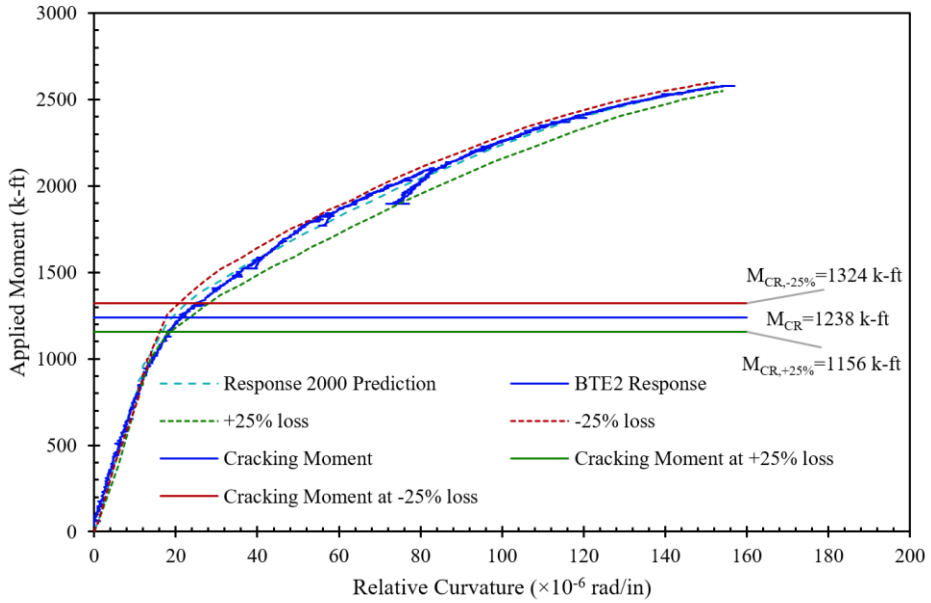

Figure 5.8: Comparison of prestress loss values of BTE2 using Response-2000.

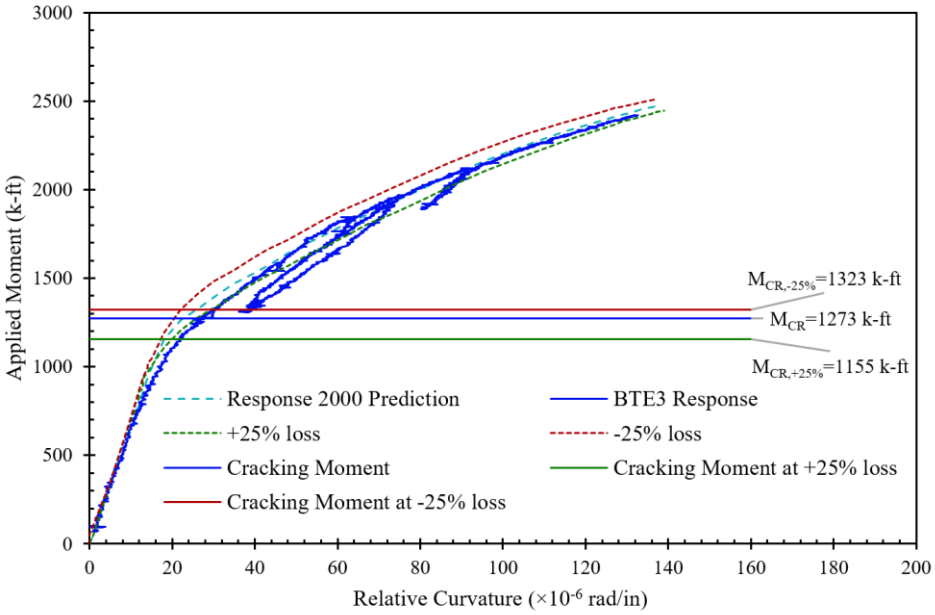

Figure 5.9: Comparison of prestress loss values of BTE3 using Response-2000.

BTE2 and BTE3 show very similar prestress loss over their 56 years of service followed by BTE4 which shows slightly higher prestress loss. BTE1 has sustained the highest prestress loss, but this specimen is the only one to have a strand heavily corroded at midspan. The moment-

curvature response with the actual curvature as predicted by Response-2000 is provided in Figure 5.10. Note that the first instance of cracking and crack reopening moment identified are experimentally observed values and were determined when the crack has already progressed 1.75 in. into the depth of the beam.

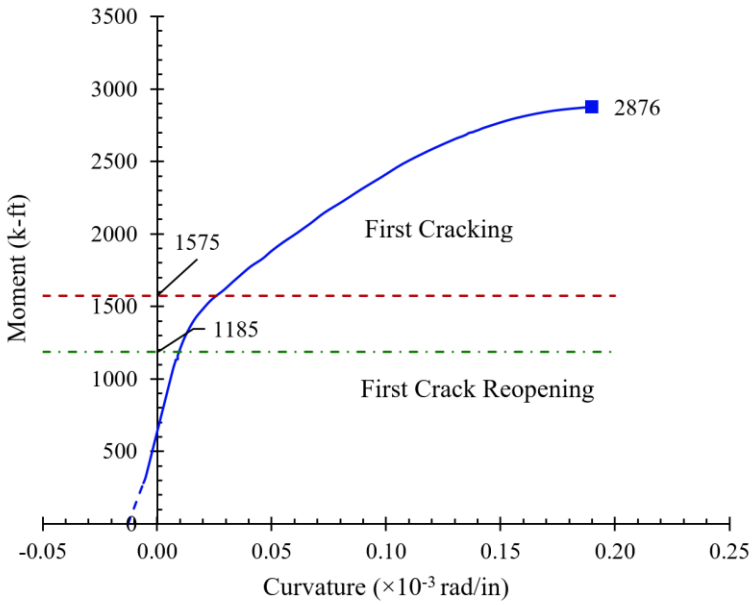

(a) BTE1

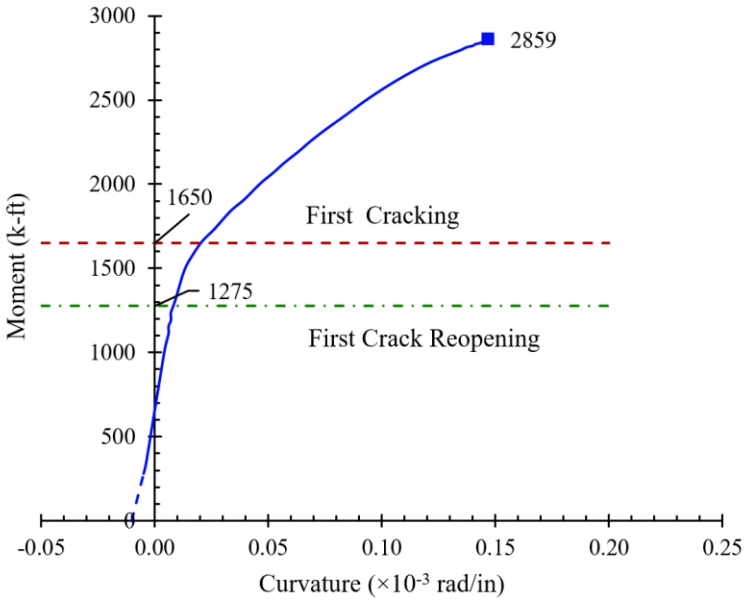

(b) BTE2

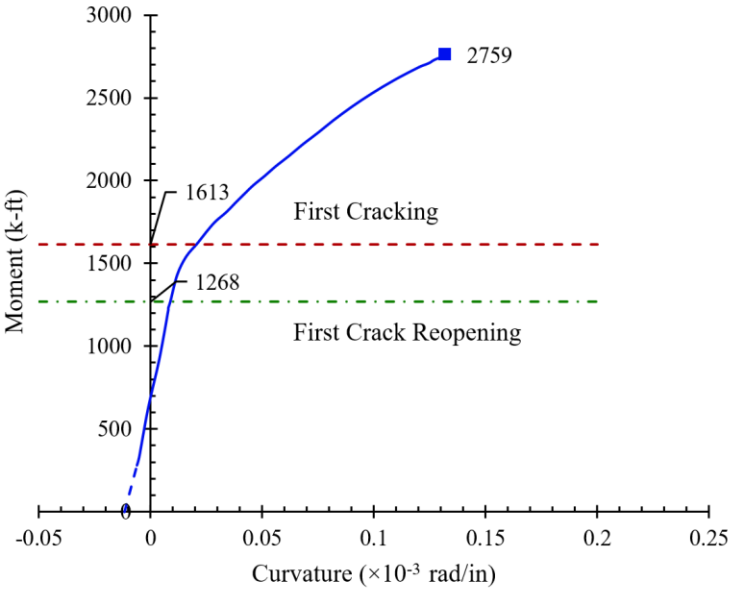

(c) BTE3

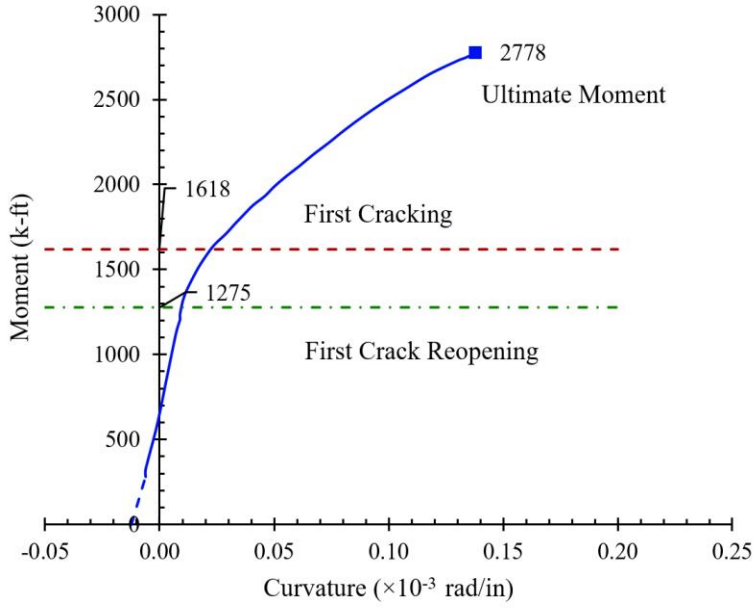

(d) BTE4

Figure 5.10: Moment-curvature response of BTE series with first instance of cracking and crack reopening in Response-2000

5.2 Comparison with Theoretical Prestress Loss

To investigate existing prestress loss estimation procedures, the experimentally determined losses were compared to theoretical loss calculation methods. Within this study, prestress loss was determined using the AASHTO LRFD Refined Method, the AASHTO-LRFD Lump-Sum Method, and AASHTO-LRFD Refined Method incorporating NCDOT assumptions. In addition, prestress loss was also determined for the four girders using measured material properties at the end of service life following AASHTO LRFD Refined Method. Generally, in design, in-situ properties should not be used for estimating losses. Specifically, specified concrete strengths should be used rather than measured strengths beyond the specified strength gain requirements. The traditional assumption is that the increase in concrete strength that occurs over the life of the structure will approximately correspond to the reduction in strength that the members will experience as a result of slow loading events. Therefore, it is not recommended to use measured concrete strengths in design or early in the life of the member to predict long-term effects or strength limit state calculations. However, this study explores the use of in-situ properties for use in service limit state calculations conducted for structures near the end of their service life. All the prestress losses calculated in this section are according to the provisions of current AASHTO LRFD standard (9th Edition, 2020). Some DOTs use older version of lump-sum estimates, AASHTO LRFD 4th Edition (2007) and the result is also shown for comparison. The theoretical losses were then compared with experimentally obtained prestress loss. Since BTE1 had one corroded strand, prestress losses were determined considering 37 strands instead of the original 38. This is a measure to account for the effect of corrosion that reduced the prestressing over its service life. The approach provides an opportunity to see how conservative or unconservative current loss prediction provisions are in such scenarios.

5.2.1 Assumptions

The prestress losses are calculated considering the girder along with the composite deck. The AASHTO LRFD Refined Method and AASHTO LRFD Lump Sum Method loss calculations require a set of assumptions. These are listed below:

1. The design concrete strength of the girder was assumed to be 5000 psi
2. The design strength of the concrete deck was assumed to be 3000 psi.

3. The effective flange width of deck was taken as 96 in., in accordance with AASHTO LRFD section 4.6.2.6 (2020).
4. The full jacking stress as the initial strand stress was used in the calculation of concrete stress at the centroid of the prestressing steel, f_{cgp}, for the elastic loss calculation.
5. In the creep calculation for final time, both composite and non-composite loads were included. Non-composite loads include the loading the bridge must carry before composite action is achieved. Typical elements/loadings included for non-composite dead loads (NCDL) are: girder self-weight, diaphragm weight (intermediate diaphragms), weight of haunches, deck weight (the slab itself). Composite loads include elements/loadings such as bridge rails (concrete parapet and railing), and Future Wearing surface.
6. In the girder-deck composite system, a future wearing course of 2 in was considered. The thickness of haunch was specified as 1.5 in the Bonner Bridge Design Plans.
7. A standard weight of 455 lb/ft indicated in the Structures Management Unit Manual of NCDOT was used to determine the weight of bridge rails which considers two bar metal rail with 2'-6" (760 mm) concrete parapet.

In the current NCDOT practice, the AASHTO assumptions for the age of the concrete at transfer, t_i, and the age of the concrete at composite deck laying, t_d are changed. In current practice, NCDOT assumes that the concrete age at transfer, t_i, is 1 day and the concrete age at composite deck laying, t_d, is 90 days. However, in the AASHTO LRFD commentary section C5.9.3.4.2c it notes that the relaxation equation of Eq. 54 in this report is a simplification of an equation given by Tadros et al. (2003) where the age at transfer is taken as 0.75 days and the age at composite deck laying is taken as 120 days (AASHTO LRFD, 2020). To be consistent with the assumptions in Eq. 54, the AASHTO LRFD loss prediction uses a concrete age at transfer, t_i, of 0.75 days and a concrete age at composite deck laying, t_d, of 120 days. Apart from these two values, the other inputs to the Refined Method loss calculation are the same as the NCDOT assumptions. Figure 5.11 shows a comparison of the theoretical and experimentally obtained prestress loss of the Bonner Bridge specimens. The subsequent sections will discuss the predicted losses in detail.

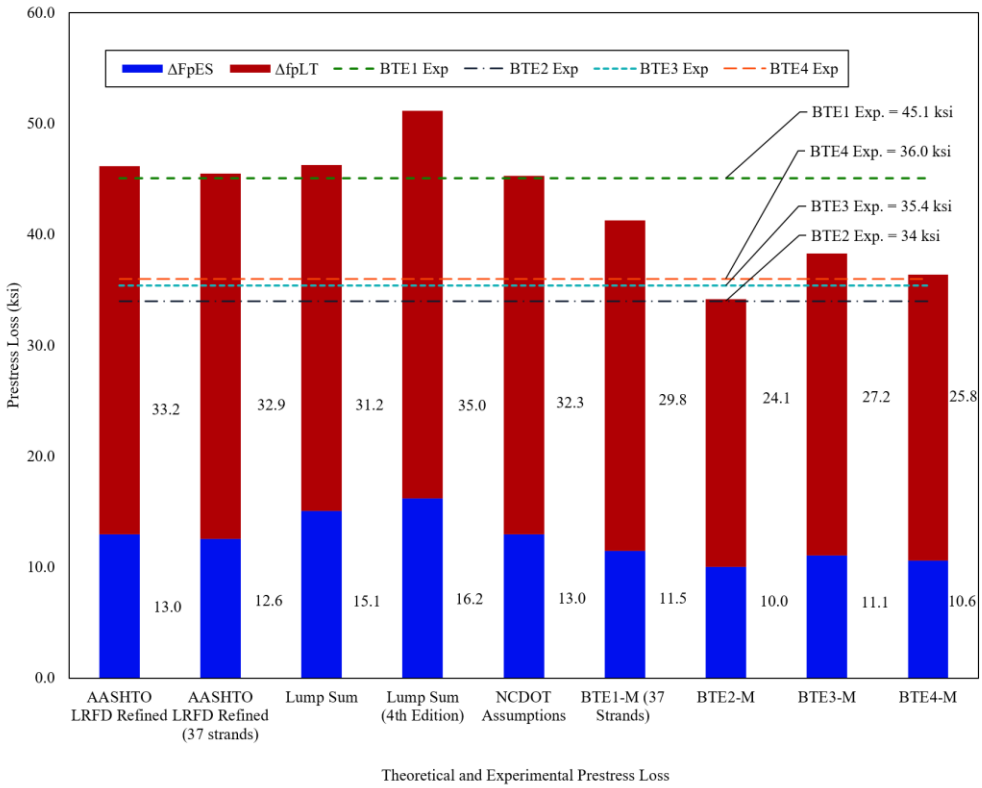

Figure 5.11: Comparison of experimental and theoretical prestress losses.

*BTE-M indicates losses calculated using the AASHTO LRFD Refined Method using tested material properties.

**ΔF_{pES} is the elastic shortening loss and ΔF_{pLT} is the long-term loss due to creep, shrinkage and relaxation

5.2.2 Elastic Shortening Loss

Both the AASHTO LRFD Refined Method and the NCDOT assumptions result in the same elastic shortening loss as shown in Figure 5.11. In comparison to the Refined Methods, the Lump Sum Methods in the 9th and 4th Edition of AASHTO LRFD Standard Specifications predict higher losses resulting from elastic shortening, by a margin of 16.7% and 25.0% respectively. On the other hand, the elastic shortening loss predictions using in-situ properties are comparatively lower by 11.6% for BTE1, 22.5% for BTE2, 14.7% for BTE3, 18.0% for BTE4 when compared to the Refined Method. The elastic shortening loss depends on material properties such as concrete strength, estimated modulus of elasticity concrete at transfer, modulus of elasticity of prestressing strand and also on the methodology used as in the case of an iterative Eq. 21 for the Refined Method or the alternative Eq. 23 used in the Lump Sum Method for this study. The design strength of the

concrete as specified in the Bonner Bridge drawings was 5.0 ksi for the girders but the measured concrete strength at the end of service life of the girders was much higher, 6.15 ksi, 9.08 ksi, 7.27 ksi and 7.97 ksi for BTE1, BTE2, BTE3 and BTE4, respectively. Since the equation for unit weight of concrete and modulus of elasticity of concrete at transfer uses the concrete strength, higher concrete strength would increase the moment due to self-weight of the girder. This reduces concrete stress at the center of gravity of prestressing tendons due to tensile stresses, f_{cgp} (Eq. 22) and at the same time over predict the modulus of elasticity at transfer which decreases the modular ratio. Moreover, the AASHTO LRFD specifies the modulus of elasticity of prestressing strand to be 28500 MPa whereas material test revealed an average value of 28000 MPa. This also decreases the modular ratio. A smaller modular ratio and concrete stress at the center of gravity of prestressing tendons causes the elastic shortening loss using in-situ properties to be lower. Table 5.5 shows the predicted elastic shortening loss, expressed as a percentage of the measured prestress losses in the girders. The results indicate the amount of prestress loss that occurs early in the service life of a prestressed concrete member in comparison to the total prestress loss that occurs over the entire service life of the structure. On average, the predicted elastic shortening losses is 27.8%, 36.9%, 35.5% and 34.9% of the measured prestress loss in BTE1, BTE2, BTE3 and BTE4 respectively.

Table 5.5: Comparison of predicted elastic shortening loss to measured prestress loss

Methods	Predicted Elastic Shortening Loss (ksi)	Elastic Shortening Loss/ Exp. Losses (%)			
		BTE1 (45.1 ksi)	BTE2 (34.0 ksi)	BTE3 (35.4 ksi)	BTE4 (36.0 ksi)
AASHTO LRFD Refined	13.0	28.7	38.1	36.6	36.0
AASHTO LRFD Refined (37 strands)	12.6	27.9	37.0	35.6	35.0
Lump Sum	15.1	33.5	44.4	42.7	42.0
Lump Sum (4th Edition)	16.2	35.9	47.7	45.8	45.0
NCDOT Assumptions	13.0	28.7	38.1	36.6	36.0
BTE1-M (37 Strands)	11.5	25.4	33.7	32.4	31.8
BTE2-M	10.0	22.3	29.6	28.4	27.9
BTE3-M	11.1	24.5	32.5	31.2	30.7
BTE4-M	10.6	23.5	31.2	30.0	29.5
Mean	**12.6**	**27.8**	**36.9**	**35.5**	**34.9**

5.2.3 Long-term Loss Components

The AASHTO LRFD Refined Method gives a measure of the various long-term loss components. The loss components are listed in Table 5.6. The table shows how the losses are spread over the two phases of the service life of the structure namely 1) Concrete at transfer and deck placement and 2) Deck placement and final age of concrete.

Table 5.6: Long-term loss components.

Long-term loss components	AASHTO LRFD Refined	AASHTO LRFD Refined (37 strands)	NCDOT Assumptions	BTE1-M (37 Strands)	BTE2-M	BTE3-M	BTE4-M
Δf_{pSR}	7.9	7.9	7.2	6.9	5.4	6.2	5.9
Δf_{pCR}	14.8	14.4	13.2	11.7	8.0	10.2	9.2
Δf_{pR1}	4.9	5.0	4.9	5.1	5.3	5.2	5.3
Δf_{pSD}	2.8	2.8	3.4	2.2	1.4	1.9	1.7
Δf_{pCD}	-0.3	-0.4	0.4	-0.3	-0.3	-0.3	-0.3
Δf_{pR2}	4.9	5.0	4.9	5.1	5.3	5.2	5.3
Δf_{pSS}	-1.8	-1.8	-1.8	-1.0	-1.0	-1.1	-1.2

In the refined estimate of long-term losses, the prestress losses due to creep and shrinkage of girder concrete between transfer and deck placement phase contributes a major portion of the loss, as much as 68.3% of the total long-term loss and 49.1%, nearly half of the total prestress loss over the entire service life of the structure. The loss due to relaxation of prestressing strands is the same for both time frames and hence is not considered for comparison. The shrinkage loss between transfer and deck placement is as much as 2.83 times (from AASHTO prestress loss values) of the shrinkage losses over the rest of the service life of member after deck placement. Rate of evaporation is high initially due to evaporation of unused water and diminishes over years. This explains the difference in shrinkage loss over the two phases. The long-term loss estimates using in-situ properties show that both creep and shrinkage losses in the first time frame (concrete transfer to deck placement) are comparatively lower in comparison to predicted losses using nominal material properties. The loss due to creep are 20.9%, 45.7%, 31.3% and 37.7% and loss due to shrinkage are 12.1%, 31.2%, 20.8%, 25.3% lower than the corresponding losses in AASHTO LRFD Refined Estimate. A study by Barr et al. (2008) states a possibility that the difference between losses among the girders may be due to differential magnitudes of creep and shrinkage stresses.

5.2.4 Total Prestress Loss

An examination of the total prestress loss due to elastic shortening and long-term losses is shown in Figure 5.11. The results show that the predictions for BTE1 are similar to the experimentally measured prestress loss in all methods except for two. The Lump Sum approach specified in 4th edition of AASHTO LRFD overestimates the loss whereas it is underestimated in AASHTO LRFD Refined Method using measured properties. The Refined Method produces nearly the same prestress loss when considering 37 strands to account for the corrosion instead of 38 strands. Lump Sum losses align with the experimental prestress loss in BTE1 but is highly conservative for the all the other girders. The Lump Sum estimate of 45 ksi provided in AASHTO Standard Specifications (1973) is a reasonable estimate for BTE1. AASHTO Refined Method and Lump Sum Method overestimated the losses for BTE2 in comparison to experimental loss. BTE2 had a concrete strength considerably higher than other specimens and nearly double the specified concrete strength, so the conservative prediction of loss is expected because a higher strength concrete will experience less long-term creep strains under the same load as a lower strength concrete. The opposite is true for BTE1, BTE3 and BTE4 which had comparatively lower concrete strength (arranged in increasing order of strength) compared to BTE2. The study shows that the prestress losses of girders can be different even if they are from the same span as in the case of Bonner Bridge specimens and theoretical loss predictions show changes in concrete strength can contribute to this variation. The test to predicted (T/P) ratio of losses are shown in Table 5.7.

Table 5.7: Test-to-predicted ratio of prestress losses (Predictions follow the code equations of AASHTO LRFD).

Girder	Experimental Loss (ksi)	Refined Method with Nominal Material Properties		Refined Method consistent with NCDOT assumptions		Refined Method with Measured Material Properties		Lump Sum Method		Lump Sum Method (4th Edition)	
		Prestress Loss (ksi)	T/P	Prestress Loss (ksi)	T/P	Prestress Loss (ksi)	T/P	Prestress Loss (ksi)	T/P	Prestress Loss (ksi)	T/P
BTE1	45.1	46.2	0.98	45.3	1.00	41.3	1.09	45	1.00	51.2	0.88
BTE2	34.0		0.74		0.75	34.2	0.99		0.76		0.66
BTE3	35.4		0.77		0.78	38.3	0.92		0.79		0.69
BTE4	36.0		0.78		0.80	36.4	0.99		0.80		0.70

The results show that the T/P ratio for losses using measured material properties can be better compared to losses obtained with nominal material properties. Predicted prestress losses in BTE2 and BTE4 have a test to predicted ratio of 0.99 and this shows for an undamaged girder, predictions are reasonable. However, for BTE1, using measured material properties gives a more conservative estimate of the losses in comparison to the measured losses, with a T/P ratio of 1.09. Although loss predictions using in-situ properties are reasonable, as explained previously, nominal material properties should be used for loss calculation at design or early in the life of the structure. The Lump Sum estimates, either from the current Edition (2020) or older edition such as 4th Edition (2007), are in general conservative with T/P ranging from 0.76-1.00 and 0.66-0.88. The higher upper bound of T/P for these methods is due to accurate prediction of losses only for BTE1 which had the corroded strand. It is only reasonable to use these methods for preliminary estimates.

5.2.5 Prestress Gain

There can be an elastic "gain" due to deck weight, superimposed dead load and live load (Service III). The literature and a survey of the DOTs indicates that some state agencies account for this while others do not. NCDOT considers elastic gains due to deck weight and superimposed dead load. Using the AASHTO LRFD Refined Method, the predicted elastic gains due to:

1) Deck weight and superimposed dead load is 3.30 ksi.
2) Live load (Service III) is 5.43 ksi.

Figure 5.12 shows the predicted final loss percentage both with and without elastic gains (with live load and without live load) as a percentage of the initial prestressing stress before transfer.

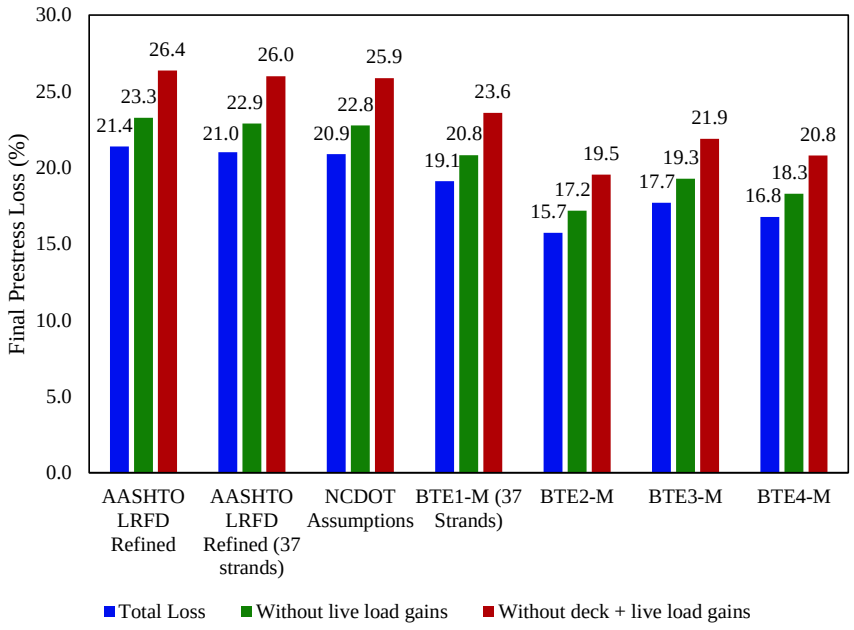

Figure 5.12: Prestress losses at service loads.

5.3 Cracking Moment and First Tensile Stress of BTE Series

Having determined the loss of prestress for the BTE series girders both experimentally and theoretically, estimates of the first cracking moment, and the moment to produce tension in the bottom fiber can be made. The capacities can later be compared to the live loads placed on the girder by a rating truck such as the HS-20 (AASHTO, 2019). This provides an estimate of the factor of safety against either the occurrence of tensile stresses in the bottom fiber of the girder or cracking in the girders while they are used in service. As observed earlier, Response-2000 can accurately predict the flexural response of the BTE series and confidently assess the prestress loss in the recovered girders. Therefore, Response-2000 can also be reliably used to model the girder with composite deck to predict the first cracking moment and tensile stress in the bottom fiber of in addition to the girder configurations received at the CFL. Additionally, using Response-2000, the ultimate capacity of the girders including the composite concrete deck can be compared to applied live loads to ascertain the factor of safety against exceedance of the flexural capacity.

To determine the cracking moment and moment where first tension occurs in the bottom fiber of the concrete for a given girder and prestress loss, Eq. 2 is modified to Eq. 4 below. In Eq. 4 P_{eff} is determined by multiplying the total strand area by the strand stress which is determined by subtracting the total losses from the initial jacking stress. M is the applied moment, and M_d is

the dead load moment. The area and moment of inertia are transformed sectional properties corresponding to the material properties of each girder.

$$\sigma = \frac{P_{eff}}{A} + \frac{P_{eff}ey}{I} - \frac{(M+M_d)y}{I} \quad (4)$$

For the cracking moment predictions, an allowable tensile stress in the concrete of $6\sqrt{f_c'}$ is used as suggested by the prestressed concrete load rating equations provided in section 6B.5.3.3 of the AASHTO Manual for Bridge Evaluation (AASHTO, 2019). For the assessment of first tension in the bottom fiber, σ in Eq. 4 is set to zero. The applied moments to cause first cracking and the onset of tension in the bottom fiber are calculated for each girder using three different amounts of prestress loss: the losses from AASHTO LRFD Refined Methods using NCDOT assumptions, the losses from AASHTO LRFD Refined Methods with adjusted inputs suggested in the AASHTO commentary, and finally, the losses measured from the laboratory testing of each specimen. Table 5.8 below shows the resulting capacities.

Table 5.8: Predicted girder applied moment for various prestress losses without deck.

Specimen	First Cracking (k-ft)			First Tensile Stress (k-ft)		
	AASHTO-NCDOT	AASHTO-Commentary	Response-2000	AASHTO-NCDOT	AASHTO-Commentary	Response - 2000
BTE1	1157	1149	1159	878	870	880
BTE2	1163	1155	1261	844	836	942
BTE3	1147	1139	1233	855	847	941
BTE4	1165	1157	1247	855	847	936

The first cracking values predicted with the application of Response-2000 in Table 5.8 are lower than those found in Chapter 4 of this report. These cracking moments are determined at the bottom fiber not at 1.75 inches above the bottom fiber as is done in chapter 4. The first cracking moment and the capacity at first tensile stress predicted by both AASHTO-NCDOT and AASHTO-Commentaries are lower compared to the Response-2000 predictions incorporating laboratory measured prestress losses. The results show that AASHTO LRFD Refined Method modified with NCDOT assumptions better predict the first cracking and first tensile stress moments of the BTE specimens in comparison to the AASHTO LRFD Refined Method using commentary suggestions.

The same first cracking and first tensile stress moments were calculated for the girders with the composite deck. Figure 5.13 shows an example of the cross-section input to Response-2000 to compute the capacities with the composite concrete deck attached. The effective flange width for the girders is taken as the tributary area of the girders, 96 in., in accordance with section 4.6.2.6 of AASHTO LRFD Bridge Design Specifications (2020) The thickness of the deck is 7 in. to represent the minimum design thickness of 7.25 in. noted on the construction drawings for the Bonner Bridge less 0.25 in. as a sacrificial wearing surface.

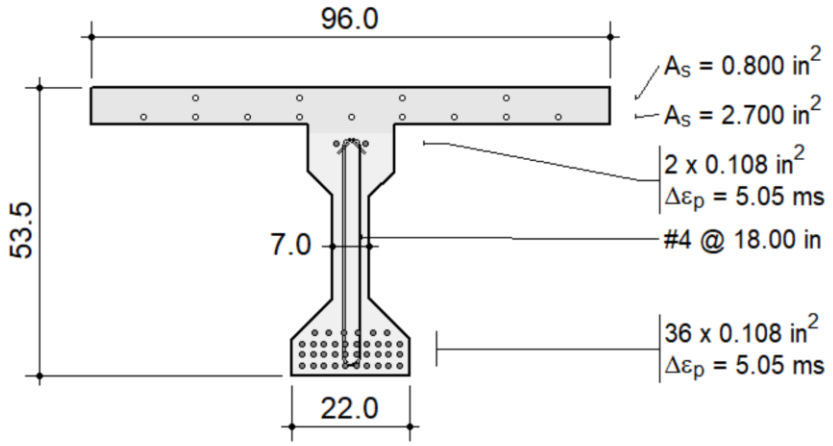

Figure 5.13: Response-2000 section for BTE2 with composite deck at midspan.

The dead load considered for this analysis includes both composite and non-composite loads such as girder, deck, diaphragm, barrier and rails, haunch, wearing course as would exist in the actual structure were included for an estimation of the capacity. Table 5.9 shows the predicted applied moment capacities for the four girders in the BTE series for the composite deck, girder system.

Table 5.9: Predicted girder applied moment for various prestress losses with composite deck.

Specimen	First Cracking (k-ft)			First Tensile Stress (k-ft)		
	AASHTO-NCDOT	AASHTO-Commentary	Response -2000	AASHTO-NCDOT	AASHTO-Commentary	Response -2000
BTE1	1311	1299	1313	866	854	868
BTE2	1303	1292	1445	794	783	936
BTE3	1294	1282	1420	827	816	953
BTE4	1350	1338	1470	848	836	968

Both Table 5.8 and 5.9 indicate that the first cracking and first tensile stress moments predicted using the losses calculated by the AASHTO LRFD Refined Method consistent with NCDOT assumptions are lower than the capacities predicted using Response-2000 that used laboratory measured losses. For BTE1, the predictions using NCDOT comments are similar to the capacity given by Response-2000. But for other BTE series specimens, which did not contain any corroded strands, the predicted capacity from Response-2000 are higher. The first cracking moment increase by 6-8% and the first tensile stress capacities are higher by 8-12%. Thus, for girders with and without the effect of corrosion, current codes and practices can predict the capacity reasonably well.

To provide additional context for the moments listed in Table 5.8 and Table 5.9, it can be compared to the live load moment per wheel line for a design truck. Appendix C6B of AASHTO Manual for Bridge Evaluation (2019) shows the live load moments per wheel for various rating trucks over various spans. For convenience, the chart is appended at the end of this report in Appendix F. The span for the Bonner Bridge girders is 61 ft 2 in, so it can be compared to the 60 ft span. The controlling live load is the live load with impact factors applied by the HS-20 truck. This design truck produces a live load moment of 512.2 k-ft. The ratio of the live load moment due to short-term loading for HS-20 truck to the capacities of the girder without deck are listed in Table 5.10 and Table 5.11. Both Table 5.10 and Table 5.11 show that, accounting for self-weight, the girders in the laboratory (without a composite deck) can support this moment without incurring cracking or tension in the bottom fiber of the concrete. The results show that the live load moment is around 40-45% of the first cracking capacity and around 55-60% of the first tensile stress capacity.

Table 5.10: Live load moment to first cracking moment capacity ratio for HS-20 loading on girders without deck for different loss quantities (M_L/C_T – Live Load Moment/ Capacity up to tensile stress of $\mathbf{6}\sqrt{\boldsymbol{f'_c}}$).

Girder	AASHTO-NCDOT		AASHTO-Commentary		Response-2000	
	First Cracking (k-ft)	*M_L/C_T	First Cracking (k-ft)	M_L/C_T	First Cracking (k-ft)	M_L/C_T
BTE1	1157	0.44	1149	0.45	1159	0.44
BTE2	1163	0.44	1155	0.44	1261	0.41
BTE3	1147	0.45	1139	0.45	1233	0.42
BTE4	1165	0.44	1157	0.44	1247	0.41

Table 5.11: Live load moment to concrete capacity up to first tensile stress ratio for HS-20 loading on girders without deck for different loss quantities (M_L/C_0 – Live Load Moment/ Capacity up to zero tensile stress).

Girder	AASHTO-NCDOT		AASHTO-Commentary		Response-2000	
	First Tensile Stress (k-ft)	M_L/C_0	First Tensile Stress (k-ft)	M_L/C_0	First Tensile Stress (k-ft)	M_L/C_0
BTE1	878	0.58	870	0.59	880	0.58
BTE2	844	0.61	836	0.61	942	0.54
BTE3	855	0.60	847	0.60	941	0.54
BTE4	855	0.60	847	0.60	936	0.55

Similar comparisons to the live load moment can be made considering the girder with composite deck. With a composite deck, results in Table 5.12 and Table 5.13 show that the live load produced by the HS-20 with impact factors does not exceed the moment for first tension in the bottom fiber of concrete or the first cracking moment, for each of the prestress loss quantities when the composite concrete deck is included in the analysis. Table 5.12 shows the ratio of live load moment to the capacity of girder for short-term loading for the HS-20 live load with impact factors if a tensile stress of $6\sqrt{f_c'}$ is permitted in the composite girders, and Table 5.13 shows the ratio of live load moment to the capacity of girder due to HS-20 for short-term loading if no tensile stress is permitted. The results in Table 5.12 and 5.13 show that the girders have much greater applied moment capacity than the demand placed on the structure by the HS-20 rating truck. The live load moment is around 35-40% of the first cracking capacity and 53-65% of the first tensile stress capacity of the girder with composite deck. Note that all demand to capacity ratios provided in this section utilize unfactored loads and strength reduction factors have been set to unity. A detailed discussion on the capacity of girder in terms of factored live loads can be found in the load rating chapter of this report.

Table 5.12: Live load moment to first cracking moment capacity ratio for HS-20 loading on girders with deck for different loss quantities (M_L/C_T – Live Load Moment/ Capacity up to tensile stress of $6\sqrt{f'_c}$).

Specimen	AASHTO-NCDOT		AASHTO-Commentary		Laboratory Measured	
	First Cracking (k-ft)	D/C	First Cracking (k-ft)	D/C	First Cracking (k-ft)	D/C
BTE1	1312	0.39	1300	0.39	1280	0.40
BTE2	1303	0.39	1292	0.40	1445	0.35
BTE3	1294	0.40	1282	0.40	1417	0.36
BTE4	1347	0.38	1335	0.38	1406	0.36

Table 5.13: Live load moment to concrete capacity up to first tensile stress ratio for HS-20 loading on girders with deck for different loss quantities (ML/C0 – Live Load Moment/ Capacity up to zero tensile stress).

Specimen	AASHTO-NCDOT		AASHTO-Commentary		Response-2000	
	First Tensile Stress (k-ft)	M_L/C_0	First Tensile Stress (k-ft)	M_L/C_0	First Tensile Stress (k-ft)	M_L/C_0
BTE1	866	0.59	854	0.60	868	0.59
BTE2	794	0.64	783	0.65	936	0.55
BTE3	827	0.62	816	0.63	953	0.54
BTE4	848	0.60	836	0.61	968	0.53

The ultimate capacity of the girders with and without the composite concrete deck can also be compared to the live load demand. Using the Response-2000 models discussed in section 5.1 above, the ultimate capacity for the girders with the composite concrete deck can be determined. The predicted moment-curvature response of the girders with composite deck is shown in Figure 5.14.

While the failure mode of the girders in the laboratory was crushing of the top flange, the capacity of the girders with their composite deck is governed by rupture of prestressing steel. Ultimate capacity of members governed by rupture of prestressing steel is minimally affected by prestress losses. This is in contrast to members governed by crushing of the top flange where

prestress loss and stress-strain behavior of the concrete will affect the ultimate capacity. Lower prestress loss will create a larger tensile stress that must be resisted by the top flange of the concrete, and therefore, for members governed by concrete crushing, the ultimate capacity may be lower if there is less prestress loss. Table 5.14 shows the predicted ultimate capacity of the girders in the short term and the live load moment (512.2 k-ft) to flexural capacity ratio for the HS-20 live load with impact factors. Note the ultimate capacity provided in Table 5.14 is the ultimate moment capacity accounting for self-weight.

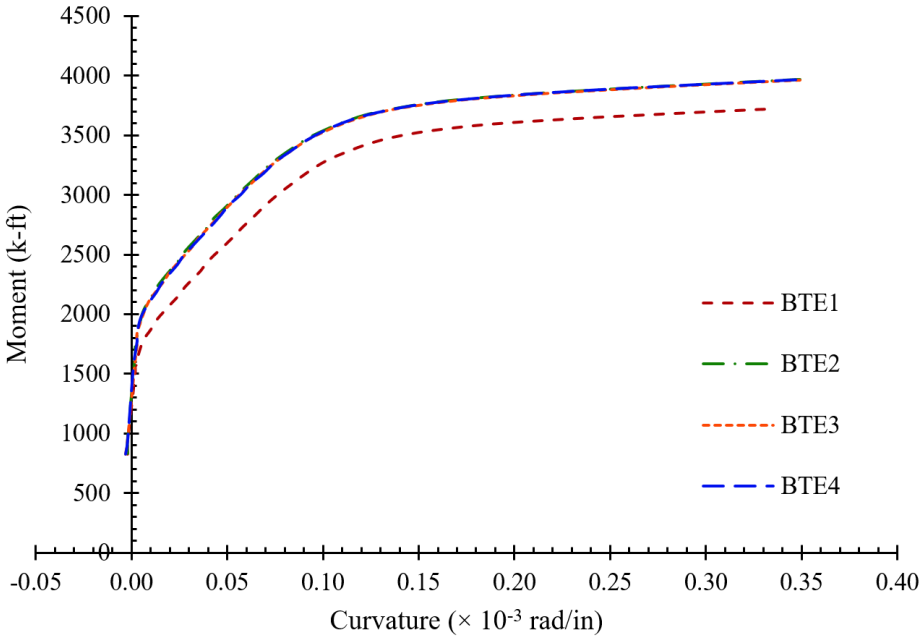

Figure 5.14: Predicted Moment-Curvature Response of Composite Girder-Deck System using Response-2000

Table 5.14: Ultimate applied moment capacity of the BTE series with composite concrete deck.

Specimen	Mu (k-ft)	Demand (k-ft)	D/C
BTE1	3838	512.2	0.133
BTE2	3966		0.129
BTE3	3964		0.129
BTE3	3962		0.129

Table 5.14 shows that all four of the girders have ultimate moment capacities that exceed the live load demand of the HS-20 truck. BTE1 has the highest D/C because of corrosion of strand at midspan, but the ratio of live load demand to flexural capacity for BTE1 is 0.133. This suggests that the girder still retains sufficient moment capacity. It is to be noted that for BTE1, the effect of corrosion was more conservatively induced by disregarding strand which leads to a lower ultimate moment capacity. The girders recovered from the Bonner Bridge all showed good performance and maintain sufficient demand to capacity ratios even when no tensile stress is permitted in the girders as required by the NCDOT. The residual capacity of the aged girders compares favorably to the demands suggested in the table of live loads provided in appendix C6B of the AASHTO Manual for Bridge Evaluation (2019).

CHAPTER 6 – LOAD RATING OF BRIDGES

In this chapter the Bonner Bridge girder data is used to conduct load rating calculations for the bridge girders using LRFR and LFR in accordance with AASHTO LRFD and AASHTO Standard Specifications. Appendix G provides additional context and bridge load rating calculations.

6.1 Background and Approaches

Bridge load rating is done on a girder-to-girder basis. The material properties previously determined underlines that each girder is unique and the prestress losses vary, although they were from the same span. The girders were instrumented during flexural testing to determine the effective prestressing force, prestress loss, cracking moment, first tensile stress capacity and ultimate flexural capacity. The tests were conducted without a composite deck. However, with the results, the capacity of structure (girder with composite deck) can be reliably estimated using Response-2000 as discussed earlier. The flexural capacity of the structure was also determined following AASHTO LRFD and AASHTO Standard Specifications in addition to prestress losses obtained in Chapter 5. Using estimates of strength and stresses from AASHTO and Response-2000, rating factors can be determined for each girder (along with composite deck). Rating factors for the girder without deck can also be determined using simply the experimental values and this can later be used to compare to the state of girder at those capacities.

The girders were load rated under both LRFR and LFR rating method. The main difference in the methods arises in the strengths and stress estimates used for calculating rating factors. Under the LRFR rating method, four approaches are discussed. These approaches are as follows:

1) The use of nominal material properties and finding prestress losses, strength and stresses according to the provisions of AASHTO LRFD.

2) The use of measured material properties and finding prestress losses, strength and stresses according to the provisions of AASHTO LRFD.

3) The use of measured material properties, and modelling in Response-2000 to find prestress loss estimates, flexural resistance and stresses.

4) The use of measured material properties and experimental data from flexural testing of the girders. It is noted that although the entire composite girder-deck system was considered but the flexural resistance was limited to the peak moment observed in flexural test.

The rating factors are discussed in the subsequent section.

6.2 LRFR and LFR Rating for BTE Series

The rating factors under LRFR and LFR rating method are listed in Table 6.1. The rating factors in this section consider the nominal material properties for prestress loss and capacity estimates. Under the LRFR method, three different limit states are used: Strength I (Inventory and Operating), Service III and Service I limit states. LFR method does not mention any limit states, rather inventory and operating rating were obtained from the factored load method and only inventory ratings from the allowable stress method. The code specifies an allowable tensile stress of $6\sqrt{f_c'}$ but since different state authorities have a policy of zero tensile stress, rating factors were compared for allowable stresses of $6\sqrt{f_c'}, 3\sqrt{f_c'}$ and 0 in both LRFR and LFR method as shown in Table 6.1.

Table 6.1: Rating using nominal material properties.

	LRFR Rating Factors					
	Strength I Inventory (HL-93)	Strength I Operating (HL-93)	Service III (HL-93) ($6\sqrt{f'_c}$)	Service III (HL-93) ($3\sqrt{f'_c}$)	Service III (HL-93) (Zero tensile stress)	Service I (HL-93)
AASHTO LRFD	1.82	2.36	1.12	0.90	0.67	2.45
AASHTO LRFD with NCDOT lossess	1.82	2.36	1.14	0.91	0.69	2.45
	LFD Rating Factors		Allowable Stress Rating Factors			
	Inventory	Operating	Inventory ($6\sqrt{f'c}$)	Inventory ($3\sqrt{f'c}$)	Inventory (0)	
AASHTO Standard	1.55	2.59	1.38	1.13	0.89	

Theoretical prestress losses in the AASHTO LRFD Refined Method and using NCDOT assumptions are similar. As a result, the rating factors are close. In both the methods, the rating factor falls below 1 if only zero tensile stress is permitted under the Service III conditions and

would require the bridge to be posted. The inventory rating factors are higher under Strength I limit state of LRFR in comparison to LFR. For all other cases, the LRFR rating factors wre lower than LFR rating factors. However, it is unlikely to compare between LRFR and LFR rating factors due to the different set of assumptions and load factors. Chen and Aswad (1996) found that the LRFD code distribution factors can be uneconomically conservative for bridges with large span-to-depth ratios. Live-load distribution factors in the current LRFD standard are obtained from a parametric study by Zokaie et al. (1991b) which considered variations in girder spacing, girder stiffness, span length, skew and slab stiffness.

Under the Service III limit state, the differences between the rating factor decreases as the allowable stress value reduces. One of the reasons for this is that LRFR has an additional live load distribution factor of 0.8 which tends to reduce the effect of live load but increases the rating factor. This reduction results in lower calculated tensile stresses in the girders thereby influencing the rating factor.

6.3 LRFR Rating of BTE Series

According to the Manual for Bridge Engineering (MBE) guidelines, it is assumed that bridges that have a rating factor greater than 1 (design load check) at the Inventory level will have satisfactory load rating for all legal loads that fall within the LRFD exclusion limits. It is also assumed that bridges may not rate (RF<1) for all state legal loads, specifically those vehicles significantly heavier than the AASHTO trucks, even if they have adequate capacity for HL-93 at the operating level. However, according to the specifications of MBE, the bridge having a rating factor greater than 1 is assumed to sufficient capacity for AASHTO legal loads. The rating factors for each girder under the LRFR rating method calculated with strength and stress estimates from AASHTO, Response-2000 and experimental results are listed in Table 6.2, 6.3, 6.4 and 6.5.

BTE1 incurred the most prestress loss because of the corroded strand. Since there was a corroded strand, the condition factor in LRFR rating was selected to be 0.95. Results in Table 6.2 show BTE1 did not meet the allowable stress criteria of $3\sqrt{f_c'}$ or zero tensile stress as the rating factor was less than 1. For BTE1, the rating factor for strength and serviceability states indicate that Response-2000 with measured properties is less conservative than estimates with nominal

properties. It should be noted that the experimental rating factors are expected to be less than the theoretical estimates as the flexural capacity of the girder without the composite deck is used. The experimental rating factors under Strength I, both inventory and operating, are greater than 1 for BTE1 which was tested to flexural failure. This shows that BTE1 have sufficient load carrying capacity for operating live load and maximum permissible live load to which the structure may be

Table 6.2: BTE1- LRFR rating factors in accordance with AASHTO LRFD provisions.

Assumptions	Strength I - Inventory	Strength I- Operating	Service III ($6\sqrt{f'_c}$)	Service III ($3\sqrt{f'_c}$)	Service III ($0\sqrt{f'_c}$)	Service I
Using Nominal Properties & Refined Loss	1.82	2.36	1.12	0.90	0.67	2.45
Using Measured Properties & Refined Loss	1.74	2.25	1.23	0.97	0.71	5.12
Response-2000 with Measured Properties	1.86	2.41	1.22	0.96	0.70	5.12
Experimental	1.24	1.61	1.18	0.92	0.66	5.12

Table 6.3: BTE2- LRFR rating factors in accordance with AASHTO LRFD provisions.

Assumptions	Strength I - Inventory	Strength I- Operating	Service III ($6\sqrt{f'_c}$)	Service III ($3\sqrt{f'_c}$)	Service III ($0\sqrt{f'_c}$)	Service I
Using Nominal Properties & Refined Loss	1.82	2.36	1.12	0.90	0.67	2.45
Using Measured Properties & Refined Loss	1.93	2.51	1.48	1.17	0.86	5.61
Response-2000 with Measured Properties	2.01	2.61	1.49	1.18	0.87	5.61
Experimental	1.25	1.62	1.49	1.18	0.87	5.61

Table 6.4: BTE3- LRFR rating factors in accordance with AASHTO LRFD provisions.

Assumptions	Strength I - Inventory	Strength I- Operating	Service III ($6\sqrt{f'_c}$)	Service III ($3\sqrt{f'_c}$)	Service III ($0\sqrt{f'_c}$)	Service I
Using Nominal Properties & Refined Loss	1.82	2.36	1.12	0.90	0.67	2.45
Using Measured Properties & Refined Loss	1.93	2.50	1.42	1.14	0.87	4.83
Response-2000 with Measured Properties	2.02	2.62	1.42	1.14	0.87	4.83
Experimental	1.14	1.48	1.42	1.14	0.87	4.83

Table 6.5: BTE4- LRFR rating factors in accordance with AASHTO LRFD provisions

Assumptions	Strength I - Inventory	Strength I- Operating	Service III ($6\sqrt{f'_c}$)	Service III ($3\sqrt{f'_c}$)	Service III ($0\sqrt{f'_c}$)	Service I
Using Nominal Properties & Refined Loss	1.82	2.36	1.12	0.90	0.67	2.45
Using Measured Properties & Refined Loss	1.92	2.49	1.42	1.13	0.84	4.67
Response-2000 with Measured Properties	2.01	2.61	1.42	1.13	0.84	4.67
Experimental	1.19	1.55	1.43	1.14	0.85	4.67

subjected, even without the consideration of the nominal resistance of composite girder-deck system. At service limit states, where allowable tensile stresses are used to to calculate rating factors, the theoretical and experimental rating factors are comparable. At Service I limit state, the experimental rating factor is greater than 1 even without considering the composite deck system.

Prestress losses in BTE2 (34.0 ksi), BTE3 (35.4 ksi) and BTE4 (36.0 ksi) were lower than BTE1 (45.1 ksi). The capacity of the girders, BTE2, BTE3 and BTE4 at the end of their service life are similar since the prestress losses are comparable, and as a result, the rating factors are nearly the same. For these three girders, the rating factors calculated from strength and stress predictions using measured properties (both AASHTO LRFD Refined Method and Response-2000) are greater than that obtained with nominal properties. The difference stems from the prediction of a much higher prestress loss (46.2 ksi) in comparison to experimental losses in the AASHTO LRFD Refined Method with nominal properties. The rating factors of all the girders are greater than 1 for all limit states except for the zero tensile stress under Service III conditions and when using nominal material properties with an allowable stress of $3\sqrt{f_c'}$ in Service III limit state. Although the girders do not meet the zero tensile stress limits, BTE2, BTE3 and BTE4 still satisfies the allowable stress criteria of $3\sqrt{f_c'}$ under Service III limit state when determined experimentally, or using measured properties in AASHTO LRFD Refined Method or Response-2000. This indicates the existing code provisions are conservative. The experimental rating factors under Strength I, both inventory and operating, are greater than 1 for BTE2, BTE3 and BTE4. This shows these aged girders have sufficient load carrying capacity at operating live load and maximum permissible live load to which the structure may be subjected, even without the consideration of the nominal resistance of composite girder-deck system. The experimental rating factors under

service conditions are very close to the rating factors calculated using stresses predicted by Response-2000.

The Rating Factor (RF) obtained above may be used to determine the safe load capacity of the bridge in tons. The capacity of the girders from the results of Response-2000 with LRFD Strength I operating and Service III inventory (allowable tensile stresses of both $6\sqrt{f_c'}$ and 0) are shown in Figure 6.1.

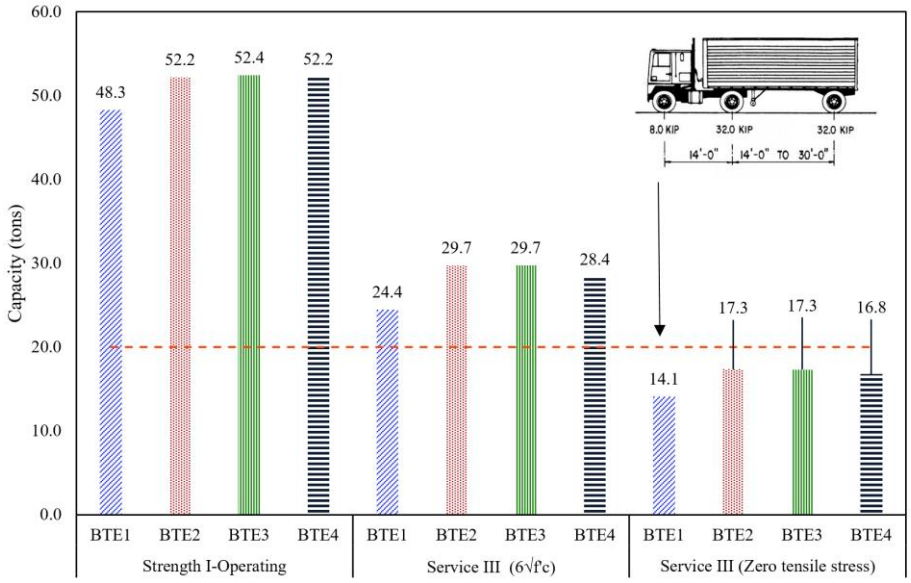

Figure 6.1: Rating capacity of Bonner Bridge girders.

The capacity of BTE1 in both strength and service limit states is the lowest among the four girders tested as it had a corroded strand and a higher prestress loss. The capacity of the girders BTE2, BTE3 and BTE4 on average were 52.3 tons in Strength-I Operating, 29.3 tons in Service III ($6\sqrt{f'_c}$) and 17.1 tons in Service III ($0\sqrt{f'_c}$). Under Service III conditions with no tensile stress permitted at the bottom of girder, the capacities of the all the BTE series girders fall below the 20 tons. Therefore, at this limit state, results indicate no girders satisfy the serviceability criteria due to the passage of a HL-93 design truck. According to the provision of AASHTO, the lowest rating factor calculated among applicable limit states determines the controlling rating factor. In the BTE series, BTE1 had the lowest rating factor and capacity at Service III limit state where only zero tensile stress is permitted. Therefore, the study indicates rating factor of BTE1 governs.

6.4 State of Girder at Rating Capacity

The flexural testing of the BTE series gives a unique opportunity to assess the behavior of member in short-term heavy loading at the end of its service life. As mentioned earlier, cracks were marked and photographed at different load stages during flexural testing of the girder which shows the state of girder under those loading condition. Figure 6.2 shows the observed cracks at a load stage of 150 kips of actuator load (1898 k-ft accounting for self-weight) and the failure of BTE1 in flexure at a moment of 2831 k-ft. It is possible to show the girder condition at this two stages and their corresponding location on the moment curvature response.

(a)

(b)

Figure 6.2: Condition of BTE1 at 150 kips of Actuator Load (corresponding to 1898 k-ft accounting for self-weight) (c) Failure of BTE1 at Ultimate Capacity (2831 k-ft)

Response-2000 can accurately predict the response of the aged prestressed girders along with estimates of cracking moment, first tensile stress moment, flexural capacity. The predicted moment-curvature response of BTE1 is shown in Figure 6.3, marked with predicted capacities under various methods and experimental capacity.

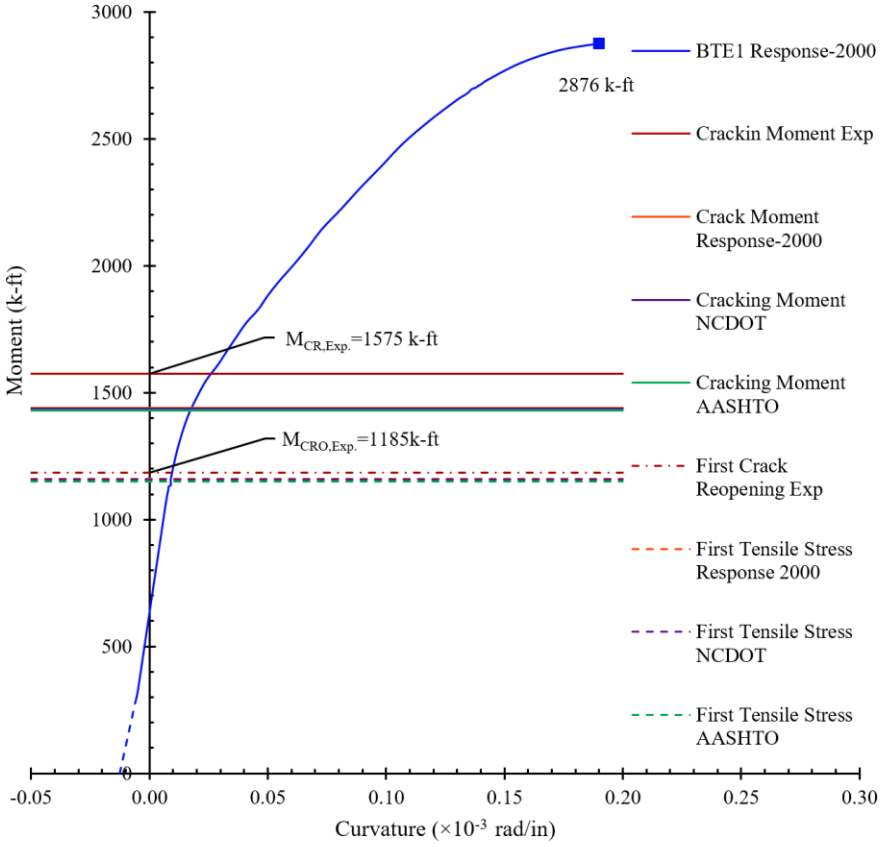

Figure 6.3: Predicted moment-curvature response of BTE1 given by Response-2000.

Rating factors for serviceability checks are calculated using allowable stress at the cracking moment ($6\sqrt{f'_c}$) and first tensile stress capacity ($0\sqrt{f'_c}$). From Figure 6.3, it is observed that the ultimate flexural capacity is 1.83 times the cracking moment and 2.43 times the crack reopening moment. The LRFR rating factor for BTE1 calculated at Service III limit state with zero tensile stress permitted at the bottom fiber of girder is less than 1. According to the guidelines of AASHTO and MBE, the bridge does not satisfy the limit. However, at a permitted tensile stress of $6\sqrt{f'_c}$, the LRFR rating factor is greater than 1 indicating the bridge does not require posting. Therefore, if the bridges are allowed a tensile stress of $6\sqrt{f'_c}$ where the moment is around 55% of its ultimate capacity, the design life could be extended (even if only the limit is extended near the end of their service life). However, if a tensile stress of $6\sqrt{f'_c}$ occurs, it could also lead to new cracks opening. This could lead to accelerated corrosion and therefore the bridge should be monitored accordingly.

Similar observations can be made for other girders of BTE series. Since BTE2, BTE3, BTE4 had similar prestresses losses, and essentially comparable response, calculations are only

shown for BTE2. Figure 6.4 shows the observed cracks at load stage of 120 kips (corresponding to a moment of 1578 k-ft accounting for self-weight) and the failure of BTE2 in flexure (2860 k-ft accounting for self-weight).

(a)

(b)

Figure 6.4: Condition of BTE2 at 120 kips of Actuator Load (corresponding to 1578 k-ft accounting for self-weight) (c) Failure of BTE1 at Ultimate Capacity (2831 k-ft).

The predicted moment-curvature response of BTE2 is shown in Figure 6.5, marked with predicted capacities under various methods and experimental capacity. From Figure 6.5, it is observed that the ultimate flexural capacity is 1.73 times the cracking moment and 2.24 times the crack reopening moment. As observed in BTE1, the LRFR rating factor for BTE2 calculated at Service III limit state with zero tensile stress permitted at the bottom fiber of girder is less than 1. According to the guidelines of AASHTO and MBE, the bridge does not satisfy the limit. However, at a permitted tensile stress of $6\sqrt{f'_c}$, the LRFR rating factor is greater than 1 and the limit would not be exceeded. Therefore, at or near cracking stress where the moment is around 58% of its ultimate capacity, the design life could be extended (even if only the limit is extended near the end

of their service life). In contrast, an allowable tensile stress of $6\sqrt{f'_c}$ could lead to cracks. This could lead to accelerated corrosion and therefore the bridge should be monitored accordingly.

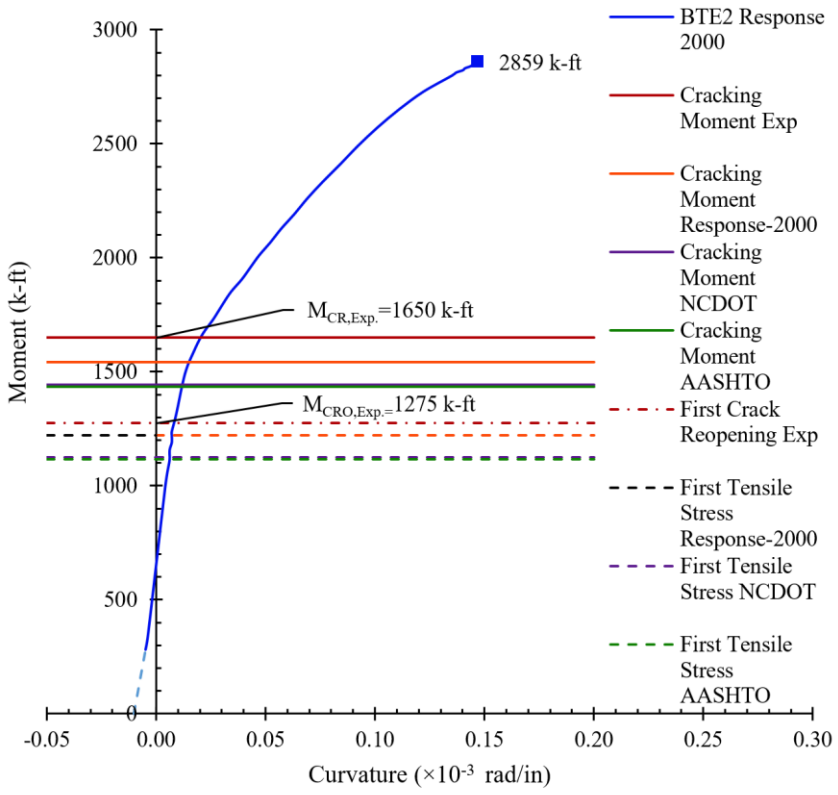

Figure 6.5: Predicted moment-curvature response of BTE2 given by Response-2000.

CHAPTER 7 – CONCLUSIONS AND RECOMMENDATIONS

This chapter summarizes key observations, conclusions and recommendations from the research program that assessed prestress losses in four girders recovered from the Herbert C. Bonner Bridge after 56 years of service. The girders were tested in flexure to determine their prestress losses and capacities after 56 years of service. The prestress loss results were compared to predictions from Response-2000, the AASHTO LRFD Refined Method, and the AASHTO Lump Sum Method. The experimental strength measurements and associated stress estimates along with calculated predictions of the behavior were used to inform a load rating calculation for the girders. Shear tests of several girders near their ends were also conducted. Below is a summary of the general conclusions, subdivided into segments for convenience:

7.1 Material Properties and General Outcomes

1. Although all girders had the same design concrete strength of 5000 psi, concrete strengths varied largely at the end of service life, as judged by cores that indicated a range of concrete compressive strengths from 6150 psi for BTE1 to 9080 psi for BTE2.
2. The steel strands all had a similar ultimate strength of 271 ksi and a modulus of elasticity of 28000 ksi, as determined from tension tests conducted on strand samples removed from undamaged areas of the girders after testing.
3. Camber measurements were taken after delivering the salvaged girders to the laboratory. BTE1 had a maximum camber of 1-7/8 in. at the midspan.
4. Experimental results showed that girders BTE2, BTE3, and BTE4 had similar levels of prestress loss, while BTE1 had a significantly higher loss of prestress which can be attributed to a fully corroded strand near midspan. The experimentally measured prestress losses are 44 ksi, 33.6 ksi, 35.4 ksi, 35.5 ksi of BTE1, BTE2, BTE3 and BTE4 respectively.
5. On average, the predicted elastic shortening losses is 27.8%, 36.9%, 35.5% and 34.9% of the measured prestress loss in BTE1, BTE2, BTE3 and BTE4 respectively. The results indicate the amount of prestress loss that occur early in the service life of a prestressed concrete member in comparison to the total prestress loss that might occur in the entire service life of the structure.

6. The moment-curvature response (relative curvature) of BTE2, BTE3 and BTE4 are very similar. BTE1 had a similar pre-cracked stiffness but a higher prestress loss (induced by corrosion) and a lower concrete strength that resulted in BTE1 having a reduced cracked stiffness. The transition from pre-cracked stiffness to cracked stiffness also occurred at a lower applied moment for BTE1.
7. During flexural testing, BTE1 and BTE2 failed by crushing of the top flange in compression. BTE1 and BTE2 had a flexural capacity of 2831 k-ft and 2860 k-ft, respectively, including self-weight. BTE3 and BTE4 were not tested to failure in order to preserve their ends for subsequent shear testing. Peak loads reached for BTE3 and BTE4 indicated flexural capacities of at least 2699 k-ft and 2698 k-ft respectively.
8. Condition assessment revealed concrete spalls in the vicinity of corroded strands. Corrosion of the strands appears to be the most common types of deterioration that occurs over the lifespan of these types of members. BTE2, BTE3, and BTE4 had multiple spalls, repairs, and sections of exposed strand, but this level of damage did not appear to affect the measured losses for this series of tests. The more significant corrosion damage in BTE1 did increase the measured prestress losses.
9. A detailed method for estimating prestressing losses in prestressed girder bridges has been proposed. In a laboratory destructive test of the girders with DIC instrumentation, this requires identifying the first instance of cracking and the crack reopening moment using two virtual extensometers, one placed on the crack and another placed in parallel at same depth but away from the crack. Results can be confirmed visually from DIC strain maps.
10. The shear capacities of the end regions of BTE3 and BTE4 were determined by testing to failure in three point loading (three tests total, one at each end). Two shear failures were achieved, with the maximum actuator capacity reached prior to failing the South end of BTE3. The applied peak shear and associated moment at peak applied load were 276 kips and 2447 k-ft, respectively. The shear capacity of BTE3 North and BTE4 South, tested outside the widened end region, had a shear capacity of 287 kips and 274 kips, respectively. The corresponding associated moments were 2585 k-ft and 2394 k-ft for BTE3 North and BTE4 South respectively. The maximum crack widths observed at the peak applied loads were 1.80 mm, 2.00 mm, and 2.50 mm for BTE3 North, BTE3 South, and BTE4 South, respectively. All failures at the ends of the girders were brittle in nature.

7.2 Modelling with Response-2000

1. Response-2000 is an accurate tool for assessing the behavior of aged infrastructure like the girders recovered from the Bonner Bridge. The predicted flexural capacity of the girders given by Response-2000 are: 2815 k-ft for BTE1, 2860 k-ft for BTE2, 2760 k-ft for BTE3 and 2780 k-ft for BTE4 with a test-to-predicted ratio ranging from 0.97 to 1.01. The mean and coefficient of variation of the predictions are 2804 k-ft and 1.6% respectively.
2. Using the stress-strain response of the concrete from measured material properties, and the stress-strain response of the prestressing strand determined from tension testing, the failure modes of BTE1 and BTE2 were correctly predicted by Response-2000 as top fiber crushing, matching the modes observed in the experiments.
3. The layered sectional analysis software Response-2000 is able to predict the moment-curvature response of the tested girders. The transition of stiffness from uncracked to cracked section behavior is accurately captured.
4. Response-2000, with the incorporation of experimental results such as average strand stress, cracking moment, and crack reopening moment at the bottom fiber of the girder, can be used to predict the prestress losses in the girders. The loss estimates are: 44.3 ksi for BTE1, 34.0 ksi for BTE2, 35.4 ksi for BTE3 and 36.0 ksi for BTE4.
5. Response-2000 was used to model the girder with a deck, and these models show that the capacity of the girder-deck composite system is governed by steel yielding.
6. A sensitivity analysis shows the experimental behavior is well within the predictions from Response-2000 when the prestress losses are varied by ±25%. Since the moment curvature behavior is somewhat sensitive to the losses, this corroborates that the predicted losses are correctly captured.
7. Although only one corroded strand was visible for BTE1, it is likely that several strands near the bottom may have been affected by corrosion. Response-2000 shows that if a higher prestress loss in the individual strands near the bottom of this section is considered compared to the loss occurring in the strands above, then the generated moment-curvature behavior aligns more precisely with the experimental results. The model with variable losses better captures the behavior and better reflects the condition of the girder with only specific bottom strands affected by corrosion.

7.3 Evaluation of Prestress Loss under AASHTO LRFD

1. The AASHTO LRFD Refined Method uses nominal material properties and gives a conservative estimate of prestress loss (except for BTE1) in comparison to the measured prestress loss, with test to predicted ratios (T/P) for the tested girders ranging from 0.74-0.78. A similar range of T/P ratios (0.75-0.80) are observed when using the AASHTO LRFD Refined Method consistent with NCDOT assumptions, except for BTE1. However, the AASHTO LRFD Refined Method using measured material properties give reasonable T/P ratios between 0.92 and 1.09 for all girders. The AASHTO LRFD Lump Sum Method specified in the current edition (9^{th} Edition, 2020) gives conservative estimates for BTE2, BTE3, and BTE4 with T/P ratios ranging from 0.76 and 0.80, whereas the Lump Sum equation from older editions of AASHTO LRFD (4^{th} Edition, 2009) have a T/P ratio rang of 0.66-0.70 for these three girders. The results indicate the older equations are very conservative. Since the prestress loss was much higher in BTE1 compared to other specimens in the BTE series, all methods gave a reasonable estimate of prestress loss in this specimen with T/P ratios between 0.88 and 1.09.
2. The prestress loss prediction formulas used by current AASHTO LRFD Specifications do not account for the variability in material properties such as concrete strength, unit weight, and modulus of elasticity at the end of service life. A higher strength concrete will experience lower long-term creep strains under the same load compared to similar members with lower strength concretes. Generally, in design, in-situ properties should not be used for estimating losses. Specifically, specified concrete strengths should be used rather than measured strengths beyond the specified strength gain requirements. The traditional assumption is that the increase in concrete strength that occurs over the life of the structure will approximately correspond to the reduction in strength that the members will experience as a result of slow loading events. Therefore, it is not recommended to use measured concrete strengths in design or early in the life of the member to predict long-term effects or strength limit state calculations. However, this study explores the use of in-situ properties for service limit state calculations conducted for structures near the end of their service life. The use of experimentally measured properties in the code equations significantly improves the predicted losses for the girders studied.

7.4 Experimental Results and Load Rating

1. At the zero tensile stress limit, both the LRFR and LFR ratings for girders in the BTE series are less than 1.
2. The LRFR rating factors calculated using prestress losses from the AASHTO LRFD Refined Method with nominal material properties, the AASHTO LRFD Refined Method consistent with NCDOT assumptions, and Response-2000 show that all girders satisfy Strength I (both inventory and operating) and Service III limit state (for an allowable stress of $6\sqrt{f'_c}$) criteria. The LRFR rating factors exceed 1.0 for all assumptions. The girders are governed by the Service III limit state, specifically BTE1 as it sustained the highest prestress loss due to corrosion.
3. If the allowable stress criteria is limited to zero tensile stress, the LRFR rating factors calculated using prestress losses from the three methods stated in Section 7.3 fall below 1.0. The LRFR rating factors range between 0.67 and 0.71 for BTE1, 0.67 and 0.87 for BTE2 and BTE3, and 0.67 and 0.84 for BTE4.
4. Experimental rating factors (following the LRFR rating method) that considers only strength and stress of the girder tested, and disregarding the capacity provided by a composite deck, still yield rating factors greater than 1. These factors are calculated under the Strength I limit state, for inventory and operating limits, with a condition factor of 0.95 applied for girders with corrosion and 1.00 for girders without visible corrosion. This result shows the girders still had sufficient safe load carrying capacity in terms of flexural resistance at the time they were removed from service. At cracking loads under the Service III limit state, the experimental rating factors range from 1.18 to 1.49, well above 1.0. However, under Service III limit states, with only zero tensile stresses permitted, rating factors fall largely below 1.0 with a 0.66 for BTE1, 0.87 for BTE2, 0.87 for BTE3, and 0.85 for BTE4, respectively.

7.5 Recommendations

1. The AASHTO LRFD Refined Estimate is a detailed approach towards measuring various prestress loss components. Using measured material properties obtained either through non-destructive testing techniques or extraction of cores, to estimate prestress losses near

the end of the service life of bridge girders gives results that more closely match experimentally determined values.

2. Response-2000 can be used to model aged prestressed concrete girders. As the study has shown the experimental behavior agrees reasonably well with the predicted behavior. Response-2000 can also be used to predict the response of girders with composite decks using experimental results from the flexural testing of girder with no deck under a variety of loading conditions.
3. In some cases prestressed concrete girders may meet the Strength I (both inventory and operating) criteria under LRFR rating. However, the girders do not meet the Service III limit state if only zero tensile stress is allowed. The stresses and strengths from the AASHTO LRFD Refined Method with nominal material properties, the AASHTO LRFD Refined Method with measured material properties and Response-2000 with measured material properties are used to inform this recommendation. The study showed the ultimate capacity of the tested girders was 2.24-2.43 times the capacity at the state of zero tensile stress and 1.73-1.83 times the capacity at the state of cracking ($6\sqrt{f'c}$ tensile stress). The results indicate that 55-58% of the flexural capacity is utilized at cracking. The benefits of allowing stress between $3\sqrt{f'c}$ and $6\sqrt{f'c}$ under service limit states, even if only at the end of the life of structure, are that the Department can avoid load posting these aged bridges and can extend the service life just enough to allocate resources accordingly. It is also important to monitor the service stresses in bridge regularly after such an allowance. An allowable tensile stress of $6\sqrt{f'c}$ could lead to cracks. This could lead to accelerated corrosion and therefore the bridge should be monitored accordingly.

IMPLEMENTATION AND TECHNOLOGY TRANSFER PLAN

RESEARCH & DEVELOPMENT

Close-Out Implementation Plan

Committee Chair: Nicholas Pierce Date: 12/01/2023

Principal Investigator: Giorgio T. Proestos Project #: 2021-09

Implementation Contact: Nicholas Pierce

Project Title: Evaluation of the Bonner Bridge Girders: Assessing Residual Capacity, Prestressing Losses and Degradation of the 56 Year Old Members

Steering and Implementation Committee and Research Team:

1. Brian Hanks
2. Gichuru Muchane
3. Trey Carroll
4. Doug Cantrell
5. Aaron Earwood
6. Pablo Hernandez
7. Randy Midgett
8. Ashvin Patel
9. Wiley Jones
10. Daniel Muller (FHWA)
11. Giorgio T. Proestos (NCSU)
12. Rudi Seracino (NCSU)
13. Greg Lucier (NCSU)
14. Curtis Bradley, Mustan Kadibhai

Project Completion: 12/31/2023

Project Cost: $255,764

Division:

- [x] Highway
- [ ] Aviation
- [ ] DMV
- [ ] Rail
- [ ] Ferry
- [ ] Public Transportation
- [ ] Planning & Programming

Was there collaboration with other DOT Divisions, Stakeholders and/or Interest Groups?

- [ ] Yes
- [x] No

- [ ] Highway
- [ ] Rail
- [ ] Public Transportation
- [ ] Aviation
- [ ] Ferry
- [ ] Planning & Programming
- [ ] DMV
- [ ] Other

Please list the specific Section:

1. _____
2. _____
3. _____
4. _____
5. _____
6. _____
7. _____

RESEARCH & DEVELOPMENT

1. Final Deliverable:

☐ Specification	☐ Manual	☑ Report
☐ Training	☑ Data/Information	☑ Presentation
☐ Software (Product)	☐ Equipment/Tool	☐ Synthesis

Explanation of Deliverables:

The project deliverables include: a) a summary of the performance of the Bonner Bridge girders based on material tests and the four full-scale experiments conducted at NCSU. b) A summary of the condition of the tested girders with respect to materials performance, structural performance and prestressing losses. c) Recommendations for procedures for estimating prestressing losses and load rating performance in the context of aged girders assessed with AASHTO LRFD and first principles approaches. d) Recommendations relating to the Structures Management Unit policies, particularly as they relate to load rating girders at service loads, in the context of aged girders with prestress losses. These deliverables have been documented in the final report that includes a summary of the experimental data and a final presentation.

2. How will this Research Project influence NCDOT?

☐ Specific Project	☑ Practice/Operation
☑ Policy	☑ Evaluation Criteria
☐ Behavior	

Explain the influence this project will have on NCDOT:

The influence this project will have on the NCDOT relates to the Structures Management Unit polices, practices and evaluation criteria for bridge structures. Specifically, the results of this research provide the basis for which policies related to prestress loss calculations in aged bridge structures and rating procedures, particularly at service loads, can be implemented. These recommended approaches have the potential to extend the usable life of ageing bridge structures in a manner that is consistent with experimental data, aligned with codes and standards, aligned with best practices and first principles approaches and in a manner that efficiently utilizes the exisiting infrastructure. Avoiding load posting or closures will result in avoiding traffic delays and associated economic impacts of structural interventions.

3. When do you intend on implementing this research?

☑ Immediate – 6 Months	☑ Currently Implemented
☐ 7 Months – 18 Months	☐ Unsure
☐ > 18 Months	

Briefly describe the process on when and how the results of this research will be implemented:

The NCDOT is already applying some of the approaches described in the recommendations of the project. The results of this research supports these approaches and supports more widely adopting the procedures. These approaches can be applied as needed and immediately in the decision making and load rating practices at the NCDOT.

RESEARCH & DEVELOPMENT

4. How will the benefits of the Research Project be measured?

- [x] Monetary/Cost Savings
- [x] Workforce/Operations Savings
- [x] Safety

Provide an explanation on the measure of success for this Research Project:

By extending the usable life of existing bridges the measure of success can be determined by the monetary and workforce/operations savings that would be associated with the repair, intervention or replacement of bridge structures nearing the end of their service life. The safety of the inventory of structures managed by the NCDOT will also be improved. The results of the research can help quantify the level of safety of bridge structures in a more refined manner than is prescribed in standards.

5. Do you need assistance in implementing this research?

- [ ] Continued Research/Tracking
- [x] No further assistance needed
- [ ] Technology Transfer/Training
- [ ] Other Assistance

Provide a brief explanation on how the additional assistance benefited the implementation of the research project:

No additional assistance is needed.

REFERENCES

AASHTO (2018) The manual for bridge evaluation, 3rd Edn. American Association of State Highway and Transportation Officials,

AASHTO. (2008). Bridging the Gap-Restoring and Rebuilding the Nation's Bridges. *Washington (DC): American Association of State Highway and Transportation Officials*.

Abdelrahman, A. A., Tadros, G., & Rizkalla, S. H. (1995). Test model for first Canadian smart highway bridge. *ACI Structural Journal*, *92*(4), 451-458.

ACI-ASCE Joint Committee 323 (1958). *Tentative Recommendations for Prestressed Concrete*. Journal of the American Concrete Institute, 29(7), 545-578.

Adam, V., Herbrand, M., & Hegger, J. (2020). Querkrafttragfähigkeit von Brückenträgern aus Spannbeton mit geringen Querkraftbewehrungsgraden. Bauingenieur, 95(11).

Alpha & Omega Group (2007). *Bonner Bridge Site Report*. Alpha & Omega Group.

American Association of State Highway and Transportation Officials (AASHTO) (2020). *AASHTO LRFD Bridge Design Specifications* (9th ed.). American Association of State Highway and Transportation Officials.

American Association of State Highway and Transportation Officials (AASHTO) (2019). *AASHTO Manual for Bridge Evaluation, with 2019 Interim Revisions* (3rd ed.). American Association of State Highway and Transportation Officials.

American Association of State Highway and Transportation Officials (AASHTO) (1973). *Standard Specifications for Highway Bridges* (11th ed.). American Association of State Highway and Transportation Officials.

American Association of State Highway and Transportation Officials (AASHTO) (2007). *AASHTO LRFD Bridge Design Specifications* (4th ed.). American Association of State Highway and Transportation Officials.

American Concrete Institute (ACI) Committee 209 (1992). *Prediction of Creep, Shrinkage, and Temperature Effects in Concrete Structures (ACI 209R-92)*. American Concrete Institute.

American Concrete Institute (ACI) Committee 214 (2021). *ACI-PRC-214.4-21: Obtaining Cores and Interpreting Core Compressive Strength Results-Guide*. American Concrete Institute.

ASCE. (2013). “2013 report card for America’s infrastructure.” ⟨http://www.infrastructurereportcard.org/a/#p/bridges/conditions-and-capacity⟩ (Jul. 3, 2013).

ASTM Standard A886/A886M-17 (2017). *Standard Specification for Steel Strand, Intended, Seven-Wire Stress-Relieved for Prestressed Concrete*. ASTM International. DOI: 10.1520/A0886_A088M-17.

Azizinamini, A., Keeler, B. J., Rhode, J., & Mehrabi, A. B. (1996). *Application of a New Nondestructive Evaluation Technique to a 25-Year-Old Prestressed Concrete Girder*. PCI Journal, 41(3), 82-95.

Bakht, B., & Jaeger, L. G. (1990). Bridge testing—A surprise every time. *Journal of Structural Engineering*, *116*(5), 1370-1383.

Barr, P. J., Kukay, B. M., & Halling, M. W. (2008). Comparison of prestress losses for a prestress concrete bridge made with high-performance concrete. *Journal of Bridge Engineering*, *13*(5), 468-475.

Bartlett, F. M., & MacGregor, J. G. (1995). *Equivalent Specified Concrete Strength from Core Test Data*. Concrete International, 17(3), 52-58.

Bažant, Z. P., and Wittmann, F. H., *Creep and Shrinkage in Concrete Structures*, Wiley & Sons, New York, 1982.

Bentz, E. C., Response-2000, http://www.ecf.utoronto.ca/~bentz/home.shtml, (last accessed Oct. 20, 2021).

Breña, S. F., Jeffrey, A. E., & Civjan, S. A. (2013). Evaluation of a noncomposite steel girder bridge through live-load field testing. *Journal of Bridge Engineering*, *18*(7), 690-699.

Chajes, M. J., Mertz, D. R., & Commander, B. (1997). Experimental load rating of a posted bridge. *Journal of Bridge Engineering*, *2*(1), 1-10.

Chajes, M. J., Shenton III, H. W., & O’Shea, D. (2000). Bridge-condition assessment and load rating using nondestructive evaluation methods. *Transportation Research Record*, *1696*(1), 83-91.

Chen, Y., & Aswad, A. (1996). Stretching span capability of prestressed concrete bridges under AASHTO LRFD. *journal of Bridge Engineering*, *1*(3), 112-120.

Civjan, S. A., Jirsa, J. O., Carrasquillo, R. L., & Fowler, D. W. (1998). Instrument to evaluate remaining prestress in damaged prestressed concrete bridge girders. *PCI journal*, *43*(2).

Collins, M. P., & Mitchell, D. (1997). *Prestressed Concrete Structures*. Response Publications.

Garber, D. B., Gallardo, J. M., Deschenes, D. J., & Bayrak, O. (2015). *Experimental Investigation of Prestress Losses in Full-Scale Bridge Girders*. ACI Structural Journal, 112(5), 553-564. DOI: 10.14359/51687909.

Ghali, A., and J. Trevino. 1985. Relaxation of Steel in Prestressed Concrete. *PCI Journal, V. 30, No. 5* (September– October: pp. 82–94).

Goble, G., Schulz, J. and Commander, B. _1992_. "Load prediction and structural response." *Final Rep. FHWA DTFH61-88-C-00053*,

Halsey, J. T., & Miller, R. (1996). *Destructive Testing of Two Forty-Year-Old Prestressed Concrete Bridge Beams*. PCI Journal, 41(5), 84-93.

Higgs, A., Barr, P. J., & Halling, M. W. (2015). *Comparison of Measured and AASHTO LRFD-Predicted Residual Prestress Forces, Shear and Flexural Capacities of High-Strength Prestressed-Concrete Bridge Girders*. ASCE Journal of Bridge Engineering, 20(1), 1-9. DOI: 10.1061/(ASCE)BE.1943-5592.0000646.

Jayaseelan, H., & Russell, B. W. (2007). *Prestress losses and the estimation of long-term deflections and camber for prestressed concrete bridges*. School of Civil Environmental Engineering, Oklahoma State University.

Magura, D. D., Sozen, M. A., & Siess, C. P. (1964). *A Study of Stress Relaxation in Prestressing Reinforcement*. PCI Journal, 9(2), 13-57.

Magura, D. D.; Sozen, M. A.; and Siess, C. P., "A Study of Stress Relaxation in Prestressing Reinforcement," *Civil Engineering Studies SRS-237*, University of Illinois, Urbana, IL, 1962, 116 pp.

National Cooperative Highway Research Program _NCHRP_. _1998_. "Manual for bridge rating through load testing." *Research Results Digest*, *234*, Transportation Research Board, National Research Council, Washington, D.C.

PCI. (2003). *Precast Prestressed Concrete Bridge Design Manual*. Chicago, Illinois: Precast/Prestressed Concrete Institute.

Pessiki, S., Kaczinski, M., & Wescott, H. H. (1996). Evaluation of effective prestress force in 28-year-old prestressed concrete bridge beams. *PCI journal*, *41*(6), 78-89.

Precast/Prestressed Concrete Institute (PCI) (2014). *Bridge Design Manual* (3rd ed., second release). Precast/Prestressed Concrete Institute.

Rizkalla, S., Zia, P., St Thorenfeldt, E. (1987)orm, T. (2011). *Predicting Camber, Deflection, Prestress Losses in Prestressed Concrete Members (FHWA/NC/2010-05)*. North Carolina Department of Transportation.

Ruggiero, D. M. (2015). *The Behaviour of Reinforced Concrete Subjected to Reversed Cyclic Shear.* [PhD Report, University of Toronto, Department of Civil Engineering, Toronto].

Russell, B. W., & Burns, N. H. (1996). Measured transfer lengths of 0.5 and 0.6 in. strands in pretensioned concrete. *PCI journal*, *41*(5).

Sanayei, M., Phelps, J. E., Sipple, J. D., Bell, E. S., & Brenner, B. R. (2012). Instrumentation, nondestructive testing, and finite-element model updating for bridge evaluation using strain measurements. *Journal of bridge engineering*, *17*(1), 130-138.

Schiebel, S., Parretti, R., Nanni, A., & Huck, M. (2002). Strengthening and load testing of three bridges in Boone County, Missouri. *Practice periodical on structural design and construction*, *7*(4), 156-163.

Steinberg, E. P. (1995). Probabilistic assessment of prestress loss in pretensioned prestressed concrete. *PCI journal*, *40(6)*, 76-85.

Tadros, M. K., Ghali, A., & Dilger, W. H. (1977). *Time-Dependent Analysis of Composite Frames*. ASCE Journal of the Structural Division, 103(ST4), 871-884.

Tadros, M.K., Al-Omaishi, N., Seguirant, S., & Gallt, J. (2003). *Prestress Loss in Pretensioned High-Strength Concrete Bridge Girders (NCHRP report 496)*. National Cooperative Highway Research Program.

Transportation Officials. (1989). *Standard specifications for highway bridges*. AASHTO.

Transportation Officials. (2002). *Standard specifications for highway bridges*. AASHTO.

Yost, J. R., Schulz, J. L., & Commander, B. C. (2005). Using NDT data for finite element model calibration and load rating of bridges. In *Structures Congress 2005: Metropolis and Beyond* (pp. 1-9).

Youakim, S. A., Ghali, A., Hida, S. E., & Karbhari, V. M. (2007). Prediction of long-term prestress losses. *PCI journal*, *52*(2).

Zokaie, T., Imbsen, R. A., & Osterkamp, T. A. (1991b). Distribution of wheel loads on highway bridges. *NCHRP Proj. Rep. 12-26*, Transportation Researc35h Board, Washington, D.C.

APPENDIX

APPENDIX A – ADDITIONAL LITERATURE REVIEW

Appendix A includes additional information beyond what is described in Chapter 2. It contains a detailed literature review of different prestress loss calculation methods and a summary of other research on prestress losses in concrete structures.

A.1 PCI Bridge Design Manual Loss Calculation Method

The current Precast/Prestressed Concrete Institute Bridge Design Manual (2014) outlines a prestress loss calculation method similar to the Refined Method from the AASHTO Specifications. However, PCI-BDM (2003) explains another time-dependent analysis to calculate prestress losses and is included in the current version of the manual. It is a Time-Step method that uses creep, shrinkage, and relaxation models to determine strains which can then be used to calculate the existing effective prestressing force. The method is based upon a cross-sectional analysis which requires section properties of the girder and deck. It uses equilibrium equations and strains in each element to find forces acting on the element. The method can be used to determine the prestress losses at any specific time in the life of the structure. The PCI-BDM (2003) has guidelines for dividing the time frames according to certain processes that lead to stress change. These processes include strand relaxation before transfer, transfer of prestress, time-dependent effects after transfer, placement of cast-in-place deck, time-dependent effects after deck-placement. The calculation procedure for the PCI-BDM (2003) method is summarized below.

First the age adjusted modulus of the concrete is computed, E^*_{ck}, for each element 'k' in the composite section. To account for the increased strain in concrete due to creep effects, the modulus of the concrete is reduced to increase strain at any applied load. The age adjusted modulus is given by Eq. 5:

$$E^*_c(t, t_0) = \frac{E_c(t_0)}{1+\chi(t,t_0)C(t,t_0)} \tag{5}$$

Where:

$$E_c(t) = 33{,}000K_1(w_c)^{1.5}\sqrt{(f'_c)_t} \tag{6}$$

$$w_c = density\ of\ concrete, kip/ft^3$$

$$K_1 = aggregate\ correction\ factor$$

$$(f_c')_t = f_c' compressive\ strength\ at\ t\ days = \frac{t}{A+Bt}(f_c')_{28} \quad (7)$$

$$(f_c')_{28} = compressive\ strength\ at\ 28\ days$$

$$A\ and\ B = constants\ (See\ Table\ 2.5.2.1\ of\ PCI\ Bridge\ Design\ Manual, 2014)$$

$$\chi(t, t_0) = aging\ coefficient$$

$$C(t, t_0) = creep\ coefficient$$

The second step is to calculate the modular ratio, n_k, for each of the elements in the section using Eq. 8 below.

$$n_k = \frac{E^*_{ck}}{E^*_c} \quad (8)$$

Where:

$$E^*_c = effective\ modulus\ of\ the\ section$$

The third step is to calculate the transformed section properties using Eq. 9, 10, and 11.

$$A = \Sigma A_k n_k \quad (9)$$

$$y = \frac{1}{A}\Sigma y_k A_k n_k \quad (10)$$

$$I = \Sigma[I_k + (y - y_k)^2 A_k] n_k \quad (11)$$

The fourth step is to compute the initial strain, ε_{0k}, and curvature, φ_{0k}, for each element in the composite section for a given time interval. The initial strains are shrinkage, creep, relaxation strains calculated at the end of the prior time interval and curvatures resulting from the stresses previously applied. As mentioned previously, this is a time step method. Therefore, strains are determined in each interval and stresses are updated accordingly to determine prestress loss at a specific age of structure. The fifth step is to calculate the restraint forces due to prestressing from the summation of restraint forces in each element 'k' as seen in Eq. 12, 13, 14, and 15.

$$N_{0k} = -E^* \varepsilon_{0k} A_k \tag{12}$$

$$N_0 = \Sigma N_{0k} \tag{13}$$

$$M_{0k} = -E^*{}_{ck} I_k \varphi_{0k} \tag{14}$$

$$M_0 = \Sigma [M_{0k} - N_{0k}(y_k - y)] \tag{15}$$

Step six is to subtract the restraint forces from the applied forces to calculate total strain and curvature for the section. See Eq. 16 and Eq. 17 for strain and curvature calculations.

$$\varepsilon = \frac{N - N_0}{E^*{}_c A} \tag{16}$$

$$\varphi = \frac{M - M_0}{E^*{}_c I} \tag{17}$$

Step seven is to calculate the strains and curvatures in each element using Eq. 18 and Eq. 19.

$$\varepsilon_k = \varepsilon - [-\varphi(y_k - y)] \tag{18}$$

$$\varphi_k = \varphi \tag{19}$$

Finally, step eight is to calculate the effective element forces and strains using the effective modulus for each element. See Eq. 20, 21, 22, and 23 for elemental forces and strains.

$$N_k = E^*{}_{ck} A_k \varepsilon_k + N_{0k} \tag{20}$$

$$\varepsilon_{fk} = \frac{N_k}{E^*{}_{ck} A_k} \tag{21}$$

$$M_k = E^*{}_{ck} I_k \varphi + M_{0k} \tag{22}$$

$$\varphi_{fk} = \frac{M_k}{E^*{}_{ck} I_k} \tag{23}$$

These eight steps are repeated for each time frame to be analyzed over the time-history of the cross section. An example of a time frame for analysis would be the time between prestress transfer and the pouring of the composite deck for a composite prestressed member. Increasing the number of time frames analyzed will refine the estimate of prestress loss, but discrete time intervals taken

between critical times in a member's life can provide an adequately refined assessment of the long-term loss.

A.2 AASHTO LRFD Bridge Design Specifications Prestress Loss Calculation Method

Member shortening due to creep and shrinkage result in a loss of tension in the prestressing strands. According to AASHTO, prestress loss includes instantaneous (elastic) losses at transfer of prestress and inelastic long-term time-dependent losses. However, if the inclusion of elastic gain due to the application of deck weight and other superimposed dead loads such as railing and barrier is considered, there can be prestress 'gains'. That is, increases in strand stress under certain conditions. These loads cause additional tensile stress in the bottom fiber of the member and hence also in the prestressed reinforcement resulting in elastic gains. Moreover, other time dependent phenomena such deck shrinkage are permanent, and these can offset the prestress loss. The effects of live load are transient and exist whenever the load is present. Some authorities account for these prestress gains in determining the total prestress loss, others conservatively ignore them. For comparison with allowable stresses specified in AASHTO LRFD, the resultant stress in the structure can be different depending on whether prestress gains are fully considered in the calculation of prestress loss, partially included or completely excluded. Prestress loss calculation detailed in AASHTO LRFD Bridge Design Specifications is discussed in more detail below.

A.2.1. Elastic Loss (or Gain)

Elastic deformations of the cross section occur at all stages of loading, but AASHTO LRFD recommends to conservatively account for elastic deformation during prestress transfer when the stress in strand is the highest. When the strands are released from the bed and prestressing force is applied, the concrete member shortens, and, in most girder structures, cambers upward between its two ends. The process occurs almost instantaneously and is not time-dependent. There is a reduction in the stress in the strands after transfer. AASHTO refers to this as the elastic loss. Self weight, if accounted for, may add additional tension to strands at the same time adding to a gain in the stress in the strands. The overall effect of these elastic deformations can be either loss at transfer or a gain depending on the type of member and loading details. According to AASHTO LRFD, the elastic shortening loss for pretensioned concrete members is given by Eq. 24.

$$\Delta f_{pES} = \frac{E_p}{E_{ci}} f_{cgp} \tag{24}$$

$$f_{cgp} = f_{pi} A_{ps} \left[\frac{1}{A_g} + \frac{{e_m}^2}{I_g} \right] - \frac{M_g e_m}{I_g} \tag{25}$$

Where:

$f_{cgp} =$ *concrete stress at the center of gravity of prestressing tendons due to the prestressing force immediately after transfer and the selfweight of the member at the section of maximum moment* (ksi)

$A_{ps} = area\ of\ prestressing\ steel\ (in^2)$

$f_{pi} = stress\ in\ prestressing\ steel\ immediately\ prior\ to\ transfer\ (ksi)$

$I_g = moment\ of\ inertia\ of\ the\ gross\ concrete\ section\ about\ the\ centroidal\ axis,\ neglecting\ reinforcement\ (in^4)$

$e_m = average\ prestressing\ steel\ eccentricity\ at\ midspan\ (in)$

$A_g = gross\ area\ of\ section\ (in^2)$

$M_g = midspan\ moment\ due\ to\ member\ self - weight\ (kip - in)$

$E_{ci} = modulus\ of\ elasticity\ of\ concrete\ at\ transfer\ (ksi)$

$E_p = modulus\ of\ elasticity\ of\ prestressing\ steel\ (ksi)$

Eq. 24 is an iterative equation. An elastic loss of 10% is initially assumed to calculate f_{cgp} using Eq. 25, which is then used to calculate a refined Δf_{pES}. If the initial assumption does not match the calculated elastic loss, the latter is used as a new guess and the process is repeated until the assumed Δf_{pES}, and refined Δf_{pES} converge. The commentary recommendation of 90% of the jacking stress is a recommended initial assumption but is otherwise unrelated to final elastic loss value. Elastic losses are only calculated separately when gross (or net) cross-section properties are used.

However, when transformed section properties are used to calculate concrete stress, elastic deformations are implicitly accounted for in long-term prestress loss calculations as the prestressing strand and the concrete are treated together as a composite section in which both the concrete and the prestressing strand are equally strained in compression by a prestressing force conceived as a fictitious external load applied at the level of the strands. Therefore, Δf_{pES} should not be included in calculating f_{cgp}. The elastic losses are essentially the same whether gross or transformed section properties are used. To avoid iteration, AASHTO LRFD also suggests an alternative equation to calculate loss due to elastic shortening in pretensioned members as follows:

$$\Delta f_{pES} = \frac{A_{ps} f_{pbt}\left(I_g + e_m^2 A_g\right) - e_m M_g A_g}{A_{ps}\left(I_g + e_m^2 A_g\right) + \frac{A_g I_g E_{ci}}{E_p}} \tag{26}$$

Where:

$$f_{pbt} = stress\ in\ prestressing\ steel\ immediately\ prior\ to\ transfer\ (ksi)$$

A.2.2. Time Dependent Losses

A.2.2.1. Approximate Lump Sum Estimate of Prestress Losses

Lump Sum estimates can be used to determine long-term prestress losses over time. As specified in AASHTO LRFD Bridge Design Specifications (Second Edition) in section 5.9.5.3, the Lump Sum estimate of prestress losses is as follows:

$$\Delta f_{pLT} = 33\left[1 - \frac{0.15\left(f_c' - 6\right)}{6}\right] + 6PPR - 8\ (ksi) \tag{27}$$

PPR is the partial prestress ratio given by

$$PPR = \frac{A_{ps} f_{py}}{A_{ps} f_{py} - A_s f_y} \tag{28}$$

Where:

$$\Delta f_{pLT} = losses\ due\ to\ long - term\ shrinkage\ and\ creep\ of\ concrete, and\ relaxation\ of\ the\ steel\ (ksi)$$

$$f_{py} = yield\ strength\ of\ prestressing\ steel\ \ (ksi)$$

$$f_y = specified\ yield\ strength\ of\ reinforcing\ bars\ (ksi)$$

$$A_s = area\ of\ nonprestress\ tension\ reinforcement\ \ (in^2)$$

$$f'_c = specified\ compressive\ strength\ of\ concrete\ at\ 28\ days, unless\ age\ is\ specified\ (ksi)$$

Eq. 27 gives an approximate estimate of time dependent losses and was derived by assuming ranges for the creep coefficient (1.6 to 2.4), ultimate shrinkage strain of concrete (0.0004 and 0.0006) and relative humidity (40% to 100%). Computerized Time-Step analysis of various members from previous studies was used to establish these range of values. As mentioned previously, Lump Sum estimates represent average conditions and are useful in preliminary design. With changes in concrete strength, environmental conditions, and other factors, the equation for Lump Sum estimates has been updated with time. The fourth edition of the AASHTO Standard (2007) has stated two separate equations in Section 5.9.5.3 for estimating long-term prestress loss due to creep and shrinkage of concrete and relaxation of steel for the following two cases:

1 For standard precast, pretensioned members subject to normal loading and environmental conditions

$$\Delta f_{pLT} = 10\frac{f_{pi}A_{ps}}{A_g}\gamma_h\gamma_{st} + 83\gamma_h\gamma_{st} + \Delta f_{pR}\ (MPa) \tag{29}$$

In which

$$\gamma_h = 1.7 - 0.01H \tag{30}$$

$$\gamma_{st} = \frac{35}{7 + f'_{ci}} \tag{31}$$

Where:

$$f_{pi} = prestressing\ steel\ stress\ immediately\ prior\ to\ transfer\ \ (MPa)$$

$$H = the\ average\ annual\ ambient\ relative\ humidity\ (\%)$$

$$\gamma_h = \ correction\ factor\ for\ relative\ humidity\ of\ the\ ambient\ air$$

$$\gamma_{st} = \ correction\ factor\ for\ specified\ concrete\ strength\ at\ time\ of\ prestress\ transfer\ to\ the\ concrete\ member$$

$$\Delta f_{pR} = \ an\ estimate\ of\ relaxation\ loss\ taken\ as\ 70\ MPa\ for\ stress\ relieved\ strand\ \ (MPa)$$

$$f'_{ci} = \ design\ concrete\ compressive\ strength\ at\ time\ of\ prestressing\ for\ pretensioned\ members\ and\ at\ time\ of initial\ loading\ for\ nonprestressed\ members\ \ (MPa)$$

2 For members other than those made with composite slabs, stressed after attaining a compression strength of 24 MPa

$$\Delta f_{pLT} = 230\left[1 - \frac{0.15(f_c' - 41)}{41}\right] + 41PPR \ \ (MPa) \tag{32}$$

The current AASHTO LRFD Bridge Design Specification (9th Edition, 2020) only includes Eq. 33 for the approximate estimate of time-dependent losses. The equation is derived by simplifying the terms in the Refined Estimate for numerous standard precast concrete girder properties. The commentary recommends using the Refined Estimate for girders other than those made with composite slabs.

$$\Delta f_{pLT} = 10.0\frac{f_{pi}A_{ps}}{A_g}\gamma_h\gamma_{st} + 12.0\gamma_h\gamma_{st} + \Delta f_{pR} \ \ (ksi) \tag{33}$$

In which

$$\gamma_h = 1.7 - 0.01H \tag{34}$$

$$\gamma_{st} = \frac{5}{1 + f_{ci}'} \tag{35}$$

Where:

$\Delta f_{pR} =$ *an estimate of relaxation loss taken as* 2.4 *ksi for low relaxation strand and in accordance with manufacturers recommendation for oher types of strand* (*ksi*)

The Lump Sum estimate of time-dependent losses is still used in practice because, according to a survey of DOTs (discussed in Section 2.2*), refined estimates often result in significantly lower values for prestress losses, whereas Lump Sum estimates from any edition of the AASHTO LRFD gives values that are comparable to or slightly higher than actual prestress losses.

A.2.2.2. Refined Estimates of Time-Dependent Losses

The AASHTO LRFD Bridge Design Specifications (2020) outlines a Refined Method of long-term prestress loss in section 5.9.3.4, Refined Estimates of Time-Dependent Losses. The Refined Method uses two different time frames over the life of a composite concrete girder to account for creep and shrinkage of the girder, strand relaxation, and deck shrinkage. The first time frame is from prestress transfer to composite deck laying, and the second time frame is from the composite deck laying to the final time of assessment. Combined, the two time frames represent the total life

of the structure. The total long-term loss of strand stress is determined by the sum of all losses and gains over the two time frames as shown in Eq. 36 below.

$$\Delta f_{pLT} = (\Delta f_{pSR} + \Delta f_{pCR} + \Delta f_{pR1})_{id} + (\Delta f_{pSD} + \Delta f_{pCD} + \Delta f_{pR2} - \Delta f_{pSS})_{df} \quad (36)$$

The terms of Eq. 33 are discussed in detail below. The first three terms are losses from the time of transfer to composite deck laying. These include strand stress losses from creep, Δf_{pCR}, and shrinkage of the girder concrete, Δf_{pSR}, and the relaxation of the prestressing steel, Δf_{pR1}. The last four terms of Eq. 36 occur between composite deck laying and the final time for analysis. These include three loss terms and one stress gain term. The loss terms include the loss of strand stress from the creep and shrinkage of the girder concrete, Δf_{pCD} and Δf_{pSD} respectively, and the relaxation of the prestressing steel, Δf_{pR2}. The stress gain term is due to the shrinkage of the composite deck concrete, Δf_{pSS}. Eq. 36 starts with the strand stress loss from girder shrinkage between transfer and deck laying, and Δf_{pSR} is given by Eq. 37.

$$\Delta f_{pSR} = \varepsilon_{bid} E_p K_{id} \quad (37)$$

Where:

$$\varepsilon_{bid} = shrinkage\ strain\ of\ girder\ from\ transfer\ to\ deck\ laying, see\ equation\ 35.$$

$$\varepsilon_{sh} = \varepsilon_{bid} = k_s k_{hs} k_f k_{tdd} * 0.48 * 10^{-3} \quad (38)$$

$$k_s = volume\ to\ surface\ area\ ratio\ factor = 1.45 - 0.13(V/S) \geq 1.00 \quad (39)$$

$$V = V_g = volume\ of\ girder\ \ (in^3)$$

$$S = S_g = surface\ area\ of\ girder\ exposed\ to\ drying\ \ (in^2)$$

$$k_f = concrete\ strength\ factor = \frac{5}{1+f'_{ci}} \quad (40)$$

$$f'_{ci} = concrete\ strength\ at\ initial\ loading, taken\ as\ 0.8f'_c\ \ (ksi)$$

$$k_{td} = time\ development\ factor = \frac{t}{12\left(\frac{100-4f'_{ci}}{f'_{ci}+20}\right)+t} \quad (41)$$

When $k_{td} = k_{tdd},\ t = \ time\ from\ transfer\ t_i\ to\ age\ of\ deck\ placement\ \ t_d$

When $k_{td} = k_{tdf},\ t = \ time\ from\ transfer\ t_i\ to\ final\ age\ of\ concrete\ \ t_f$

$$k_{hs} = humidity\ factor\ for\ shrinkage = 2.00 - 0.014H \tag{42}$$

$H = average\ annual\ ambient\ humidity, see\ Figure\ 1.4$

$E_p = prestressing\ steel\ modulus\ of\ elasticity\ \ (ksi)$

$$K_{id} = transformed\ section\ coefficient = \frac{1}{1+\frac{E_p A_{ps}}{E_{ci} A_g}\left(1+\frac{A_g e_{pg}^2}{I_g}\right)[1+0.7\Psi_b(t_f,t_i)]} \tag{43}$$

$e_{pg} = eccentricity\ of\ prestressing\ force\ to\ girder\ centroid\ \ (in.)$

$\Psi_b(t_f, t_i) = creep\ coefficient\ from\ transfer, t_i\ (days), to\ final\ time, t_f(days)$

$$\Psi_b(t_f, t_i) = 1.9 k_s k_{hc} k_f k_{tdf} * t_i^{-0.118} \tag{44}$$

$$k_{hc} = humidity\ factor\ for\ creep = \ 1.56 - 0.008H \tag{45}$$

$E_{ci} = modulus\ of\ elasticity\ of\ concrete\ at\ transfer$

$$= \ 120{,}000 K_1 w_c^{2.0} f'^{0.33}_{ci}\ \ (ksi) \tag{46}$$

$w_c = 0.145\ kcf\ for\ normal\ weight\ concrete\ or\ 0.140 + 0.001 f'_c$

$K_1 = aggregate\ correction\ factor$

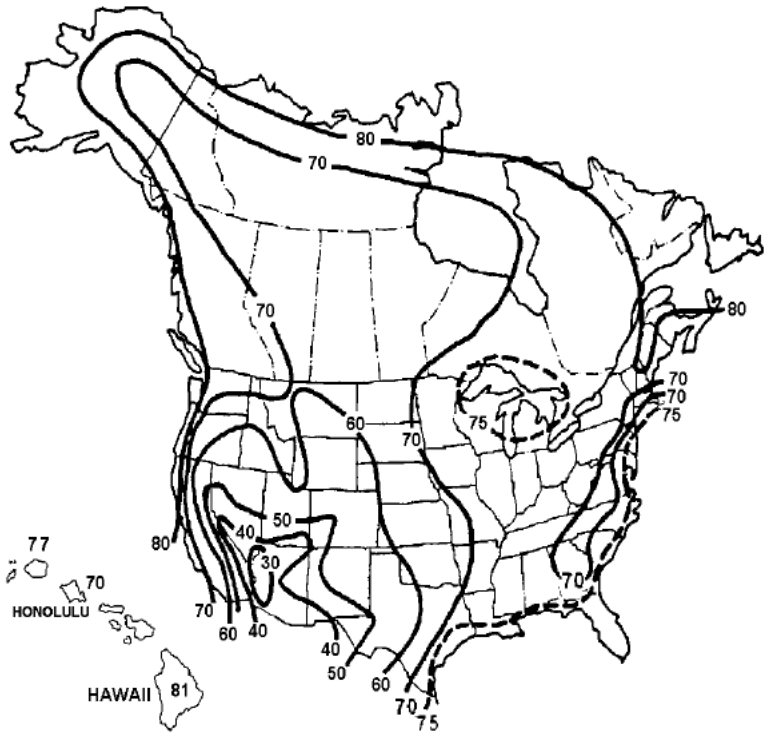

Figure A.1: Average annual relative ambient humidity for North America, in percent, (reproduced from AASHTO LRFD Bridge Design Specifications, 2020).

The loss of strand stress due to girder creep between transfer and deck laying is given by Eq. 47.

$$\Delta f_{pCR} = \frac{E_p}{E_{ci}} f_{cgp} \Psi_b(t_d, t_i) K_{id} \ \text{(ksi)} \tag{47}$$

Where:

$$\Psi_b(t_d, t_i) = creep\ coefficient\ from\ transfer, t_i\ (days), to\ deck\ placement, t_d(days) = \\ = 1.9 k_s k_{hc} k_f k_{tdd} * t_i^{-0.118} \tag{48}$$

The remaining loss between transfer and deck placement is the loss of strand stress from strand relaxation given by Eq. 49.

$$\Delta f_{pR1} = \frac{f_{pt}}{K_L}\left(\frac{f_{pt}}{f_{py}} - 0.55\right) \ (ksi) \tag{49}$$

Where:

$$f_{pt} = stress\ in\ prestressing\ steel\ immediately\ after\ transfer,$$

$$taken\ not\ less\ than\ 0.55 f_{py}\ \ (ksi)$$

$$K_L = prestressing\ steel\ type\ factor, 30\ for\ low\ relaxation\ strand\ and\ otherwise\ 7$$

The second time frame includes the losses between deck laying and the final time. Each of these components is outlined below. Eq. 50 gives the strand stress reduction from girder shrinkage between the time of deck laying and the final time. Note that Eq. 50 uses K_{df}, the transformed section coefficient of the composite section, to calculate the loss due to shrinkage because the structure has a composite concrete deck in the second time frame.

$$\Delta f_{pSD} = \varepsilon_{bdf} E_p K_{df}\ \text{(ksi)} \tag{50}$$

Where:

$$\varepsilon_{bdf}\ = shrinkage\ strain\ of\ girder\ from\ deck\ laying\ to\ final\ time = \varepsilon_{bif} - \varepsilon_{bid}$$

$$\varepsilon_{bif} = shrinkage\ strain\ of\ girder\ from\ time\ of\ transfer\ to\ final\ time$$

$$= k_s k_{hs} k_f k_{tdf} * 0.48 * 10^{-3} \tag{51}$$

$$K_{df} = transformed\ section\ coefficient\ that\ accounts\ for\ timedependent\ interaction$$

$$between\ concrete\ and\ bonded\ steel\ in\ the\ section\ being\ considered\ for\ time\ period$$

$$between\ deck\ placement\ and\ final\ time$$

$$= \frac{1}{1+\frac{E_p A_{ps}}{E_{ci} A_c}\left(1+\frac{A_c e_{pc}^2}{I_c}\right)[1+0.7\Psi_b(t_f,t_i)]} \tag{52}$$

$$A_c = area\ of\ section\ calculated\ using\ the\ gross\ composite\ concrete\ section$$

$$properties\ of\ thegirder\ and\ the\ deck\ and\ the\ deck - to - girder\ modular\ ratio\ \ (in^2)$$

$$e_{pc} = \ eccentricity\ of\ prestressing\ force\ with\ respect\ to\ centroid\ of\ composite$$

$$section\ (in.), positivein\ typical\ construction\ where\ prestressing\ force$$

$$is\ below\ centroid\ of\ section = y_c - e_m \quad (53)$$

The strand stress reduction due to girder creep between deck laying and the final time is given by Eq. 54.

$$\Delta f_{pCD} = \frac{E_p}{E_{ci}} f_{cgp}[\Psi_b(t_d, t_i) - \Psi_b(t_d, t_i)]K_{df} + \frac{E_p}{E_c}\Delta f_{cd}\Psi_b(t_f, t_d)K_{df} \ \ (ksi) \quad (54)$$

Where:

$$\Delta f_{cd} = change\ in\ concrete\ stress\ at\ centroid\ of\ prestressing\ strands\ due\ to\ long\ term$$

$$losses\ between\ transfer\ and\ deck\ placement, combined\ with\ deck\ weight\ and$$

$$superimposed\ loads$$

$$= -\left(\Delta f_{pSR} + \Delta f_{pCR} + \Delta f_{pR1}\right)\frac{A_{ps}}{A_g}\left(1 + \frac{A_g e_{pg}^2}{I_g}\right) - \left(\frac{M_{sd}+M_h(+*M_d)}{I_g} + \frac{(M_b+M_{ws})e_{pc}}{I_c}\right. \ \ (ksi) \quad (55)$$

In which:

$$M_{sd} = moment\ due\ to\ deck\ self - weight\ \ (k-ft)$$

$$M_h = moment\ due\ to\ haunch\ \ (k-ft)$$

$$M_b = moment\ due\ to\ barrier\ and\ rails\ \ (k-ft)$$

$$M_{ws} = moment\ due\ to\ future\ wearing\ course\ \ (k-ft)$$

$$*\ M_d = moment\ due\ to\ diaphragm\ \ (k-ft)\ (considered\ by\ NCDOT\ but\ may\ not$$

$$be\ used\ regularly$$

$$\Psi_b(t_f, t_d) = creep\ coefficient\ from\ deck\ placement, t_d\ (days), to\ final\ time, t_f(days)$$

$$= 1.9k_s k_{hc} k_f k_{tddf} t_d^{-0.118} \quad (56)$$

$$k_{tddf} = time\ development\ factor\ determined\ for\ the\ time\ period\ between\ deck\ placement\ and\ final\ time,$$

The strand relaxation from the time of deck laying to the final time is given by Eq. 57. The AASHTO LRFD Bridge Design Specifications assumes that the relaxation after the deck laying is equivalent to the relaxation between transfer and deck laying.

$$\Delta f_{pR2} = \Delta f_{pR1} \tag{57}$$

Eq. 58 concludes the terms in the long-term loss summation shown in Eq. 36. Eq. 58 is the prestress gain due to shrinkage of the composite concrete deck, Δf_{pSS}. A key term in Eq. 58 is Δf_{cdf}, the change in the concrete stress at the centroid of the prestressing strand due to the shrinkage of the concrete deck, and this value is given by Eq. 59.

$$\Delta f_{pSS} = \frac{E_p}{E_c} \Delta f_{cdf} K_{df} \left[1 + 0.7\Psi_b\left(t_f, t_d\right)\right] \tag{58}$$

Where:

$$\Delta f_{cdf} = \frac{\varepsilon_{ddf} A_d E_{c\,deck}}{\left[1+0.7\Psi_d\left(t_f,t_d\right)\right]} \left(\frac{1}{A_c} - \frac{e_{pc} e_d}{I_c}\right) \tag{59}$$

$$\varepsilon_{ddf} = shrinkage\ strain\ of\ deck\ concrete = k_s k_{hs} k_f k_{tddf} * 0.48 * 10^{-3}$$

$$In\ which\ k_s uses\ the\ volume\ to\ surface\ ratio\ \left(\frac{V}{S}\right)\ of\ deck\ and\ time\ development\ factor\ k_{tddf} uses\ t\ as\ the\ time\ from\ deck\ placement\ to\ final\ time$$

$$\Psi_d\left(t_f, t_d\right) = deck\ creep\ coefficient$$

$$e_d = eccentricity\ of\ deck\ to\ gross\ composite\ section = y_d - y_c\ (in) \tag{60}$$

$$E_{c\,deck} = modulus\ of\ elasticity\ of\ deck\ concrete\ (ksi)$$

$$A_d = area\ of\ deck\ concrete\ \ (in^2)$$

The long-term loss and gain components discussed above combined with the elastic shortening of the girder resulting from prestress transfer are used to determine the strand stress at the final time of analysis. Eq. 61 computes the total loss of strand stress from the stress immediately before transfer.

$$\Delta f_{pT} = \Delta f_{pES} + \Delta f_{pLT} \tag{61}$$

In practice, this prestress loss is again offset by an elastic gain due to deck weight, superimposed dead load and live loads (Service III). The elastic gain due to deck weight and superimposed dead load after deck placement is permanent. However, a survey of peer departments of transportation indicates it depends on each state's policy whether to account for these elastic gains, as this would reduce the prestress loss and result in a higher effective prestress in the strands.

A.3 Prestress Loss - AASHTO Standard Specifications for Highway Bridges

Refined and lump estimates of prestress loss, similar to AASHTO LRFD Bridge Design Specifications, are also specified in AASHTO Standard Specifications for Highway Bridges (2002). The provisions for prestress loss were first recognized in the 1971 Interim Specifications which stated the following equation for prestress loss:

$$\Delta f_s = ES + SH + CR_C + CR_S \tag{62}$$

Where:

$$\Delta f_s = total\ loss\ of\ prestress$$
$$ES = loss\ due\ to\ elastic\ shortening$$
$$SH = loss\ due\ to\ concrete\ shrinkage$$
$$CR_C = loss\ due\ to\ creep\ of\ concrete$$
$$CR_S = loss\ due\ to\ relaxation\ of\ prestressing\ steel$$

The prestress loss calculation method outlined in the current AASHTO Standard Specification for Highway Bridges (17th Edition, 2002) is briefly stated below. Losses due to elastic shortening after release of prestressing force in pretensioned members is determined by Eq. 63 which is the same as stated in AASHTO LRFD Specifications.

$$ES = \frac{E_s}{E_{ci}} f_{cir} \quad (63)$$

Where:

$$E_s = \text{modulus of elasticity of prestressing steel strand, which can be assumed to be } 28 \times 10^6 \text{ psi}$$

$$E_{ci} = \text{modulus of elasticity of concrete in psi at transfer of stress} = 33w^{\frac{3}{2}}\sqrt{f'_{ci}}$$

In which w is the concrete unit weight in pcf and f'_{ci} is in psi

$$f_{cir} = \text{concrete stress at the center of gravity of the prestressing steel due to prestressing force and dead load of beam immediately after transfer; reduced tendon stress can be taken as } 0.63f'_s \text{ for stress relieved strand}$$

Unlike AASHTO LRFD in which the refined estimate is used to calculate shrinkage, creep and relaxation losses in two time frames, AASHTO Standard specifications determines the individual loss components over the entire service life. Losses due to creep, shrinkage and relaxation of prestressing strands in pretensioned members are determined by Eq. 64, 65 & 66.

Creep of Concrete:

$$CR_C = 12f_{cir} - 7f_{cds} \quad (64)$$

Where:

$$f_{cds} = \text{concrete stress at the center of gravity of the prestressing steel due to all dead loads except the dead load present at the time the prestressing force is applied.}$$

Shrinkage:

$$SH = 17000 - 150\,RH \quad (65)$$

Relaxation of Prestressing Steel:

For stress relieved 250 to 270 ksi strand,

$$CR_S = 20{,}000 - 0.4\,ES - 0.2(SH + CR_c) \quad (66)$$

AASHTO Standard Specifications also state a Lump Sum estimate of 45 ksi for pretensioned members or structures that consist of regular properties such as normal weight concrete, normal prestress levels, and average exposure conditions. Although reasonable, these are not used in practice currently.

A.4 Review of Research on Prestress Loss

This research project also involves thoroughly investigating the best practices and prior research conducted on understanding prestress losses in bridge structures. The literature was reviewed to examine studies related to the effects of creep, shrinkage, and relaxation on prestress loss and their findings as well as experimental methods for measuring prestress loss in prestressed concrete bridge structures. This review provides background for the experimental program developed and outlined in Chapter 3 and Appendix B of this report.

A.4.1. Creep, Shrinkage, and Relaxation

Significant research has been performed on creep, shrinkage, and relaxation for both normal and high strength concretes. An overview of research used to develop the models for creep, shrinkage, and relaxation as seen in Section A.2.2.2 is presented below. NCHRP Report 496 (2003) outlines the work of Tadros et al. (2003) on modelling and estimating these long-term effects, and is a major contribution to modifying the prestress loss equations in the 4th Edition of AASHTO LRFD Bridge Design Specifications (2007). Findings of Tadros et al. (2003), along with other studies, are discussed below. Research performed by Magura et al. (1964) investigated the relaxation properties of prestressing reinforcement from 501 different tests to develop an expression for estimating the amount of stress relaxation over time. Magura et al. (1964) suggested that the major variables effecting the amount of relaxation to be initial stress ratio, the type of steel, pre- versus post-tensioning, and temperature. In general, the researchers found that higher initial stress results in higher levels of relaxation, and this major component is the primary variable in the equation developed by Magura et al. for predicting relaxation as a function of time (1964). The other parameters were found to be secondary and were not explicitly accounted for in the equation presented by Magura et al. (1964). The equation from Magura et al. (1964) for relaxation is the basis for the equation presented by Tadros et al. in NCHRP Report 496 (Tadros et al., 2003), and a simplified version of the equation presented by Tadros et al. is found in the AASHTO LRFD Bridge Design Specifications as Eq. 46 above (AASHTO, 2020). While temperature alone was not considered to be a major factor in relaxation of steel by Magura et al. (1964), Tadros et al. note that during the casting of pretensioned concrete structures, the amount of prestressing is impacted by the temporary increase in temperatures from curing (Tadros et al., 2003). The resulting thermal

expansion reduces strand stresses, and this loss is fixed after the bond between concrete and strand forms.

The factors effecting the shrinkage of concrete have been examined by numerous researchers (Tadros et al., 2003). The shrinkage of concrete is a factor of relative humidity, water-to-cement ratio, ambient temperature, aggregate properties, and volume-to-surface area ratio of a concrete member (Tadros et al., 2003). Tadros et al. (2003) measured shrinkage strain in 12 high strength concrete mixes and found significant differences between the measured and predicted shrinkage. Figure A.2 is an example of measured shrinkage as compared to predicted shrinkage, as reported by Tadros et al. (2003).

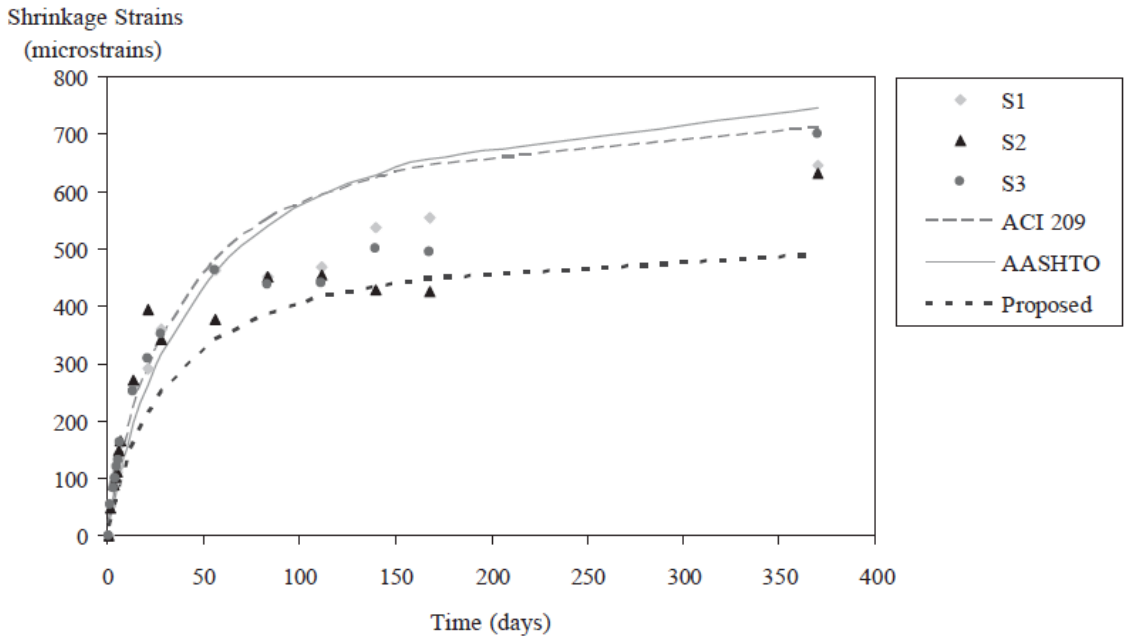

Figure A.2: Shrinkage for Washington mix WA10G-S (reproduced from Tadros et al., 2003).

Based on their shrinkage measurements, the researchers concluded that existing predictions of shrinkage strain needed refinement. Tadros et al. (2003) suggested an equation for shrinkage strain based on an ultimate shrinkage strain of 480 microstrain multiplied by correction factors for concrete strength, relative humidity, volume-to-surface area ratio, and the time development of concrete. The proposed equation by Tadros et al. has a significantly lower ultimate shrinkage strain when compared to the 1992 ACI Committee 209 value of 780 microstrain (ACI, 1992), and produces results that are in close agreement with the measured data (Tadros et al., 2003). The

shrinkage equation developed by Tadros et al. (2003) from their experimental work is the basis for the AASHTO LRFD Bridge Design Specifications shrinkage strain calculation presented in Eq. 38 above (AASHTO, 2020).

In addition to relaxation and shrinkage, long-term loss in prestressed concrete structures is caused by concrete creep. Like shrinkage, the variables that influence the creep of concrete have been identified by numerous researchers (Tadros et al., 2003). Literature shows a commonly used creep model was initially developed by Collins and Mitchell (1997). Tadros et al. (2003) then introduced updated creep models based on results of several experiments which were later incorporated in the AASHTO LRFD Bridge Design Specifications (2007). The variables influencing concrete creep include the type and volume of aggregate, the volume of cement paste, the duration of concrete stress, and the member geometry (Tadros et al., 2003). Tadros et al. (2003) conducted creep strain measurements alongside the shrinkage strain studies performed on 12 different concrete mixes discussed above. Figure A.3 shows an example of measured creep strains as compared to predicted creep strains.

From these data, Tadros et al. (2003) proposed a new formula for predicting creep in concrete by suggesting a new model for the creep coefficient. Like the shrinkage strain formula, the creep coefficient formula proposed by Tadros et al. (2003) is the basis for the creep coefficient formula found in AASHTO LRFD Bridge Design Specifications shown in Eq. 44 above (AASHTO, 2020).

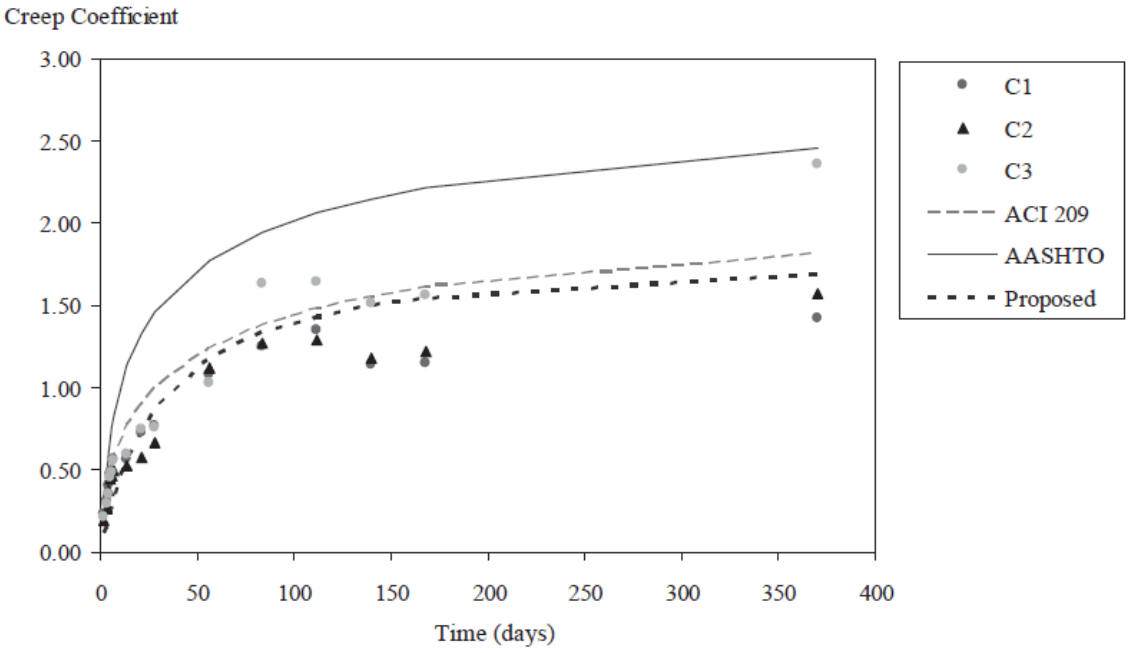

Figure A.3: Creep for Washington mix WA10G-01 load at 1 day (reproduced from Tadros et al., 2003).

Many studies on the creep, shrinkage, and relaxation effects that contribute to prestress loss, like those performed by Tadros et al. (2003) discussed above, have been performed (Bažant and Wittmann, 1982; Ghali and Trevino, 1985; Magura et al., 1962; Youakim et al., 2007; Rizkalla et al., 2011). However, in a concrete member, the loss components interact with one another as the structure ages. The interaction of the loss components in actual structures is not considered in specific creep, shrinkage, and relaxation studies. The accuracy of the predicted prestress loss in a structure is dependent on the accuracy of the models for the loss components, how those loss models interact with each other, and how the structure's material properties change over time. Rizkalla et al. (2011) studied the prediction of camber in prestressed concrete structures, and to accurately predict camber, an accurate prediction of prestress loss was required. Rizkalla et al. (2011) suggest that to improve the prediction of prestress loss, the ultimate strength of the concrete should be increased from the specified strength to account for the long-term increase in concrete strength beyond 28 days. Both shrinkage and creep effects are dependent on the concrete strength, so as concrete strength increases over time, creep and shrinkage strains will accumulate more slowly. The interaction of these two loss components complicates the long-term behavior, which is further complicated by their dependence on a constantly changing concrete strength over the life

of a structure. The suggestion by Rizkalla et al. (2011) to increase concrete strength illustrates the sensitivity of prestress loss assessment in real structures.

A.4.2. Experimental Investigations into Prestress Loss in Structures

To assess the accuracy of prestress loss predictions, an experimental method for determining existing prestessing stress is required. A review of previous experiments in the literature related to the assessment of prestress loss in concrete bridge structures is discussed below.

Azizinamini et al. (1996) conducted destructive testing of a 54 ft. long, 25-year-old Nebraska Type III prestressed concrete girder to verify a nondestructive prestress loss estimation technique they proposed. The Nebraska Type III girder shares the same cross-sectional dimensions as the AASHTO Type III girders recovered from the Bonner Bridge, and, like the Bonner Bridge girders, contained 7/16" diameter, Grade 250, stress-relieved strand pretensioned to 175 ksi or 70% of the ultimate stress. For this test, Azizinamini et al. (1996) subjected the 25-year-old girder to four-point bending to induce flexural cracking in the bottom flange of the girder. After flexural cracks were produced, the girder was unloaded so that strain transducers and foil gauges could be placed across a flexural crack. The girder was reloaded, and the strain transducers were used to determine the reopening of flexural cracks by the change in the stiffness with increasing load. The test setup and load-strain results from one of the two strain transducers is shown in Figure A.4.

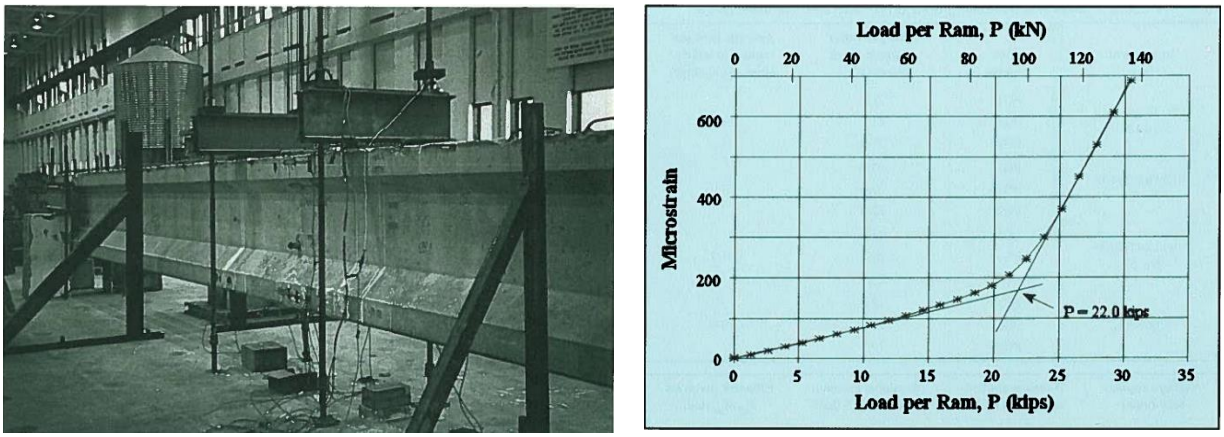

Figure A.4: Load testing and load-strain response of Nebraska Type III Girders (reproduced from Azizinamini et al., 1996).

After determining the crack reopening applied load from the strain transducers, Azizinamini et al. (1996) calculated the reopening moment for use in Eq. 67 below where M is the moment at crack reopening, P_{eff} is the effective remaining prestressing force, M_d is the dead load moment, e is the eccentricity of the prestressing strand from the neutral axis, A is the cross-sectional area, and S_b is the bottom fiber section modulus of the girder.

$$\frac{M}{S_b} = \frac{P_{eff}}{A} + \frac{P_{eff}e}{S_b} - \frac{M_d}{S_b} \tag{67}$$

At crack reopening, the stress across the crack at the extreme tension fiber is zero, so the bottom fiber tensile stress from applied and dead load moments equals the uniform compressive stress over the area combined with the compressive stress from the eccentricity of the prestressing. From this equation, they found that the average strand stress was 138.8 ksi, or a 20.7% decrease from the original tensioning stress. Azizinamini et al. (1996) found the 1989 AASHTO Standard Specification estimated the losses to be 25.7%, so the AASHTO estimate was conservative when compared to the experimentally determined value.

Halsey and Miller (1996) tested two 29 ft. long, 40-year-old inverted T-beams in three-point bending to determine prestress loss. Clip gauges placed through the depth of the specimen and on the top and bottom flanges were used to record strain during the flexural test. The prestress loss was determined using two different values, the observed cracking moment and the crack reopening moment. The state of stress in a prestressed concrete beam under simply supported state without load, at the point of cracking and at crack reopening is shown in Figure A.5.

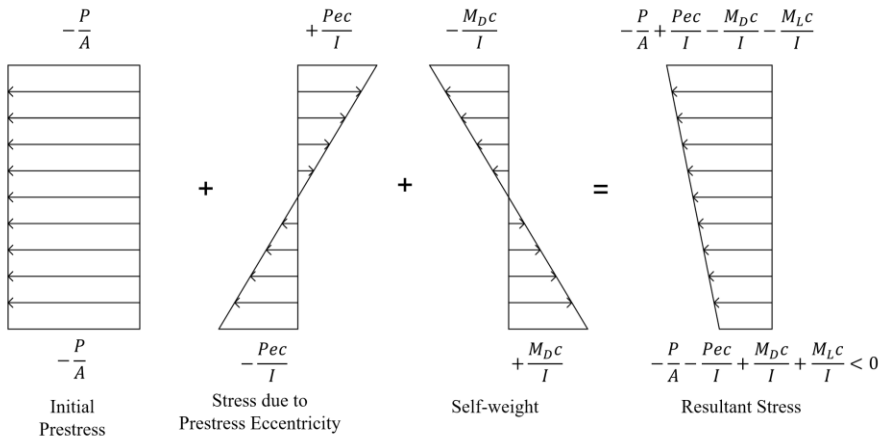

(a)

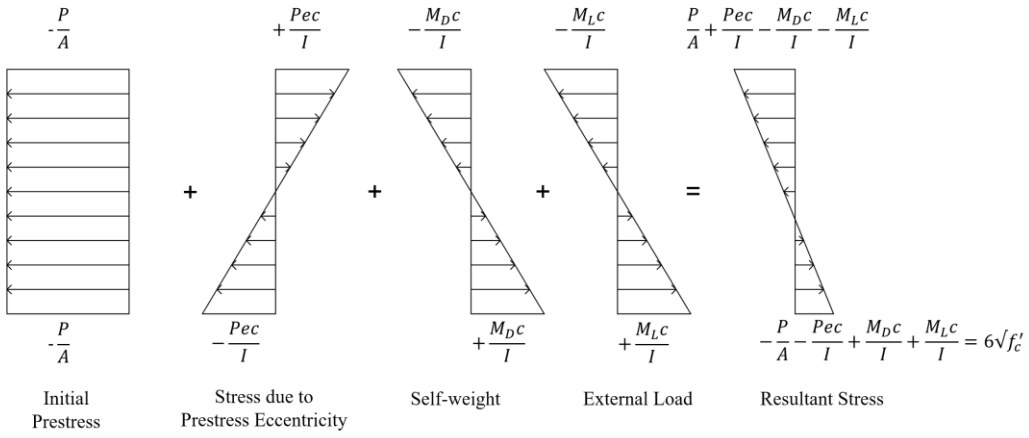

(b)

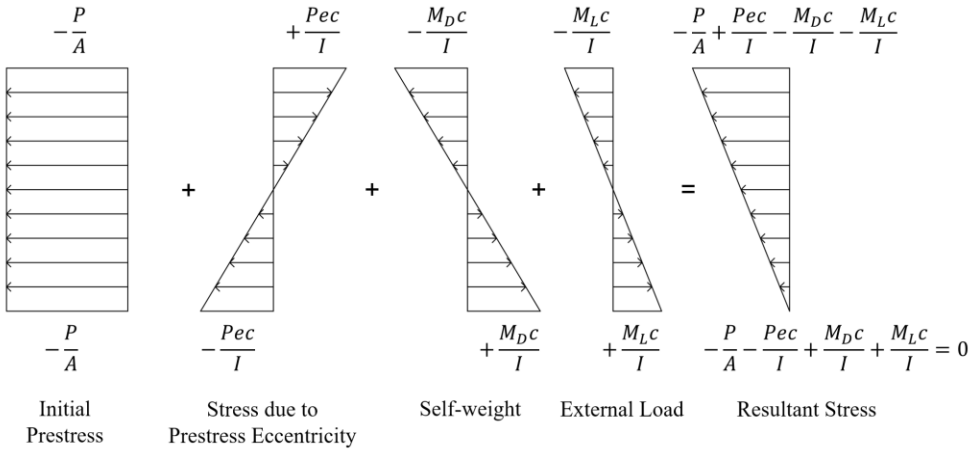

(c)

Figure A.5: Stress in girder at midspan due to initial prestress, self-weight and external loads (a) Simply supported state without any external load (b) At cracking (c) At crack reopening

After the beams were first cracked, they were unloaded and additional strain gauges were placed across the cracks to determine the crack reopening moment. Figure A.6 shows the clip gauges placed on the beam and the load-crack opening data for determining the crack reopening moment.

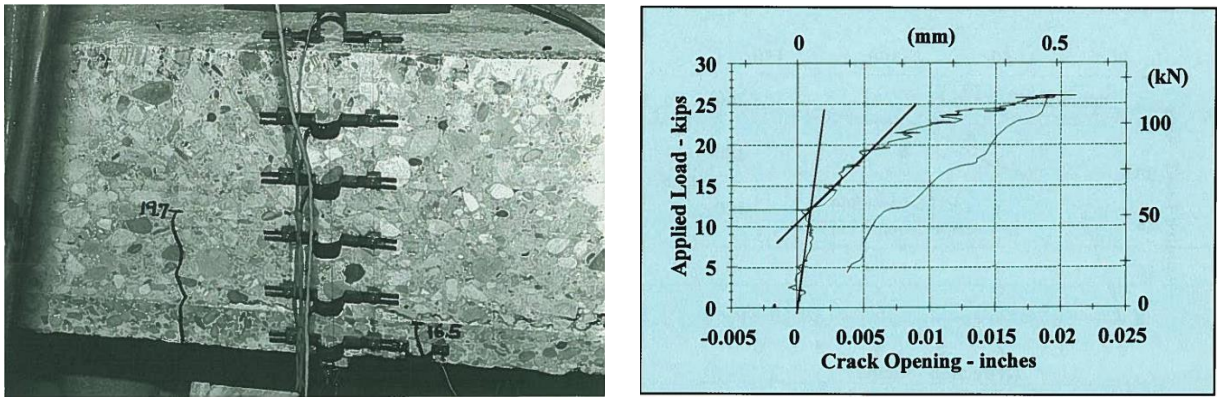

Figure A.6: Clip gauges on inverted T-beam elevation view and post cracking load-crack opening data (reproduced from Halsey and Miller, 1996).

The benefit of using the crack reopening moment instead of the first cracking moment to determine the amount of current prestressing is that the tensile capacity of the concrete does not contribute to estimating the moment at which zero tensile stresses are in the bottom fiber. Otherwise, the assumed tensile capacity of the concrete changes the estimate of prestress loss, and an overestimate of concrete tensile capacity can cause the prediction of prestress loss to be unreasonably high. In addition to flexural testing of two beams, one untested beam had the prestress loss assessed by cutting a strand. A 12 in. section of strand was exposed, a single wire was strain gauged, and the strand was cut with bolt cutters. The compressive strain registered by the strain gauge was used to determine the stress in the strand. The measured stress was 99.7 ksi, a 34% loss from the assumed tensioning stress of 150 ksi. The prestress loss results from testing beams 1 and 2 and strand cutting of beam 3 is shown in Table A.1 along with the 1989 AASHTO Standard Specification prediction of prestress loss.

Table A.1: Prestress loss test results (adapted from Halsey and Miller, 1996).

Method	Loss of prestressing, ksi	Percentage Loss
1989 AASHTO Specifications	40.3	27%
Observed cracking moment	31.5 Beam 1	21% Beam 1
	40.3 Beam 2	27% Beam 2
Crack opening load	29.3 Beam 1	20% Beam 1
	35.0 Beam 2	23% Beam 2
Cutting a strand	50.3	34%

The strand cutting of the untested beam showed the highest loss percentage, but the other two methods show reasonably good agreement with losses predicted by AASHTO Standard Specifications. Assuming a prestress loss of 20%, the sectional analysis program Response-2000 was used to predict steel strain during testing, and the results were compared to strain gauge data from a gauge glued to a strand prior to testing. The results are shown in Figure A.7, and RESPONSE shows good agreement with measured strand strains. This suggests that the RESPONSE software performs well for analysis of aged prestressed concrete structures.

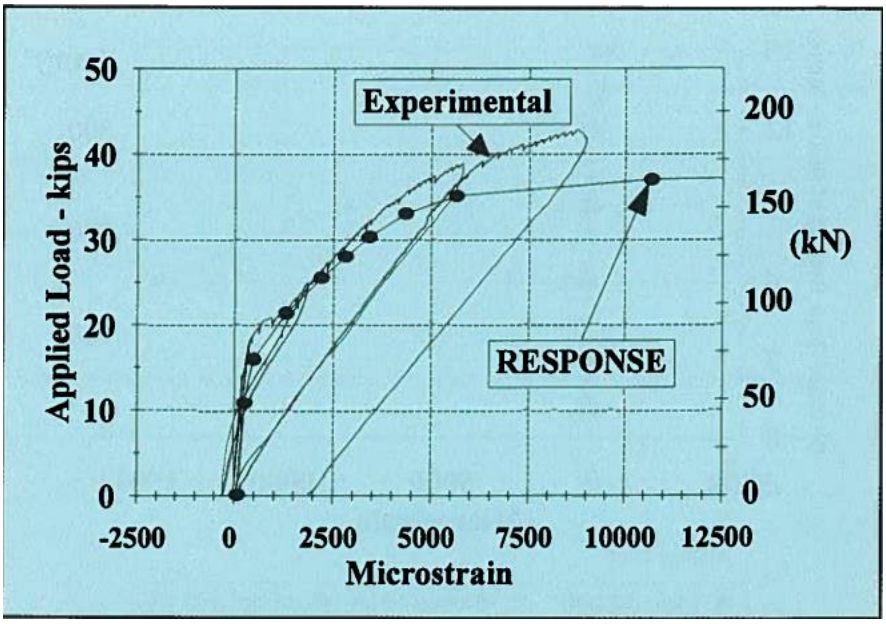

Figure A.7: RESPONSE steel strain prediction compared to experimental results (reproduced from Halsey and Miller, 1996).

Garber et al. (2015) tested a total of 30 specimens to compare measured prestress loss to predicted losses. The girders were produced in several different configurations and stored at multiple different locations to test the effects of configuration and local conditions on the prestress loss. To determine the prestress loss of the girders, they were tested in four-point bending, and the stiffness-deflection data were used to determine the cracking load. It was assumed that cracking was indicated by a sudden reduction in girder stiffness as deflection increased. The tensile capacity of the concrete was determined using split cylinder testing, and the effective prestressing force could, therefore, be determined from the applied moment at cracking. The test setup and an example of the stiffness-deflection results can be seen in Figure A.8.

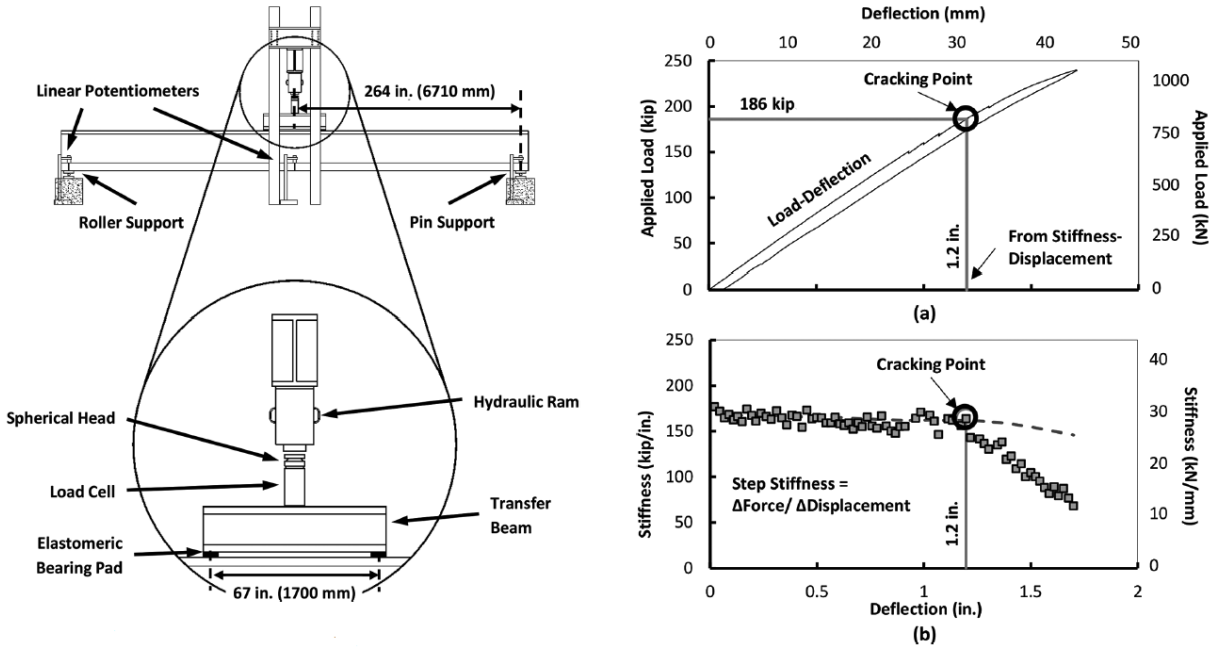

Figure A.8: Test setup and stiffness-deflection results (reproduced from Garber et al., 2015).

Since specimens were cast for testing rather than using in-service structures, vibrating wire gauges (VWG) could be cast into the specimens at midspan to measure the changes in concrete stress over time. The prestress loss determined from the flexural testing of the girder were compared to the losses measured with the VWGs. Garber et al. (2015) determined that the flexural testing provided an accurate estimate of prestress loss. The comparison of losses determined from flexural testing and VWGs is shown in Figure A.9. The final age of specimens in Series I, Series II, Series III and Series IV ranged from 939-980 days, 922-955 days, 675-703 days and 230-259 days respectively.

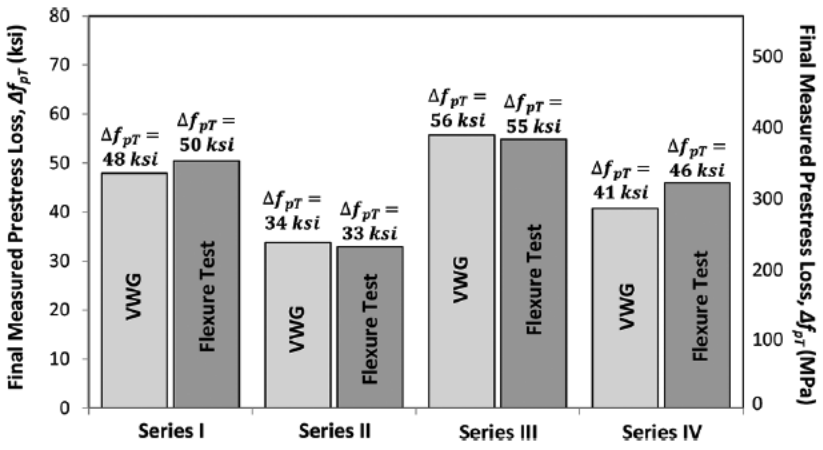

Figure A.9: Comparison of loss measurements from VWGs and flexural testing (reproduced from Garber et al., 2015).

The measured losses for the girders were compared to predicted losses using the 2012 AASHTO LRFD Bridge Design Specifications Refined Method. The average estimate to measured loss ratio for the AASHTO Refined Method was 1.49 which indicates that the estimate of loss is conservative for girders examined at final age ranging from approximately 6 months to 2.5 years.

Higgs et al. (2015) tested four AASHTO Type I girders recovered from the I-15 bridge spanning highway 400 South in Orem, Utah. The girders were tested in three-point bending to determine the prestress loss. Like Azizinamini et al. (1996) and Halesy and Miller (1996), the girders were loaded until visible cracking had occurred. After cracking was induced, the girders were unloaded, and foil strain gauges were placed across an existing crack to determine the crack reopening. The moment-strain response of girder G3 is shown in Figure A.10. Higgs et al. (2015) determined what they refer to as the "decompression moment", the moment required to produce zero stress at the extreme tension fiber, by extrapolating the two linear portions of the moment-strain curve.

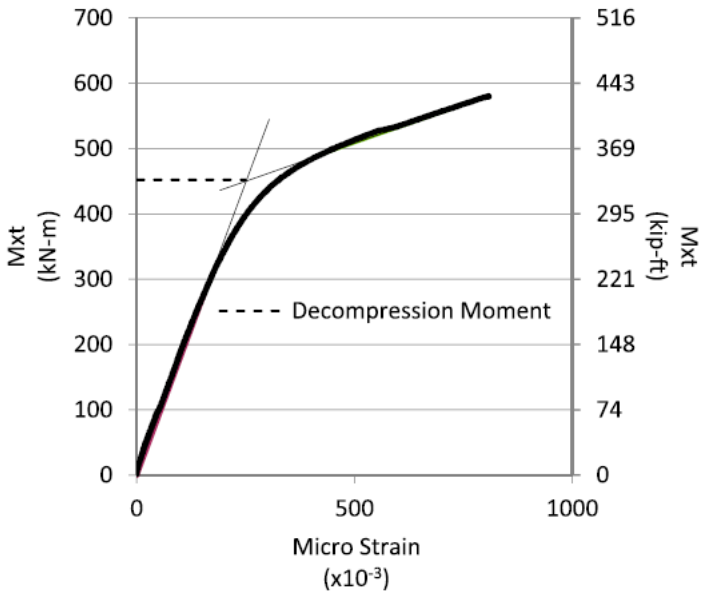

Figure A.10: Moment-strain curve for strain gauge over flexural crack on girder G3 (reproduced from Higgs et al., 2015).

Using the decompression moment and the following equation, Higgs *et al.* determined the residual total force in the stressing strand for each of the four tested girders. The difference between Eq. 68 and Eq. 67 used by Azizinamini et al. (1996) is Higgs et al.'s (2015) use of composite section properties for the applied moment term, M_{xt}, because the salvaged girders had some residual composite deck attached. Azizinamini et al. (1996) did not have a composite section.

$$\sigma = -\frac{P}{A_g} - \frac{Pe_{pg}C_g}{I_g} + \frac{M_{sw}C_g}{I_g} + \frac{M_{xt}C}{I} \tag{68}$$

The residual prestress of each of the four girders is presented in Table A1.2 below along with the predicted prestress using the 2012 AASHTO LRFD approximate and Refined Methods. The flexural testing produced consistent estimates of prestress loss that compared reasonably to the predictions made by AASHTO.

Table A.2: Residual girder prestress from tests (reproduced from Higgs et al., 2015).

Residual Prestress Source	**Magnitude [MPa (ksi)]**
Experimental Girder G1	1,100 (159)
Experimental Girder G2	1,110 (161)
Experimental Girder G3	1,070 (155)
Experimental Girder G4	1,080 (157)
Experimental Girder Average	1,090 (158)
Calculated AASHTO approximate method	1,060 (154)
Calculated AASHTO refined method	1,100 (160)

The experiments in the literature discussed above indicate that flexural testing of prestressed concrete bridge girders to ascertain cracking moment and crack reopening moment can provide an accurate assessment of the residual prestressing force in the strand. Unless concrete tensile strength is known, the literature indicates that the use of crack reopening moment is a more reliable measure of prestress loss because it minimizes the contribution of concrete tensile strength in the flexural behavior. The literature also finds prestress loss predictions made by AASHTO tend to be conservative for the tested structures. However, the structures tested in the literature are not as old as the girders recovered from the Bonner Bridge. Additionally, while previous experiments collect strain at discrete locations through the depth during testing, displacement data collected using Digital Image Correlation (DIC) equipment has not previously been obtained. Collection of DIC data allow the cracking behavior of the girder and the strains in the concrete to be assessed over a large portion of the span throughout testing. The age of the Bonner Bridge girders and the use of DIC data make the results of laboratory testing the recovered girders a valuable dataset in the assessment of prestress losses in aging infrastructure.

APPENDIX B - ADDITIONAL EXPERIMENTAL PROGRAM DETAILS

Appendix B provides additional details on the experimental program such as the detailed test setup, instrumentation, and loading protocol for the BTE series.

B.1 Material Properties

B.1.1 Prestressing Steel Properties

The prestressing steel in the girders of the Bonner Bridge was specified in the original construction drawings to be 7/16″ diameter stress-relieved strand tensioned to 18,900 lbs. No additional information about the strand was provided in the construction drawings, and thus tension tests were performed on strands removed from the girder. Although the grade of steel for the strand was not specified in the drawings, the nominal ultimate stress is likely 250 ksi, as corroborated by the measured peak stress in the tension tests and the specified jacking force on the drawings. The ACI-ASCE Joint Committee 323 published in their Tentative Recommendations for Prestressed Concrete (1958) that the maximum jacking stress for stress relieved strand should be 0.7 times the ultimate stress at nearly the same time the Bonner Bridge was designed. Using this recommendation with an assumed ultimate stress of 250 ksi, the recommended jacking stress is 175 ksi. ASTM standard A886/A886M-17 (2017) indicates that the nominal area for a 7/16” seven-wire strand is 0.108 sq. in., thus, the recommended jacking stress of 175 ksi would require a force of 18,900 lbs; the exact value specified on the construction drawings for the Bonner Bridge. Therefore, the ultimate strength for this strand is assumed to be 250 ksi, classified by ASTM as Grade 250 (ASTM, 2017).

The force displacement results of tension tests of four strands removed from BTE1 are shown in Figure B.1. The grip wedges used to hold the strand for tension testing concentrate stress at the grip and caused three of the four strands to fail at the grips prior to reaching the ultimate strand stress. Additionally, strand number three in Figure B.1 shows slip of the strand in the grip just prior to yielding. Strand number 1 is the only strand that ruptured between the grips, and it sustained an ultimate force of 28,960 lbs. Figure B.2 (left) shows strand number 1 after rupture. According to ASTM Standard A886/A886M-17 (2017), the strength of a 7/16” Grade 250 strand

must meet or exceed 27 kips, and the yield strength of the strand must meet or exceed 23 kips. As shown in Figure B.1, the strands exceeded that required yield and rupture strength.

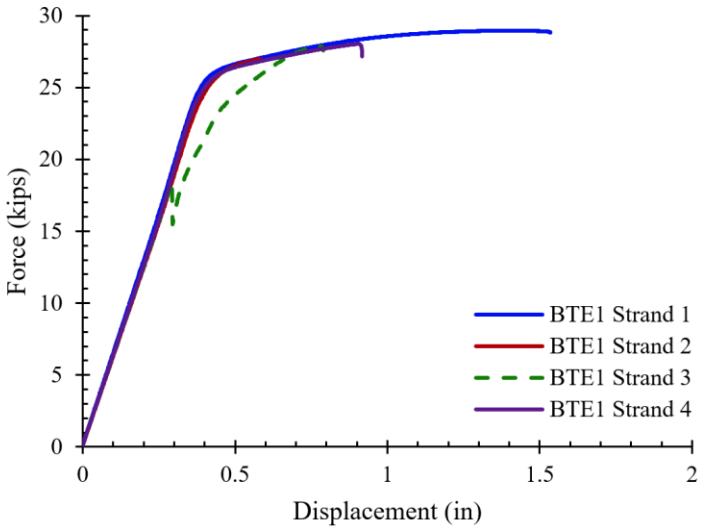

Figure B.1: Force-displacement of strand from BTE1.

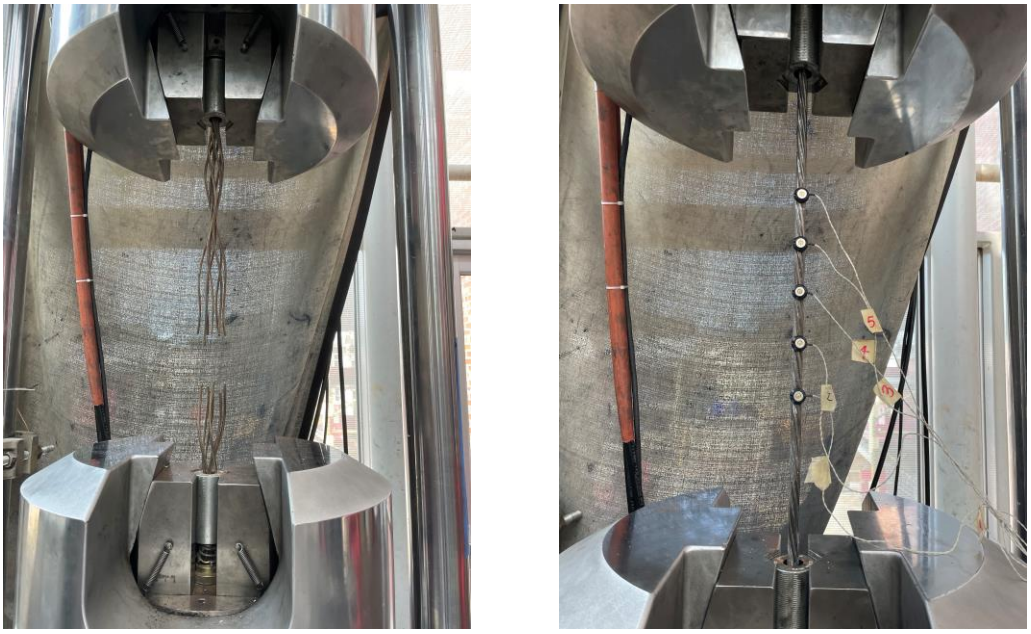

Figure B.2: BTE1 strand number 1 rupture (left) & instrumentation on BTE2 strand (right)

To better model the stress-strain response of the BTE series strands, five strands taken from BTE2 were tested in tension to failure and were instrumented with a non-contact displacement

measurement system (see Section B.2.3 for a description of the instrumentation). The instrumentation system measured the three-dimensional displacement of LED targets placed along the strand length throughout each tension test, and allowed the full stress-strain behavior of the strands to be characterized. Figure B.2 (right) shows the LED instrumentation on a strand, and Figure B.3 shows the stress-strain behavior measured for the five strands harvested from BTE2.

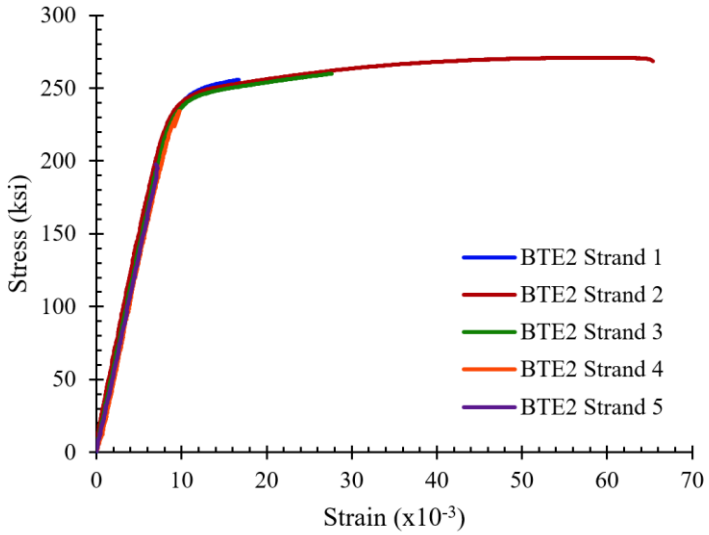

Figure B.3: BTE2 strand stress-strain response.

As with BTE1, only one strand (strand 2) ruptured between the grips for the BTE2 strand tension tests. However, the behavior of the remaining of BTE2 strands suggested their ultimate strength would be very similar to strand 2. Using strand 2 as a representative strand for BTE2, a modified Ramberg-Osgood curve can be fit to the strand stress-strain response. Collins and Mitchell (1997) recommend the use of a modified Ramberg-Osgood function to model the behavior of prestressing strand, and the modified Ramberg-Osgood curve is given by Eq. 69 below where f_p is the strand stress and ε_{pf} is the strain in the strand. The constants *A*, *B*, and *C* are provided in Table B.1 below along with elastic modulus, E_p, and ultimate stress, f_{pu}, for BTE2 strand 2. The constants from the original Modified Ramberg-Osgood equation developed by Collins and Mitchell (1997) were changed to better fit the test data obtained from strand testing. Figure B.4 shows the modified Ramberg-Osgood curve compared to the actual stress-strain response for BTE2 strand 2.

$$f_p = E_p \varepsilon_{pf} \left\{ A + \frac{1-A}{\left[1+\left(B\varepsilon_{pf}\right)^C\right]^{1/C}} \right\} \leq f_{pu} \tag{69}$$

Table B.1: Constants for Modified Ramberg-Osgood Curve.

Modified Ramberg-Osgood	
A	0.025
B	114
C	9
E_p (ksi)	28,000
f_{pu} (ksi)	271

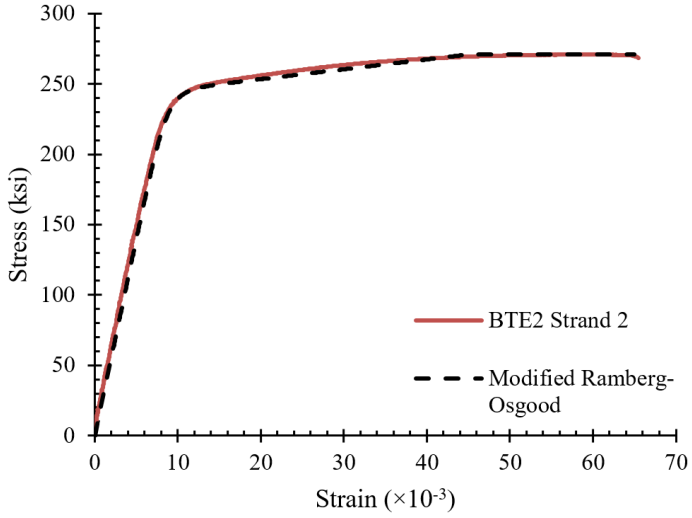

Figure B.4: BTE2 strand 2 modified Ramberg-Osgood curve.

The modified Ramberg-Osgood curve represents the strand behavior well. To ensure that the curve representing BTE2 strand 2 is a good representation of the strand from both BTE1 and BTE2, the force-displacement response from all strands tested from BTE1 and BTE2 were plotted in Figure B.5 to compare behaviors. The behavior of all strands is similar, and the response of BTE1 strand 1 is very close to the response of BTE2 strand 2.

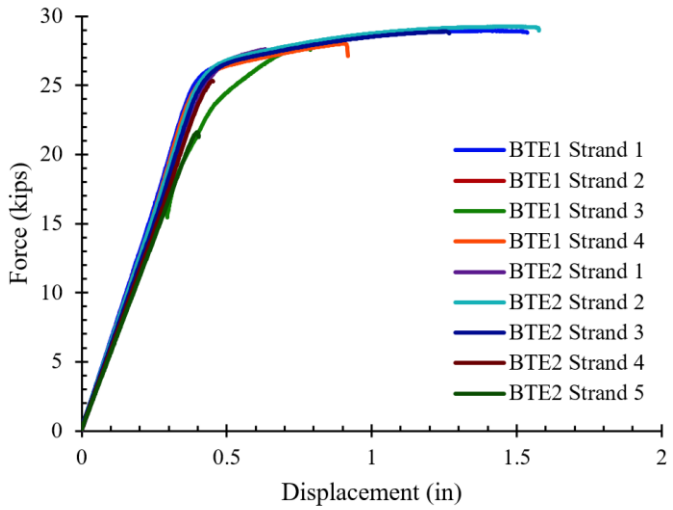

Figure B.5: BTE1 and BTE2 strand comparison.

Because the behaviors of the strands from these two beams were very similar, the modified Ramberg-Osgood curve fitted to BTE2 strand 2 was used for modeling strand behavior in all four of the BTE specimens. The end regions of BTE1 and BTE2 were not heavily stressed during flexural tests of these beams, so the strands recovered for tension testing were taken from the ends of these two girders. The end regions of girders BTE3 and BTE4 were tested to failure in shear, and therefore, strand samples were not taken from these regions.

B.1.2 Concrete Properties

B.1.2.1 Girder Concrete

Concrete compressive strength for the Bonner Bridge girders was specified as 5000 psi, and the deck concrete was specified as 3000 psi. Typically, traditional concrete mixes exceed their specified strength at 28 days and continue to increase in strength over time. As such, numerous cores were taken from the top flange of each girder (after flexure and shear testing) to determine the ultimate strength and elastic modulus of the concrete roughly 56 years old concrete. Figure B.6 shows the coring process for the girders. Since the cores were removed from the top of the girder, any residual concrete deck at the top of the core had to be cut away after core extraction. The cores were nominally 3.75 in. diameter, so the beam was cored to a depth of 12 in. to provide a suitable length-to-diameter ratio of the finished cores after rough material at the bottom and concrete deck

material at the top were trimmed away. After saw-cutting, the ends of each core were ground flat, smooth, and parallel using a cylinder grinder to make flat bearing surfaces for the neoprene compression test caps. Figure B.7 shows the deck concrete being removed from the top of the cores.

Figure B.6: Girder top flange coring.

The elastic modulus and ultimate strength of the concrete were determined by testing cores to failure in compression with three, 60 mm (2.36 in.) long strain gauges bonded to the outer surface. Gauges were evenly spaced 120 degrees around the surface of each core at the mid-height, configured to measure strain in the longitudinal axis of the cylinder. The test setup and strain gauges can be seen in Figure B.8.

Figure B.7: Deck concrete removal by saw-cutting.

Figure B.8: Core compression testing.

Data obtained from compression tests of each core were adjusted using the ACI 214.4-21 (2021) recommendations for interpreting the compressive strength of concrete cores. ACI214.4-

21 (2021) utilizes Eq. 70 for correcting the measured compressive strength, f_{core}, to account for effects of the coring process on the strength.

$$f_c = F_{l/d} F_{dia} F_{mc} F_d f_{core} \tag{70}$$

Note $F_{l/d}$ is the length-to-diameter ratio factor, F_{dia} is the core diameter factor, F_{mc} is the core moisture condition factor, and F_d is the coring damage correction factor. Table B.2 is adapted from ACI 214.4-21 (2021) and Bartlett and MacGregor (1995), and shows the recommended correction factors. For this study, the girder concrete cores are corrected using constants corresponding to the air-dried condition, and the deck concrete cores are corrected using constants corresponding to the as-received condition. The diameter correction factor is conservatively taken as 1.00 for all cores, since the diameter of all cores is 3.75 in. instead of 4.00 in. The measured dimensions of each core were recorded to calculate correction factors for length-to-diameter ratio and core diameter. The height of each core and the diameter at the top, middle, and bottom of each core were measured using calipers as shown in Figure B.9. The dimensions of the BTE1 cores are shown in Table B.3 along with the measured compressive strengths.

Table B.2: Core strength correction factors (adapted from ACI214.4-21, 2021 and Bartlett and MacGregor, 1995).

Factor		**Mean value**	**Coefficient of variation V, percent**
$F_{l/d}$: l/d ratio†	As- received‡	$1-\{0.130-\alpha f_{core}\}(2-\frac{l}{d})^2$	$2.5(2-\frac{l}{d})^2$
	Soaked 48 hours	$1-\{0.117-\alpha f_{core}\}(2-\frac{l}{d})^2$	$2.5(2-\frac{l}{d})^2$
	Air dried‡	$1-\{0.144-\alpha f_{core}\}(2-\frac{l}{d})^2$	$2.5(2-\frac{l}{d})^2$
F_{dia}: core diameter	2 in. (50mm)	1.06	11.8
	4 in. (100mm)	1.00	0.0
	6 in. (150mm)	0.98	1.8
F_{mc}: core moisture content	As- received‡	1.00	2.5
	Soaked 48 hours	1.09	2.5
	Air dried‡	0.96	2.5
F_d: damage due to drilling		1.06	2.5

*To obtain equivalent in-place concrete strength, multiply measured core strength by appropriate factor(s) inaccordance with Eq. (9.1)
†Constant α equals $3(10^{-6})$ 1/psi for f_{core} in psi, or $4.3(10^{-4})$ 1/MPa for f_{core} in MPa
‡Standard treatement specified in ASTM C42/C42M

Figure B.9: Core measurements taken with calipers.

The mean measured compressive strength of concrete from BTE1 was 6050 psi. The values for correction factors given by ACI 214.4-21 (2021) and the corrected compressive strength of the girder concrete are also listed in Table B.3. After applying the correction factors suggested in ACI 214.4-21 (2021) the compressive strength of BTE1 was 6150 psi.

Table B.3: Dimensions with measured and corrected compressive strength of BTE1 concrete.

Core	Length (in)	D_{top} (in)	D_{mid} (in)	D_{bot} (in)	$D_{average}$ (in)	$L/D_{average}$	$f'_{c,measured}$ (psi)	$F_{l/d}$	F_{dia}	F_{mc}	F_d	f_{core} (psi)	$f'_{c,corrected}$ (psi)
1	7.25	3.73	3.75	3.75	3.74	1.94	6261	1.00	1.00	0.96	1.06	6261	6368
2	7.94	3.71	3.71	3.73	3.72	2.14	5884	1.00	1.00	0.96	1.06	5884	5973
3	7.88	3.73	3.75	3.73	3.74	2.11	5931	1.00	1.00	0.96	1.06	5931	6026
4	6.63	3.70	3.70	3.73	3.71	1.79	6177	0.99	1.00	0.96	1.06	6177	6250
5	8.06	3.75	3.73	3.74	3.74	2.16	6371	1.00	1.00	0.96	1.06	6371	6464
6	7.50	3.75	3.73	3.75	3.74	2.00	5664	1.00	1.00	0.96	1.06	5664	5764
7	8.00	3.75	3.74	3.73	3.74	2.14	5788	1.00	1.00	0.96	1.06	5788	5875
8	7.88	3.74	3.75	3.75	3.75	2.10	6109	1.00	1.00	0.96	1.06	6109	6209
9	7.94	3.75	3.74	3.75	3.75	2.12	6440	1.00	1.00	0.96	1.06	6440	6542
10	7.70	3.75	3.75	3.75	3.75	2.05	5887	1.00	1.00	0.96	1.06	5887	5988
						Mean	6051					Mean	6146
						C.O.V. (%)	4.29					C.O.V. (%)	4.24
						S.D.	259					S.D.	260

*S.D. is the Standard Deviation.
†C.O.V. is the Coefficient of Variation.

In addition to the ultimate concrete compressive strength, the modulus of elasticity of the concrete was of interest to develop an accurate model of the concrete behavior for use in predicting the girder capacity and prestress loss. Collins and Mitchell (1997) recommend the use of the modified Popovics constitutive relationship for the compressive behavior of concrete where f_c is the compressive stress at any strain ε_{cf}. The Popovics relationship is given by Eq. 71, 72, 73, 74 and 75 for concrete strengths in units of psi:

$$\frac{f_c}{f'_c} = \frac{n\left(\varepsilon_{cf}/\varepsilon'_c\right)}{n-1+\left(\varepsilon_{cf}/\varepsilon'_c\right)^{nk}} \tag{71}$$

Where:

$$E_c = 40{,}000\sqrt{f'_c} + 1{,}000{,}000 \tag{72}$$

$$n = 0.8 + \frac{f'_c}{2500} \tag{73}$$

$$\varepsilon'_c = \frac{f'_c}{E_c}\frac{n}{n-1} \quad (74)$$

$$k = 0.67 + \frac{f'_c}{9000} \quad (75)$$

A Popovics constitutive relationship for the ten cores taken from BTE1 was created utilizing Eq. 71, 72, 73, 74, and 75 above. However, the concrete modulus predicted using Eq. 72 above under-predicts the modulus of the concrete for many cores. The initial concrete modulus provided by the average strain gauge response and the predicted modulus from Eq. 72, $E_{c,Popovics}$, is provided in Table B.4. The compressive strength for each core used in Eq. 72 is the corrected ultimate strength provided in Table B.3.

Table B.4: Measured and Popovics predicted BTE1 concrete modulus (T/P is the Test to Predicted Ratio).

Core	E_c (ksi)	$E_{c,Popovics}$ (ksi)	T/P
1	4249	4165	1.02
2	4713	4068	1.16
3	4003	4080	0.98
4	4285	4144	1.03
5	4831	4193	1.15
6	5014	4010	1.25
7	4600	4043	1.14
8	4270	4127	1.03
9	5657	4210	1.34
10	5427	4069	1.33
		Mean	**1.14**
		C.O.V.	**11.4%**

The test to predicted ratio for BTE1 cores is greater than one for all but one core, so the actual measured concrete stiffness has been used in place of the stiffness provided by Eq. 72 for the Popovics constitutive models. The values for modulus and the calculated strain at peak stress are provided in Table B.5 for the ten cores taken from BTE1. Figure B.10 shows the Popovics relationships in comparison to the measured stress-strain response from the strain gauges placed on each core. Utilizing the measured concrete modulus, the Popovics relationships fit the measured

data well up through peak stress. Post peak stress, the concrete from BTE1 showed abrupt failures as seen in Figure B.11. The cores were tested in force control, so the post peak behavior could not be observed, but the rapidly decreasing strength predicted by the Popovics relationship shown in Figure B.10 appears reasonable.

Table B.5: Modulus and strain at peak stress for BTE1 cores utilizing Popovics relationship.

Core	f'_c (psi)	E_c (ksi)	ε'_c (x10^{-3})
1	6368	4249	2.11
2	5973	4713	1.83
3	6026	4003	2.16
4	6250	4285	2.08
5	6464	4831	1.88
6	5764	5014	1.68
7	5875	4600	1.85
8	6209	4270	2.07
9	6542	5657	1.62
10	5988	5427	1.59
Mean	**6150**	**4710**	**1.89**
C.O.V. (%)	**4.24%**	**11.5%**	**11.3%**
S.D.	**260**	**539**	**0.21**

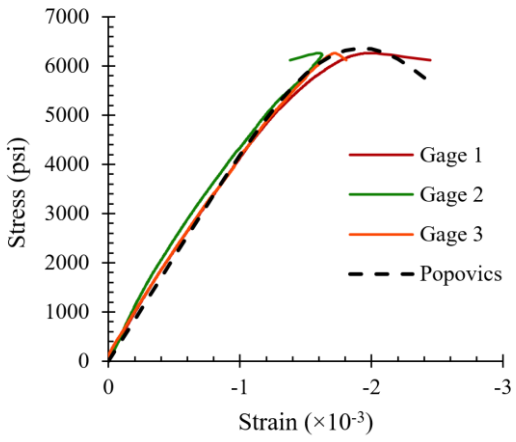

BTE1 Core 1

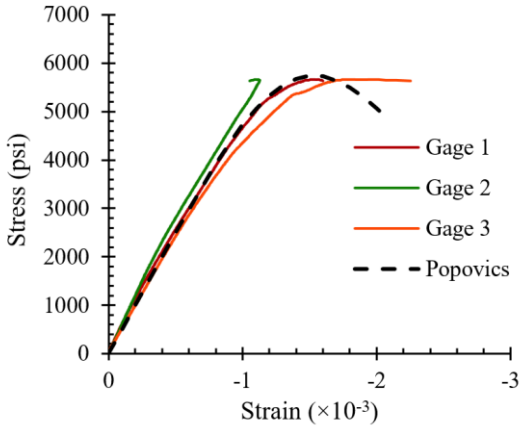

BTE1 Core 6

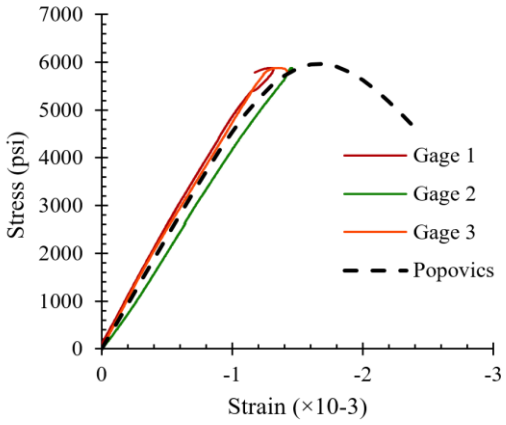

BTE1 Core 2

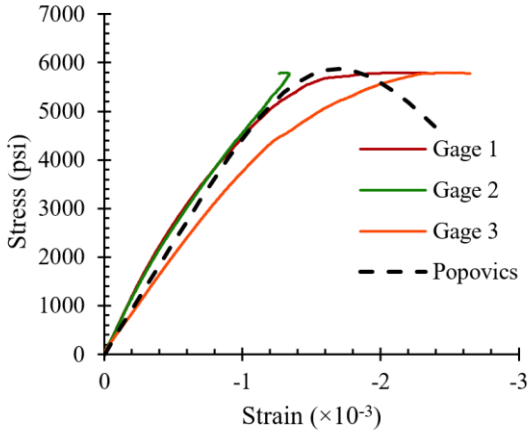

BTE1 Core 7

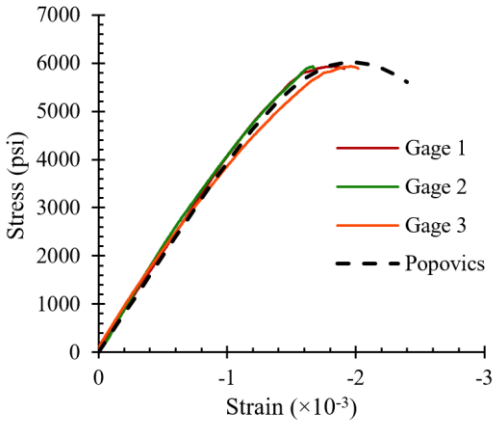

BTE1 Core 3

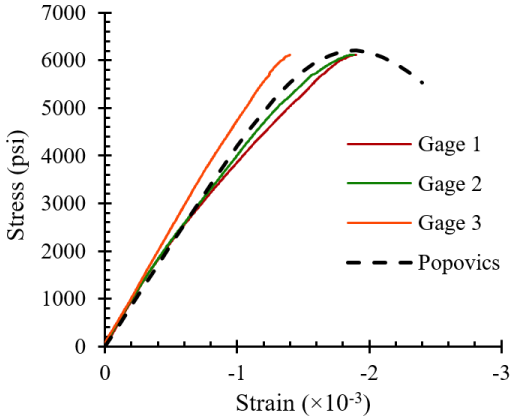

BTE1 Core 8

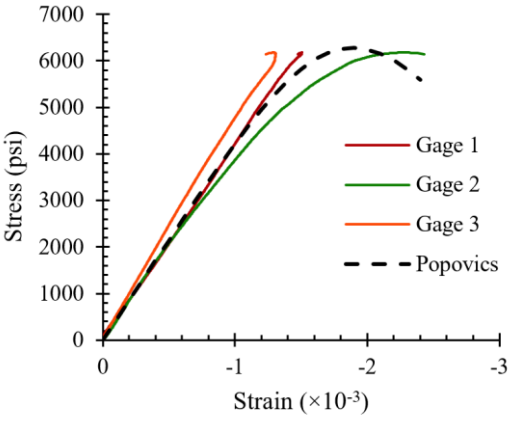

BTE1 Core 4

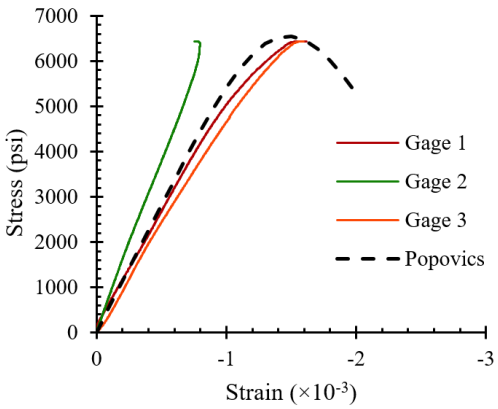

BTE1 Core 9

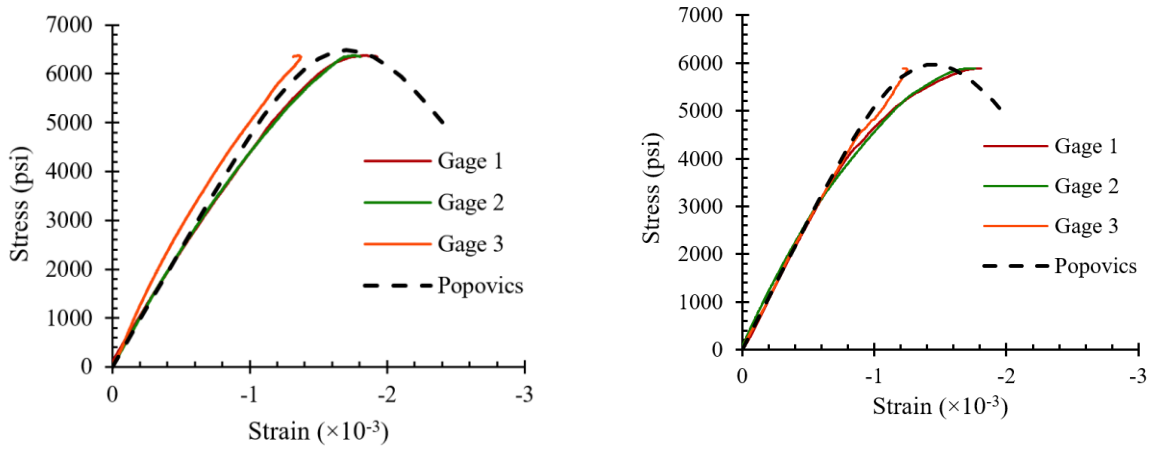

Figure B.10: BTE1 core stress-strain response.

Figure B.11: Typical failure of core from BTE1.

As the data show, the Popovics relationship fits the behavior of each BTE1 core well. The strain gauges show some variability even for a single core, which is indicative that the differences are coming from the approach used and not the concrete itself. Moreover, extraction of cores tends to have an effect on the compression response compared to cast cylinders. Therefore, a modified Popovics relationship using the mean compressive strength, modulus, and strain at peak stress

from Table B.5 was used for modeling the BTE1 girder concrete. Figure B.12 shows the average Popovics curve in comparison to the measured stress-strain response from the strain gauges on each of the BTE1 cores. The modified Popovics curve matches the experimental response from the core data reasonably well, and the relationship is used as the constitutive model for the concrete in BTE1 in subsequent sections of this report.

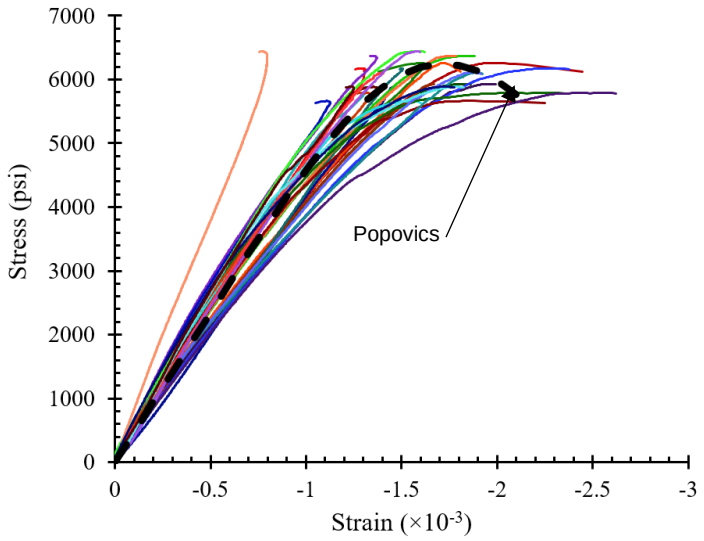

Figure B.12: Average Popovics relationship for BTE1.

Similar tests were conducted and analysis performed to measure the concrete properties of other girders. Five cores were collected from each of BTE2, BTE3, and BTE4 to ascertain the stress strain response of the concrete in each girder. The dimensions and measured strengths of the cores from BTE2, BTE3, and BTE4 can be seen in Table B.6, Table B.7, and Table B.8, respectively. The mean measured strengths for BTE2, BTE3, and BTE4 were 8930 psi, 7140 psi, and 7836 psi, respectively. Like the cores from BTE1, the cores from BTE2, BTE3, and BTE4 were corrected using correction factors from ACI 214.4-21 (2021). The values for correction factors given by ACI 214.4-21 (2021) and the corrected compressive strength of BTE2, BTE3 and BTE4 are also listed in in Tables B.6, B.7, and B.8, respectively. After applying the correction factors, the compressive strength of BTE2 was 9080 psi, BTE3 was 7270 psi, and BTE4 was 7974 psi.

Table B.6: Dimensions with measured and corrected compressive strength of BTE2 cores.

Core	Length (in)	D_{top} (in)	D_{mid} (in)	D_{bot} (in)	$D_{average}$ (in)	$L/D_{average}$	$f'_{c,measured}$ (psi)	$F_{l/d}$	F_{dia}	F_{mc}	F_d	f_{core} (psi)	$f'_{c,corrected}$ (psi)
1	7.65	3.65	3.65	3.67	3.66	2.09	9091	1.00	1.00	0.96	1.06	9091	9242
2	7.62	3.67	3.66	3.66	3.66	2.08	9853	1.00	1.00	0.96	1.06	9853	10019
3	7.67	3.66	3.66	3.66	3.66	2.10	8743	1.00	1.00	0.96	1.06	8743	8887
4	7.41	3.67	3.66	3.67	3.67	2.02	8945	1.00	1.00	0.96	1.06	8945	9102
5	7.64	3.66	3.66	3.66	3.66	2.09	8011	1.00	1.00	0.96	1.06	8011	8145
						Mean	**8929**					**Mean**	**9079**
						C.O.V. (%)	**7.42**					**C.O.V. (%)**	**7.43**
						S.D.	**663**					**S.D.**	**675**

Table B.7: Dimensions with measured and corrected compressive strength of BTE3 cores.

Core	Length (in)	D_{top} (in)	D_{mid} (in)	D_{bot} (in)	$D_{average}$ (in)	$L/D_{average}$	$f'_{c,measured}$ (psi)	$F_{l/d}$	F_{dia}	F_{mc}	F_d	f_{core} (psi)	$f'_{c,corrected}$ (psi)
1	7.61	3.72	3.72	3.72	3.72	2.05	6197	1.00	1.00	0.96	1.06	6197	6304
2	7.48	3.73	3.73	3.74	3.73	2.00	7123	1.00	1.00	0.96	1.06	7123	7248
3	7.54	3.72	3.72	3.72	3.72	2.03	6838	1.00	1.00	0.96	1.06	6838	6957
4	7.58	3.72	3.72	3.73	3.72	2.04	7616	1.00	1.00	0.96	1.06	7616	7749
5	7.52	3.72	3.72	3.72	3.72	2.02	7931	1.00	1.00	0.96	1.06	7931	8070
						Mean	**7141**					**Mean**	**7266**
						C.O.V. (%)	**9.48**					**C.O.V. (%)**	**9.49**
						S.D.	**677**					**S.D.**	**689**

Table B.8: Dimensions with measured and corrected compressive strength of BTE4 cores.

Core	Length (in)	D_{top} (in)	D_{mid} (in)	D_{bot} (in)	$D_{average}$ (in)	$L/D_{average}$	$f'_{c,measured}$ (psi)	$F_{l/d}$	F_{dia}	F_{mc}	F_d	f_{core} (psi)	$f'_{c,corrected}$ (psi)
1	7.40	3.69	3.72	3.67	3.72	1.99	7915	1.00	1.00	0.96	1.06	7915	8054
2	7.50	3.71	3.71	3.66	3.72	2.02	7363	1.00	1.00	0.96	1.06	7363	7492
3	7.50	3.73	3.72	3.66	3.72	2.02	8033	1.00	1.00	0.96	1.06	8033	8175
4	7.42	3.72	3.72	3.67	3.72	1.99	7467	1.00	1.00	0.96	1.06	7467	7599
5	7.44	3.74	3.72	3.66	3.73	1.99	8401	1.00	1.00	0.96	1.06	8401	8549
						Mean	**7836**					**Mean**	**7974**
						C.O.V. (%)	**5.43**					**C.O.V. (%)**	**5.43**
						S.D.	**425**					**S.D.**	**433**

As with BTE1, a Popovics stress-strain relationship was fit to the stress strain results from BTE2, BTE3, and BTE4 core testing. The measured concrete modulus is used in the Popovics relationship for BTE2, BTE3, and BTE4 because the concrete modulus predicted by Eq. 72 above tends to under-predict modulus for this concrete mix. The measured and predicted moduli for BTE2, BTE3 and BTE4 are shown in Table B.9.

Table B.9: Measured and Popovics predicted concrete moduli of BTE2, BTE3, and BTE4

Girder	BTE2			BTE3			BTE4		
Core	*Ec* (ksi)	$Ec_{,Popovics}$ (ksi)	T/P	*Ec* (ksi)	$Ec_{,Popovics}$ (ksi)	T/P	*Ec* (ksi)	$Ec_{,Popovics}$ (ksi)	T/P
1	6336	4814	1.32	4845	4149	1.17	5062	4559	1.11
2	6808	4971	1.37	6796	4376	1.55	4844	4432	1.09
3	6835	4740	1.44	5680	4308	1.32	5743	4585	1.25
4	7096	4783	1.48	6621	4491	1.47	4934	4457	1.11
5	5908	4580	1.29	5393	4562	1.18	4672	4666	1
Mean			**1.38**	**Mean**		**1.34**	**Mean**		**1.11**
C.O.V.			**5.93%**	**C.O.V.**		**12.90%**	**COV**		**8.09%**

The concrete strength, measured modulus, and calculated strain at peak stress for each core of BTE2, BTE3, and BTE4 are shown in Table B.11. The Popovics relationship for each individual core, like BTE1, matches the measured stress-strain response reasonably well as shown in Fig. B.13, Fig. B.14, and Fig. B.15.

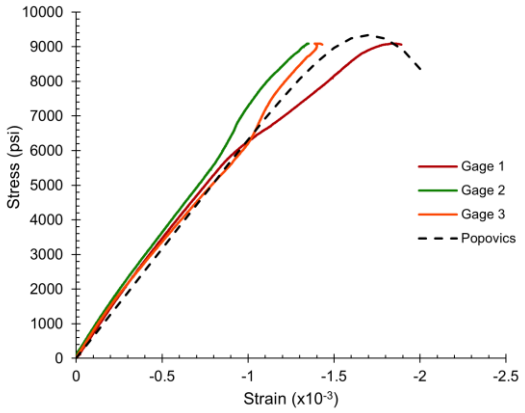

BTE2 Core 1

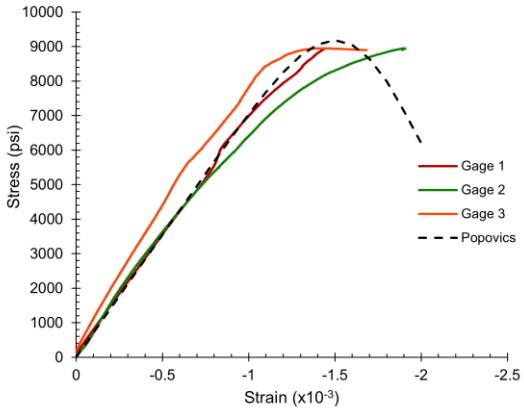

BTE2 Core 4

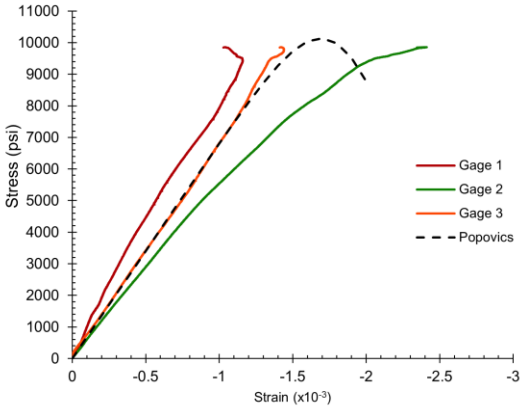

BTE2 Core 2

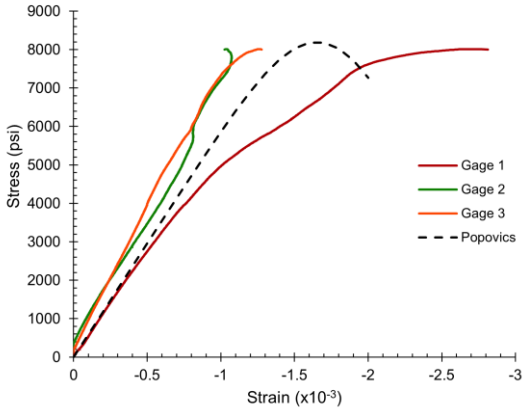

BTE2 Core 5

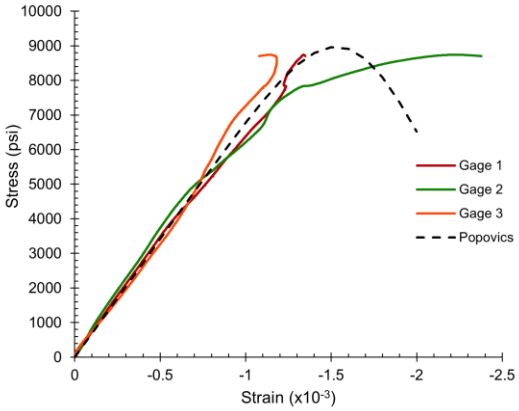

BTE2 Core 3

Figure B.13: BTE2 core stress-strain response.

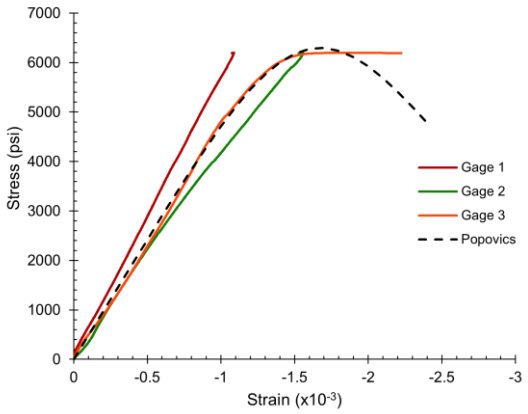

BTE3 Core 1

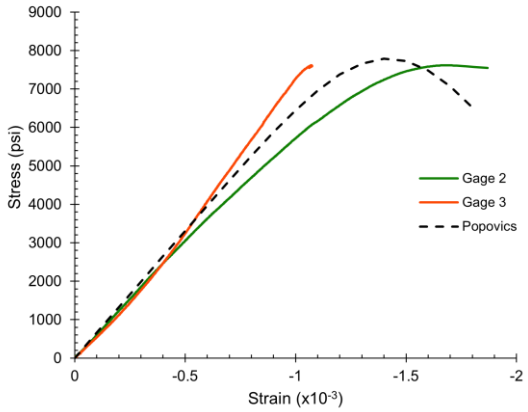

BTE3 Core 4

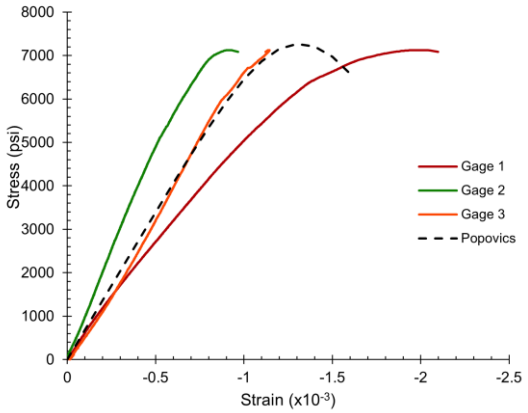

BTE3 Core 2

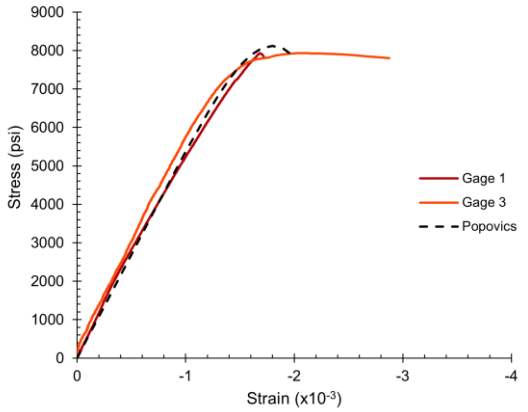

BT3 Core 5

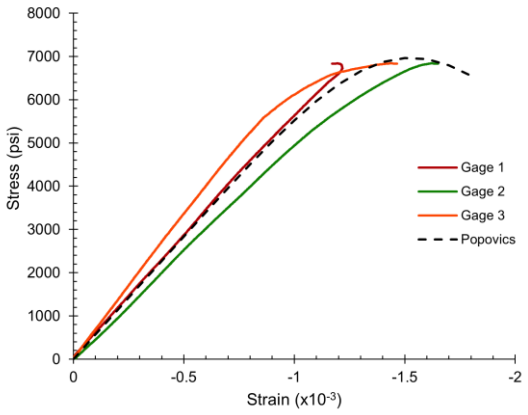

BTE3 Core 3

Figure B.14: BTE3 core stress-strain response

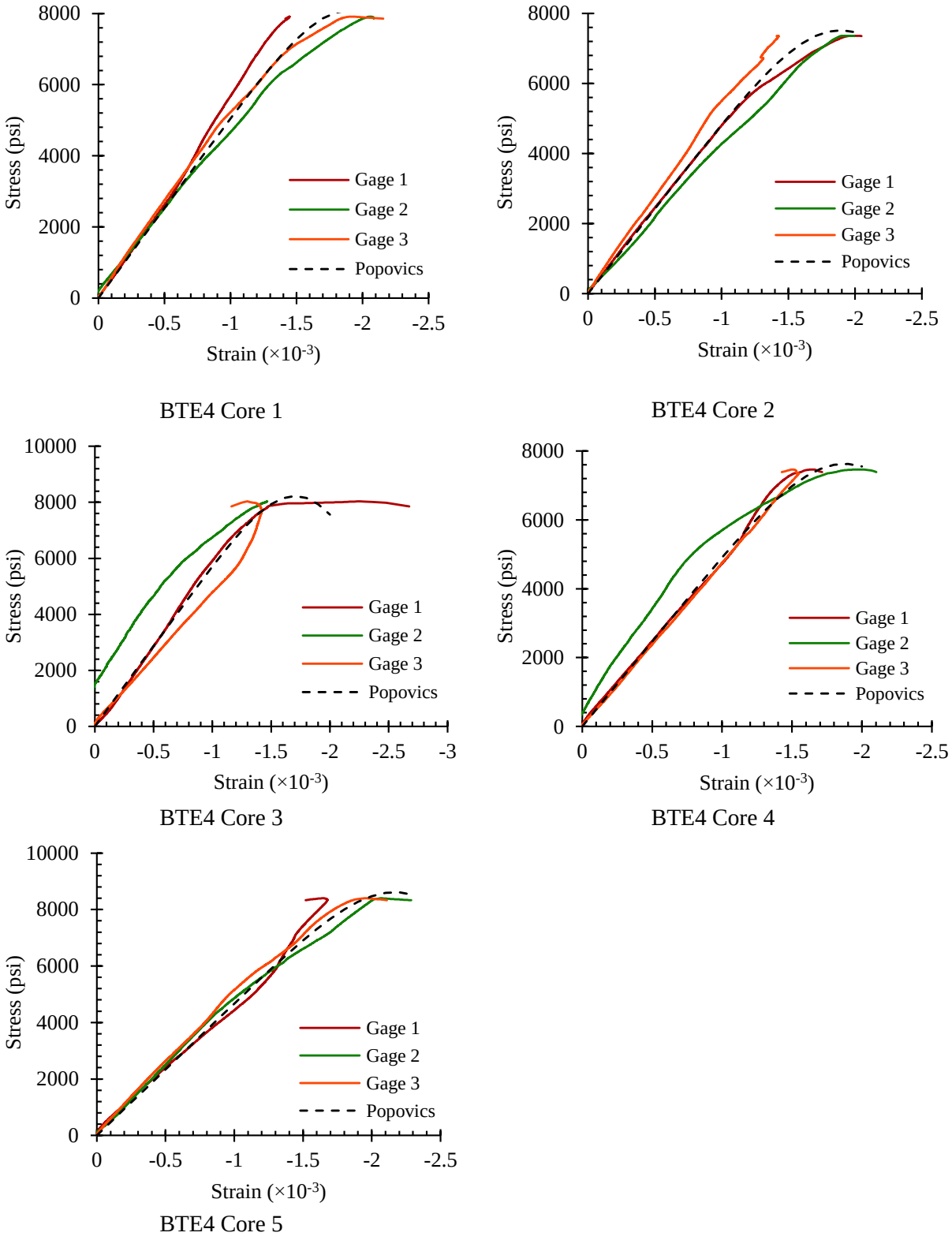

Figure B.15: BTE4 core stress-strain response

A modified Popovics relationship utilizing the average values from Table B.10, analogous to BTE1, was used to model the concrete behavior for each of BTE2, BTE3, and BTE4, as shown in Figure B.16, B.17, and B.18.

Table B.10: Modulus and strain at peak stress for BTE2, BTE3 and BTE4 cores utilizing Popovics relationship.

Girder	BTE2			BTE3			BTE4		
Core	f'_c (psi)	E_c (ksi)	ε'_c ($\times 10^{-3}$)	f'_c (psi)	E_c (ksi)	ε'_c ($\times 10^{-3}$)	f'_c (psi)	E_c (ksi)	ε'_c ($\times 10^{-3}$)
1	9242	6336	1.85	6304	4845	1.84	8054	5062	2.09
2	10019	6808	1.83	7248	6796	1.44	7492	4844	2.07
3	8887	6835	1.67	6957	5680	1.68	8175	5743	1.86
4	9102	7096	1.63	7749	6621	1.55	7599	4934	2.06
5	8145	5908	1.81	8070	5393	1.97	8549	4672	2.37
Mean	**9080**	**6600**	**1.76**	**7270**	**5870**	**1.7**	**7974**	**5051**	**2.09**
C.O.V. (%)	**7.43**	**7.16**	**5.74**	**9.49**	**14.10**	**12.40**	**5.43**	**8.16**	**8.62**
S.D.	**675**	**472**	**0.1**	**689**	**827**	**0.21**	**433**	**412**	**0.18**

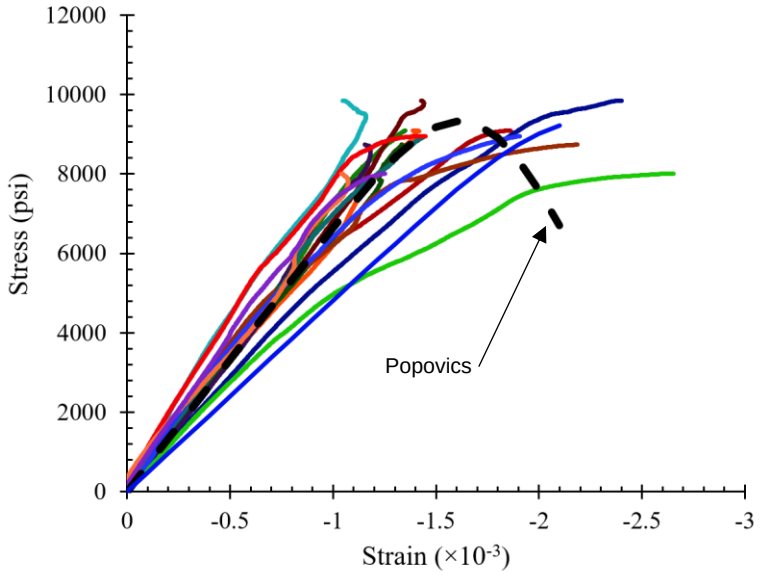

Figure B.16: Average Popovics relationship for BTE2.

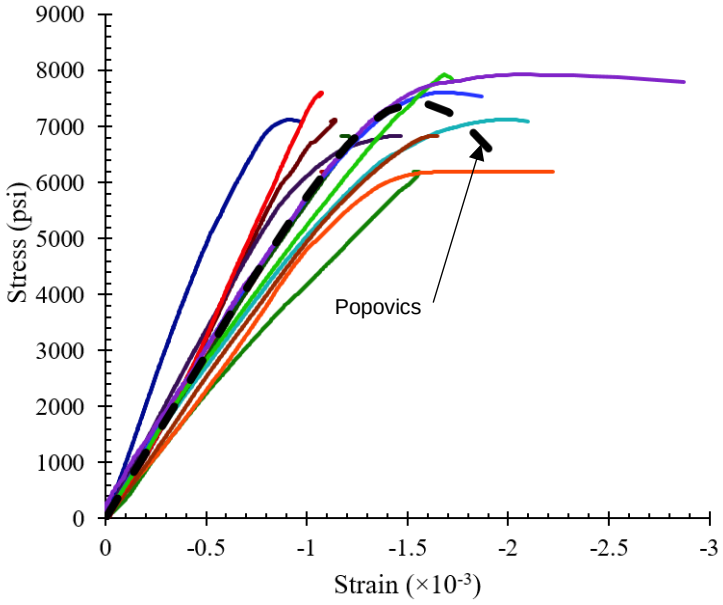

Figure B.17: Average Popovics relationship for BTE3.

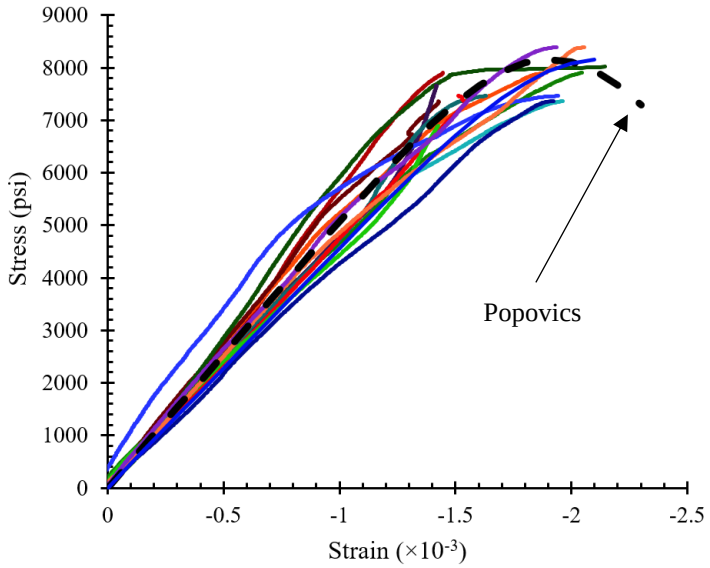

Figure B.18: Average Popovics relationship for BTE4.

As with BTE1, the modified Popovics curves using the average concrete compressive strength, modulus, and strain at peak stress represents well the measured stress-strain response from core testing of BTE2, BTE3, and BTE4. The modified Popovics relationships shown above

for each of the BTE specimens are used to model the concrete in the respective girders in subsequent sections of this report.

B.1.2.2 Deck Concrete

To estimate the compressive strength and modulus of the deck concrete, three deck cores were recovered during deconstruction of the Bonner Bridge, and were tested in a similar procedure to the girder cores. The cores salvaged by the authors but were taken from the deck by the contractor to create lifting locations in the deconstruction process. While it is not known whether the collected samples correspond to the span 142, they provide an estimate of the concrete deck properties. The dimensions of each core were recorded as shown in Table B.11, along with the measured compressive strengths. The mean measured strength of the deck concrete is 5480 psi. The values for correction factors given by ACI 214.4-21 (2021) and the corrected compressive strength of the deck concrete are provided in Table B.11. After applying the correction factors suggested by ACI 214.4-21 (2021) the compressive strength of the concrete deck was 5550 psi.

Table B.11: Dimensions with measured and corrected compressive strengths of deck cores.

Core	Length (in)	D_{top} (in)	D_{mid} (in)	D_{bot} (in)	$D_{average}$ (in)	$L/D_{average}$	$f'_{c,measured}$ (psi)	$F_{l/d}$	F_{dia}	F_{mc}	F_d	f_{core} (psi)	$f'_{c,corrected}$ (psi)
1	6.75	3.7	3.7	3.71	3.71	1.82	5296	1.00	1.00	0.96	1.06	5296	5367
2	6.69	3.7	3.73	3.73	3.73	1.79	6460	0.99	1.00	0.96	1.06	6460	6539
3	7.75	3.7	3.73	3.73	3.73	2.08	4677	1.00	1.00	0.96	1.06	4677	4756
						Mean	**5480**					**Mean**	**5550**
						C.O.V. (%)	**16.53**					**C.O.V. (%)**	**16.32**
						S.D.	**905**					**S.D.**	**906**

The deck concrete cores show higher variability in ultimate strength, but all of these cores contained reinforcing steel which likely created weak planes in the cylinder. Figure B.19 illustrates how the deck cores failed by splitting between the included steel reinforcement.

Figure B.19: Deck core failure around steel reinforcement.

The values for concrete modulus, E_c, and strain at peak stress, ε'_c, as given by the Popovics relationship above for the deck cores can be seen in Table B.12. Utilizing these values and the corrected values for compressive strength of the deck concrete given in Table B.11, a Popovics stress-strain curve can be plotted alongside the measured stress-strain response for each of the three strain gauges on the tested deck cores. The comparison of the Popovics relationship to the measured stress-strain response of the deck can be seen in Figure B.20. Due to a faulty gauge, the data provided by gauge 1 on deck core 3 was ignored. The Popovics stress-strain prediction matches well to the measured stress-strain response of the deck cores.

Table B.12: Modulus and strain at peak stress for the deck cores utilizing Popovics relationship.

Core	f'_c (ksi)	E_c (ksi)	ε'_c (x10^{-3})
1	5367	3911	2.06
2	6539	4215	2.18
3	4756	3736	2.00
Mean	**5550**	**3950**	**2.08**
C.O.V. (%)	**16.3**	**6.14**	**4.26**
S.D.	**906**	**243**	**0.09**

The Popovics relationship accurately represents the individual deck core behavior, so like the girder concrete, a Popovics relationship representing the average behavior for the deck is used for modeling the residual deck on the girders in subsequent sections. Utilizing the mean compressive strength, modulus, and strain at peak stress for the deck concrete as shown in Table B.12, a modified Popovics relationship representing the average behavior for the deck concrete was created. Figure B.21 shows the average Popovics relationship in comparison to the measured stress-strain results from all gauges on each of the tested deck cores. As previously mentioned, due to the reinforcing steel present in the deck cores, the ultimate strength is not as consistent, but the modified Popovics curve represents well the concrete compressive behavior and is likely conservative for the ultimate strength of the deck concrete. A possible reason may be the use of neoprene caps, which would exacerbate any tendency towards splitting modes, due to stress concentrations around the edges, particularly if 3.75″ diameter cylinders are tested in 4″ diameter caps.

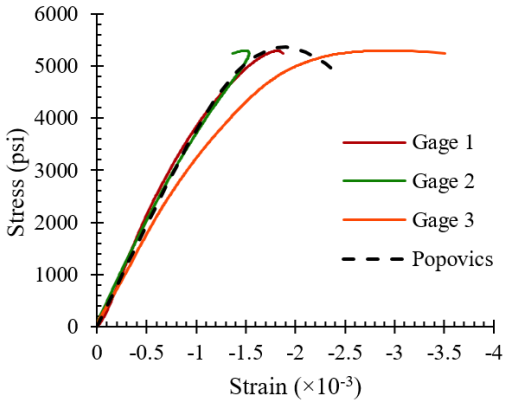

Deck Core 1

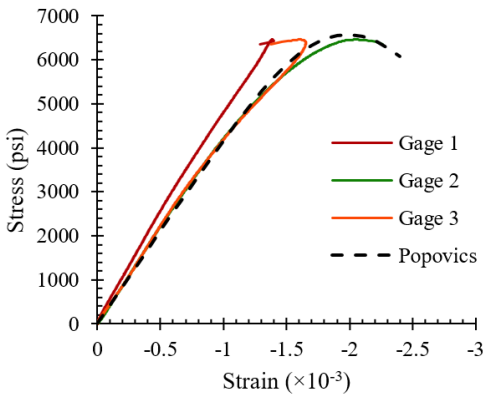

Deck Core 2

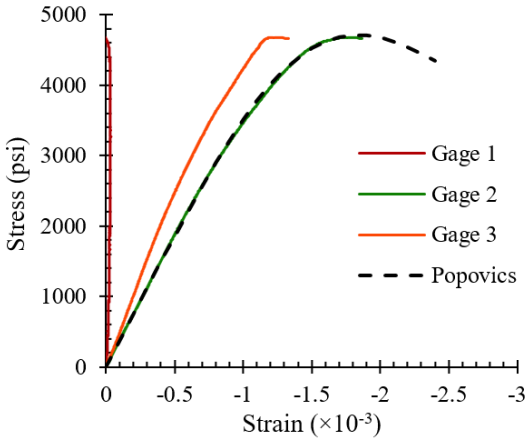

Deck Core 3

Figure B.20: Deck core stress-strain response.

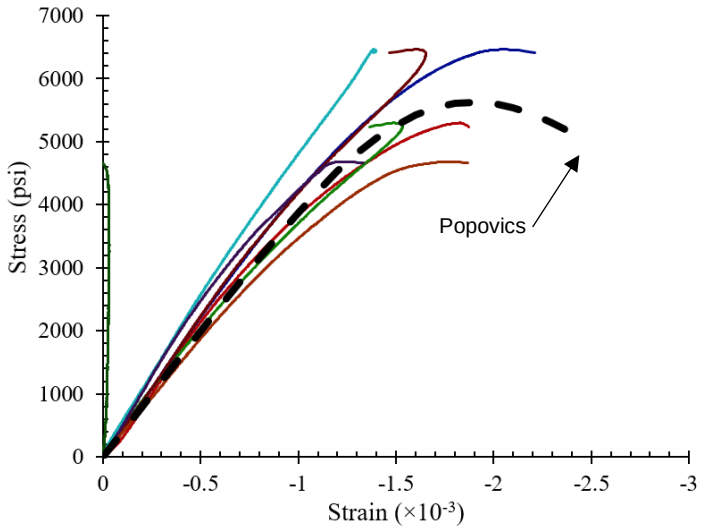

Figure B.21: Average Popovics relationship for deck concrete.

B.2 Instrumentation for Flexure Tests

B.2.1 String Potentiometers

Five string potentiometers were placed underneath the beam at an even spacing of 119 in. to measure the vertical displacement of the beam throughout loading. The string potentiometer layout can be seen in Figure 3.20 and Figure B.22. The string potentiometer displacements would theoretically include the vertical displacement of the strong floor during loading, but the stiffness of the strong floor is far higher than that of the girder and does not contribute significantly to the total measured deflection.

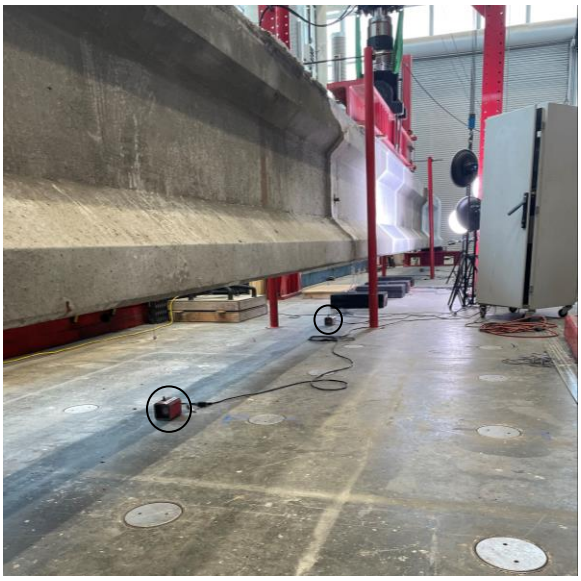

Figure B.22: String potentiometers underneath a girder.

B.2.2 Strain Gauges

To capture the longitudinal strain profile through the section depth, strain gauges with a 60 mm (2.36 in.) gage length were placed at midspan. These gauges were located 2 in. and 43 in. up from the bottom of each girder on the east side face, and are referred to as Set 1. The gauges were placed over a thin epoxy patch applied to provide a smooth bonding surface over the concrete. A second set of gauges, set 2, was placed 5 in. to the North of the midspan gauges to provide redundancy in case of a midspan gauge failure. These strain gauges can be seen in Figure B.23.

Figure B.23: Strain gauges at the top (left) and bottom (right) of a girder.

B.2.3 Optical LED Displacemen Measurements

The Optotrak Certus HD system uses cameras to track infrared light emitting diode markers (LEDs) on the girder surface to capture the 3D position the markers throughout testing. During testing, data were collected continuously using a single camera at 10 Hz. The LED markers were placed in a 7x7 grid with 8 in. center to center horizontal spacing and a variable vertical spacing to fit the markers on the flat surfaces of the girder elevation. In total, 49 LED markers were placed on the beam. The LED grid dimensions can be seen in the inset of Figure B.23 above, and the complete grid prior to testing can be seen in Figure B.24.

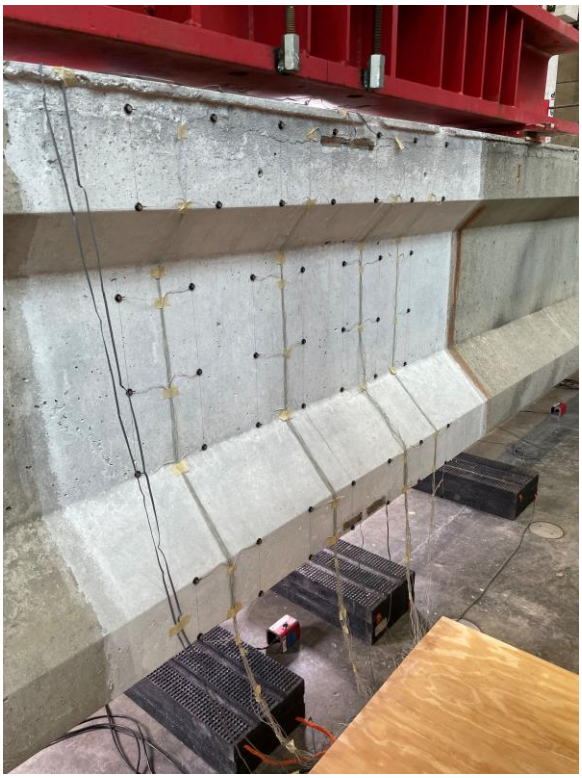

Figure B.24: Optical LED grid at midspan.

B.2.4 Digital Image Correlation Data

DIC was used to measure the three dimensional displacement field of a speckled surface throughout loading. For the BTE series of tests, images from the digital cameras were taken at 2 Hz. Black speckles applied over a thin layer of white paint provide contrast for the system. For the BTE series of tests, the speckles were approximately 0.05 in. in diameter and were applied using

both a speckle roller and a felt tip marker. Before testing, the system of two cameras was calibrated the day before and the morning of testing to ensure error was minimized and the desired field of view was captured. The speckle pattern and camera setup can be seen in Figure B.25 below.

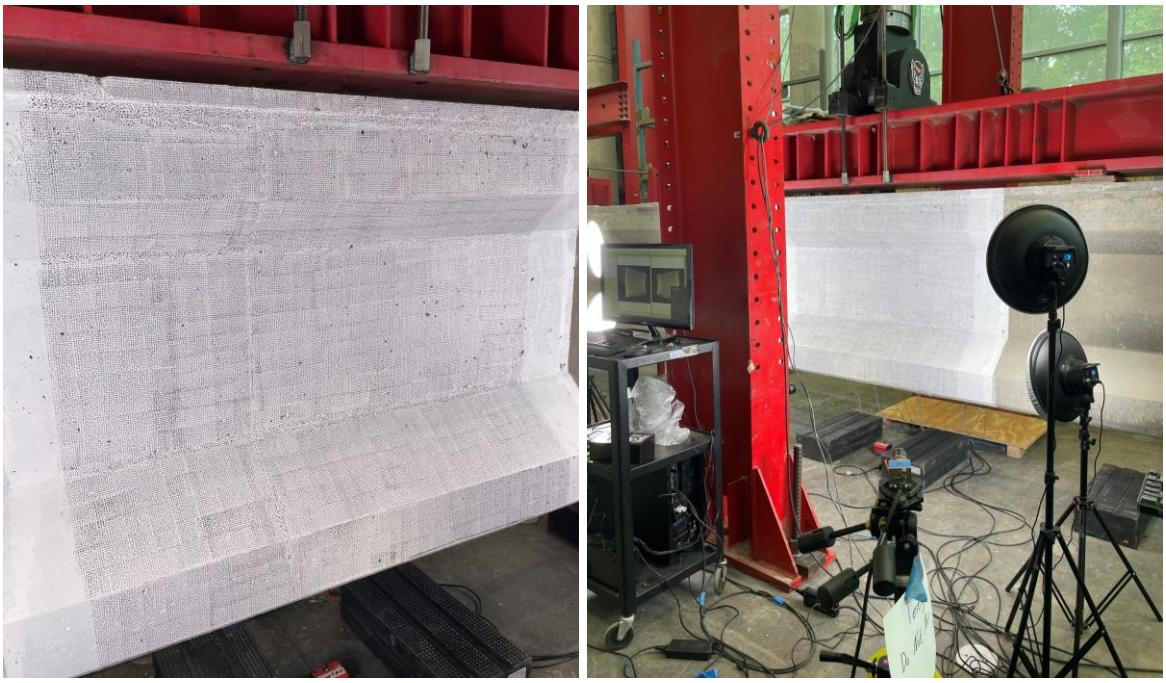

Figure B.25: DIC speckle pattern and camera setup.

The DIC data give the full three-dimensional (3D) displacement field of the measured surface. The displacement field can be used to determine the kinematic response of the beam, strains in the uncracked regions, and average strains over larger areas. Additionally, virtual extensometer measurements can be obtained between any of the captured points. The data are used to assess cracking of the specimen from crack onset through failure. The DIC data for each test are presented in Chapter 4 of this report. Some of the extensometers used for post-processing can be seen in Figure B.26 below.

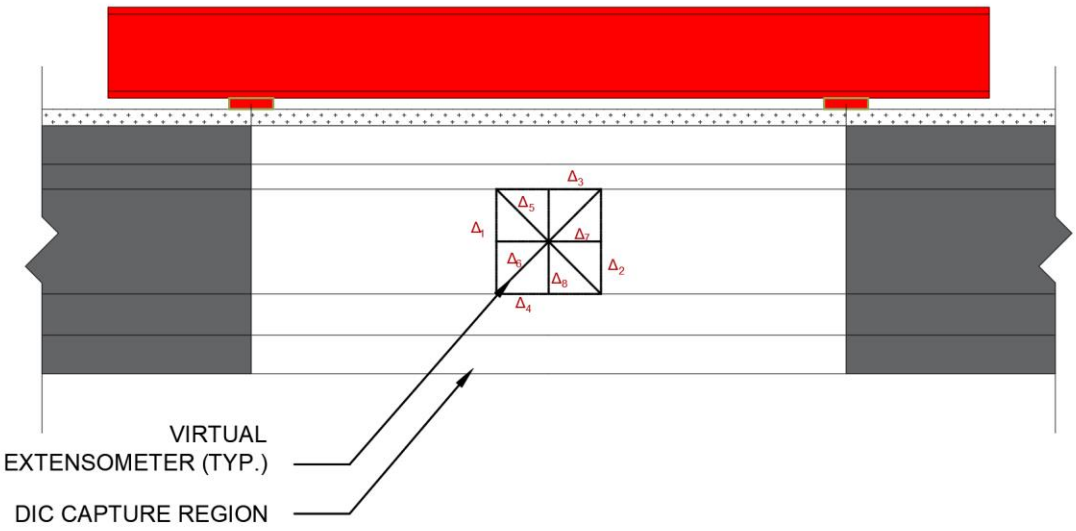

Figure B.26: DIC virtual extensometers.

B.3 Loading Protocol

The flexural testing of the BTE series occurred in two stages: load cycles near cracking and monotonic loading to failure. The load cycles are used to determine the cracking characteristics and prestress losses of the girder, and the monotonic loading to failure was used to determine the ultimate capacity of the girders. The first stage of flexural testing involves three load-unload cycles performed at four load levels. The load cycles was performed in force control at a loading rate of 1 kip per second. To maintain a constant load rate for each cycle, a linear ramp function was used. For BTE1 the nominal load levels were: 80, 100, 125, and 150 kips of applied actuator load. These load levels were selected to apply moments just below and just above the expected first cracking moment for the girder, thus carefully being able to capture first cracking. Cycles after first cracking were applied so that loads required to reopen the cracks could be measured. The moment at first cracking is higher than the moment required to overcome the compressive stress from prestressing because of the tensile strength of the concrete. The moment to re-open existing cracks, the crack reopening moment, is not influenced by the tensile strength of the concrete and corresponds to the load required to overcome the force of prestressing. This crack reopening moment can then be used to determine the prestress loss from elastic equations for the stresses in the section. Similar approaches have been conducted in the literature with success (Azizinamini *et al.*, 1996; Garber et al., 2015; Halsey and Miller, 1996; Higgs et al., 2015). Between cycles, the load was reduced to a

minimum of 5 kips of applied actuator load, rather than zero, to ensure the spreader beam did not lift off the load plates and shift. For BTE2, BTE3 and BTE4, the spacing of the loading plates reduced from 9 ft. to 7 ft. apart. Thus, the levels of applied load were reduced to keep the levels of applied moments the same between all tests. Therefore, the cyclic load levels for BTE2, BTE3, and BTE4 changed to: 75, 95, 115, and 130 kips of actuator load.

After unloading from cycling near cracking, the actuator was switched from force control to displacement control for the monotonic loading phase of each test. During this transition, at least 5 kips of actuator load was maintained to keep the test frame aligned for the remainder of the test. The displacement rate was ½ in. per minute for the monotonic loading. During the test, the loading was stopped at predetermined loads so that the girders could be approached, photographs taken, and cracks marked and measured with a crack comparator. These pauses in loading are referred to as load stages, and at each load stage, the applied load was reduced by at least 10% to ensure the specimen was safe to approach. Since the specimens were predicted to have sudden failures due to concrete crushing, the load stages were stopped at relatively low loads for safety. Monotonic loading of BTE3 and BTE4 was stopped at approximately 95% of the lowest peak moment attained from BTE1 and BTE2 to provide the opportunity for shear testing of the BTE3 and BTE4 girder end regions.

APPENDIX C – ADDITIONAL EXPERIMENTAL OBSERVATIONS

Appendix C provides additional details of the experimental results. It discusses results from the flexural tests of the BTE1, BTE2, BTE3 and BTE4 specimens.

C.1 BTE1 Flexural Testing

The flexural testing of BTE1 began on July 2nd, 2021with load cycles at low load levels to determine initial cracking and crack reopening loads. The load levels and also the corresponding shear refer to the actuator force and this force labelling convention remains consistent in the discussion below. The applied moment due to actuator load does not include moment due to self-weight but it exists throughout the loading period. Unless otherwise specified, applied moment always refers to the moment due to actuator load throughout the report. Three load cycles are conducted at each load level. The first load level reached 80 kips of actuator load corresponding to 40 kips of applied shear and an applied moment of approximately 1010 k-ft. As previously mentioned, the trough of the linear ramp cycles was 5 kips of actuator load to ensure no movement in the test apparatus occurred from spreader beam liftoff. During the three cycles up to 80 kips there was no audible or visible cracking on the girder. The next load level reached 100 kips of actuator load corresponding to 50 kips of applied shear and an applied moment of approximately 1260 k-ft. As with the 80 kip load level, there was no audible or visible change to the beam during the 100 kip load level cycles. From 100 kips, the load level increased to 125 kips of actuator load corresponding to 62.5 kips of applied shear and an applied moment of 1580 k-ft. During the three cycles to 125 kips, flexural cracking on the beam was observed. Additionally, flexure-shear cracking became visible just outside of the loading plates during this set of cycles. Finally, the load level reached 150 kips of actuator load corresponding to 75 kips of applied shear and an applied moment of 1900 k-ft. During the first loading up to 150 kips the more corroded of the two patched strands mentioned in the condition assessment of BTE1 audibly ruptured around 140 kips of actuator load. The rupture of the strand corresponded to further flexural crack opening at the strand rupture location. During the cycles up to 150 kips, cracks were observed to open and close.

After the load cycles at four load levels, the girder was unloaded and then again monotonically loaded to failure with several load stages. The first load stage was taken at 150 kips

of actuator load. While conducting load stages, it was noted that the load frame shifted slightly during the earlier phase when load cycles were conducted. After the first load stage, it was determined that the testing should be stopped and the test frame should be re-centered above the specimen and post-tensioned to the strong floor. To further reduce eccentricity, the decision was made to replace the fiber board under the load plates with grout so the spreader beam would be level. Grout was used beneath the load plates for all subsequent tests.

After the girder was centered underneath the actuator, the test frame was post-tensioned to the strong floor with approximately 350 kips of force, the monotonic testing of the girder resumed on July 8th, 2021. The DIC system had to be moved between the two sets of tests which required recalibration of the system, thus the strains measured after unloading from the first test are not included in the second test. However, the residual strains from unloading the first test are within the noise threshold for the DIC system and do not significantly affect the results. While the residual strains are negligible, the small permanent deflection of the beam measured by the string potentiometers in the cyclic testing have been added to the deflection measurements for the second test for consistency. The first load stage on the second day of testing was again taken at150 kips of actuator load. The crack pattern and widths were checked for any change from the observations at the same load stage from the previous day. The crack widths and pattern did not change between the first and second day of loading for this load stage. Monotonic loading of the specimen was resumed until the next load stage at 175 kips. While loading to the 175 kip load stage, additional flexural cracks opened and significant flexure-shear cracks could be seen on either side the loading plates outside the flexural region. The load was reduced significantly before approaching the specimen for this load stage. Cracks widened and extended from the first load stage. After the second load stage, it was determined that further load stages should not be conducted for safety reasons. A summary of the cracks marked and measured at the load stages is provided in Figure C.1.

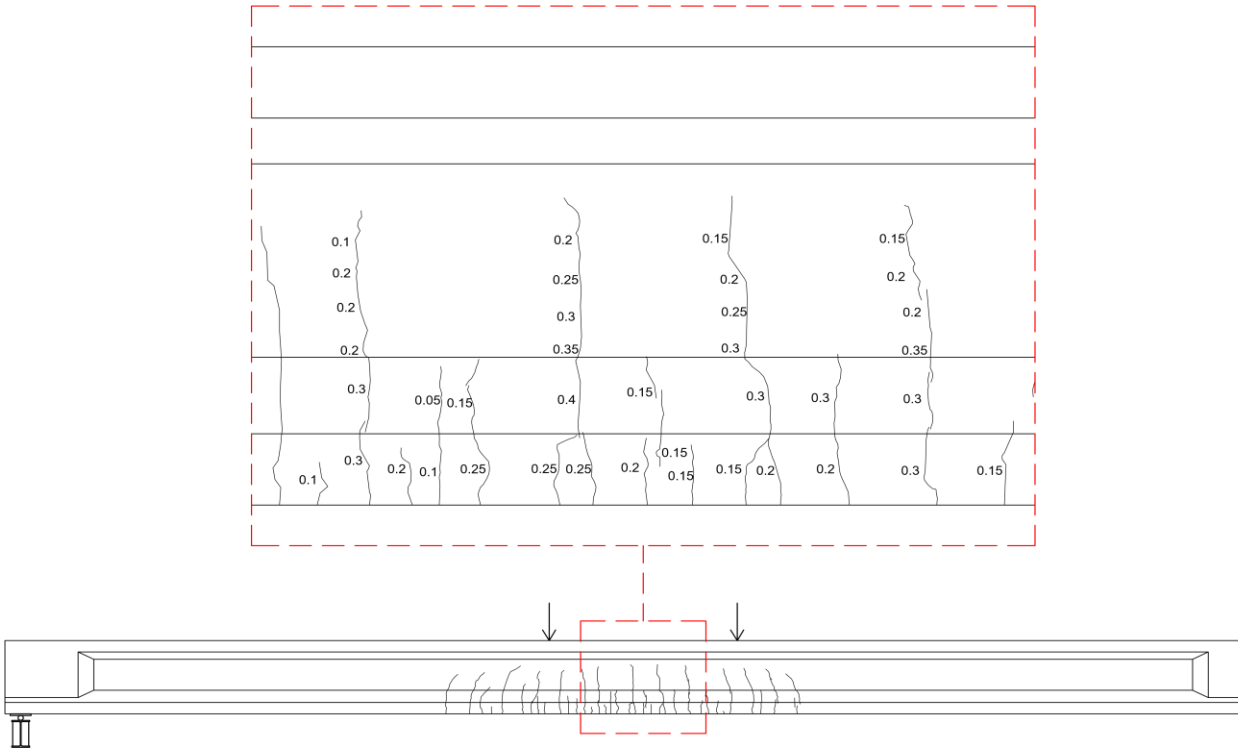

BTE1 Load Stage 1

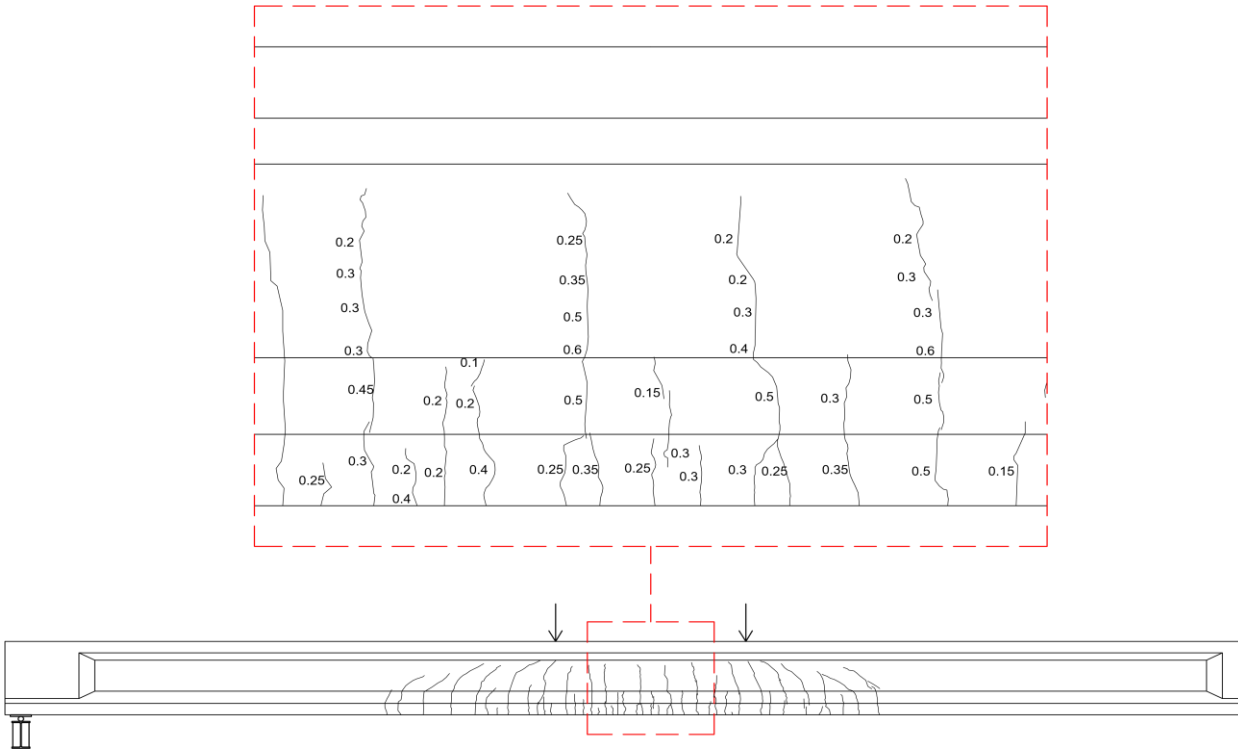

BTE1 Load Stage 2

Figure C.1: BTE1 load stage crack diagrams (Crack widths are in mm).

The specimen was monotonically loaded to failure which occurred at 201 kips of actuator load. The corresponding applied peak moment was 2550 k-ft. The specimen failed by crushing of the top flange due to flexural compression. After crushing of the top flange, the girder broke into two pieces by separating along one of the flexure-shear cracks extending towards the loading plate. The separation of the girder along the flexure-shear crack is a post-peak phenomenon, and failure of the girder was caused by crushing of the top flange, not flexure-shear cracking. The failed specimen can be seen in Figure C.2.

Figure C.2: Photo of BTE1 after failure.

The load versus midspan displacement curves for the load cycles and monotonic loading to failure can be seen in Figure C.3. The deflection at peak load for the girder was 7.85 in. at the onset of crushing in the compression flange. Additionally, the girder displacement at each of the five string potentiometers along the span for the monotonic loading can be seen in Figure C.4. The string potentiometers showed symmetrical displacement of the girder.

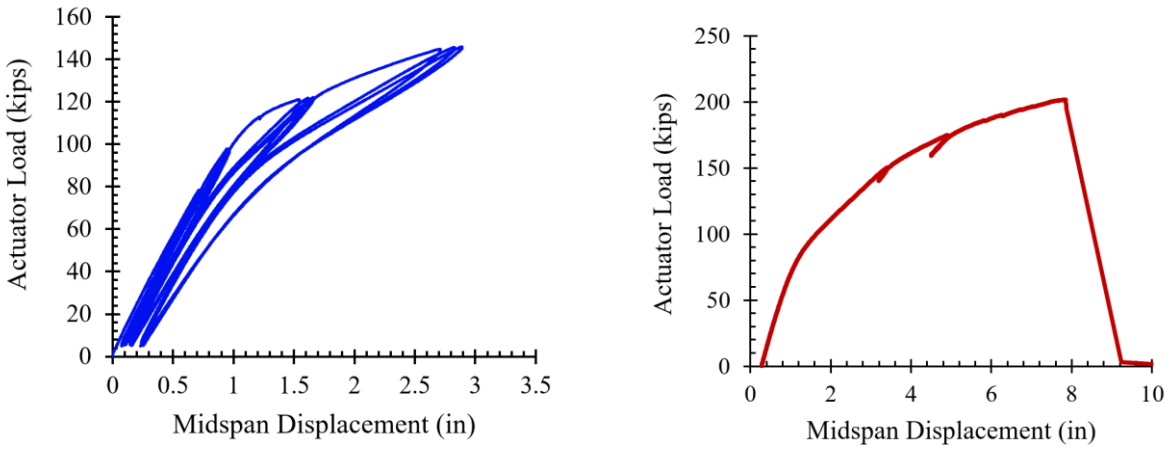

Load Cycles Monotonic Loading

Figure C.3: BTE1 load versus midspan displacement for load cycles (day 1) and monotonic (day 2) loading.

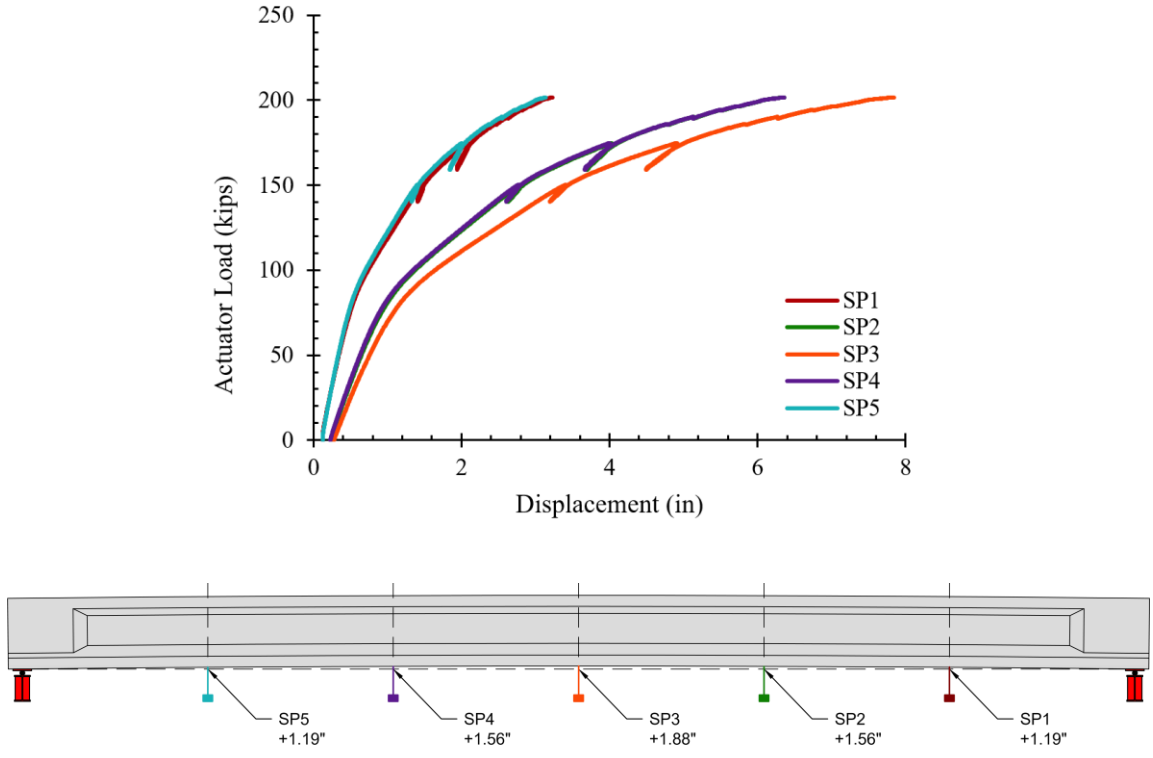

Initial Displacement

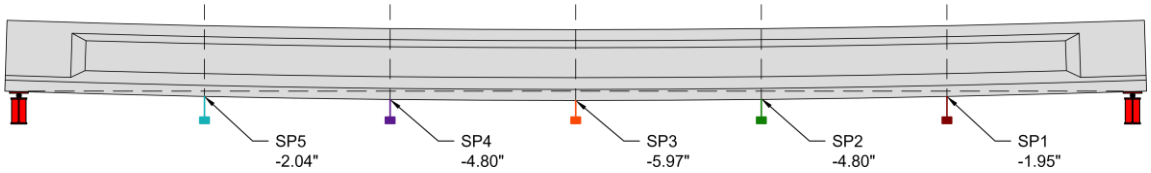

Figure C.4: BTE1 displacement along the length.

In addition to load deflection data, the strains through the depth of the member were determined using both strain gauges and DIC data. The strain gauges show the strains though the depth during the elastic uncracked portion of the loading, but they are subject to damage after cracks propagate underneath the strain gauge. The strain gauges are also used to corroborate the cracking loads of the girder at the gauge location. Figure C.5 shows the top and bottom strains from each set of gauges, set 1 and set 2 (see section A2.2.2) throughout the load cycles.

As can be seen in Figure 4.5 above, the top strains remain elastic throughout the load cycles, and the bottom gauges indicate cracking of the girder. To compare DIC results to the strain gauge data, points were used at the same location as the first set of strain gauges corresponding to the girder's midspan. The results from the DIC points can be seen in Figure C.6.

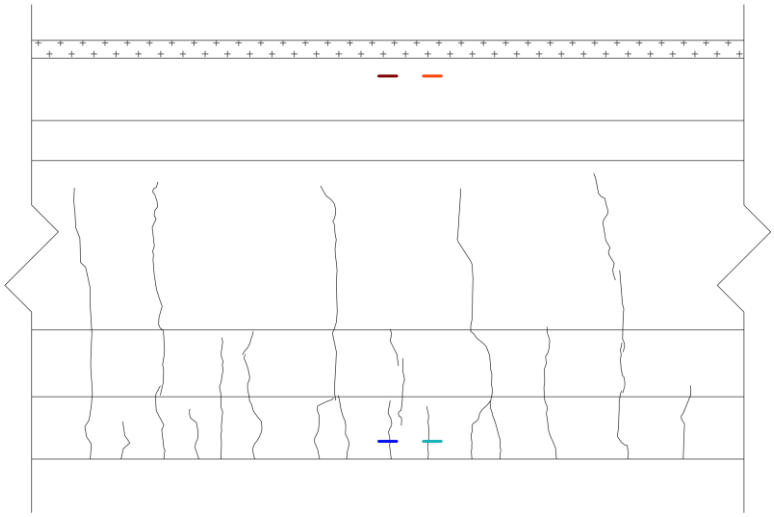

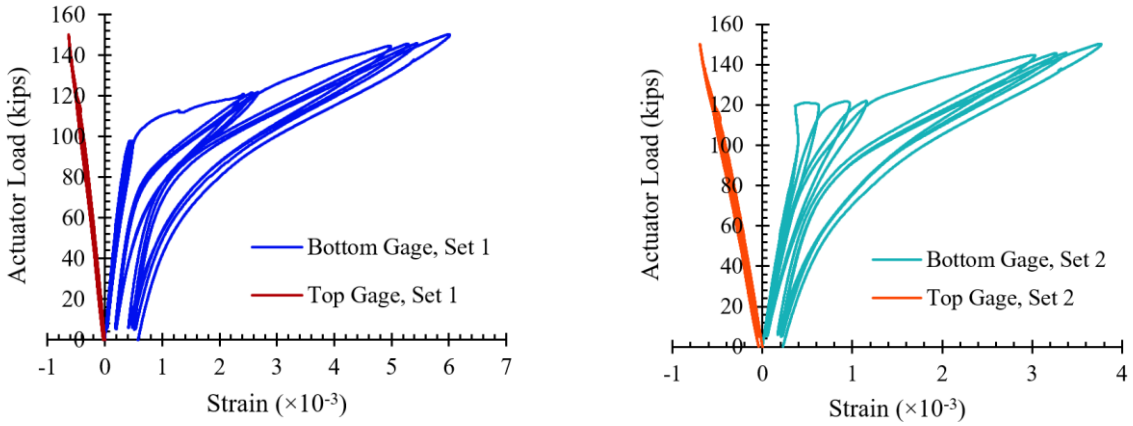

Figure C.5: BTE1 strain gauge data through three load cycles at each load level. Bottom gauge, set 1 (blue), top gauge, set 1 (red), bottom gauge, set 2 (teal), top gauge, set 2 (orange).

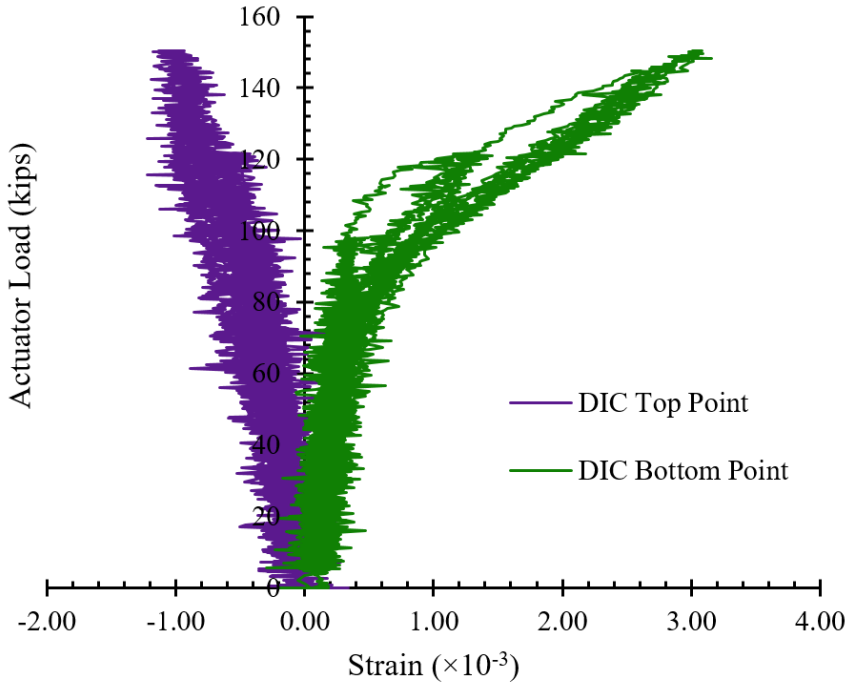

Figure C.6: BTE1 DIC point strains at girder midspan through load cycles at each load level.

As with the strain gauges, DIC shows that the top strains remain elastic throughout the load cycles. Bottom strains, however, remain elastic only up to the point of cracking. Cracking corresponds to the change in stiffness observed in Figure C.6. Strain from the DIC point near the

bottom flange is compared to the average bottom strain gauge behavior for the cracking cycle in Figure C.7. The response agrees reasonably well. The discrepancies arise from differences in gauge lengths of the measurements. A more detailed discussion will occur in subsequent sections.

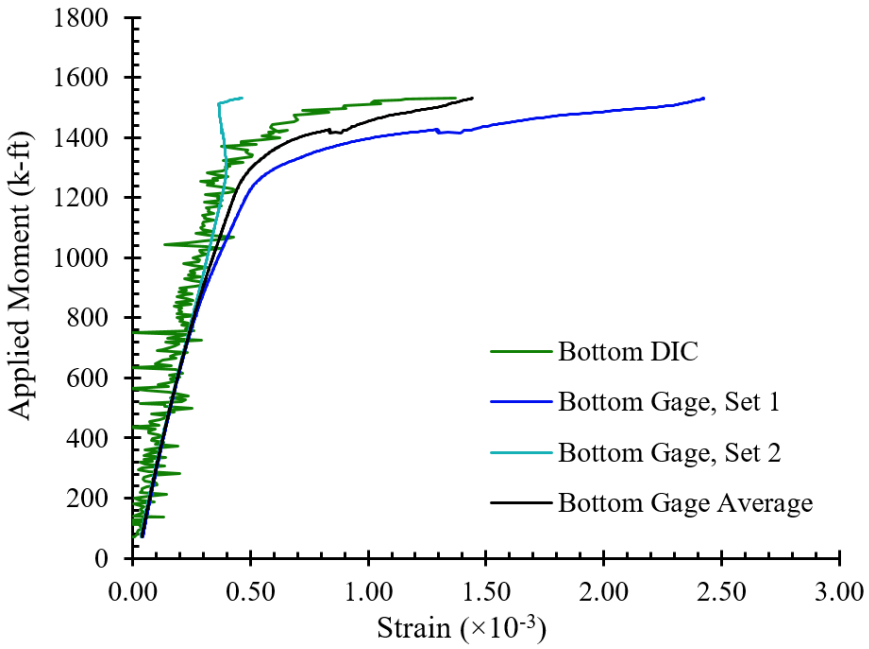

Figure C.7: BTE1 strain comparison between DIC and strain gauge for first cycle up to 125 kips actuator load.

To further understand strains through the depth during loading, horizontal extensometers were used in DIC post-processing at four locations through the depth near midspan. These extensometers provide longitudinal strains through the depth for each image taken during the test. The strains through the depth can be seen for each of the four load steps during load cycles, the two load stages of monotonic loading, and the ultimate load for the girder in Figure C.8.

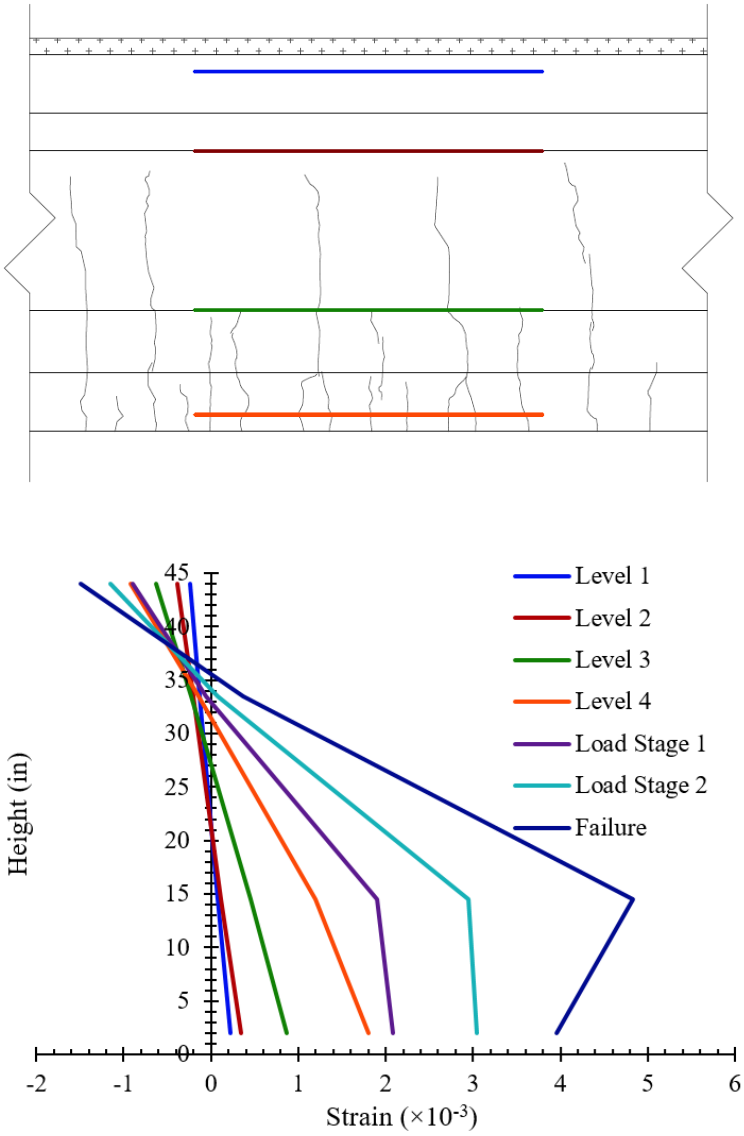

Figure C.8: BTE1 DIC horizontal extensometer strain profile.

The longitudinal strains from the DIC extensometers initially indicate a linear distribution of strains through the depth. Above 125 kips of actuator load, however, the strains do not remain linear from the top to the bottom of the specimen during loading. The strains remain linear from the top of the section to a height of approximately 15 in., but the bottom of the section does not show linearly increasing strain. The discontinuity in strain is likely due to the debonding of the

surface concrete at very high tensile strains, and this observation is consistent with data collected by other researchers (Halsey and Miller, 1996).

Virtual extensometers in DIC post-processing were also used to determine the elongation across cracks during the load cycles to determine when the initial crack first opened and closed. Before cracking of the specimen, the virtual extensometer reads elastic elongation of the girder, but at cracking the extensometer elongation jumps suddenly. Upon unloading, the extensometer elongation decreases rapidly until the crack is closed. Then, the slope of the applied moment-extensometer elongation curve becomes almost the same as the uncracked section. Note that the virtual extensometer was placed over the first crack that occurred on the girder, and the location and elongation of the extensometer can be seen in Figure C.9. The extensometer elongation is a five point moving average of the DIC data.

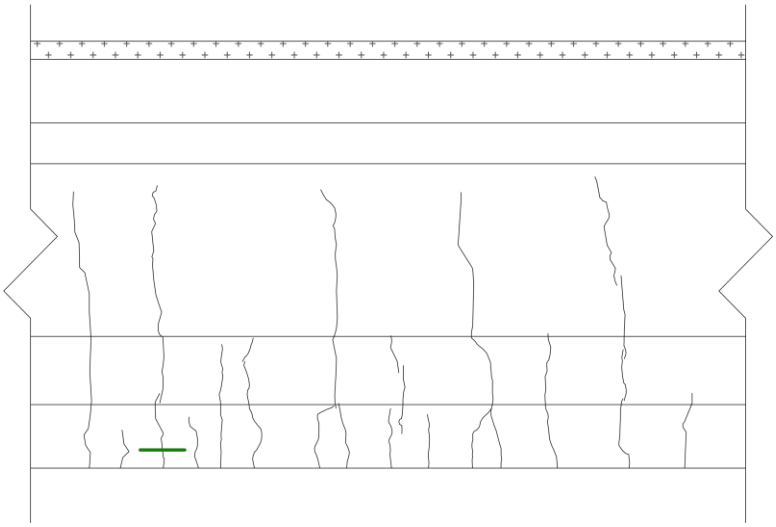

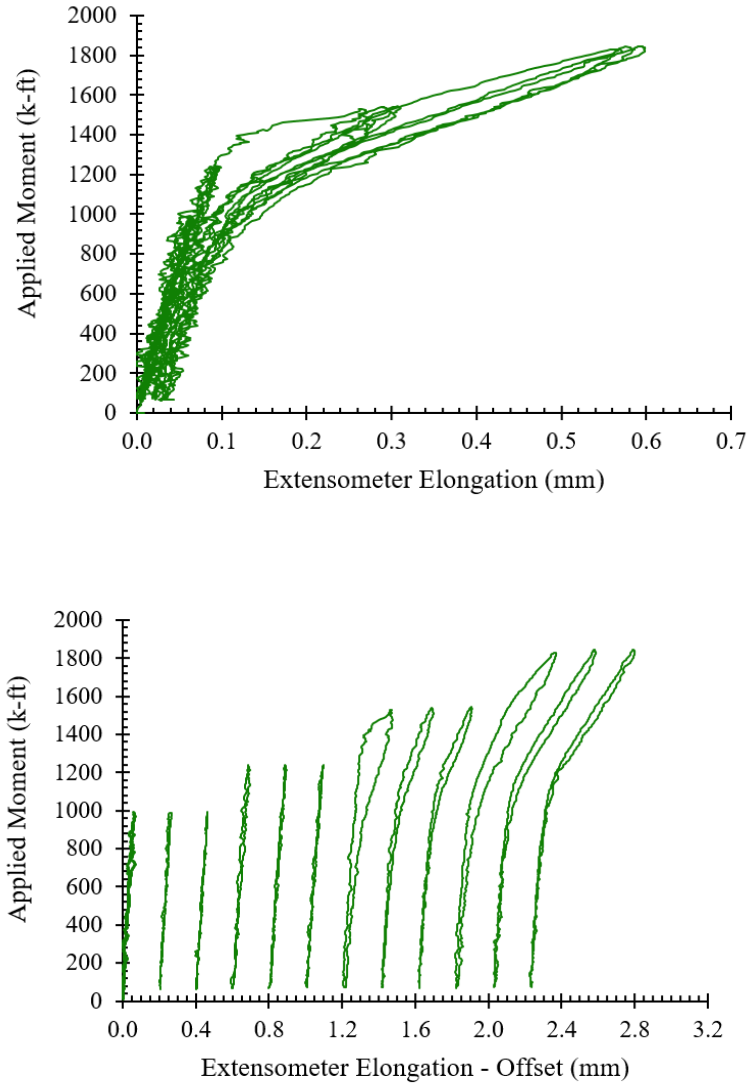

Figure C.9: BTE1 first crack virtual extensometer.

Extensometer elongation was offset after each load cycle and plotted against applied moment as shown in Figure C.9. The three cycles for load steps of 80 and 100 kips of actuator load are only producing elastic strains in the girder because the lines are a constant slope. The first cycle up to 125 kips of actuator load is the first instance of cracking in the girder because there is a sudden increase in the extensometer's elongation. After cracking, the extensometer shows higher elongations for a given moment because the cracks take a significant force to close after opening (Ruggiero, 2015). Figure C.10 highlights on the first cycle up to 125 kips of actuator load, and the

transition from uncracked extensometer elongation to cracked elongation can be seen. However, the exact point of stiffness change requires careful investigation.

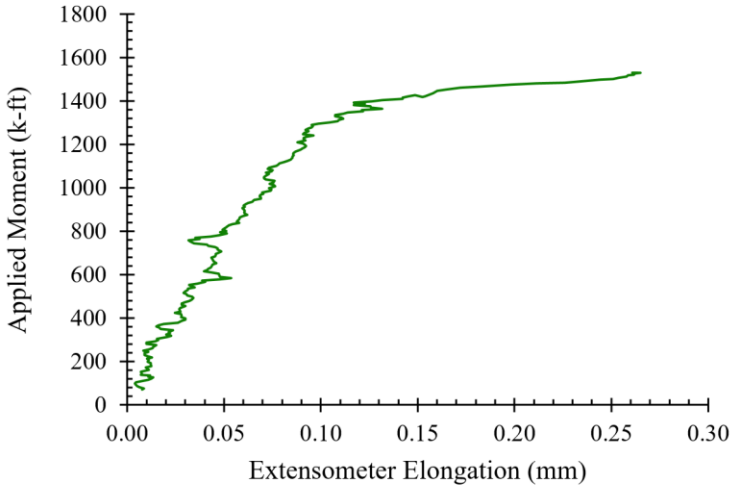

Figure C.10: BTE1 applied moment versus extensometer elongation showing stiffness change due to cracking.

To determine first cracking, DIC strain maps (principal strain ε_1) at the instant when crack first appeared was captured and a pair of extensometers were placed one at the crack and one right beside it to observe how the principal strain and extensometer elongation changes as load increases. This was done to compare how the behavior of extensometer elongation changes with and without a crack. Virtual extensometer E0 was placed at the crack and E1 at the same height right beside the crack, parallel to E0 as shown in Figure C.11. Both the extensometers are at a distance of 1.75 in from the bottom of girder.

The E0 and E1 extensometer elongation was plotted against the applied load. The extensometer placed between cracks provides measurements of the elastic elongation throughout the loading. The extensometer placed over the crack provides detailed crack opening and closing data. At a load of 102.3 kips, the extensometer placed at the location of first crack show an abrupt change in elongation (Figure C.12). This sudden change in elongation occurs when the crack forms. Both the extensometer elongations agree up to first cracking. The point at which they

diverge can be used to determine when first cracking occurs more accurately. The DIC strain map at this particular instant shows very high strains around the extensometer indicating either the crack has formed or is on the verge of propagating.

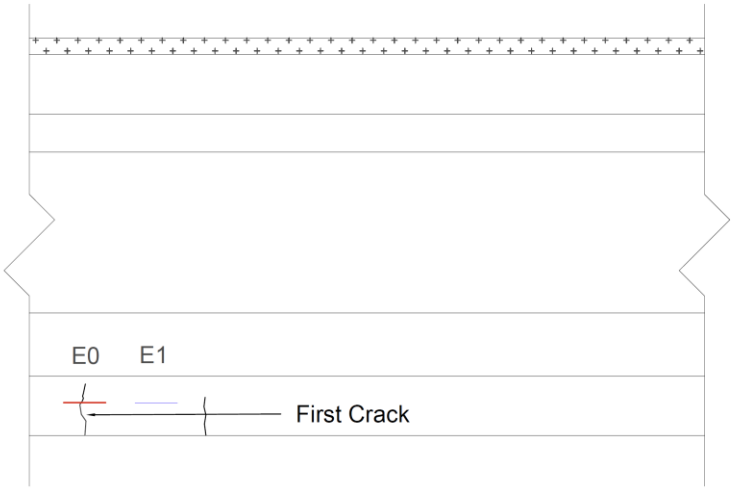

Figure C.11: Location of extensometers on first crack and between cracks.

To further verify the load at which first cracking occurs, a 20 point moving average of the extensometer elongation versus load was plotted against the midspan displacement. The filtering approach helps make clear when the section transitions from uncracked to a cracked section. Figure C.12 shows the average slope starts to increase at an applied moment of 1295 k-ft (or load of 102.3 kips) corresponding to a displacement of 24.7 mm. The strain map at the instant corresponding to this moment show very high strains and maps the shape of a crack. The strain diagrams indicate the crack has already initiated and the tip of crack has reached the extensometer E0 (Figure C.13) at an applied moment of 1295 k-ft. The crack only becomes obvious at an applied moment of 1350 k-ft where it has extended past the extensometer into the depth of girder. As the crack progresses further into the girder, changes in extensometer elongation becomes more rapid and noisier and it becomes difficult to identify a cracking point. Thus, the cracking moment is 1295 k-ft for BTE1. The DIC strain map is a useful tool to see the location and depth of cracks, and a two-fold approach where changes in slopes of extensometer elongation versus load is monitored simultaneously with the DIC strain maps can be used to pinpoint where the crack first appeared and the length of crack at that particular instant.

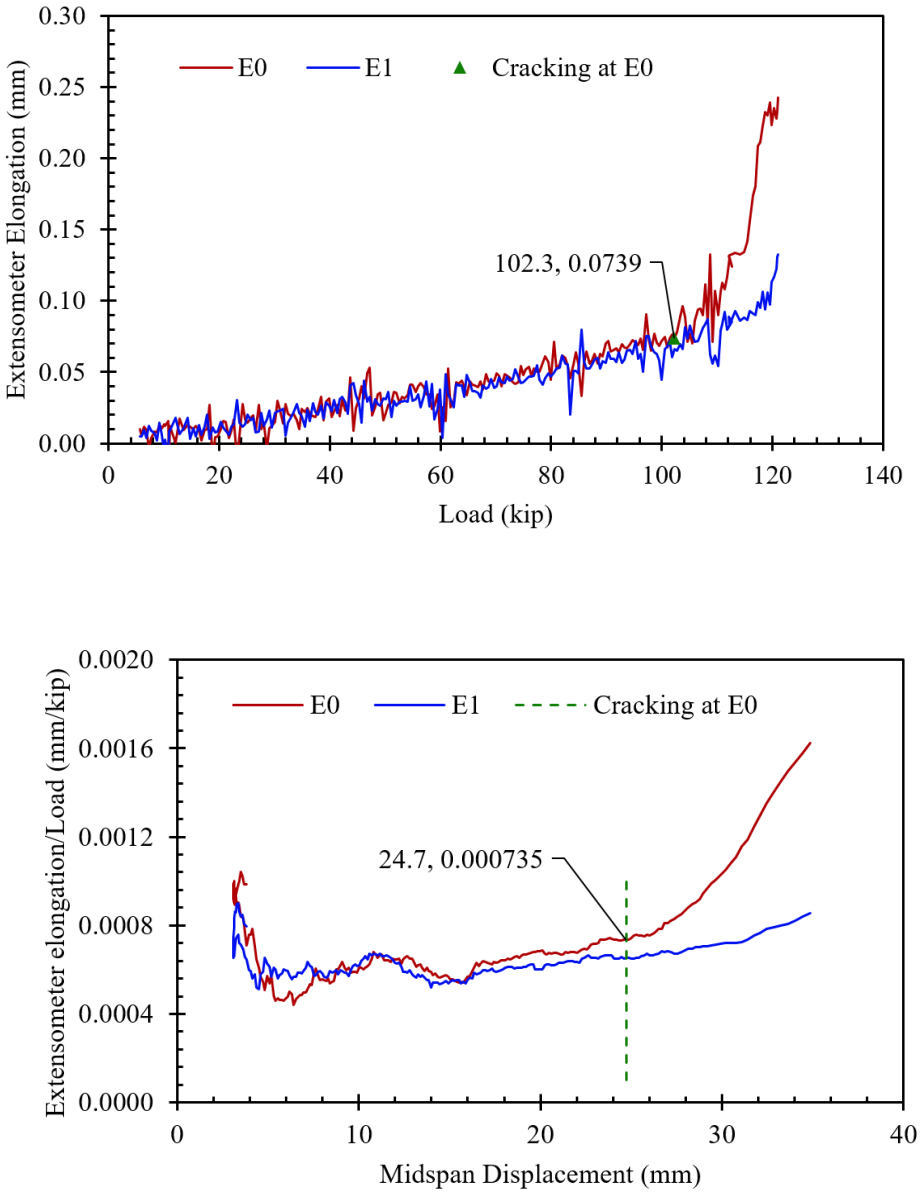

Figure C.12: Identifying first instance of cracking of BTE1.

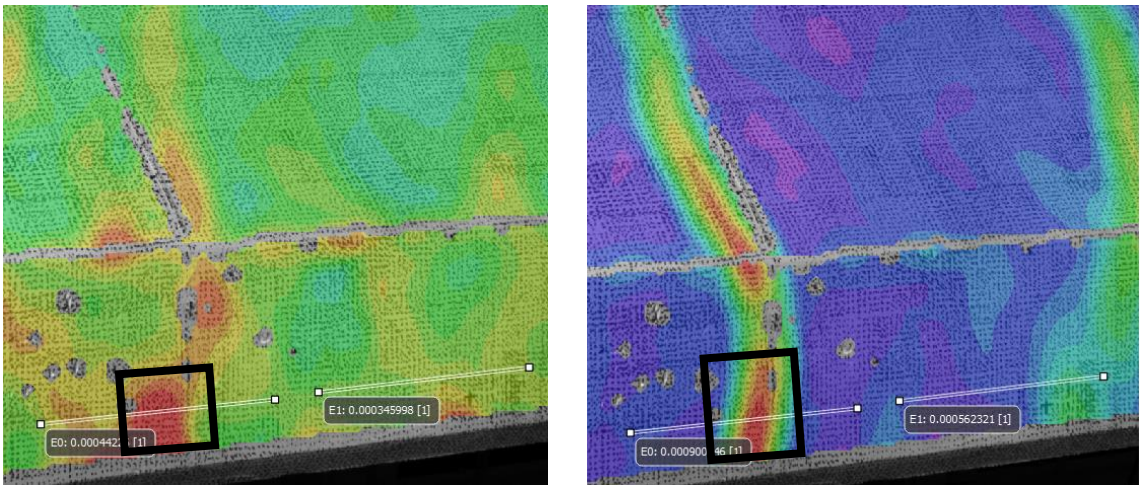

(a) (b)

Figure C.13: Principal Strain Map, ε_1 (a) At Cracking Moment of 1295 k-ft (b) When crack is obvious at 1350 k-ft.

The crack reopening moment can be found using the same procedure as the cracking moment (Figure C.14). To avoid influence from accumulated damage from cyclic loading, the first load cycle after the crack has appeared is used to determine the crack reopening moment. Extensometer elongation is plotted against load for the two extensometers placed on crack and between cracks. The point of divergence marks the crack reopening. A filtering approach which plots 20 point moving average of stiffness of extensometer elongation/load against midspan displacement is used to estimate the crack reopening moment accurately. The crack-reopening moment correspond to the instant when the tip of crack just touches an extensometer after it reopens in the DIC strain map (Figure C.15). The crack reopening moment was found to be 905 k-ft for BTE1.

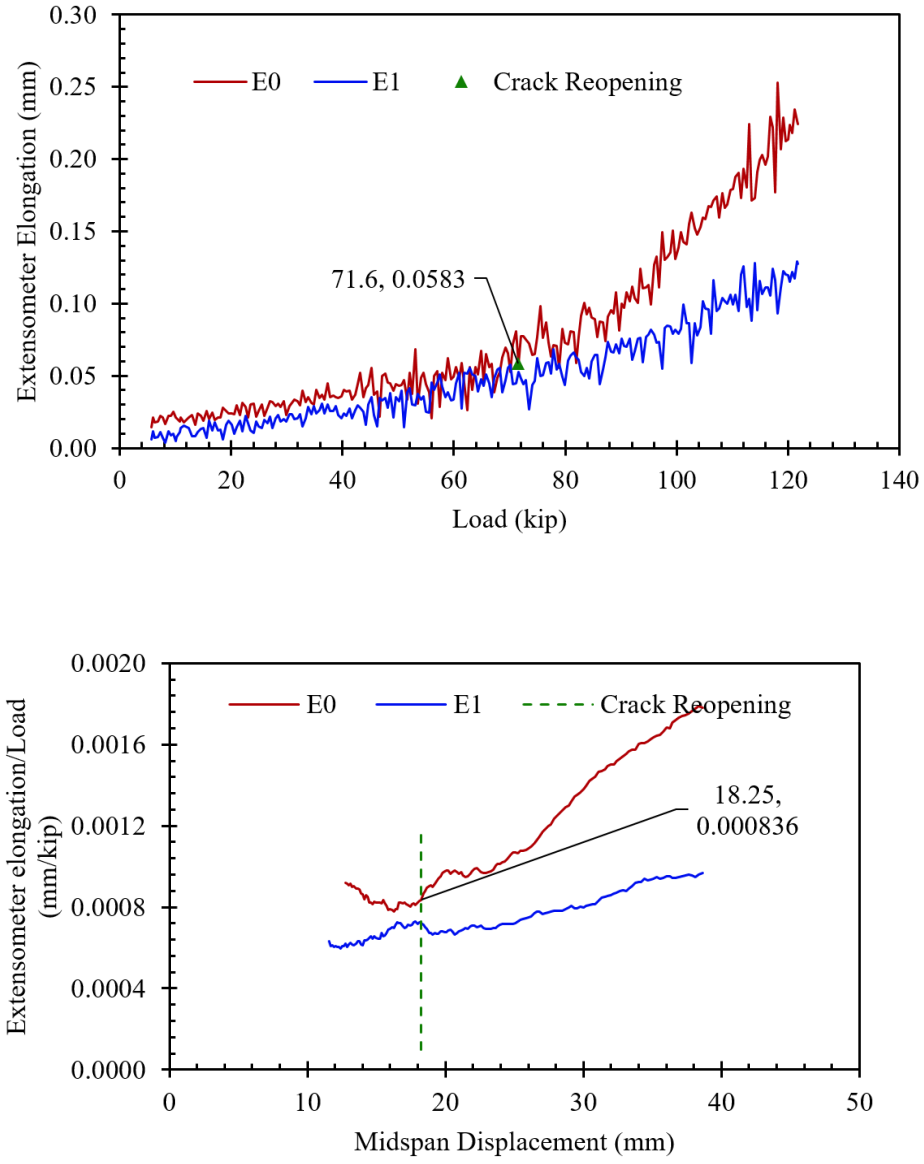

Figure C.14: Identifying first instance of cracking reopening of BTE1.

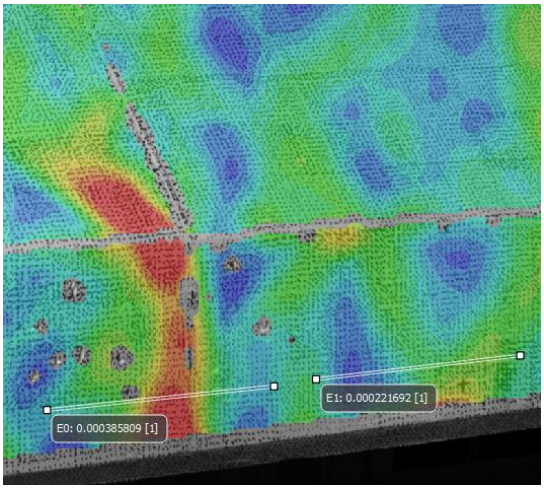

Figure C.15: Principal Strain (ε_1) map at Cracking Reopening Moment.

The cracking moment and crack reopening moment also agrees with the applied moment versus extensometer elongation plot as used in previous studies by Azizinamini *et al.* (1996) and shown in Figure C.16.

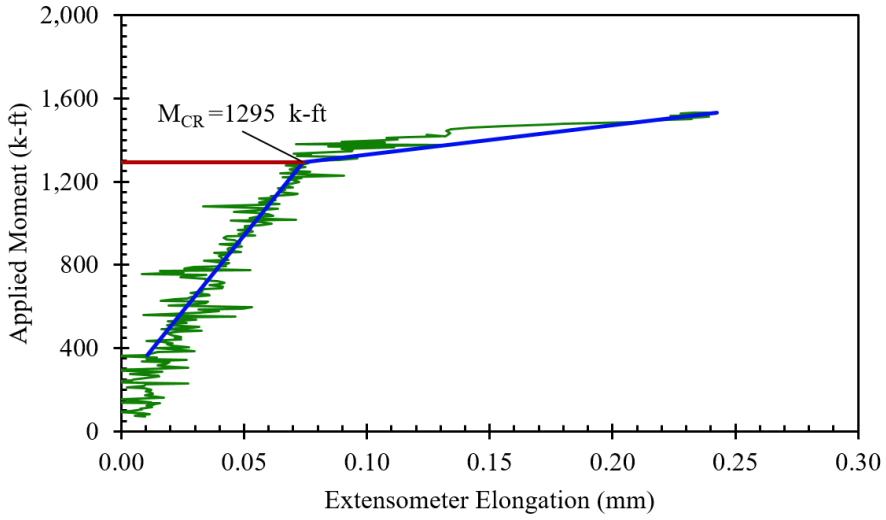

(a)

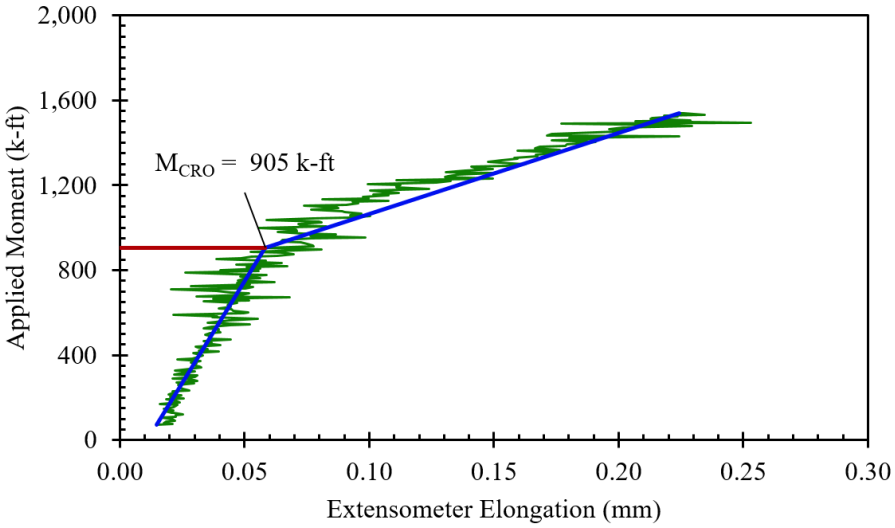

(b)

Figure C.16: BTE1 applied moment versus extensometer elongation with bi-linear approach to find (a) Cracking Moment (b) Crack Reopening Moment.

The first cracking and crack reopening moments found above requires observation of strain maps generated in DIC post-processing of the principal strain, ε_1. Figure C.17 and Figure C.18 below show the initial cracking of the girder and the reopening of the crack, respectively.

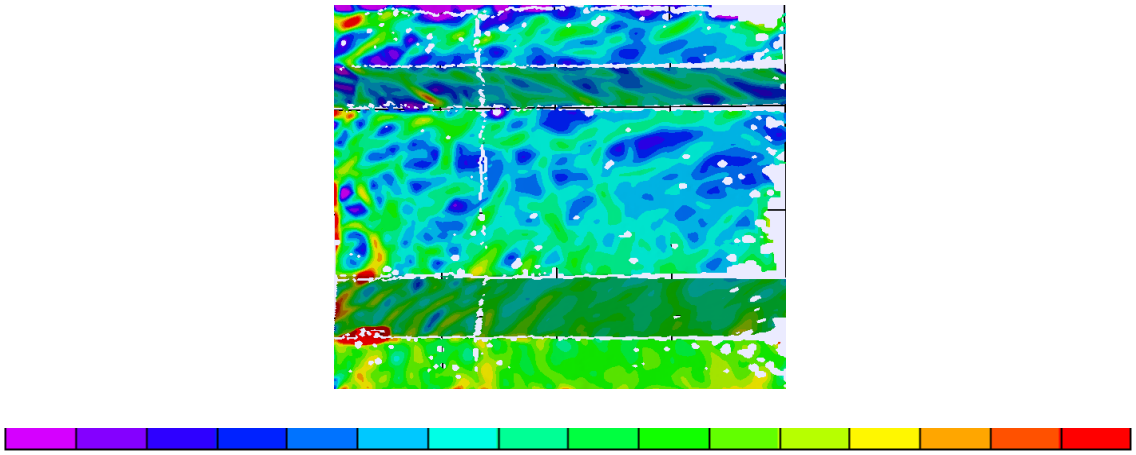

-0.000355 Prior to cracking: M=1200 k-ft 0.0007

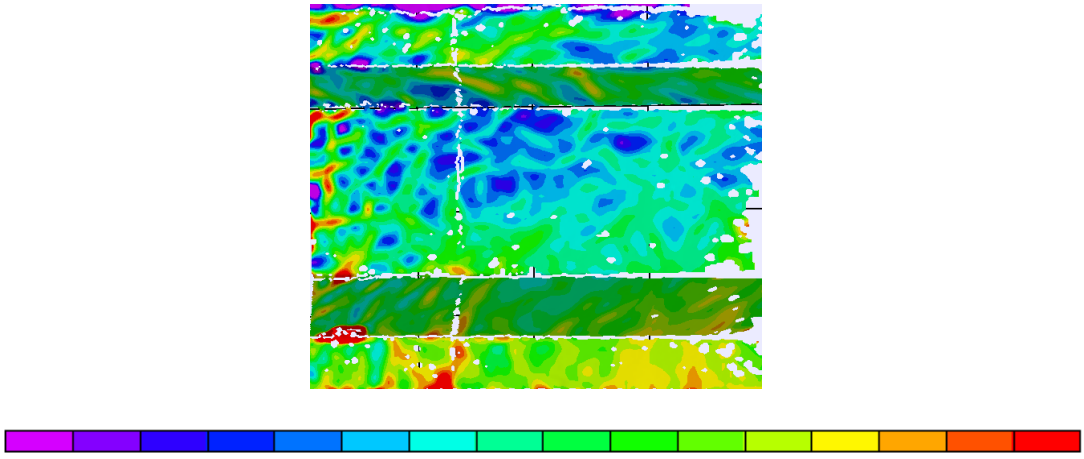

-0.000425 First Cracking: M = 1295 k-ft 0.000675

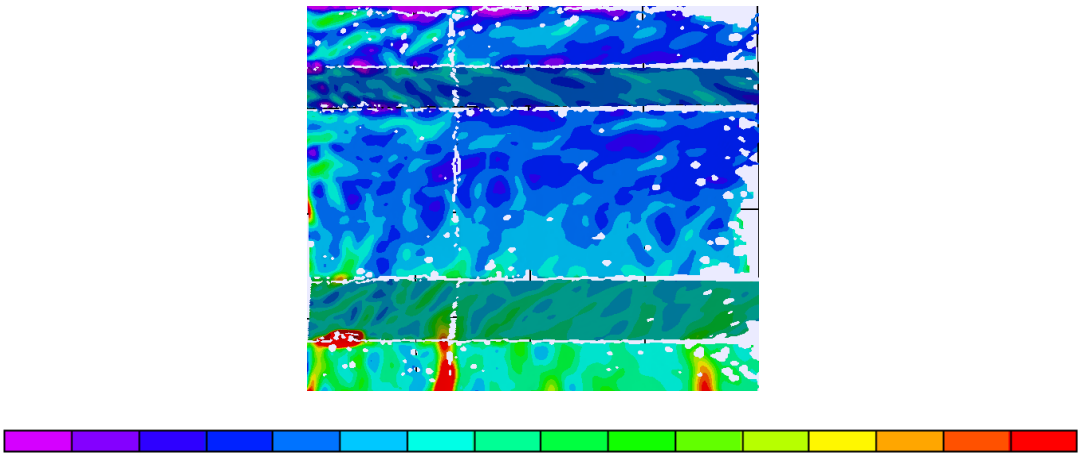

-0.00044 Post-cracking: M=1430 k-ft 0.00133

Figure C.17: BTE1 principal strain maps (ε_1) indicating cracking.

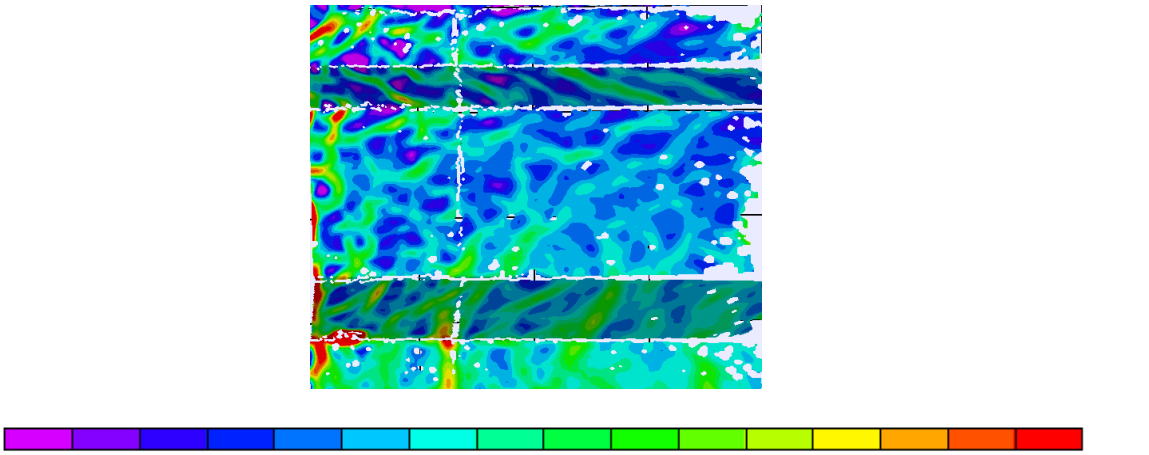

-0.00027 Prior to -reopening: M=600 k-ft 0.000705

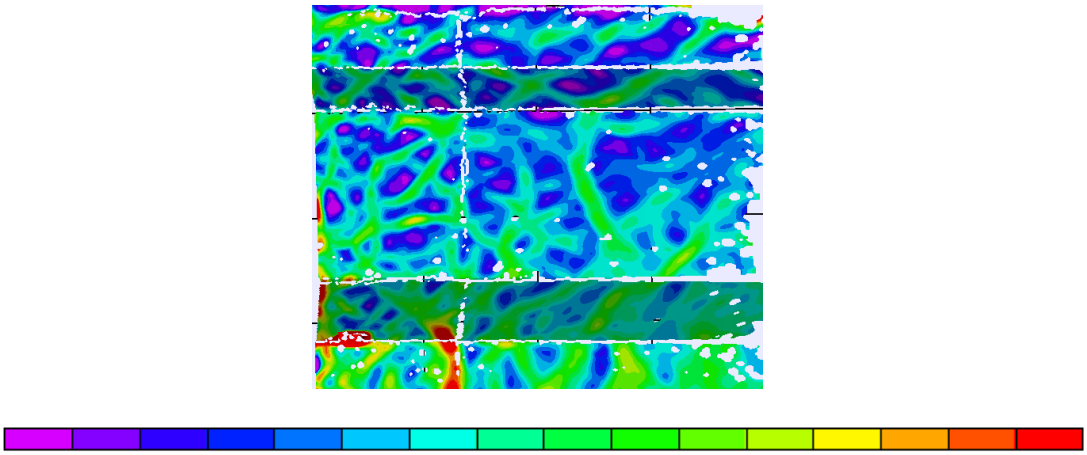

-0.0003 Crack reopening: M=905 k-ft 0.000845

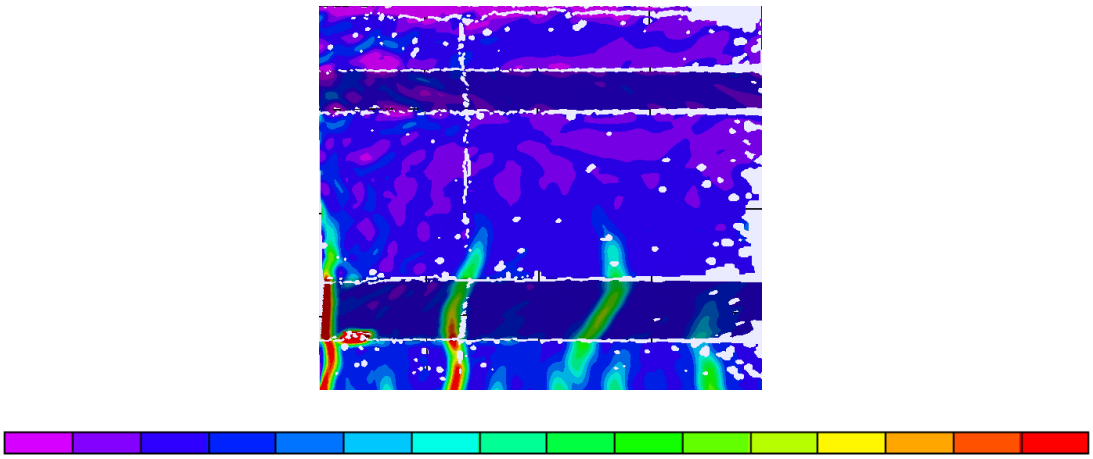

-0.00054 Post reopening: M=1460 k-ft 0.0039

Figure C.18: BTE1 crack reopening principal strain maps (ε_1).

The principal strain, ε_1, maps for each of the four cyclic load steps, the two load stages of monotonic loading, and the ultimate load are provided in Figure C.19. These maps show tensile strains with strain concentrations around the flexural cracks. Figure C.20 shows the ultimate load strain maps for axial strains, ε_x and ε_y, shear strain, γ_{xy}, and principal strains, ε_1 and ε_2.

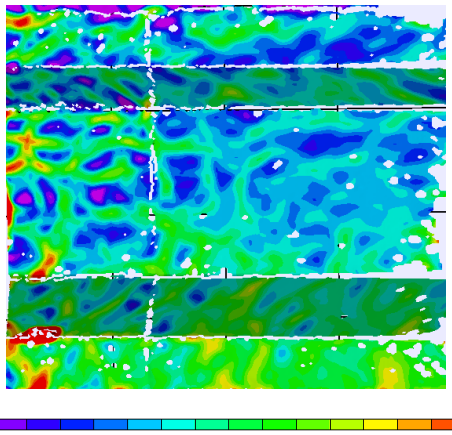

-0.000285 0.00061

Load Step 1: 80k actuator load

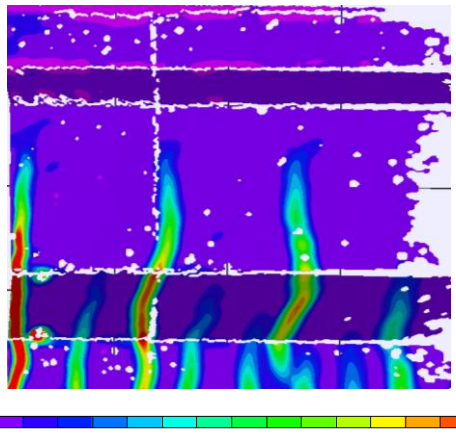

-0.00095 0.01105

Load Stage 1: 150k actuator load

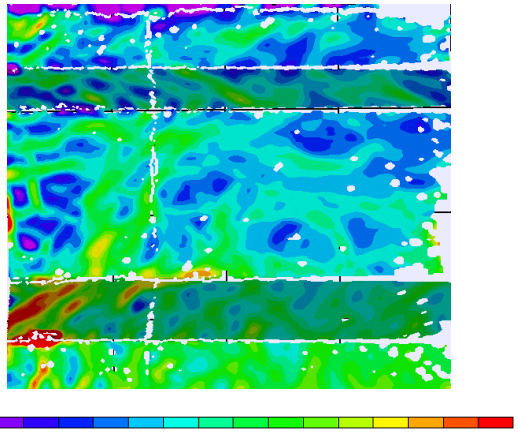

-0.00042 0.00088

Load Step 2: 100k actuator load

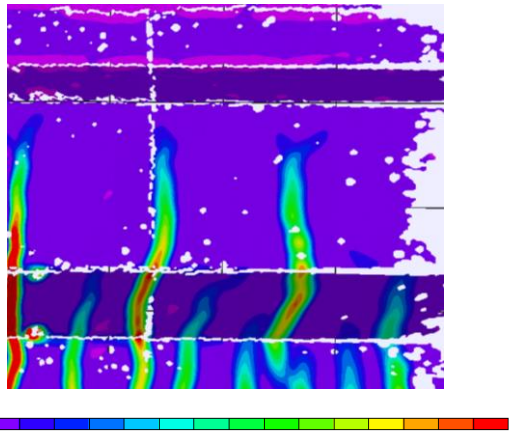

-0.0012 0.0161

Load Stage 2: 175k actuator load

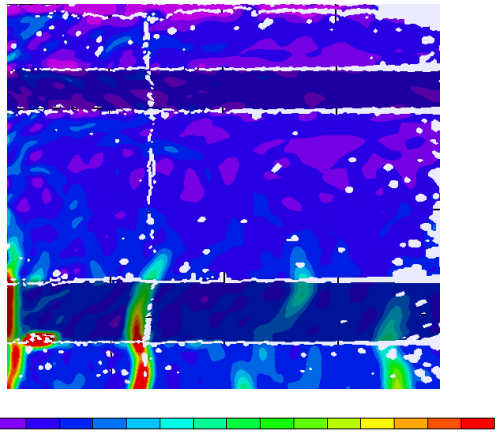

-0.00054 0.00348

Load Step 3: 125k actuator load

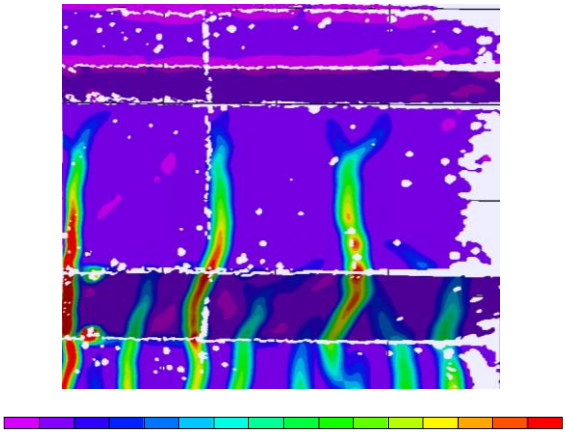

-0.0016 0.0228

Peak Load: 201k actuator load

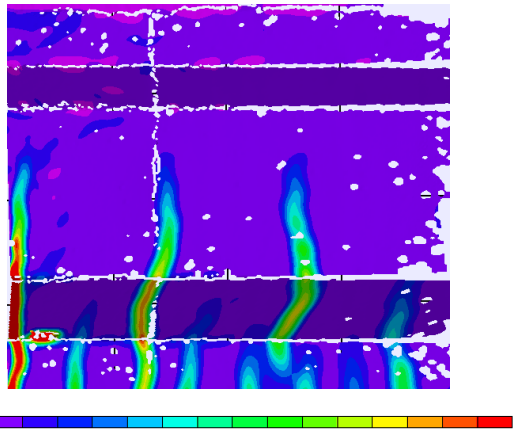

-0.00095 0.01055

Load Step 4: 150k actuator load

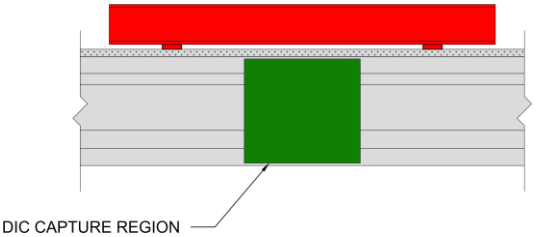

Figure C.19: Principal strain, ε_1, maps for BTE1.

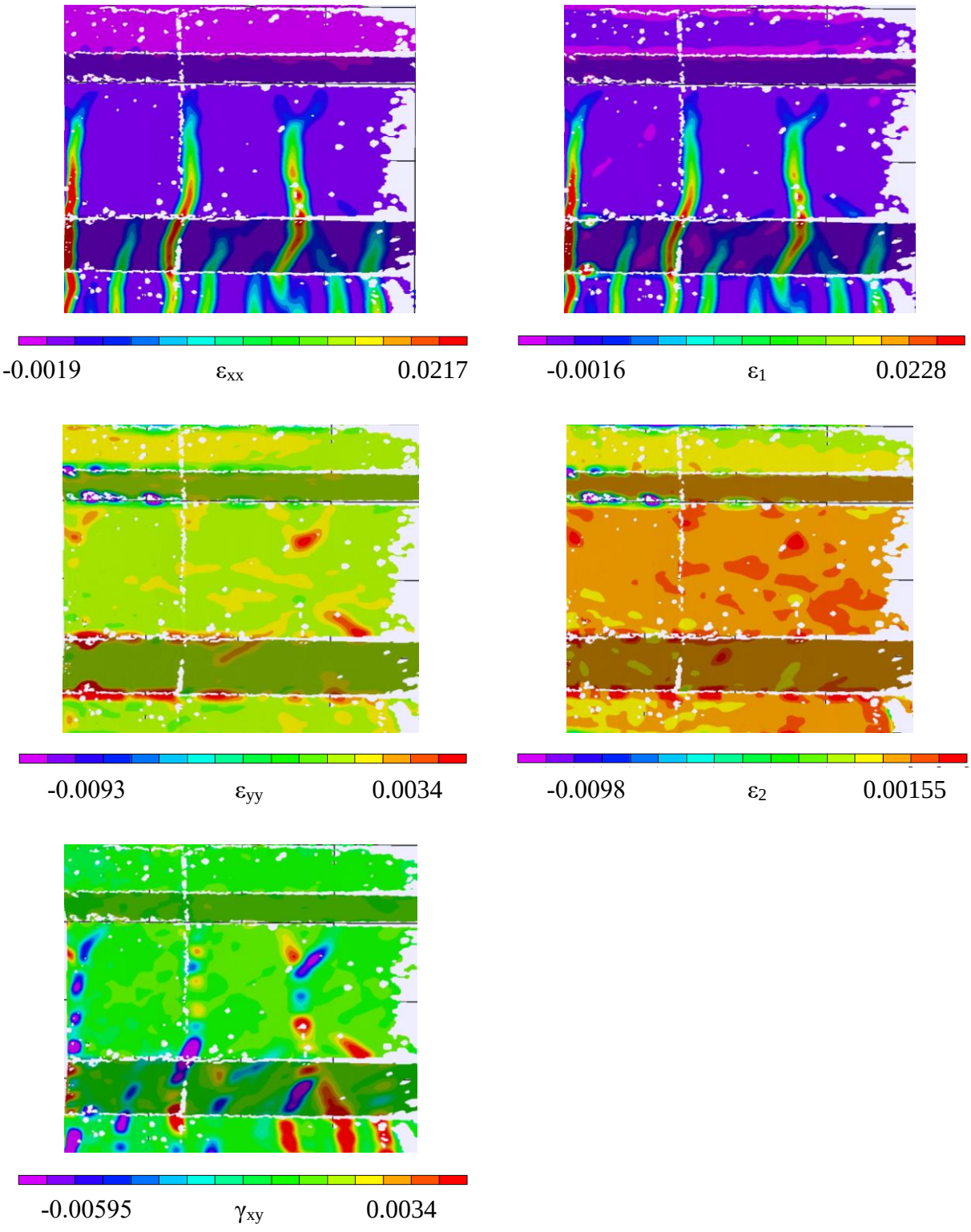

Figure C.20: BTE1 peak load strain maps.

C.2 BTE2 Flexural Testing

The experimental testing of BTE2 began on September 1st, 2021 with load cycles at low load levels to determine cracking and crack reopening moments. The first load level for load cycles reached 75 kips of actuator load corresponding to 37.5 kips of applied shear and an applied moment of approximately 985 k-ft. As with BTE1, the trough of the linear ramp cycles maintained at least 5 kips of actuator load to ensure no movement in the test apparatus occurred from spreader beam liftoff. During the three cycles up to 75 kips, there was no audible or visible cracking on the girder. The next load level reached 95 kips of actuator load corresponding to 47.5 kips of applied shear and an applied moment of approximately 1250 k-ft. As with the 75 kip load level, there was no audible or visible events during the 95 kip load level cycles. From 95 kips the load level was increased to 115 kips of actuator load corresponding to 57.5 kips of applied shear and an applied moment of 1510 k-ft. During the three cycles to 115 kips, flexural cracking on the beam was observed and the crack opening and closing was observed. Finally, the load level reached 130 kips of actuator load corresponding to 65 kips of applied shear and an applied moment of 1710 k-ft. Flexural cracks became visibly wider from the previous load levels, and crack propagation into the web was observed. Additionally, flexure shear cracking became visible near the load plates in the shear spans.

After the load cycles at four load levels, the girder was unloaded and then again monotonically loaded to failure with several load stages. The first load stage was taken at 100 kips of actuator load. During this load stage, cracks were marked and measured with a crack comparator and photos were taken of the specimen. Monotonic loading of the specimen was resumed until the next load stage at 120 kips occurred. Both the 100 kip and 120 kip load stages were lower than the highest load level attained during load cycles, so no additional cracking was observed during these load stages. The next load stage occurred at 140 kips of actuator load, and while loading to 140 kips, additional cracking was observed and flexure shear cracking continued to propagate into the shear spans. The final load stage occurred at 160 kips of actuator load. While loading to the 160 kip load stage, additional flexural cracks opened, small portions of the concrete deck began to spall off, and significant flexure-shear cracks could be seen on either side of the loading plates outside the flexural region. The load was reduced significantly before approaching the specimen for this load stage. After the 160 kip load stage, it was determined that further load staging should not be

conducted for safety. A summary of the cracks marked and measured at the load stages is provided in Figure C.21.

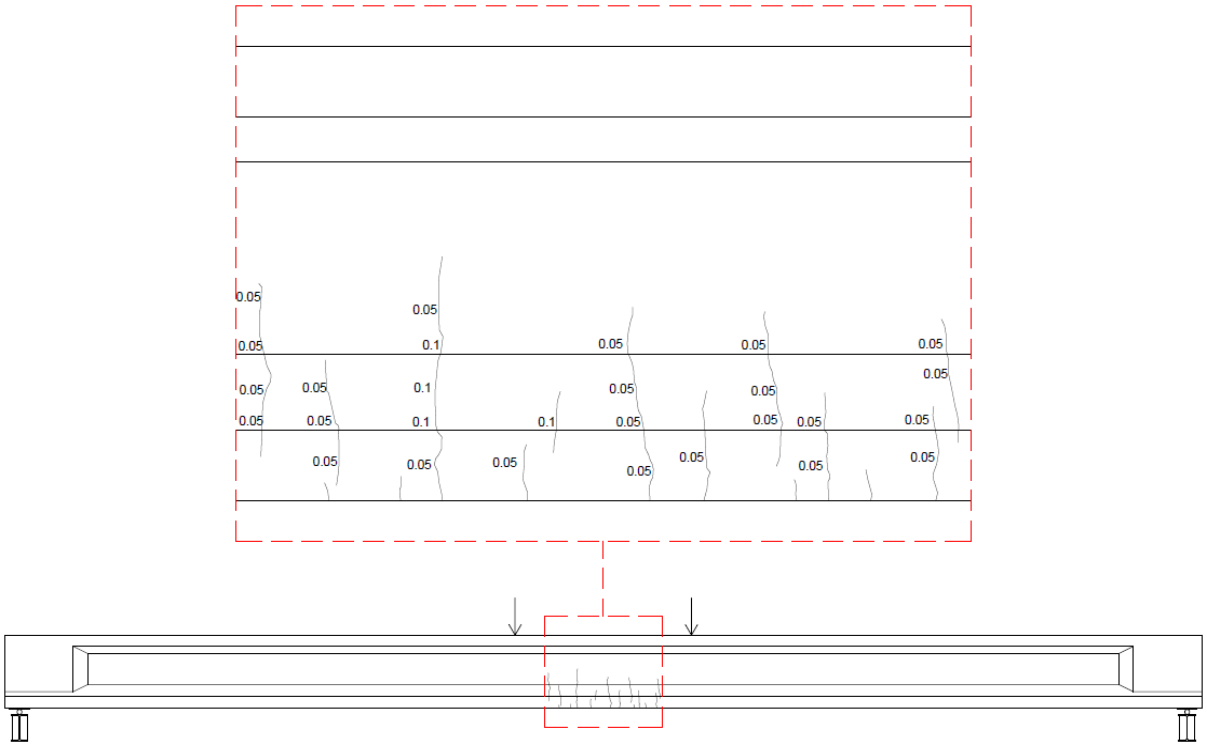

BTE2 Load Stage 1

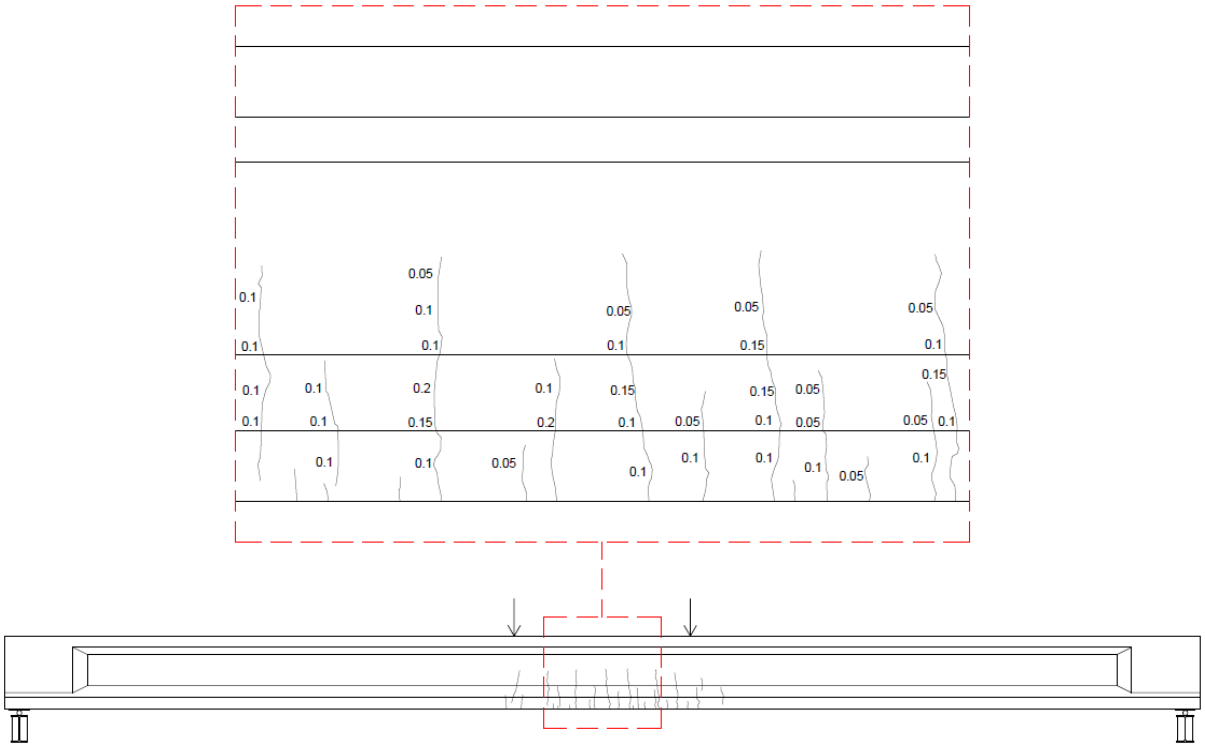

BTE2 Load Stage 2

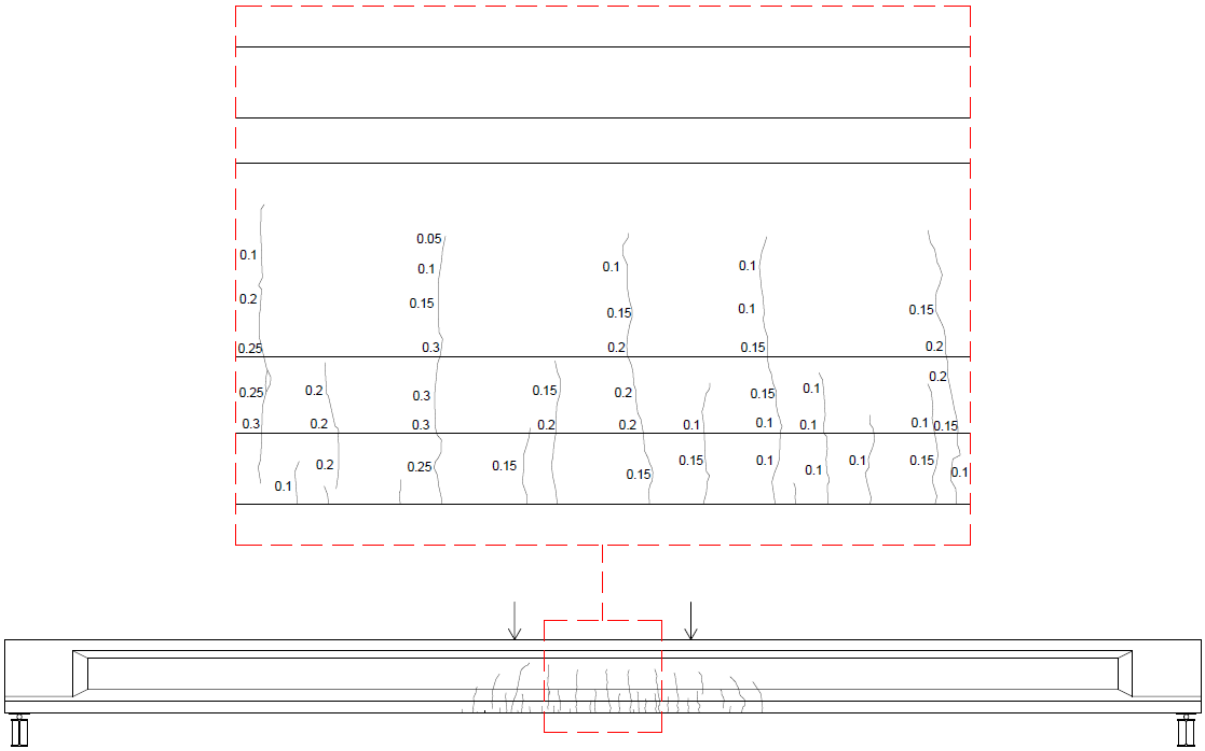

BTE2 Load Stage 3

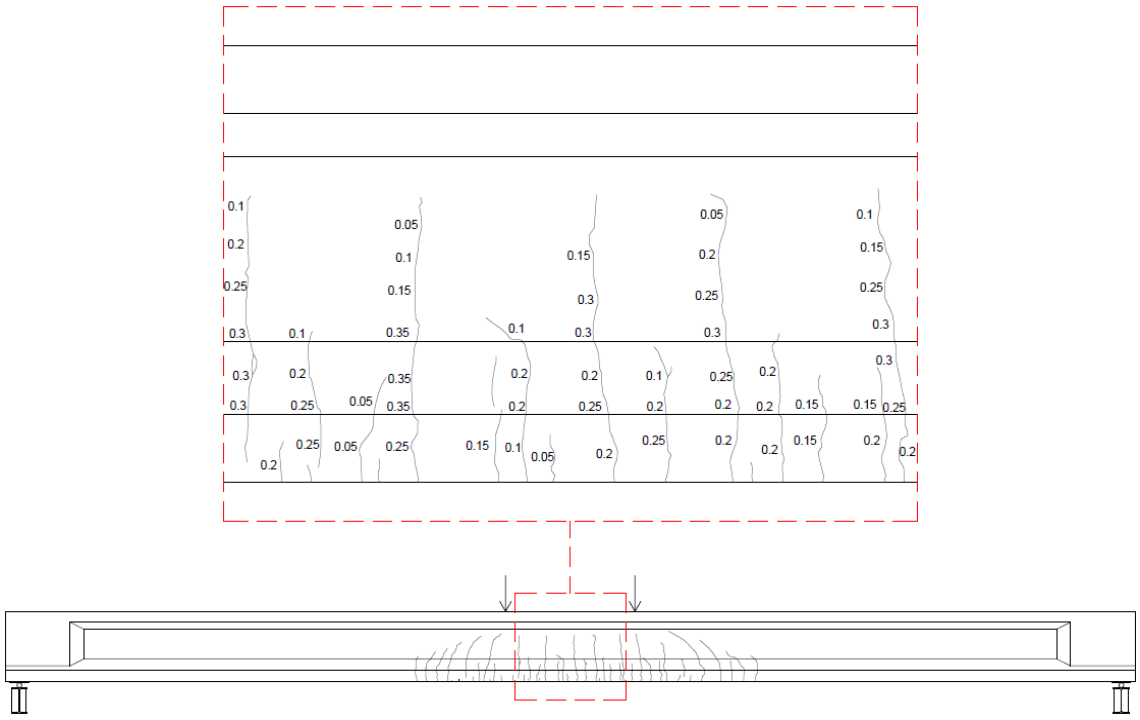

Figure C.21: BTE2 load stage crack diagrams (Crack widths are in mm).

The specimen was then monotonically loaded to failure which occurred at 196 kips of actuator load. The corresponding applied peak moment was 2570 k-ft. Similar to BTE1 the specimen failed by crushing of the top flange due to flexural compression, and after crushing of the top flange, the girder broke into two pieces by separating along one of the flexure-shear cracks extending towards the loading plate. The separation of the girder along the flexure-shear crack is occurred after the peak load was reached. The initiation of failure of the girder was caused by crushing of the top flange, not flexure-shear cracking. The failed specimen can be seen in Figure C.22.

Figure C.22: Photo of BTE2 after failure.

The load versus midspan displacement curves for the load cycles and monotonic loading to failure can be seen in Figure C.23. The deflection at peak load of the girder was 6.58 in. at the onset of crushing in the compression flange. The girder displacement at each of the five string potentiometers along the span for the monotonic loading can be seen in Figure C.24.

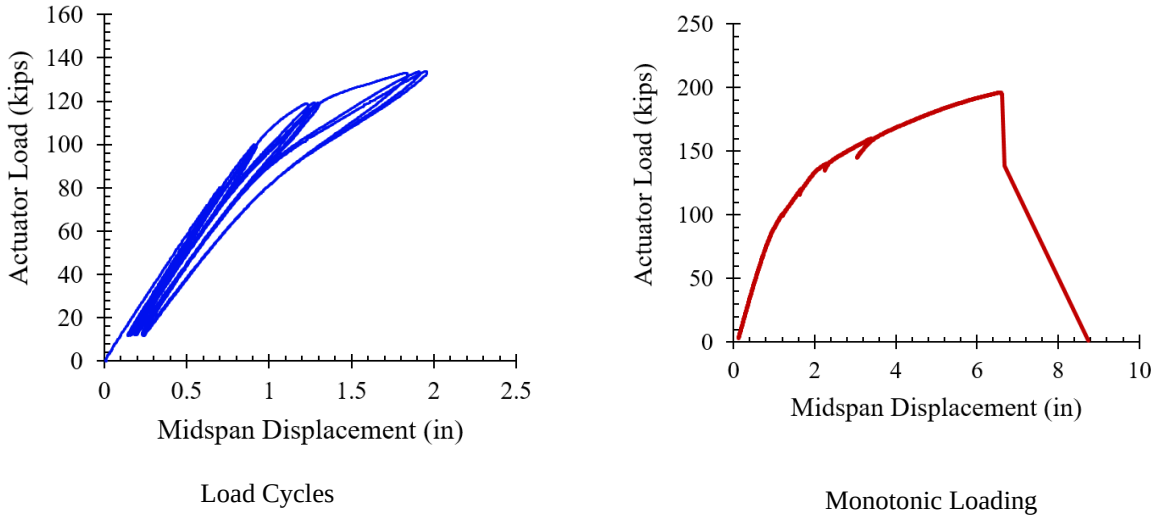

Figure C.23: BTE2 load versus midspan displacement for load cycles and monotonic loading to failure.

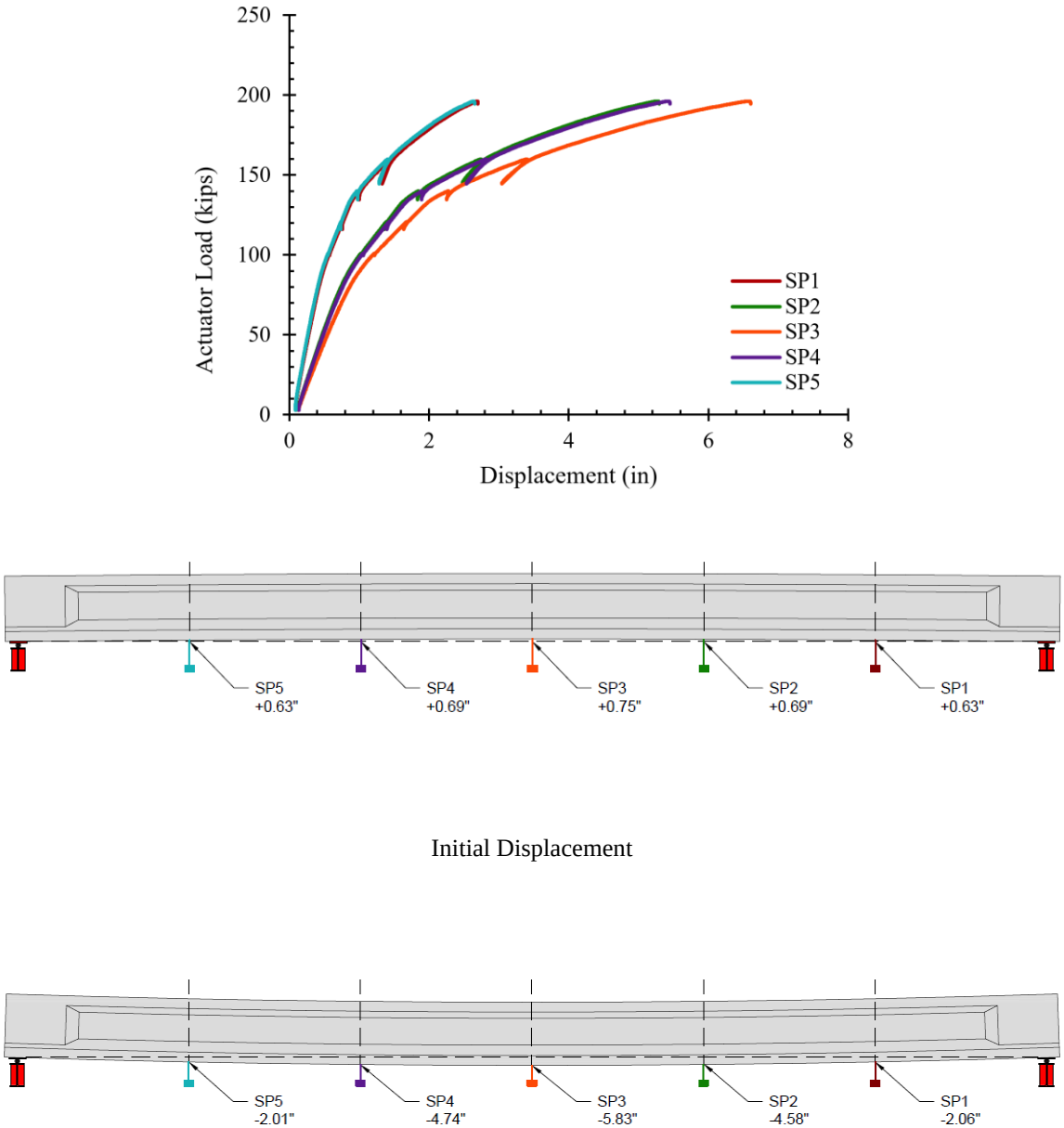

Figure C.24: BTE2 displacement along the length.

In addition to load deflection data, the strains through the depth of the member were determined using both strain gauges and DIC data. Figure C.25 shows the top and bottom strains from each set of gauges, set 1 and set 2, throughout the load cycles performed at each load level.

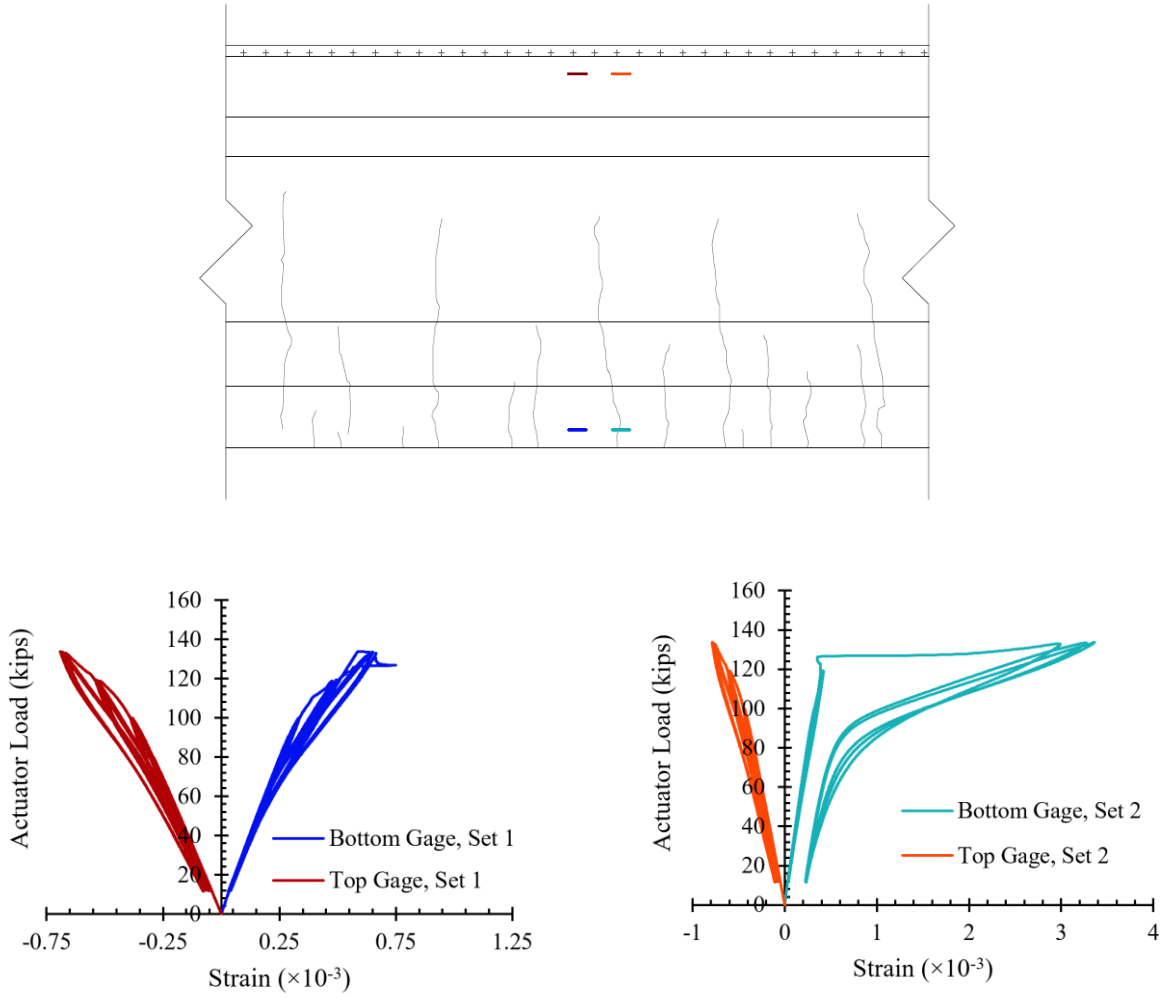

Figure C.25: BTE2 strain gauge data through load cycles at each load level. Bottom gauge, set 1 (blue), top gauge, set 1 (red), bottom gauge, set 2 (teal), top gauge, set 2 (orange).

As can be seen in Figure C.25, the top strains remain elastic throughout the load cycles, and the bottom gauges indicate cracking of the girder. The bottom gauge on the second set crossed a crack and shows dramatic increases in strain post cracking. To compare DIC results to the strain gauge data, points were used at the same location as the first set of strain gauges corresponding to the girder's midspan. The results from the DIC points can be seen in Figure C.26.

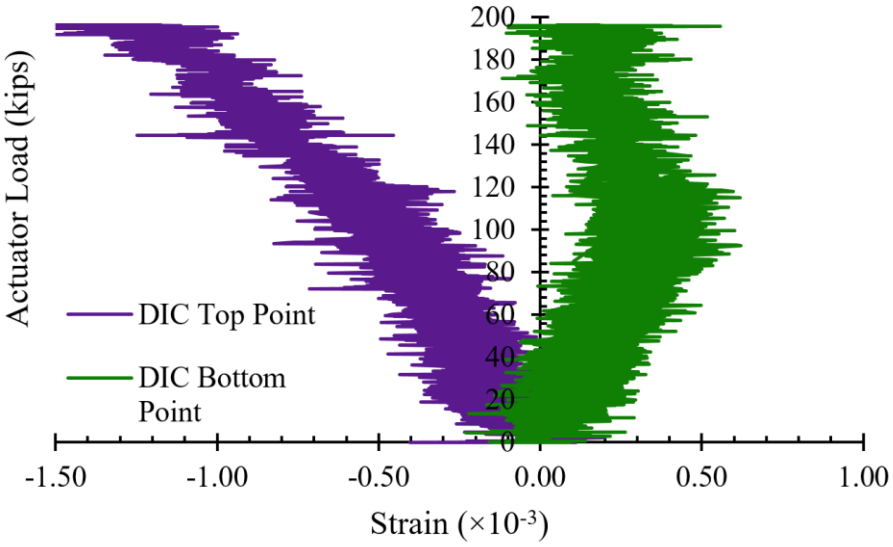

Figure C.26: BTE2 DIC point strains at girder midspan through load cycles.

As with the strain gauges, DIC shows that the top strains remain elastic throughout the load cycles. Also, the DIC point near the bottom flange indicates lower strains at higher actuator loads, so the concrete beneath the point is becoming debonded at higher strains. Strains from the DIC point near the bottom flange are compared to the average bottom strain gauge behavior for the cracking cycle in Figure C.27. The response agrees reasonably well. The discrepancies arise from the differences in gauge lengths of the measurements. A more detailed discussion will occur in subsequent sections.

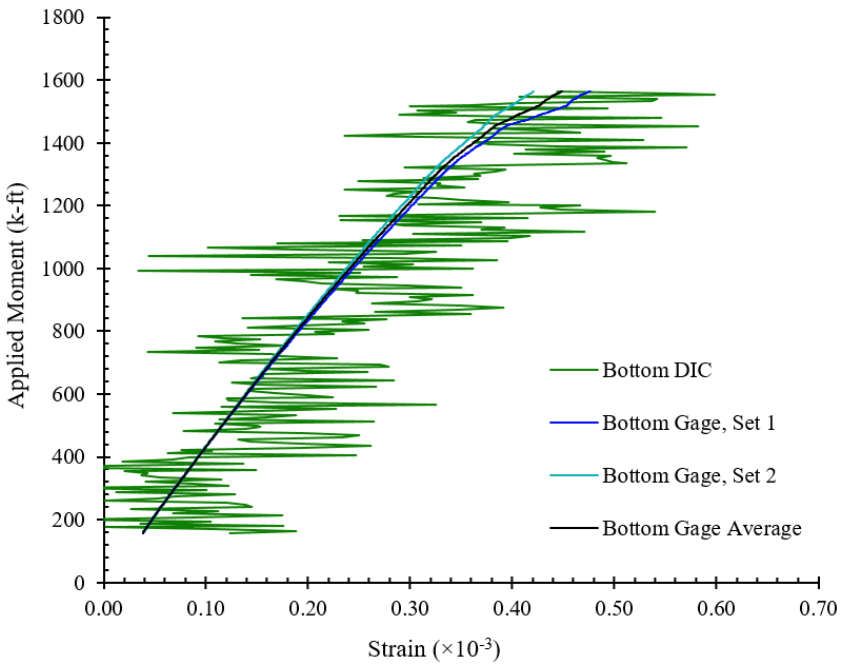

Figure C.27: BTE2 strain comparison between DIC point and strain gauge comparison for first cycle to 115 kips actuator load.

To further investigate the strains through the depth during loading, horizontal extensometers were used in DIC post-processing at four locations through the depth near midspan. These extensometers provide longitudinal strains through the depth for each image taken during the test. The strains through the depth can be seen for each of the four load steps during load cycles, the four load stages of monotonic loading, and the ultimate load for the girder in Figure C.28.

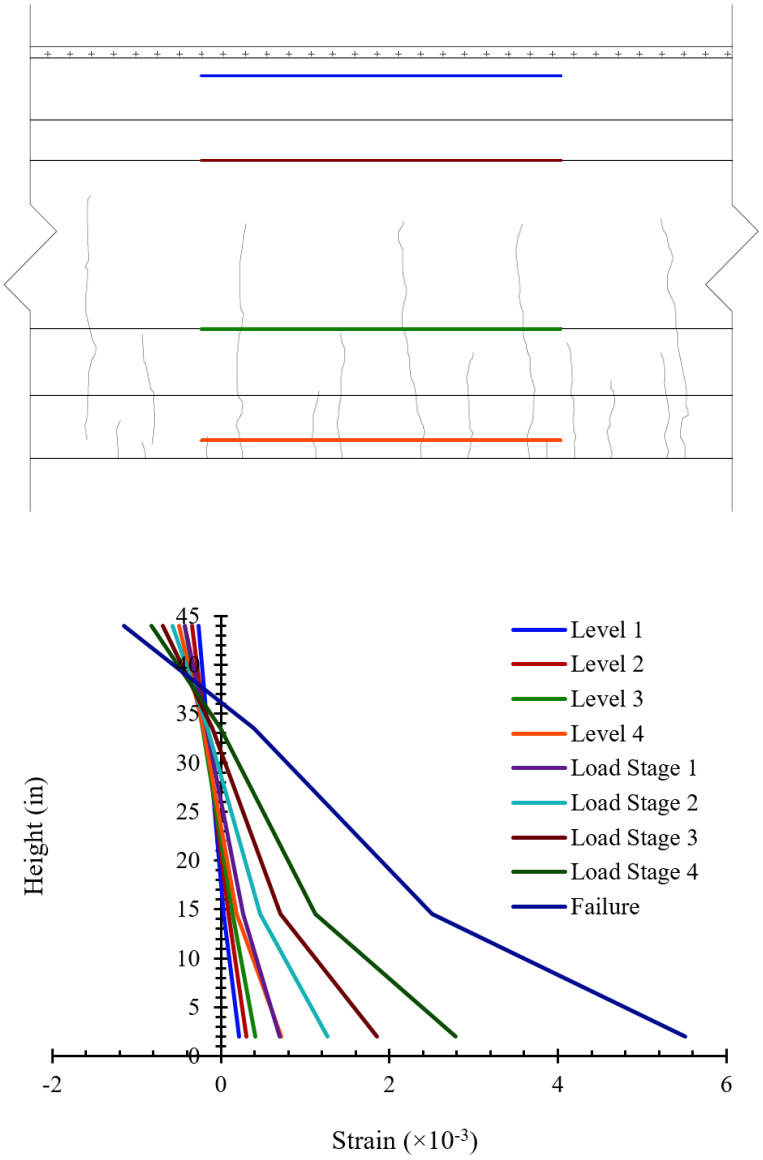

Figure C.28: BTE2 DIC horizontal extensometer strain profile.

The longitudinal strains from the DIC extensometers initially indicate a linear distribution of strains through the depth. As can be seen in Figure C.28, for loads greater than 130 kips the strain reading at 15 in. above the bottom of the girder is less than expected for a linear strain variation. However, the strain variation from the top to the bottom of the specimen is linear when the strains at 15 in. height are omitted.

Virtual extensometers in DIC post-processing were also used to determine the elongation across cracks during the load cycles to determine when first cracking occurs, when closing occurs

and when crack reopening occurs. Before cracking of the specimen, the virtual extensometer reads elastic elongation of the girder, but at cracking the extensometer elongation increases suddenly. Upon unloading, the extensometer elongation decreases rapidly until the crack is closed. Then, the slope of the applied moment-extensometer elongation curve returns to that of the uncracked section. The virtual extensometer was placed over the first crack that occurred on the girder, and the location and elongation of the extensometer can be seen in Figure C.29. The extensometer elongation is a five point moving average of the DIC data.

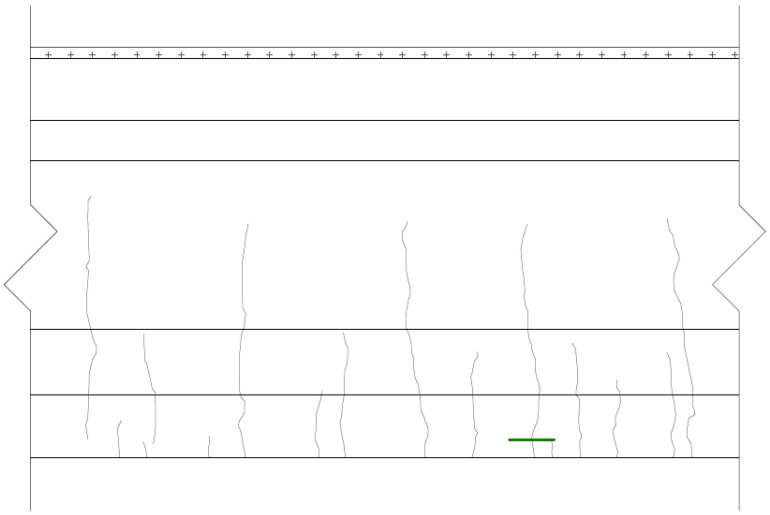

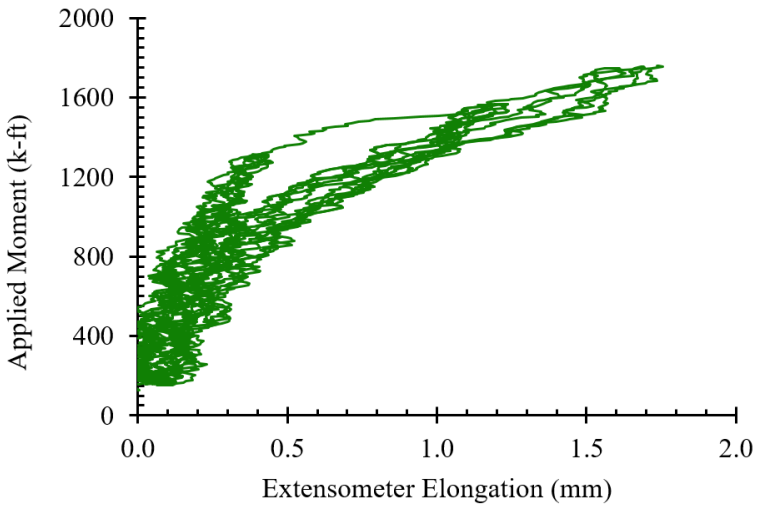

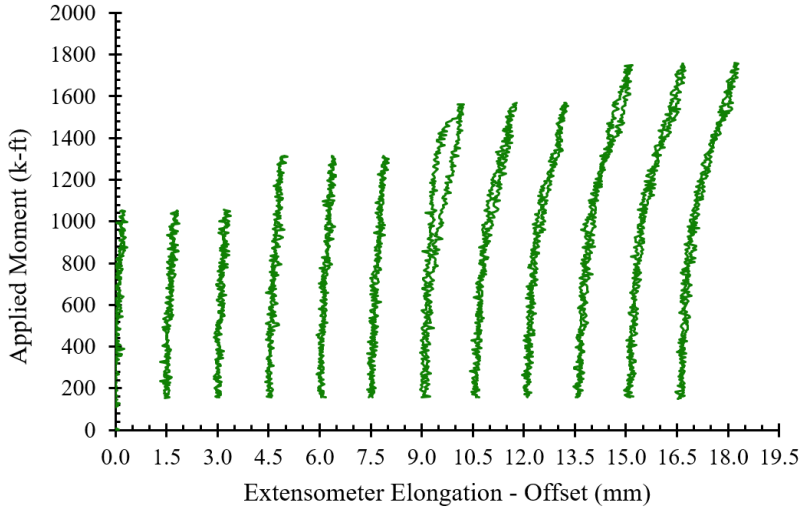

Figure C.29: BTE2 first crack virtual extensometer.

The extensometer elongation was offset after each cycle and plotted against applied moment as shown in Figure C.29. The three cycles for load steps of 75 and 95 kips of actuator load remain elastic. The first cycle up to 115 kips of actuator load is the first instance of cracking in the girder; there is a sudden increase in the extensometer's elongation at the peak load for that cycle. Figure C.30 highlights on the first cycle up to 115 kips of actuator load, and the transition from uncracked extensometer elongation to cracked elongation can clearly be seen. However, the exact point of stiffness change requires careful investigation.

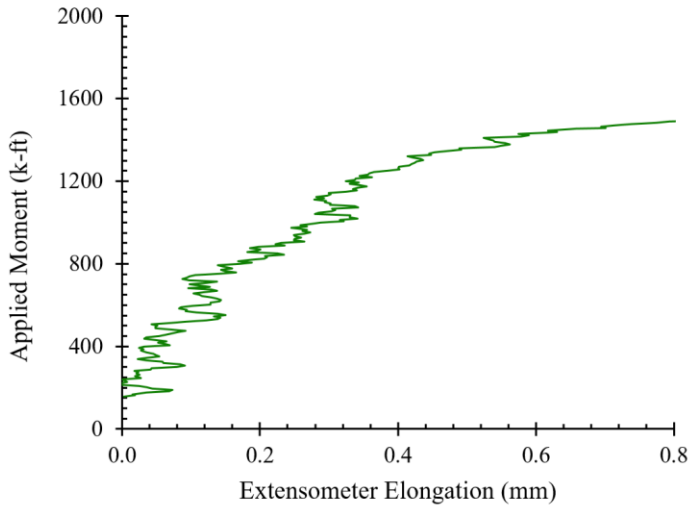

Figure C.30: BTE2 applied moment versus extensometer elongation to determine cracking.

To determine first cracking, DIC strain maps at the instant when crack first appeared was captured and a pair of extensometers were placed, E0 was placed at the location of first crack and E1 placed away from the crack both at a distance of 1.75 in from the bottom flange of the girder. This was done to compare how the behavior of extensometer elongation changes with and without a crack. The E0 and E1 extensometer elongation was plotted against the applied load. The extensometer placed between cracks provide measurements of the elastic elongation throughout the loading. The extensometer placed over the crack provides detailed crack opening and closing data. E1 and E0 both shows elastic elongation but an abrupt change in slope occurs at a load of 104 kips for E0 (Figure C.31). This sudden change in elongation occurs marks the onset of cracking. Both the extensometer elongations agree up to first cracking. The point at which they diverge can be used to determine when first cracking occurs more accurately. The DIC strain map at this instant shows very high strains around the extensometer indicating, either the crack has formed or is on the verge of propagating. To further verify the load at which first cracking occurs, a 20 point moving average of the extensometer elongation versus load was plotted against the midspan displacement. The filtering approach helps make clear when the section transitions from uncracked to a cracked section. Figure C.31 shows the average slope starts to increase at an applied moment of 1370 k-ft (or load of 104.3 kips) corresponding to a displacement of 26.7 mm (Midspan displacement of 23.4 mm in Figure 4.31 is the displacement from moving average). The strain map

at the instant corresponding to this moment also show very high strains and maps the shape of a crack (Figure C.32). Thus, the cracking moment for BTE2 is 1370 k-ft.

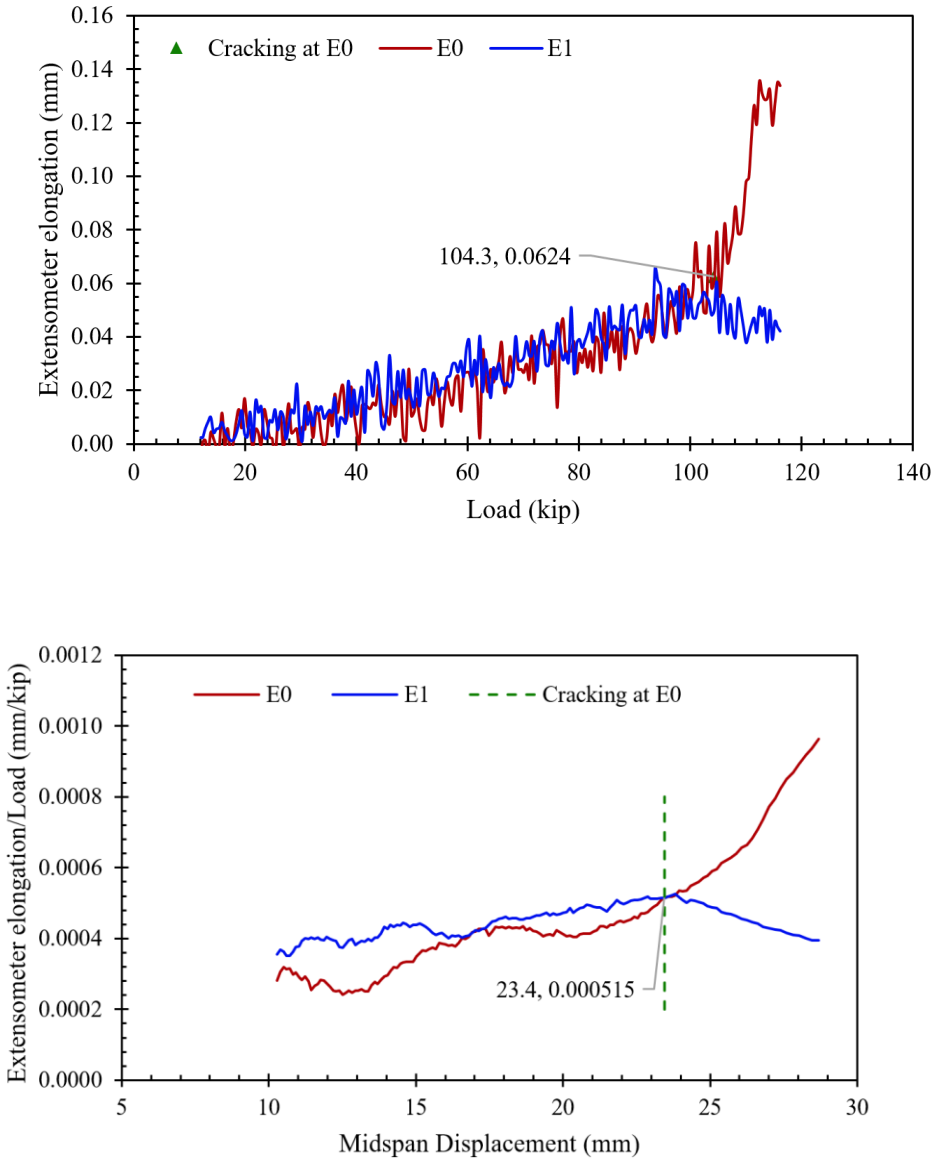

Figure C.31: Identifying first instance of cracking of BTE2.

Figure C.32 shows the principal strain map at the cracking moment where high strains can be observed at the extensometer location indicating either cracking has occurred or is on the verge of propagating.

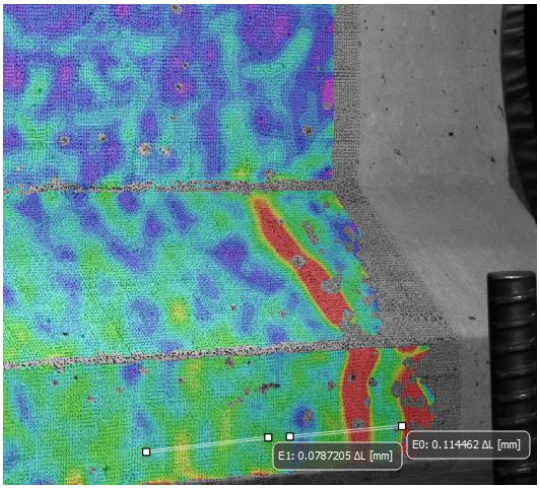

Figure C.32: Principal strain (ε_1) map at Cracking Moment.

The crack reopening moment can be found using the same procedure as the cracking moment (Fig. C.33). To avoid influence from accumulated damage from load cycles, the first load cycle after the appearance of first crack is used to determine the crack reopening moment. Extensometer elongation was plotted against load for the two extensometers and the point of divergence was roughly determined. A filtering approach was then used which involves plotting the stiffness of extensometer elongation/load against midspan displacement to determine the crack reopening moment. The crack reopening moment was verified with the DIC strain map at the same instant which shows high strains at the extensometer location marking the reopening of the flexural crack (Fig. C.34). The crack reopening moment was found to be 995 k-ft.

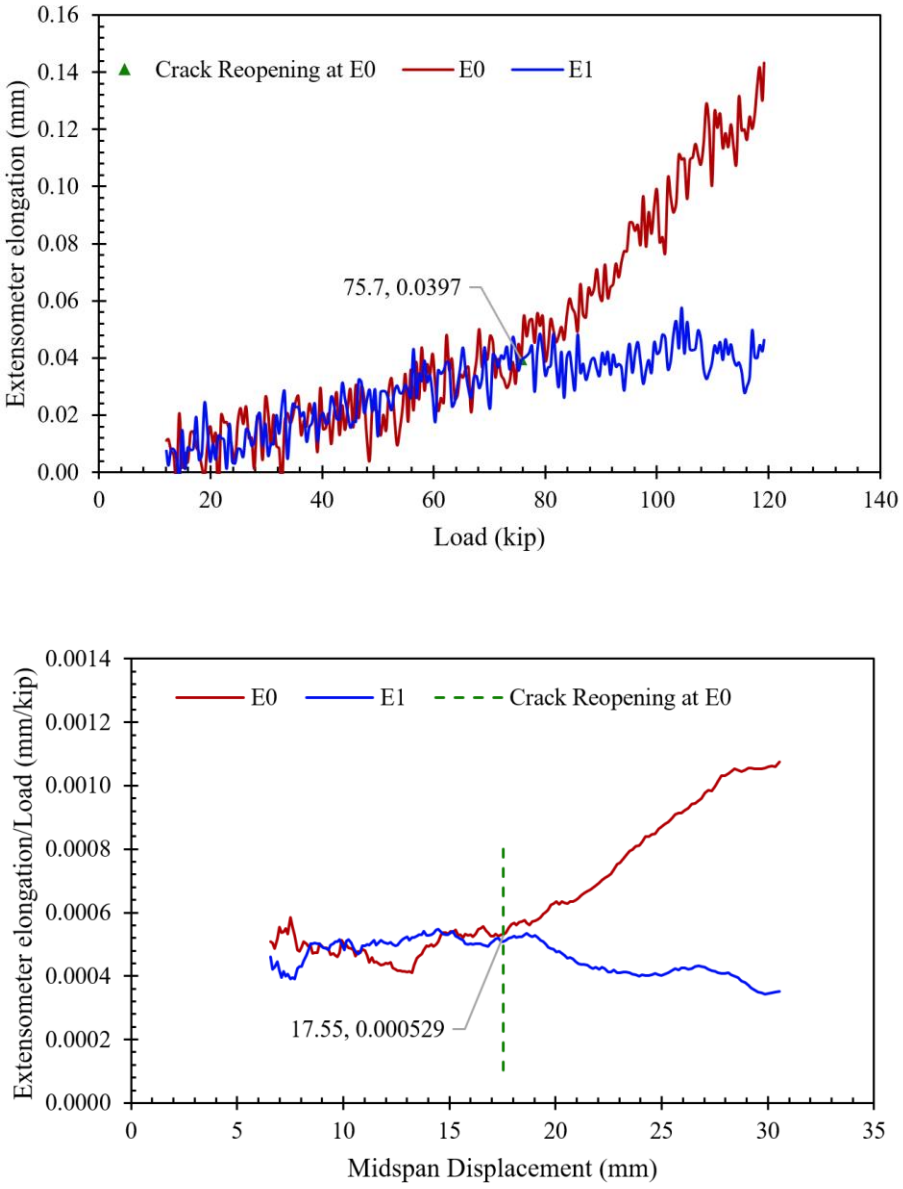

Figure C.33: Identifying first instance of crack reopening of BTE2

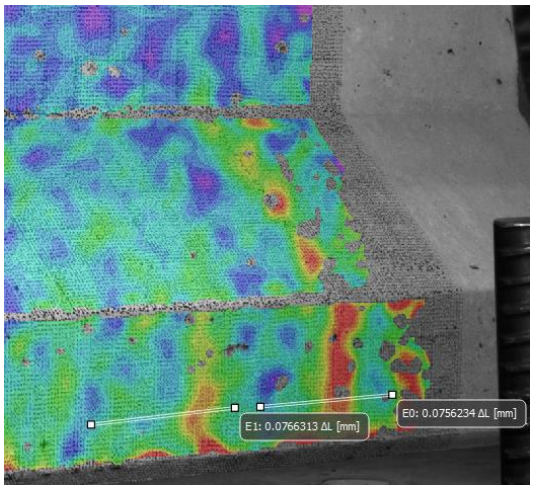

Figure C.34: Principal Strain Map (ε_1) at Cracking Reopening Moment.

The cracking moment and crack reopening moment also agrees with the applied moment versus extensometer elongation plot as used in previous studies by Azizinamini *et al.* (1996) and shown in Figure C.35.

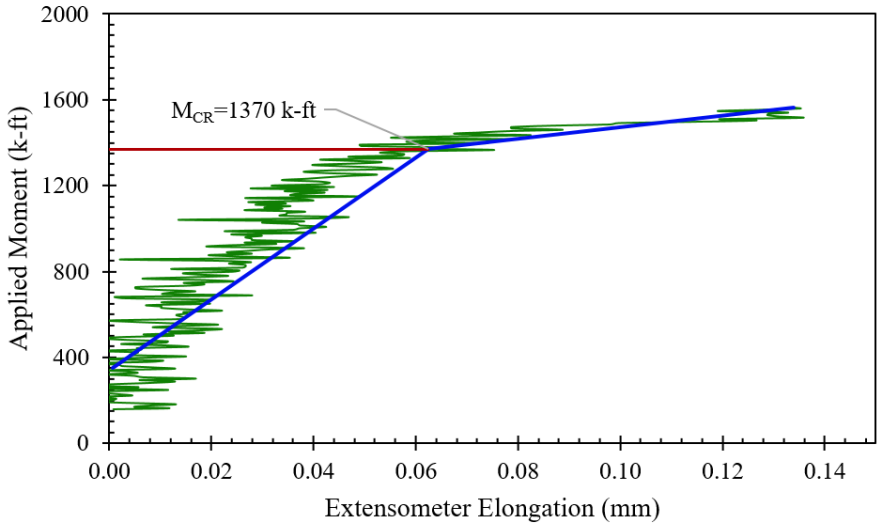

(a)

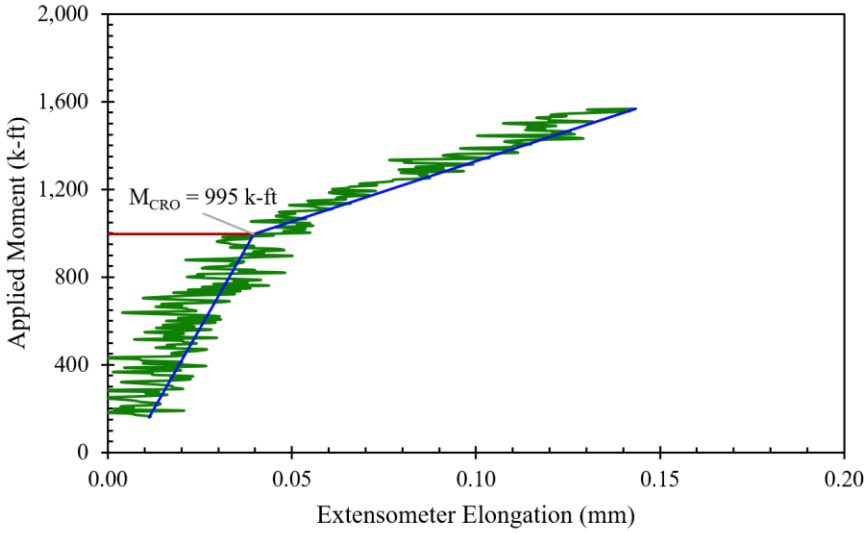

(b)

Figure C.35: BTE2 applied moment versus extensometer elongation with bi-linear approach to find (a) Cracking Moment (b) Crack Reopening Moment.

The first cracking and crack reopening moments requires careful observation of strain maps generated in DIC post-processing of the principal strain, ε1. Figure C.36 and Figure C.37 show the initial cracking of the girder and the reopening of the crack, respectively.

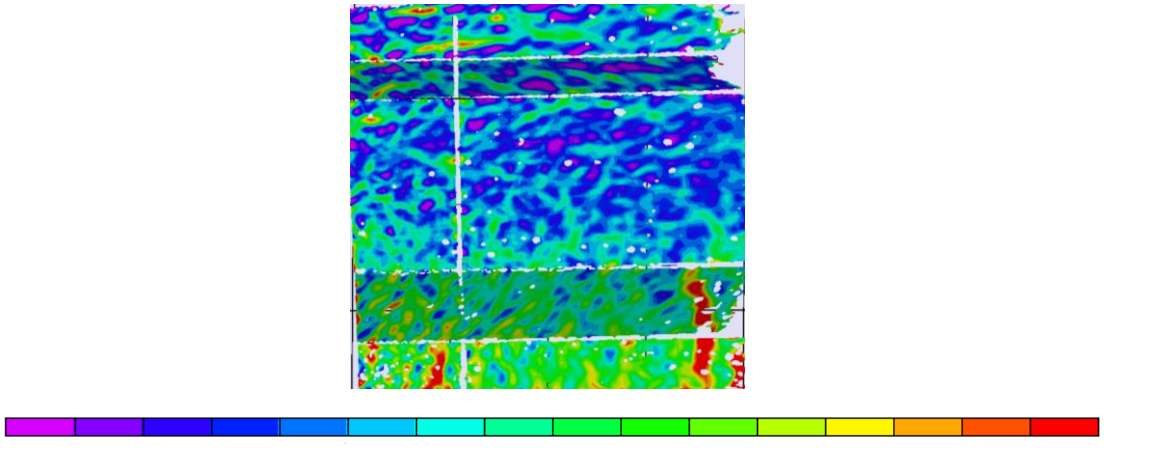

-0.000215 0.000745

Prior to cracking: M=1200 k-ft

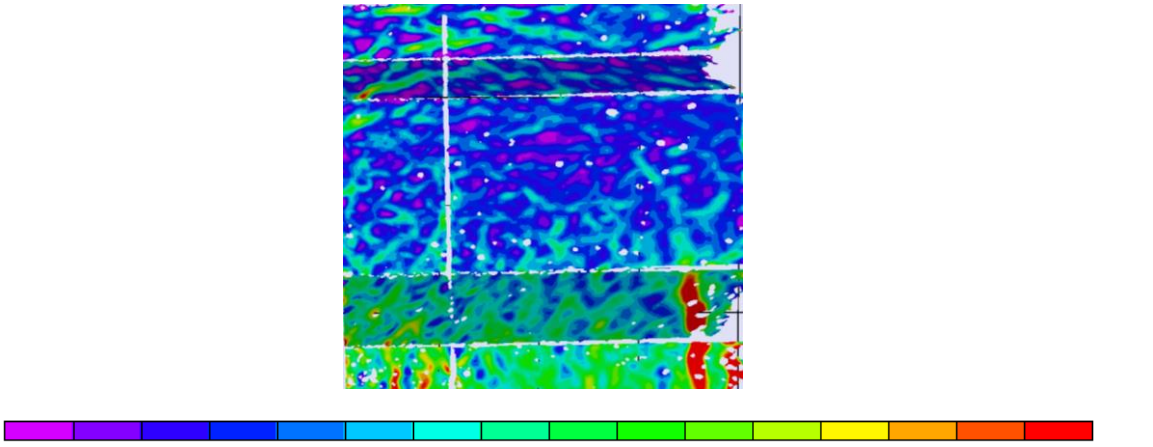

-0.00021 0.001

Cracking: M=1370 k-ft

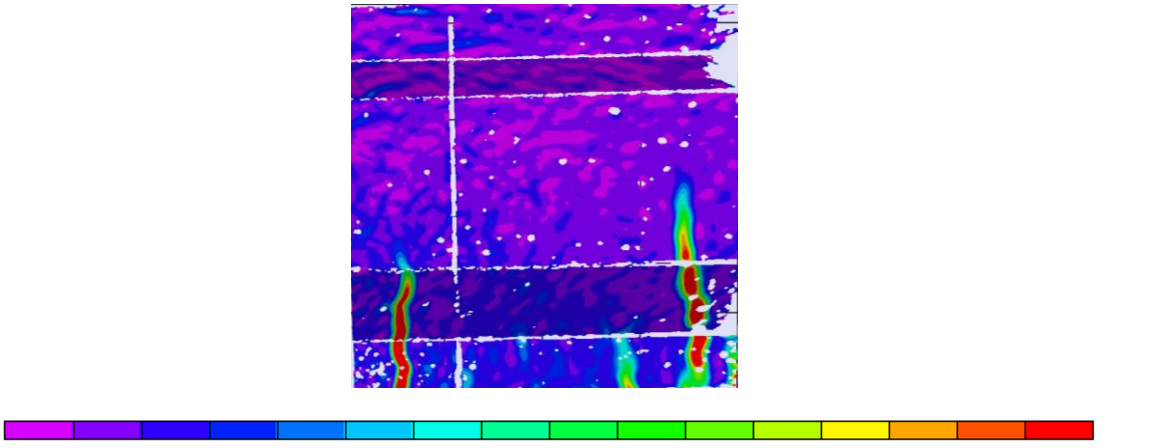

-0.00022 0.00352

Post-cracking: M=1565 k-ft

Figure C.36: BTE2 principal strain maps (ε_1) indicating cracking.

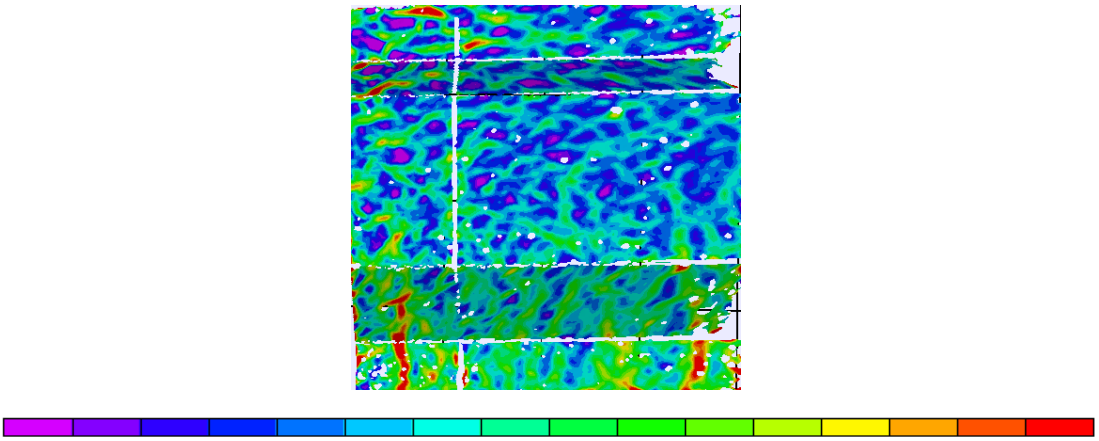

-0.00022 0.00066

Prior to reopening: M=650 k-ft

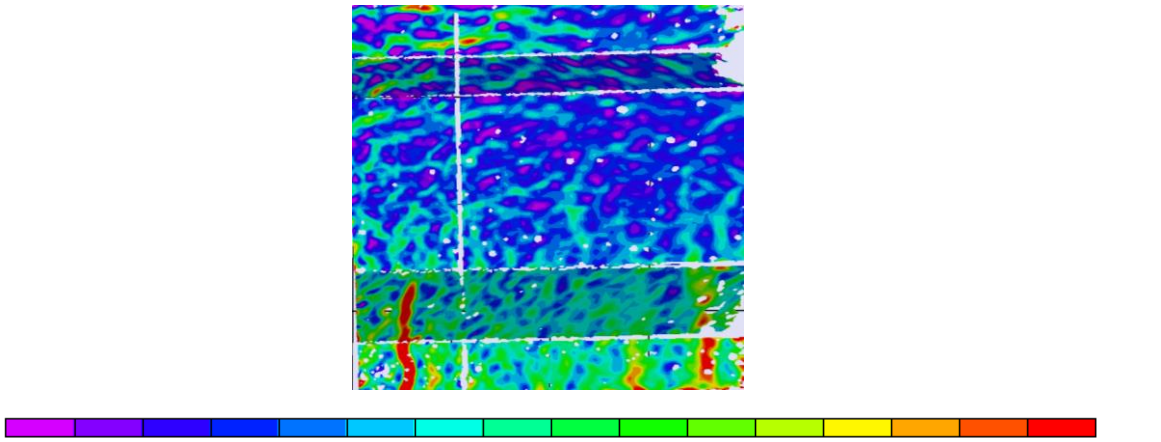

-0.000185 0.000815

Crack reopening: M=995 k-ft

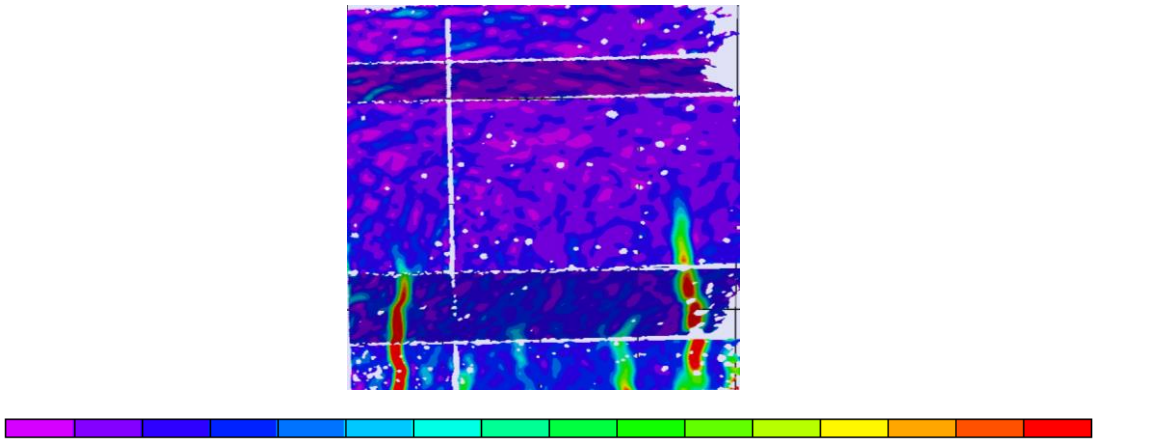

-0.00022 0.00268

Post-reopening: M=1400 k-ft

Figure C.37: BTE2 principal strain maps (ε_1) indicating crack reopening.

Strain maps for the full DIC field of view between the load plates are provided below. The principal strain, ε_1, maps for each of the four cyclic load steps, the four load stages of monotonic loading, and the ultimate load are provided in Figure C.38. These maps show tensile strains with strain concentrations around the flexural cracks. Figure C.39 shows the ultimate load strain maps for axial strains, ε_x and ε_y, shear strain, γ_{xy}, and principal strains, ε_1 and ε_2.

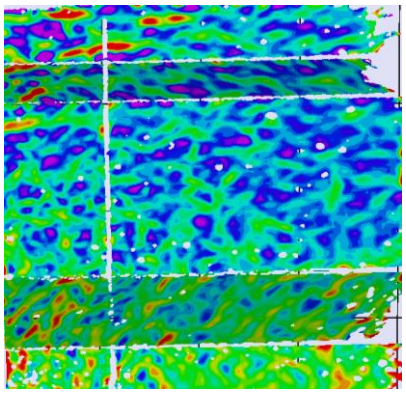

-0.00021 0.000575

Load Step 1: 75k actuator load

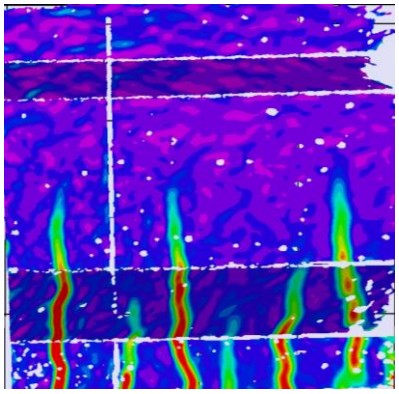

-0.00022 0.00278

Load Stage 1: 100k actuator load

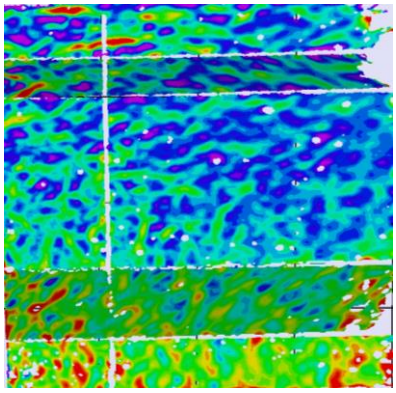

-0.000215 0.000635

Load Step 2: 95k actuator load

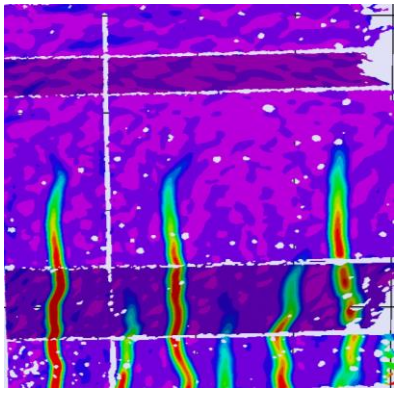

-0.00025 0.0057

Load Stage 2: 120k actuator load

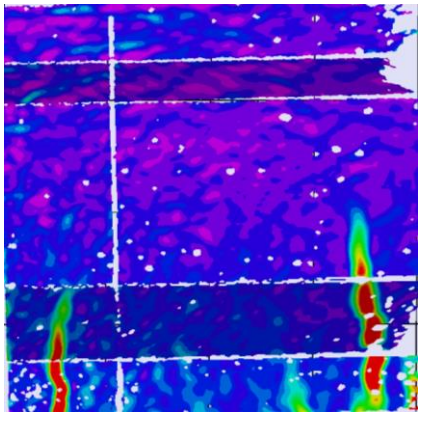

-0.00026 0.00266

Load Step 3: 115k actuator load

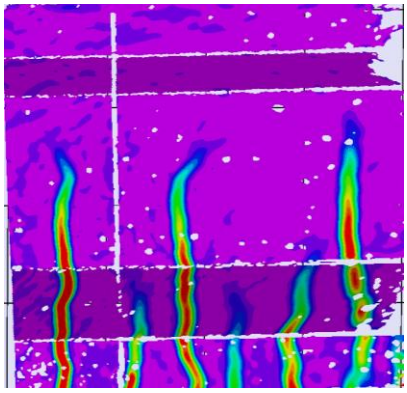

-0.00025 0.00895

Load Stage 3: 140k actuator load

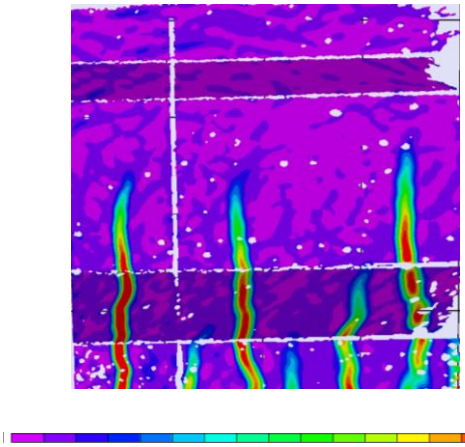

-0.00025 0.00645

Load Step 4: 130k actuator load

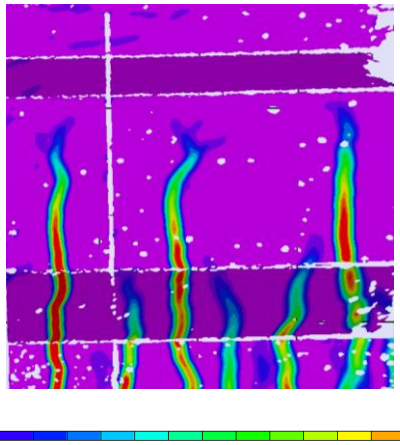

-0.0003 0.0139

Load Stage 4: 160k actuator load

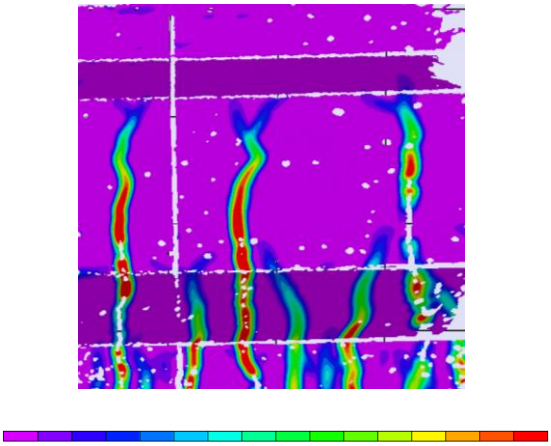

-0.0004 0.0218

Peak Load: 196k actuator load

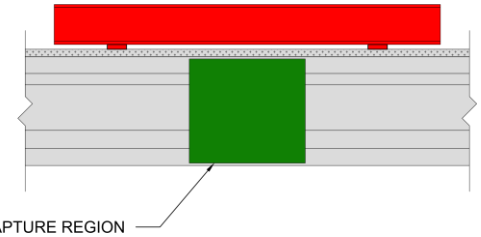

Figure C.38: Principal strain, ε_1, maps for BTE2.

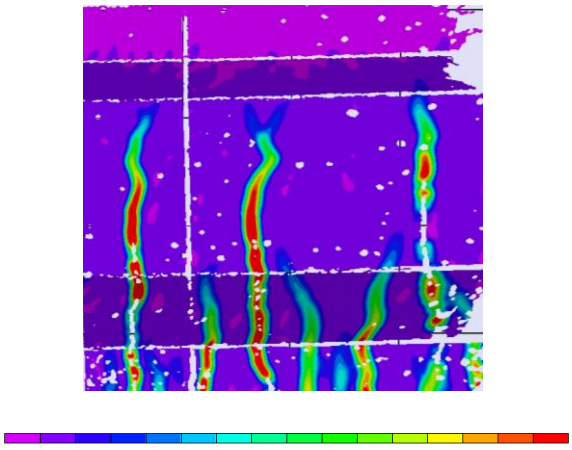

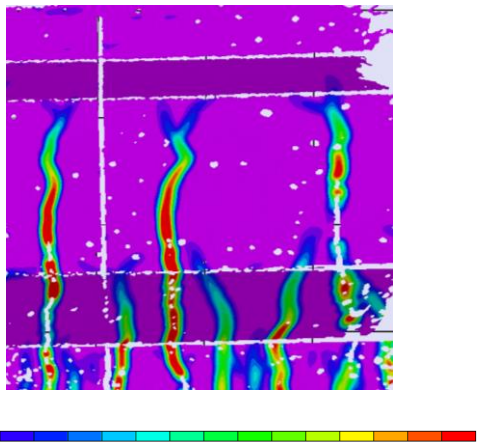

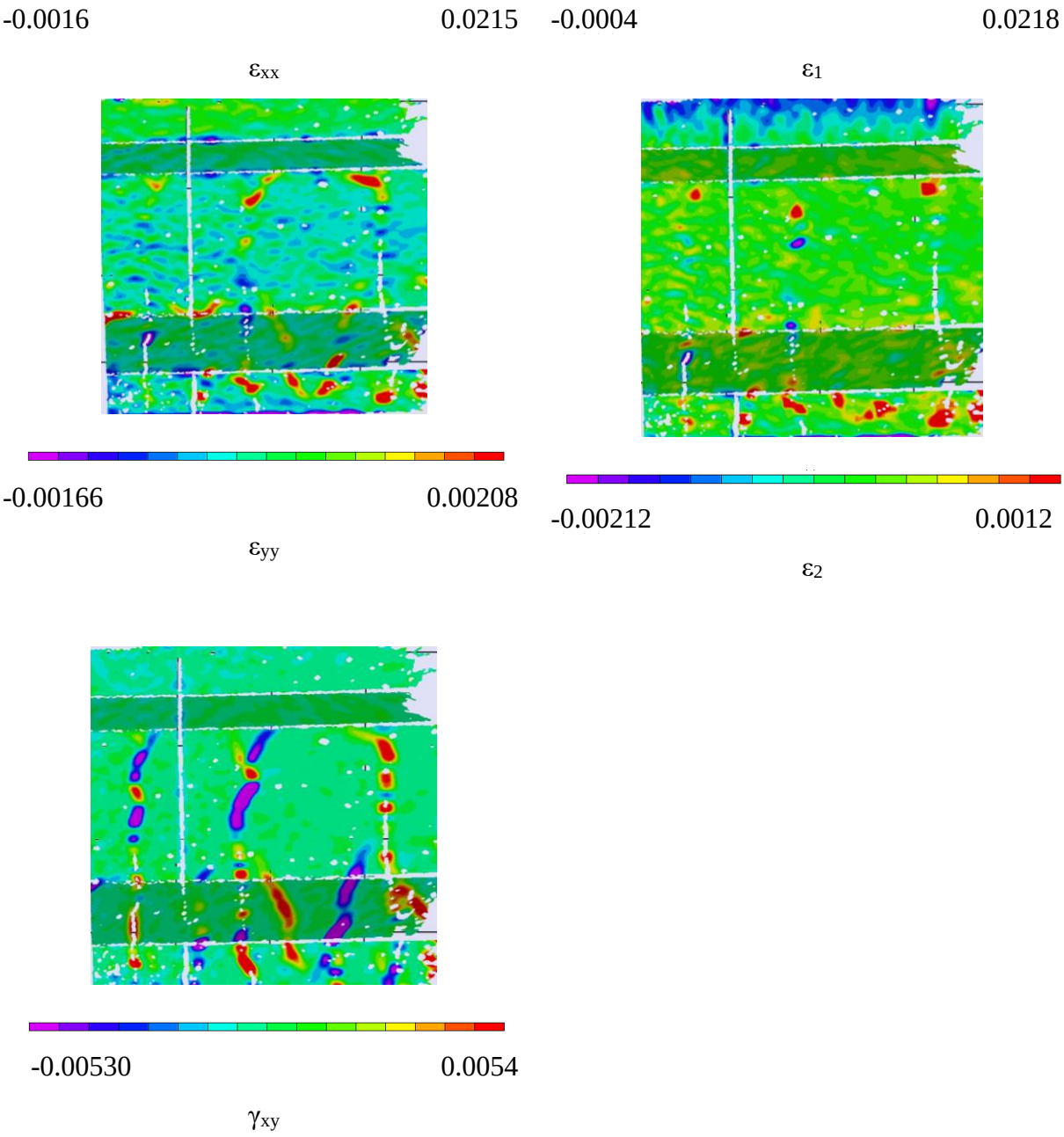

Figure C.39: BTE2 peak load strain maps.

C.3 BTE3 Flexural Testing

The experimental testing of BTE3 began on October 1st, 2021 with load cycles at different load levels to determine cracking and crack reopening moments. Like BTE2, the first load level for three load cycles reached 75 kips of actuator load corresponding to 37.5 kips of applied shear and an applied moment of approximately 985 k-ft. Consistent with previous tests, the trough of the

linear ramp cycles maintained at least 5 kips of actuator load to ensure no movement in the test apparatus occurred from spreader beam liftoff. During the three cycles up to 75 kips, there was no audible or visible cracking of the girder. The next load level reached 95 kips of actuator load corresponding to 47.5 kips of applied shear and an applied moment of approximately 1250 k-ft. As with the 75 kip load level, no audible or visible events were observed up to the 95 kip load level cycles. From 95 kips the load level was increased to 115 kips of actuator load corresponding to 57.5 kips of applied shear and an applied moment of 1510 k-ft. During the three cycles to 115 kips, flexural cracking on the beam began and the crack opening and closing was observed. Finally, the load level increased to 130 kips of actuator load corresponding to 65 kips of applied shear and an applied moment of 1710 k-ft. Flexural cracks became visible from a distance, and crack propagation into the web could be observed. Flexure shear cracking started to become visible in the web near the load plates in the shear spans.

After the load cycles at four load levels, the specimen was monotonically loaded with several load stages. The first load stage was taken at 100 kips of actuator load. During this load stage, cracks were marked and measured with a crack comparator and photos were taken of the specimen. Monotonic loading of the specimen was resumed until the next load stage at 120 kips occurred. Both the 100 kip and 120 kip load stages were lower load than the highest cyclic load level, so no additional cracking was observed during these load stages. The next load stage occurred at 140 kips of actuator load, and while loading to 140 kips, additional crack opening could be observed, and flexure shear cracking continued to propagate into the shear spans. The final load stage occurred at 160 kips of actuator load. During the loading to 160 kips, a controller limit was tripped at 150 kips that stopped hydraulic flow to the actuator momentarily. Without hydraulic flow to the actuator, the load reduced to 100 kips before hydraulic supply was restored and loading continued to 160 kips. As can be seen in the figures that follow there was no detrimental effect on strength or stiffness. While loading to the 160 kip load stage, more flexural cracks opened and flexure-shear cracks continued to widen and propagate from the load plates into the shear span. Consistent with BTE2, load staging was stopped after the 160 kip load stage, and the specimen was then monotonically loaded to peak. A summary of the cracks marked and measured at the load stages is provided in Figure C.40.

Prior to the test, it was decided to stop loading of BTE3 at 184 kips of actuator load to keep the entire span of BTE3 intact for future end region testing. The 184 kips of actuator load corresponds to 95% of the lowest peak moment attained in BTE1 and BTE2. Some concrete in the top flange began to spall off at 180 kips of actuator load which indicates the girder was approaching a flexural compression failure much like BTE1 and BTE2. The monotonic loading was stopped prior to flexural failure at 184 kips of actuator load corresponding to 2420 k-ft of applied moment.

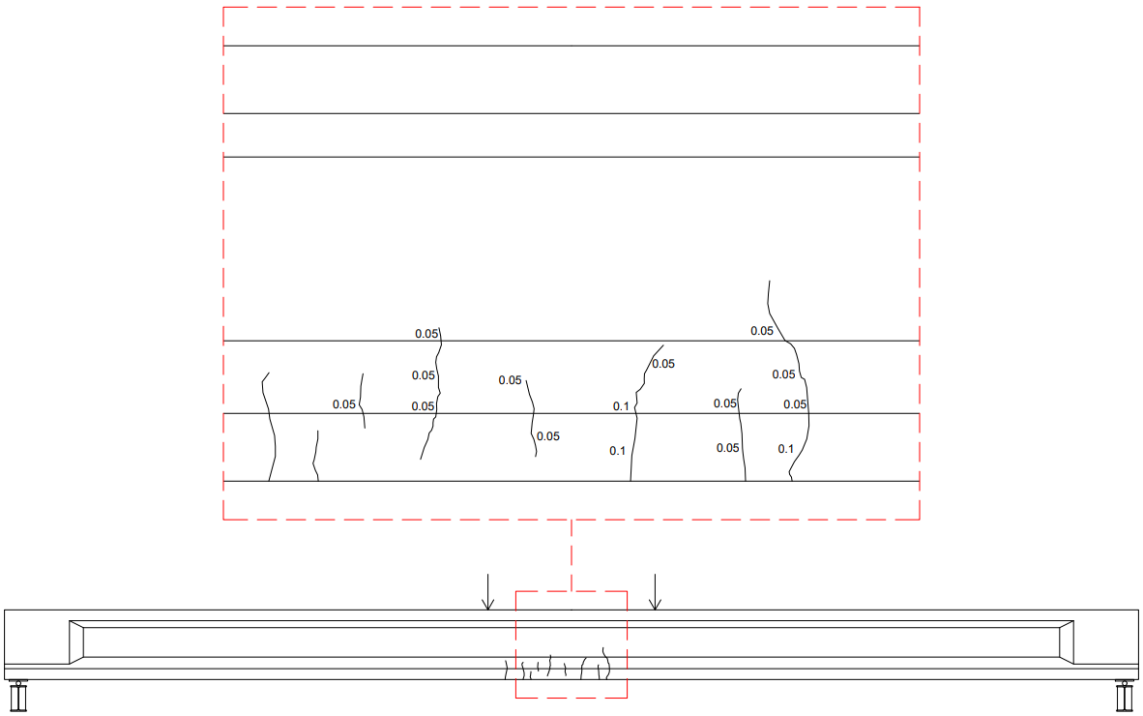

BTE3 Load Stage 1

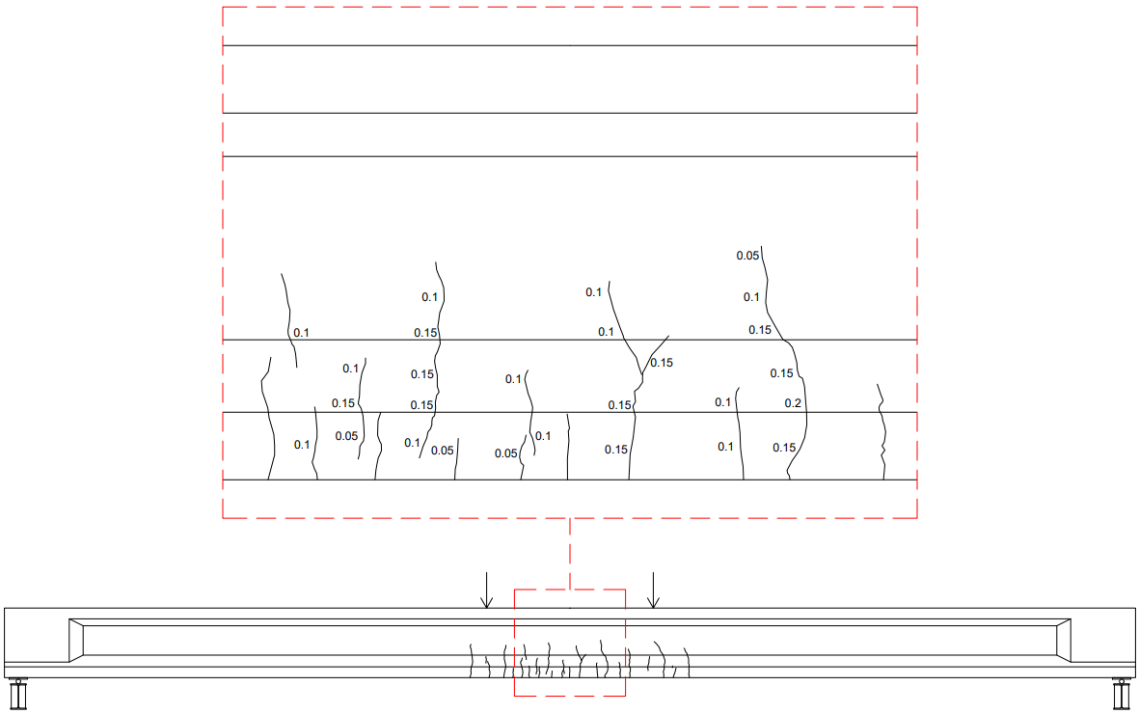

BTE3 Load Stage 2

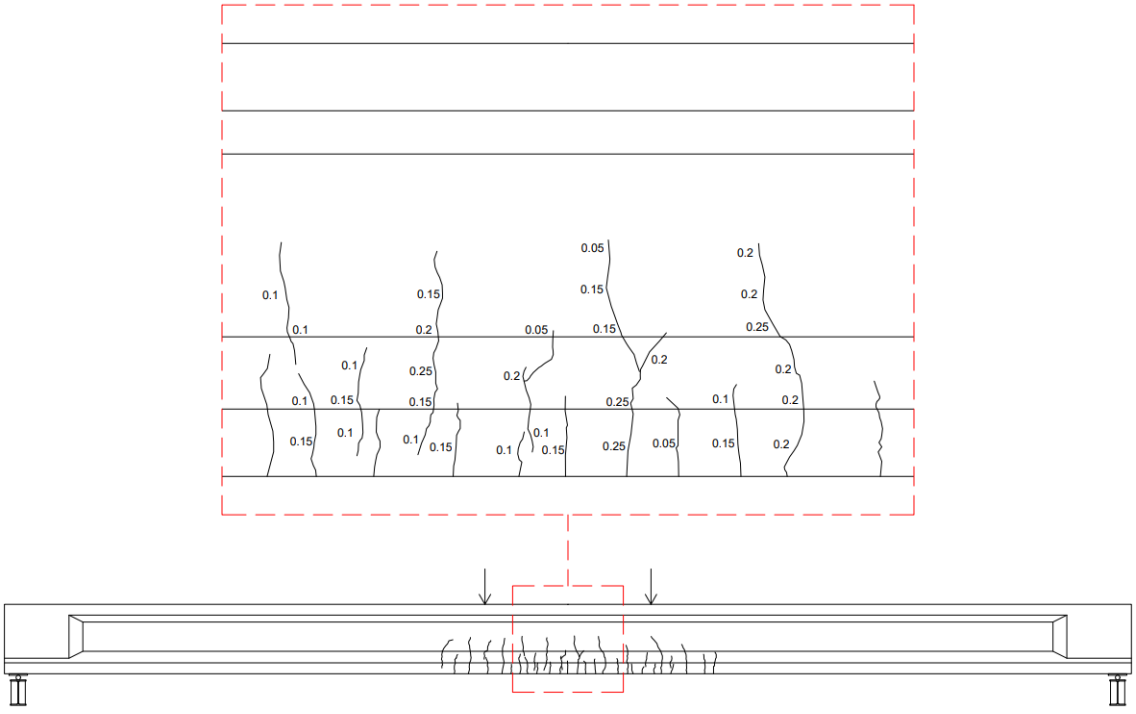

BTE3 Load Stage 3

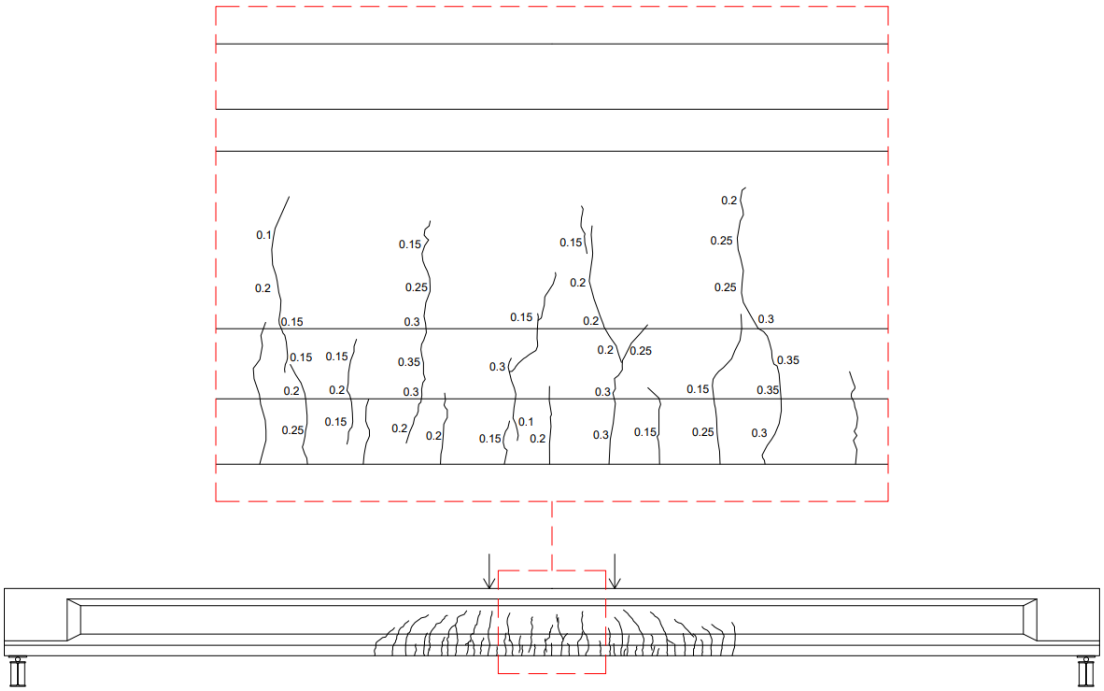

BTE3 Load Stage 4

Figure C.40: BTE3 load stage crack diagrams (Crack widths are in mm).

The load versus midspan displacement curves for the load cycles and monotonic loading to peak can be seen in Figure C.41. The maximum deflection of the girder was 5.41 in. at the peak applied load of 184 kips. The girder displacement at each of the five string potentiometers along the span for the monotonic loading can be seen in Figure C.42.

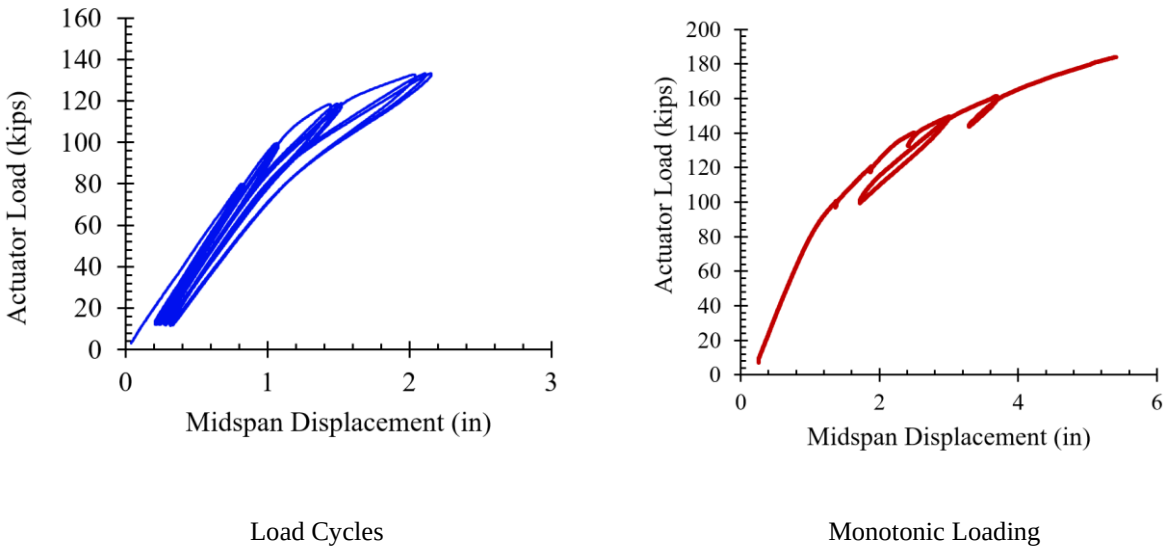

Load Cycles Monotonic Loading

Figure C.41: BTE3 load versus midspan displacement for load cycles and monotonic loading.

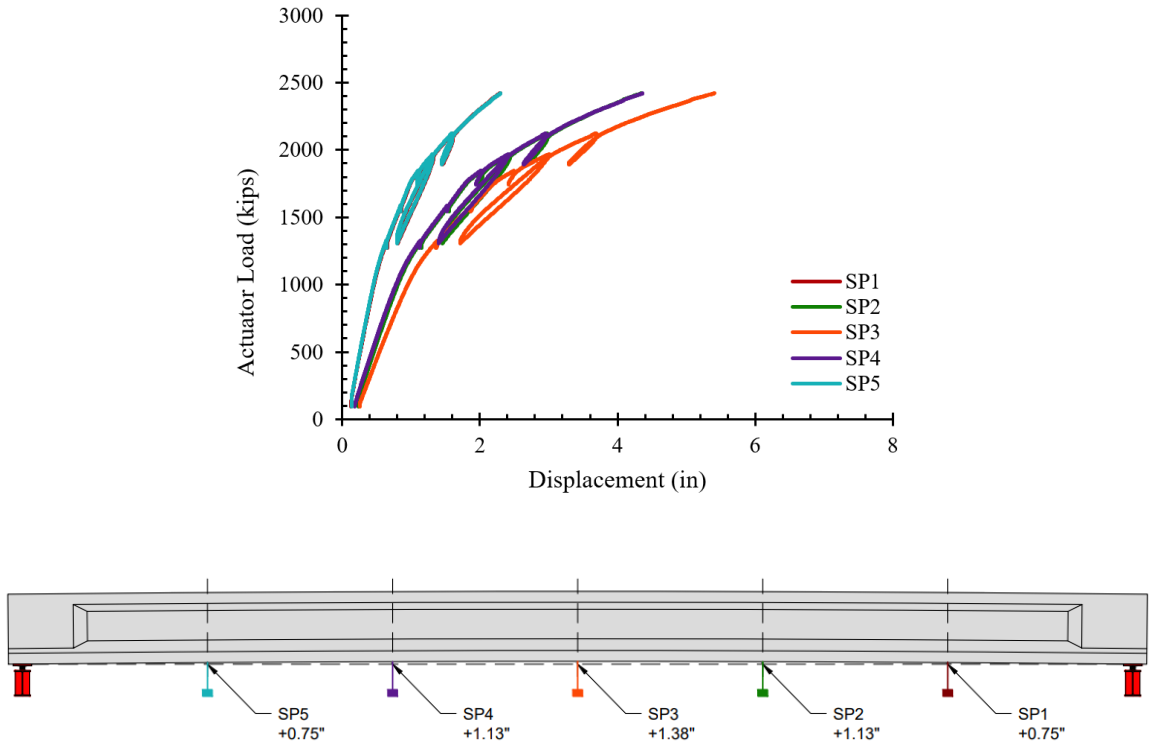

Initial Displacement

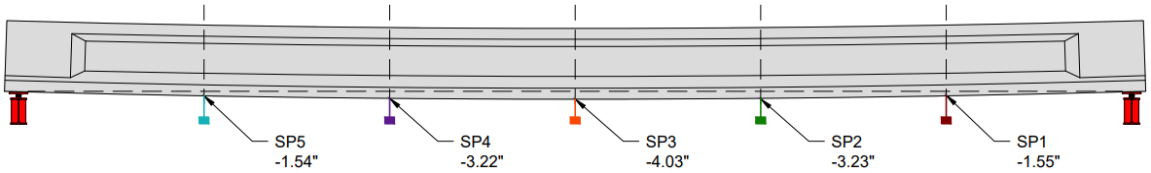

Displacement at Peak Load

Figure C.42: BTE3 displacement along the length.

In addition to load deflection data, the strains through the depth of the member were determined using both strain gauges and DIC data. Figure C.43 shows the top and bottom strains from each set of gauges, set 1 and set 2 throughout the load cycles conducted at four load levels..

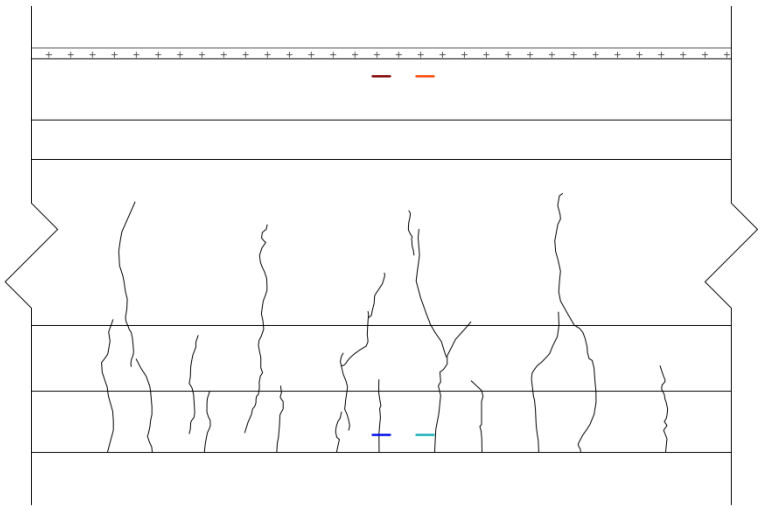

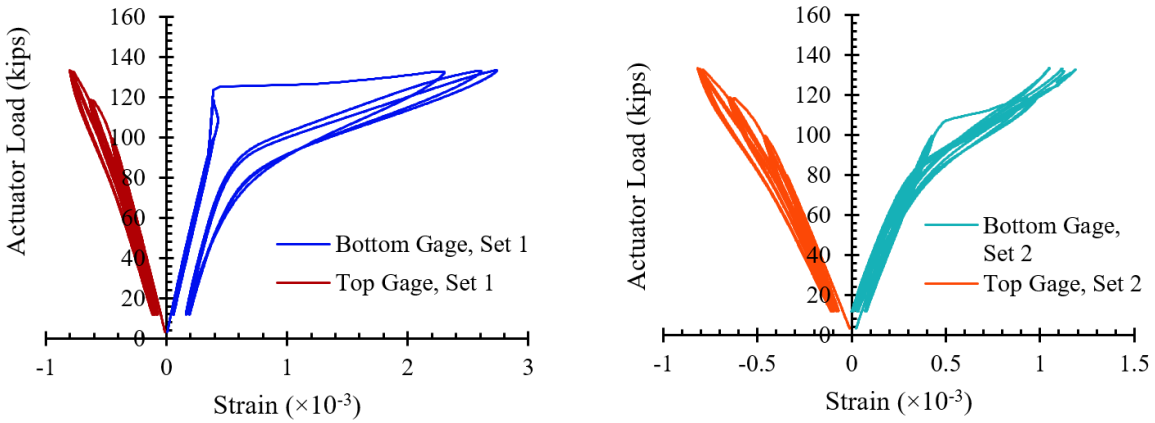

Figure C.43: BTE3 strain gauge data through three load cycles at each load level. Bottom gauge, set 1 (blue), top gauge, set 1 (red), bottom gauge, set 2 (teal), top gauge, set 2 (orange).

As can be seen in Figure C.43 above, the top strains remain elastic throughout the load cycles, and the bottom gauges indicate cracking of the girder. The bottom gauge on the second set crossed a crack and shows dramatic increases in strain post cracking. To compare DIC results to the strain gauge data, points were used at the same location as the first set of strain gauges corresponding to the girder's midspan. The results from the DIC points can be seen in Figure C.44.

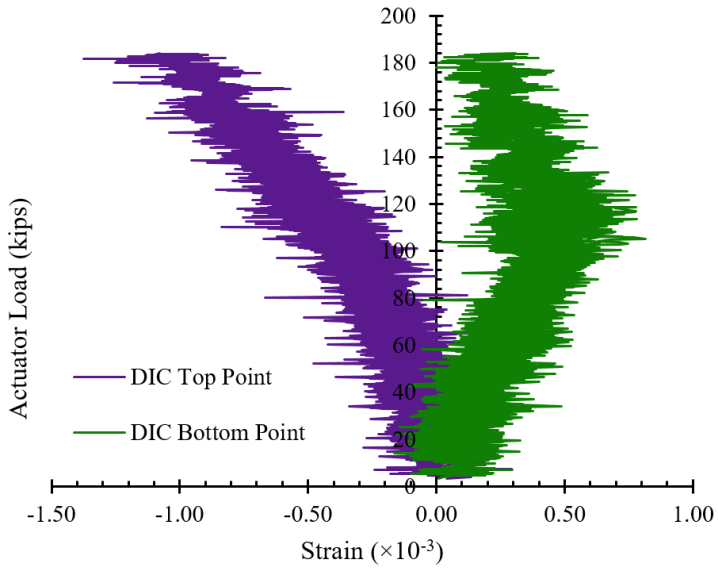

Figure C.44: BTE3 DIC point strains at girder midspan through load cycles at each load level.

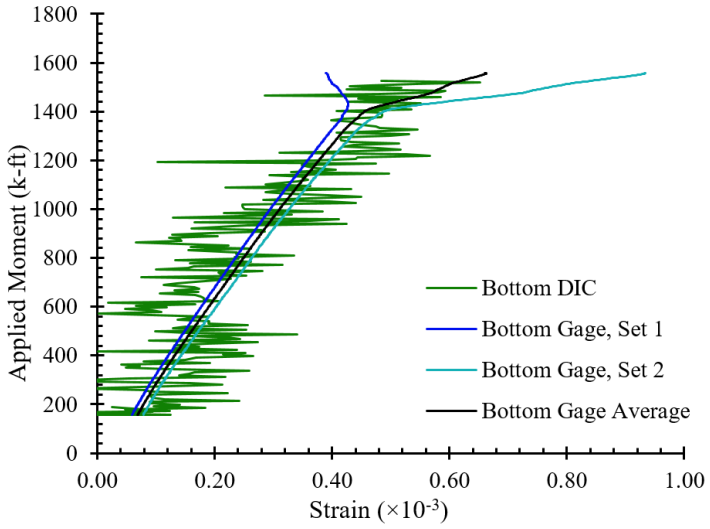

Figure C.45: BTE3 strain comparison between DIC point and strain gauge for first cycle up to 115 kips actuator load.

As with the strain gauges, DIC shows that the top strains remain elastic throughout the load cycles. Bottom strains remain elastic only up to the point of cracking. Cracking corresponds to change in stiffness observed in Figure C.44. Also, like BTE2, the DIC point near the bottom flange indicates lower strains at higher actuator loads, so the concrete beneath the point is becoming debonded at higher strains. The strains from DIC bottom point is compared to the average bottom strain gauge behavior for the cracking cycle in Figure C.45. The response agrees reasonable well. To further understand strains through the depth during loading, horizontal extensometers were used in DIC post-processing at four locations through the depth near midspan. These extensometers provide longitudinal strains through the depth for each image taken during the test. The strains through the depth can be seen for each of the four load steps during load cycles, the four load stages of monotonic loading, and the ultimate load for the girder in Figure C.46.

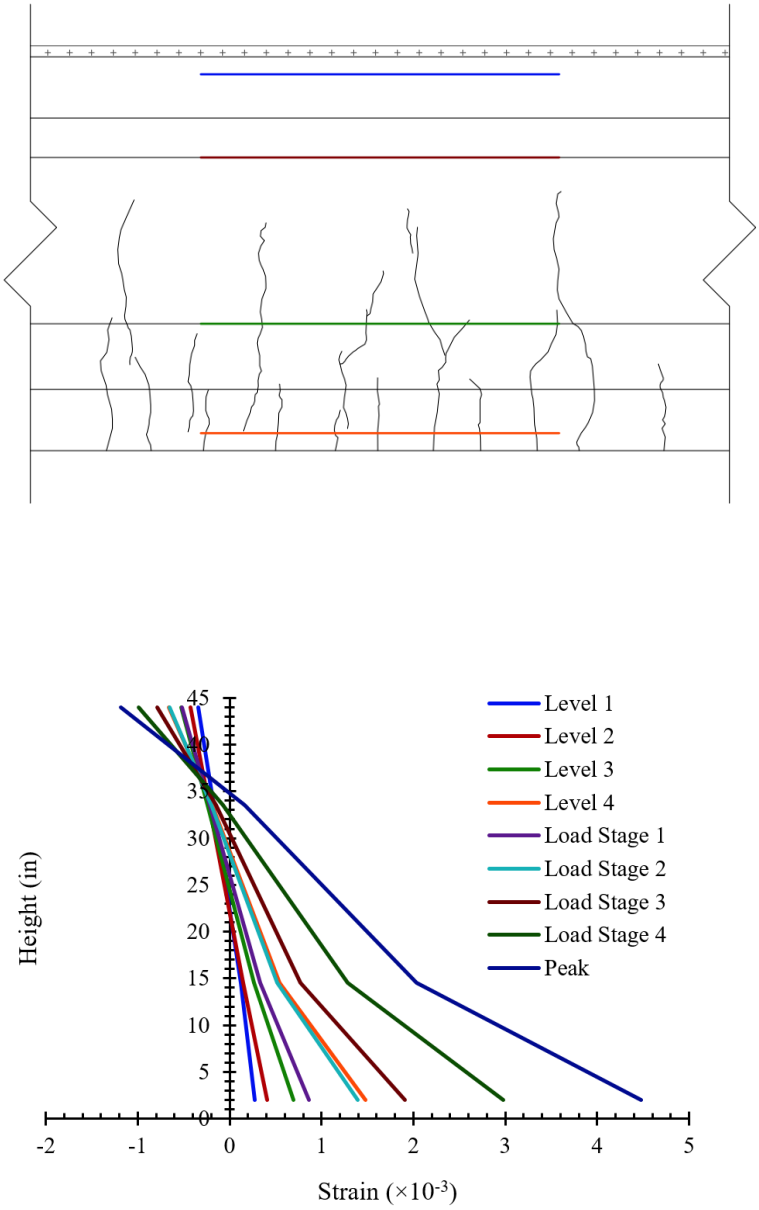

Figure C.46: BTE3 DIC horizontal extensometer strain profile.

The longitudinal strains from the DIC extensometers initially indicate a linear distribution of strains through the depth. Figure C.28 shows that, like BTE2, the strain reading at 15 in. above the bottom of the girder reads is less than expected for a linear strain variation at loads greater than 130 kips. However, the strain variation from the top to the bottom of the specimen remains linear when the strains at 15 in. height are omitted.

Virtual extensometers in DIC post-processing were also used to determine the elongation across cracks during the load cycles to determine when the crack first opened, when the crack closed and when the crack re-opened. Before cracking of the specimen, the virtual extensometer reads elastic elongation of the girder, but at cracking the extensometer elongation increases suddenly. Upon unloading, extensometer elongation decreases rapidly and when the crack has closed, the slope of the applied moment-extensometer elongation curve becomes similar to that of the uncracked section. The virtual extensometer was placed over the first crack that occurred on the girder, and the location and elongation of the extensometer can be seen in Figure C.29. The extensometer elongation is a five point moving average of the DIC data.

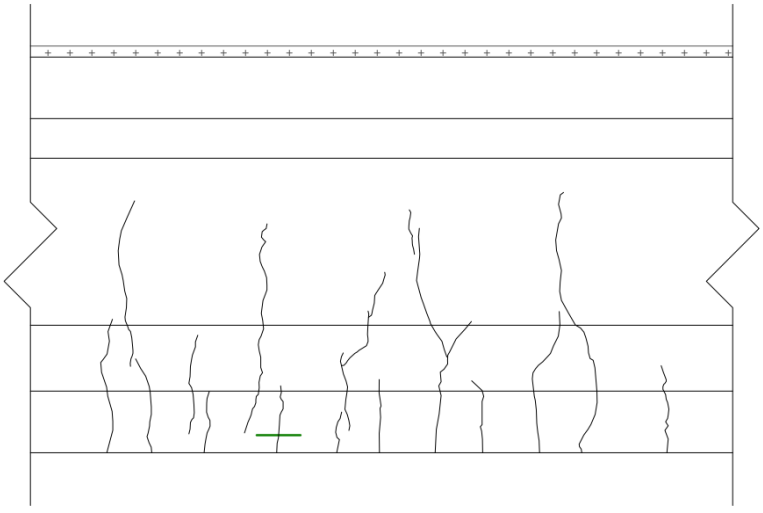

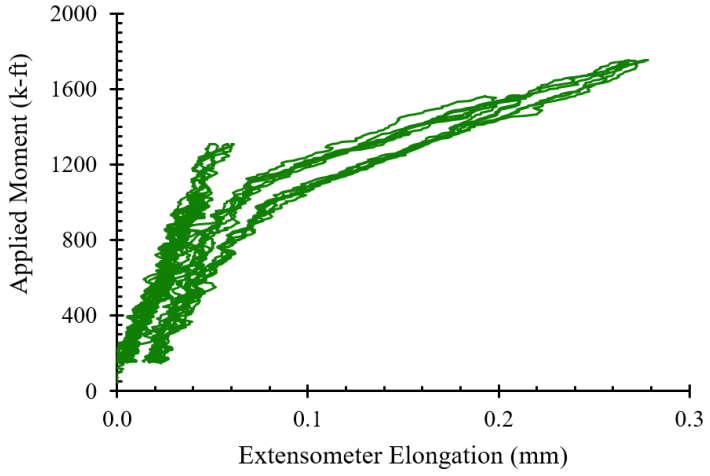

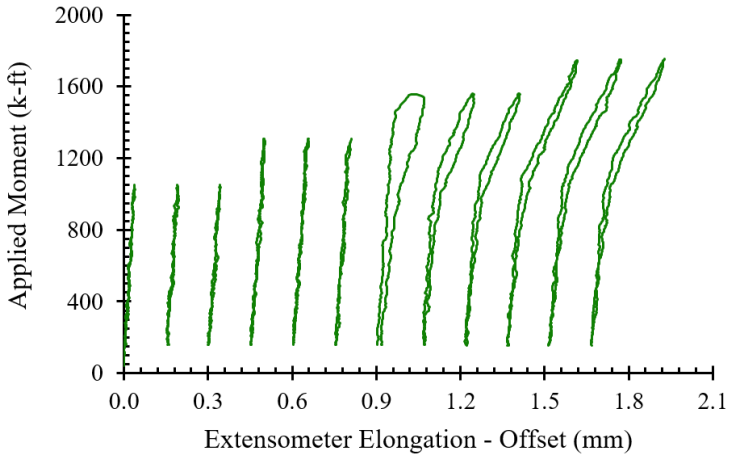

Figure C.47: BTE3 first crack virtual extensometer.

Figure C.47 shows the applied moment against extensometer elongation with an offset of elongation for each cycle. The three cycles for load steps of 75 and 95 kips of actuator load remain elastic. The first cycle up to 115 kips of actuator load is the first instance of cracking in the girder because there is a sudden increase in the extensometer's elongation at the peak load for that cycle. Figure C.48 highlights on the first cycle up to 115 kips of actuator load, and the transition from uncracked extensometer elongation to cracked elongation can be seen. However, the determination of exact point of stiffness change requires careful investigation.

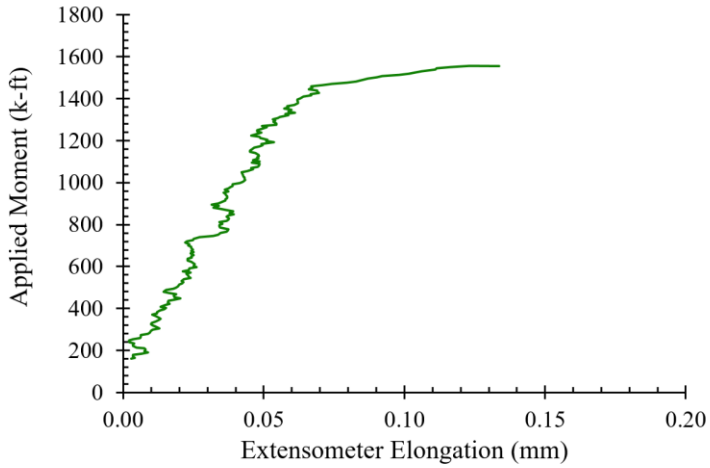

Figure C.48: BTE3 applied moment versus extensometer elongation showing stiffness change during cracking.

The cracking moment and crack reopening moment was determined following the approach outlined for BTE1 and BTE2 where two virtual extensometers were used. The extensometer E1 was placed on the crack and the E5 placed between cracks. Both the extensometers are at a distance of 1.75 in from the bottom of girder. The E0 and E1 extensometer elongation was plotted against the applied load. The extensometer placed between cracks provides measurements of the elastic elongation throughout the loading. The extensometer placed over the crack provides detailed crack opening and closing data. At a load of 101.4 kips, the extensometer placed at the location of first crack show a sharp change in elongation (Figure C.49). This sudden change in elongation occurs when the crack forms. Both the extensometer elongations agree up to first cracking. The point at which they diverge can be used to determine when first cracking. To further verify the load at which first cracking occurs, a 20 point moving average of the extensometer elongation versus load was plotted against the midspan displacement (Figure C.49). The filtering approach helps make clear when the section transitions from uncracked to a cracked section. The average slope starts to increase at an applied moment of 1334 k-ft corresponding to a displacement of 28.0 mm (26.7 mm in Figure C.49 is the moving average value and lower than the actual displacement) which matches with the corresponding DIC strain map (Figure C.50). The DIC strain map at this particular instant shows high strains around the extensometer indicating

either the crack has formed or is on the verge of propagating. Thus, the cracking moment is 1334 k-ft.

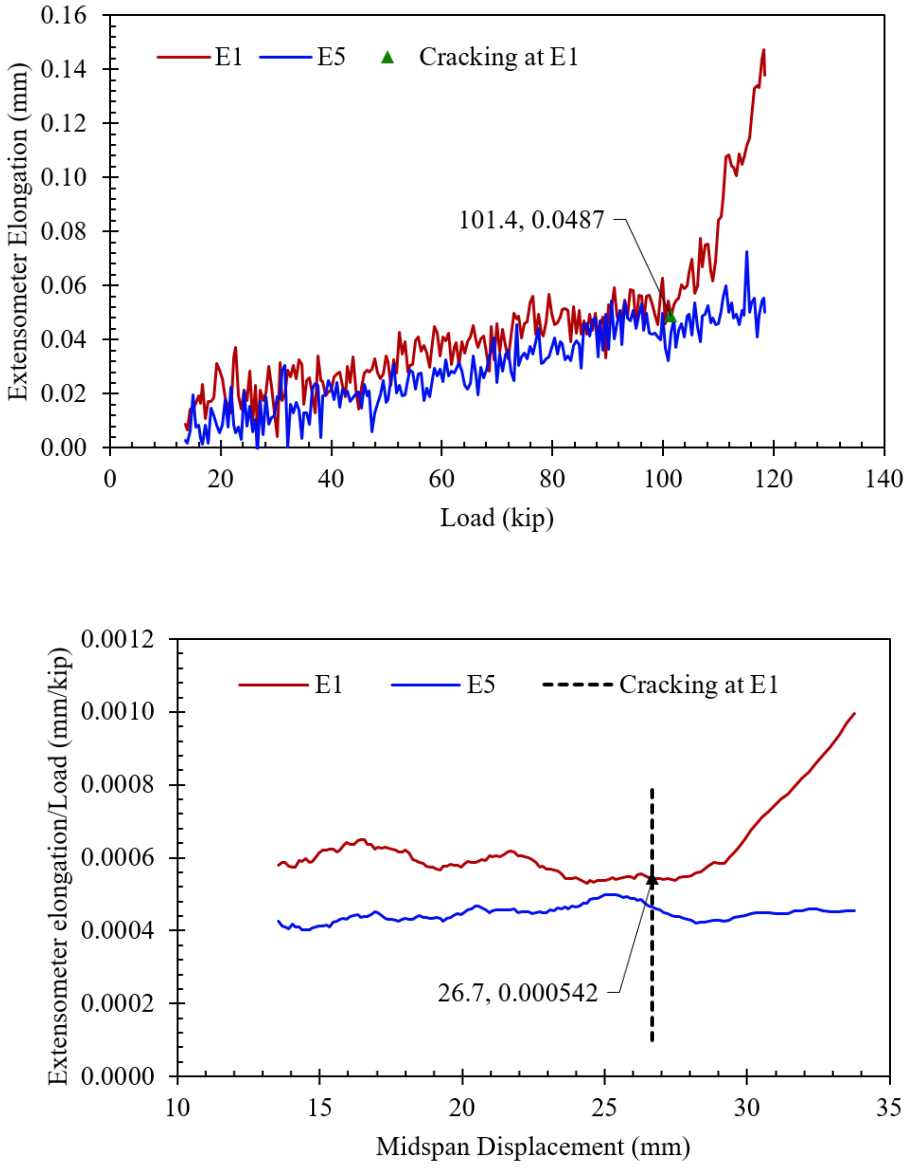

Figure C.49: Identifying first instance of cracking of BTE3.

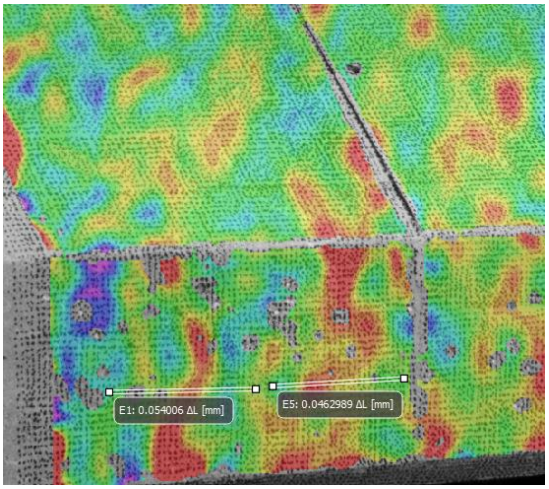

Figure C.50: Principal strain (ε_1) map at Cracking Moment

The crack reopening moment was determined in a similar way by placing extensometer E0 on the crack and E4 away from the crack. The crack reopening moment was found to be 991 k-ft (Figure C.51). The DIC strain map corresponding to an applied moment of 991 k-ft shows high strains around the extensometer indicating the crack has either reopened up to the height of the extensometer E0 or on the verge of propagating (Figure C.52).

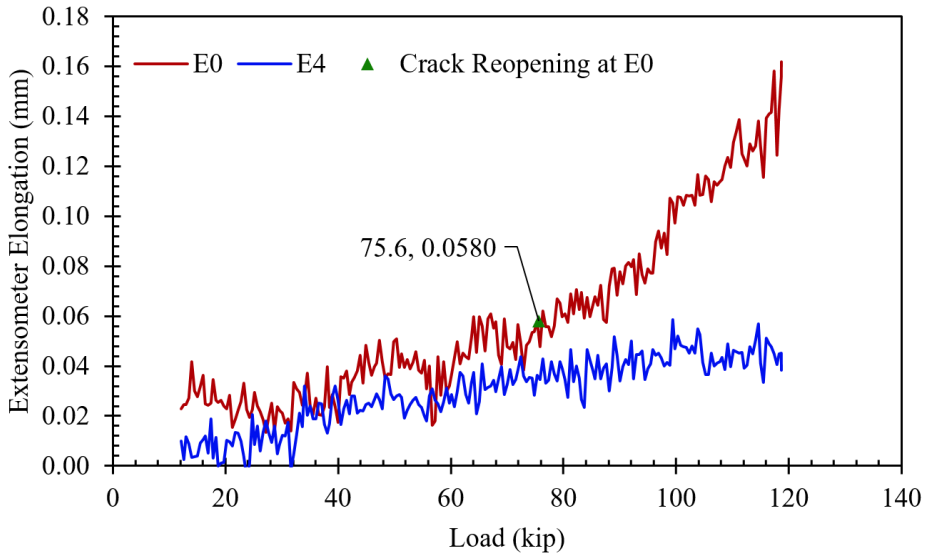

Figure C.51: Identifying first instance of crack reopening of BTE3.

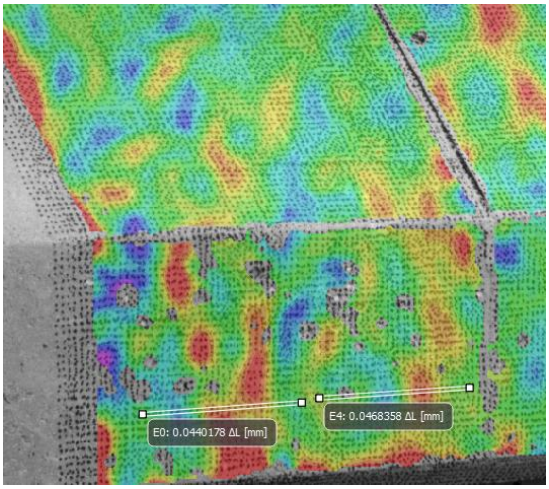

Figure C.52: Principal strain (ε_1) map at Cracking Reopening Moment

The cracking moment and crack reopening moment also agrees with the applied moment versus extensometer elongation plot as shown in Figure C.53.

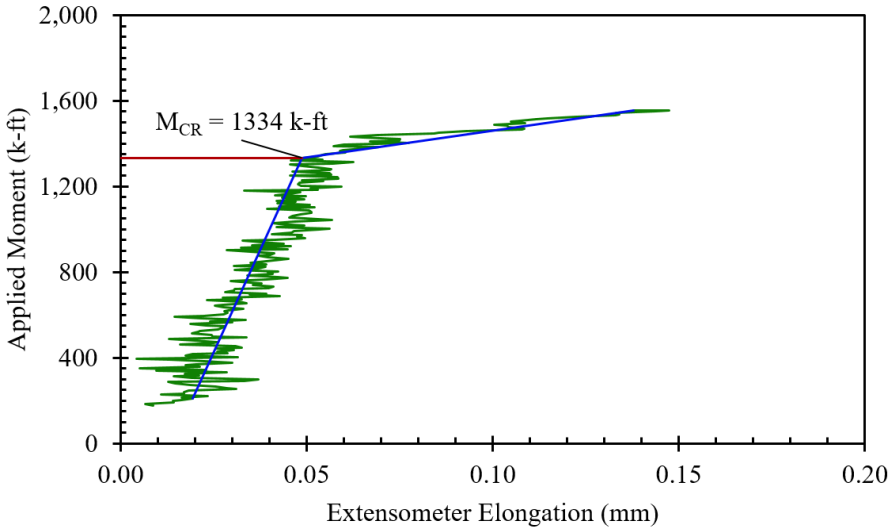

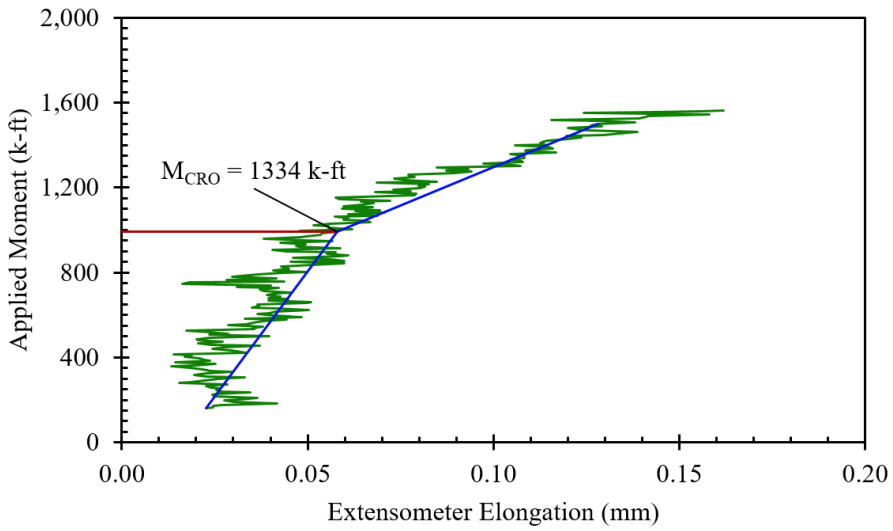

Figure C.53: BTE3 applied moment versus extensometer elongation with bi-linear approach to find (a) Cracking Moment (b) Crack Reopening Moment.

The first cracking and crack reopening moments found above are corroborated by strain maps generated in DIC post-processing of the principal strain, ε_1. Figure C.54 and Figure C.55 show the initial cracking of the girder and the reopening of the crack, respectively.

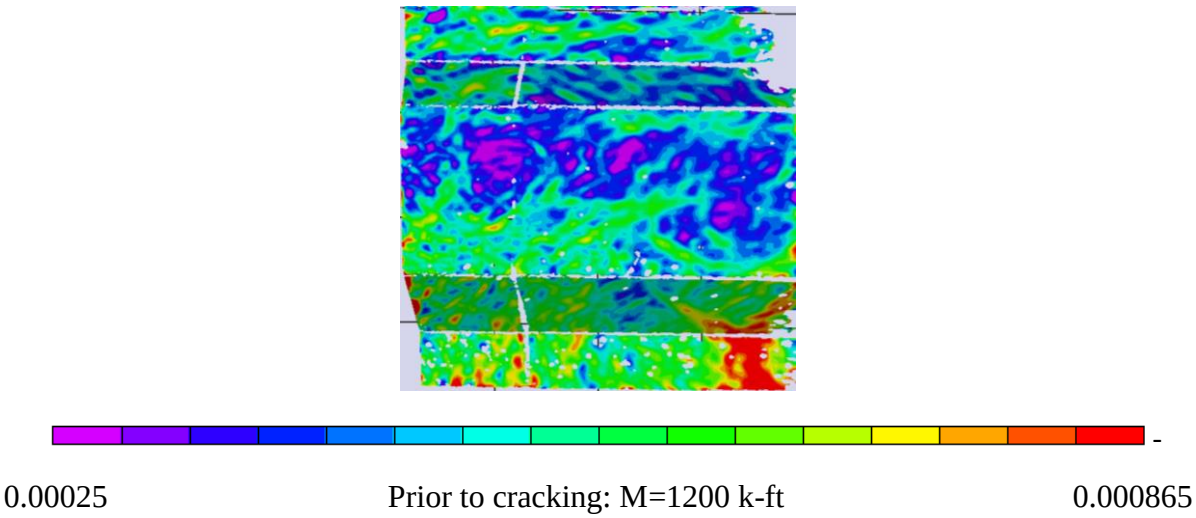

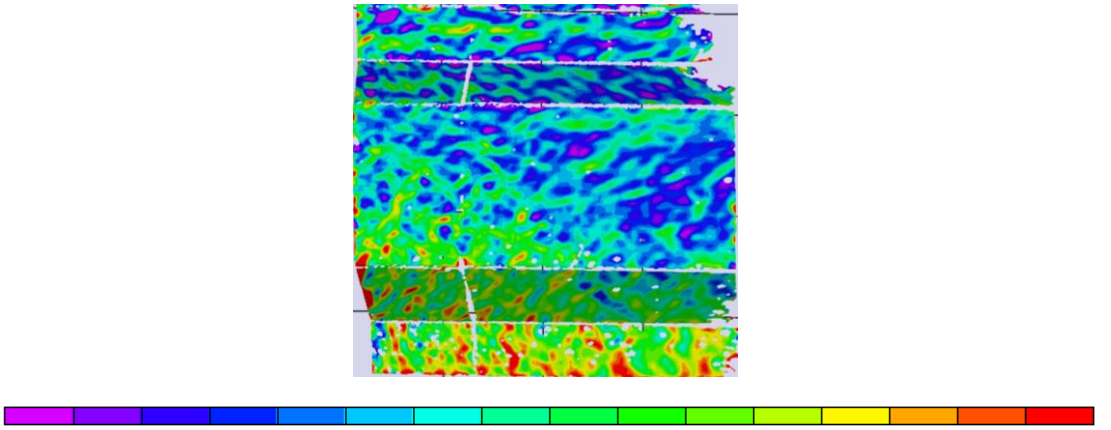

-0.00023 Cracking: M=1334 k-ft 0.00071

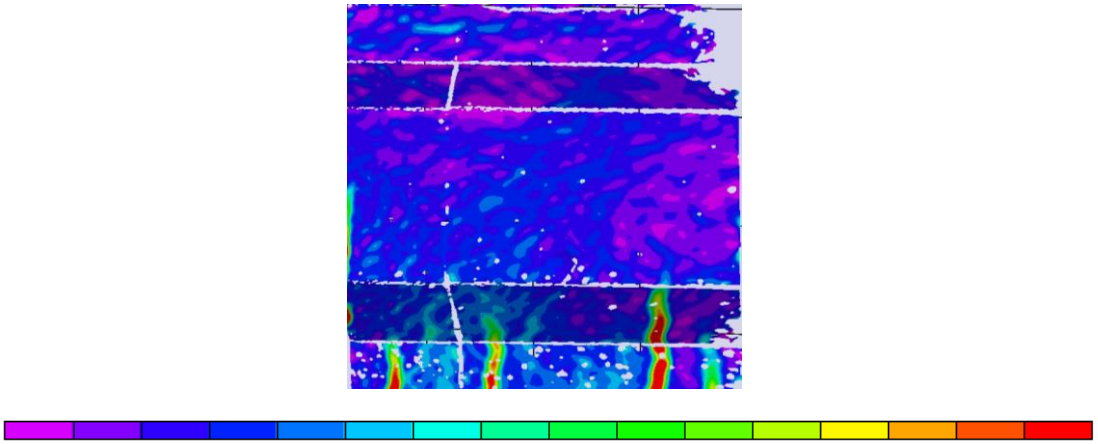

-0.00028 Post-cracking: M=1550 k-ft 0.00268

Figure C.54: BTE3 principal strain maps (ε_1) indicating cracking.

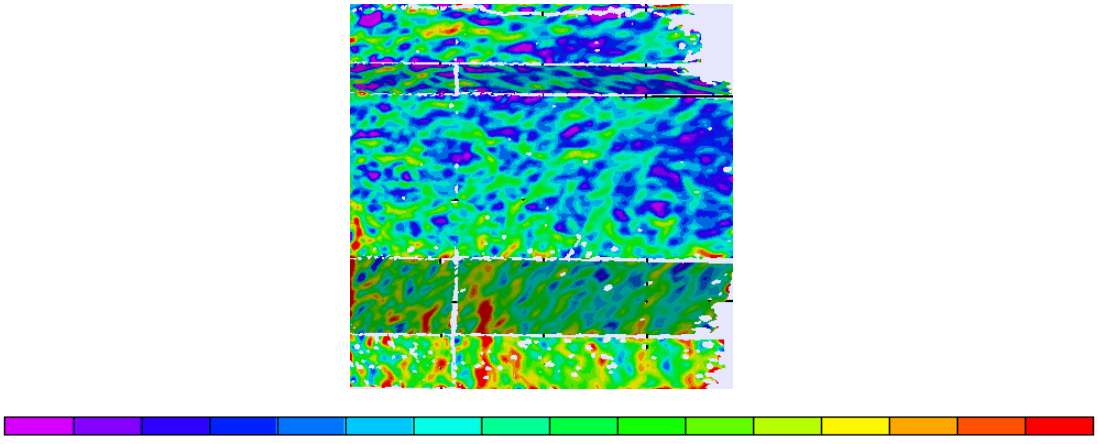

-0.000205 Prior to reopening: M=900 k-ft 0.00064

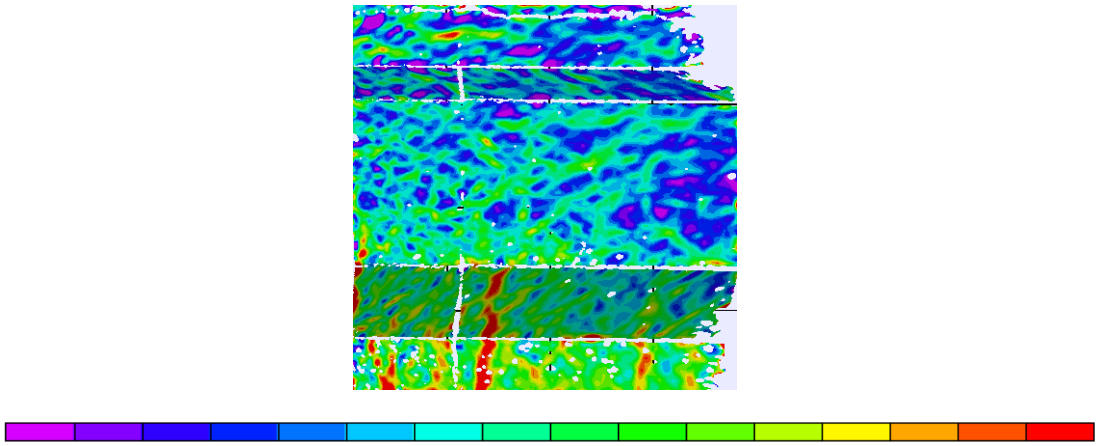

-0.00021 Crack reopening: M=990 k-ft 0.000725

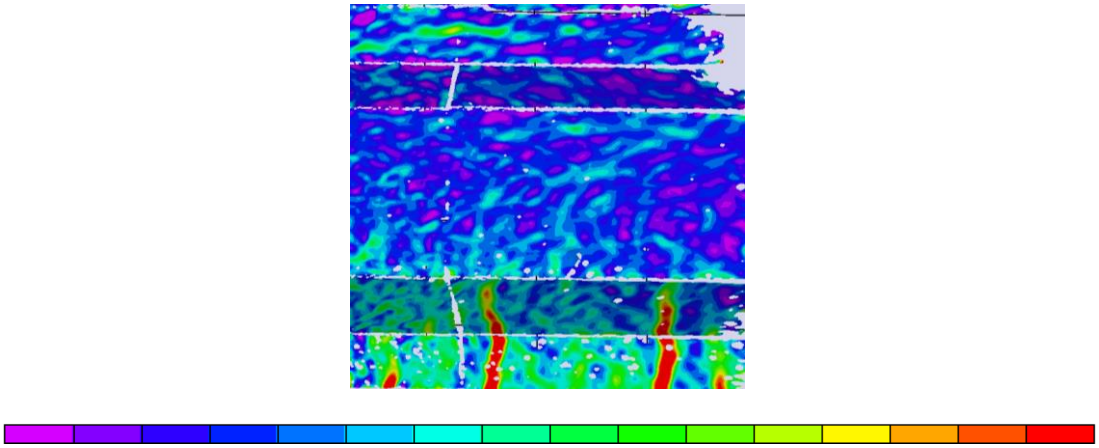

-0.00017 Post reopening: M=1200 k-ft 0.00118

Figure C.55: BTE3 principal strain maps (ε_1) indicating crack reopening.

Strain maps for the full DIC field of view between the load plates are provided below. The principal strain, ε_1, maps for each of the four load steps during load cycles, the four load stages of monotonic loading, and the ultimate load are provided in Figure C.56. These maps show tensile strains with strain concentrations around the flexural cracks. Figure C.57 shows the peak load strain maps for axial strains, ε_x and ε_y, shear strain, γ_{xy}, and principal strains, ε_1 and ε_2.

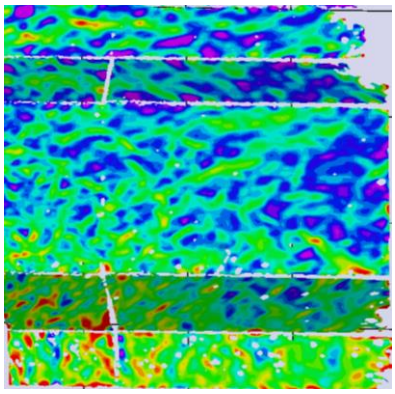

-0.000205 0.000595

Load Step 1: 75k actuator load

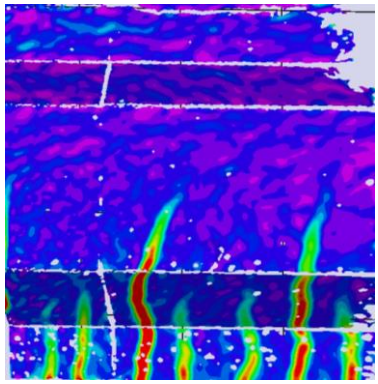

-0.00022 0.0025

Load Stage 1: 100k actuator load

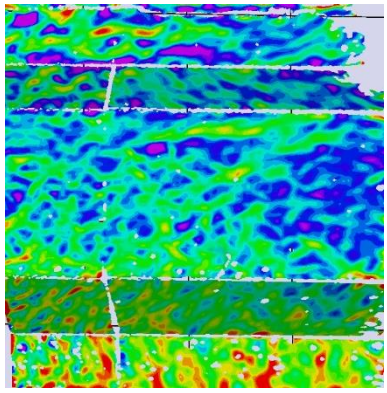

-0.00022 0.00065

Load Step 2: 95k actuator load

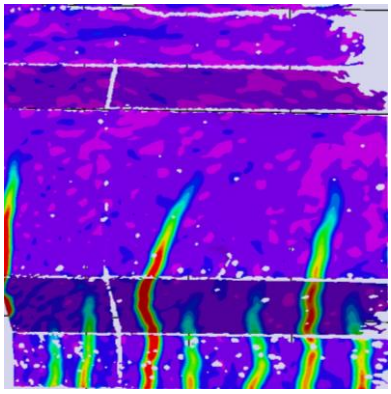

-0.0003 0.0053

Load Stage 2: 120k actuator load

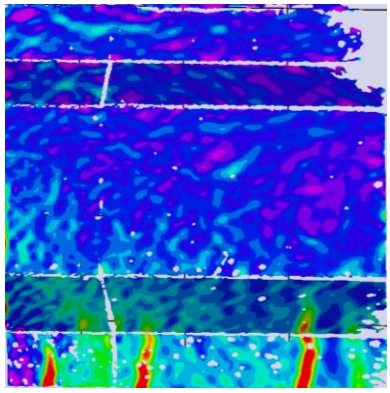

-0.00029 0.00188

Load Step 3: 115k actuator load

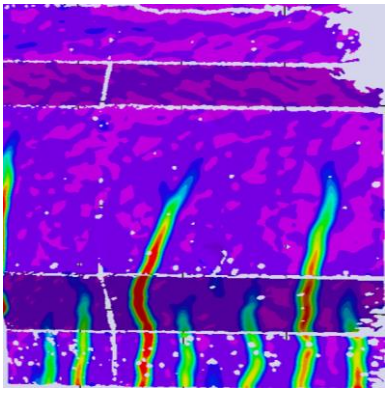

-0.0004 0.00835

Load Stage 3: 140k actuator load

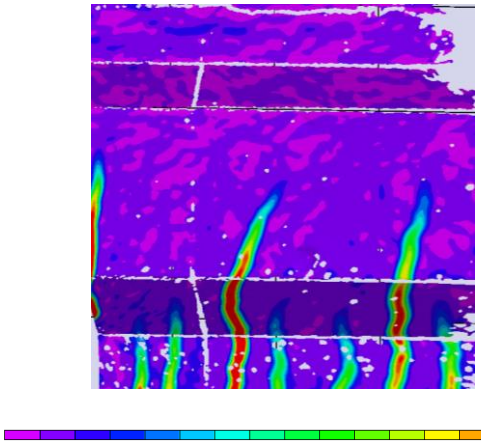

-0.0003 0.00625

Load Step 4: 130k actuator load

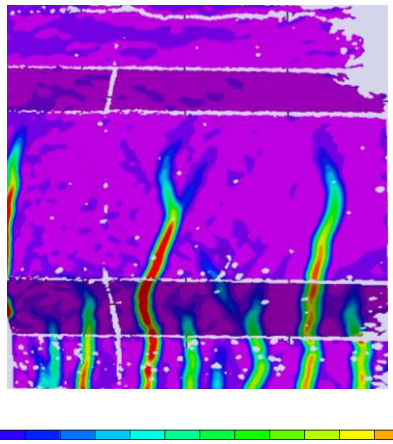

-0.0005 0.0129

Load Stage 4: 160k actuator load

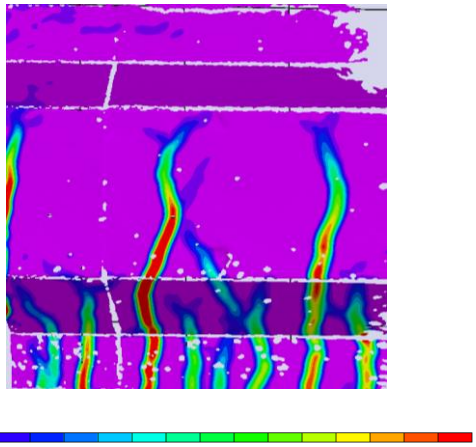

-0.0005 0.0187

Peak Load: 184k actuator load

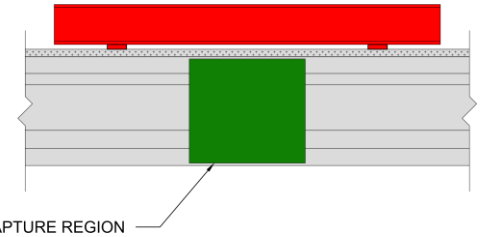

Figure C.56: Principal strain, ε_1, maps for BTE3.

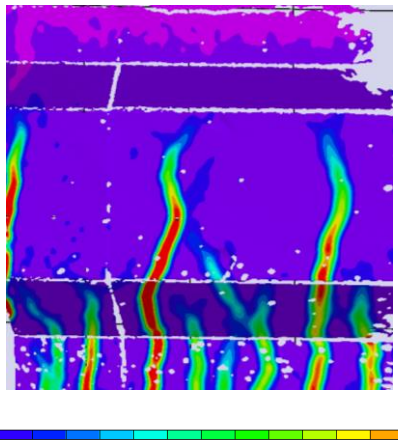

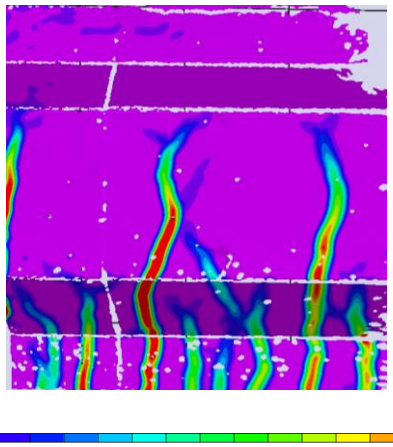

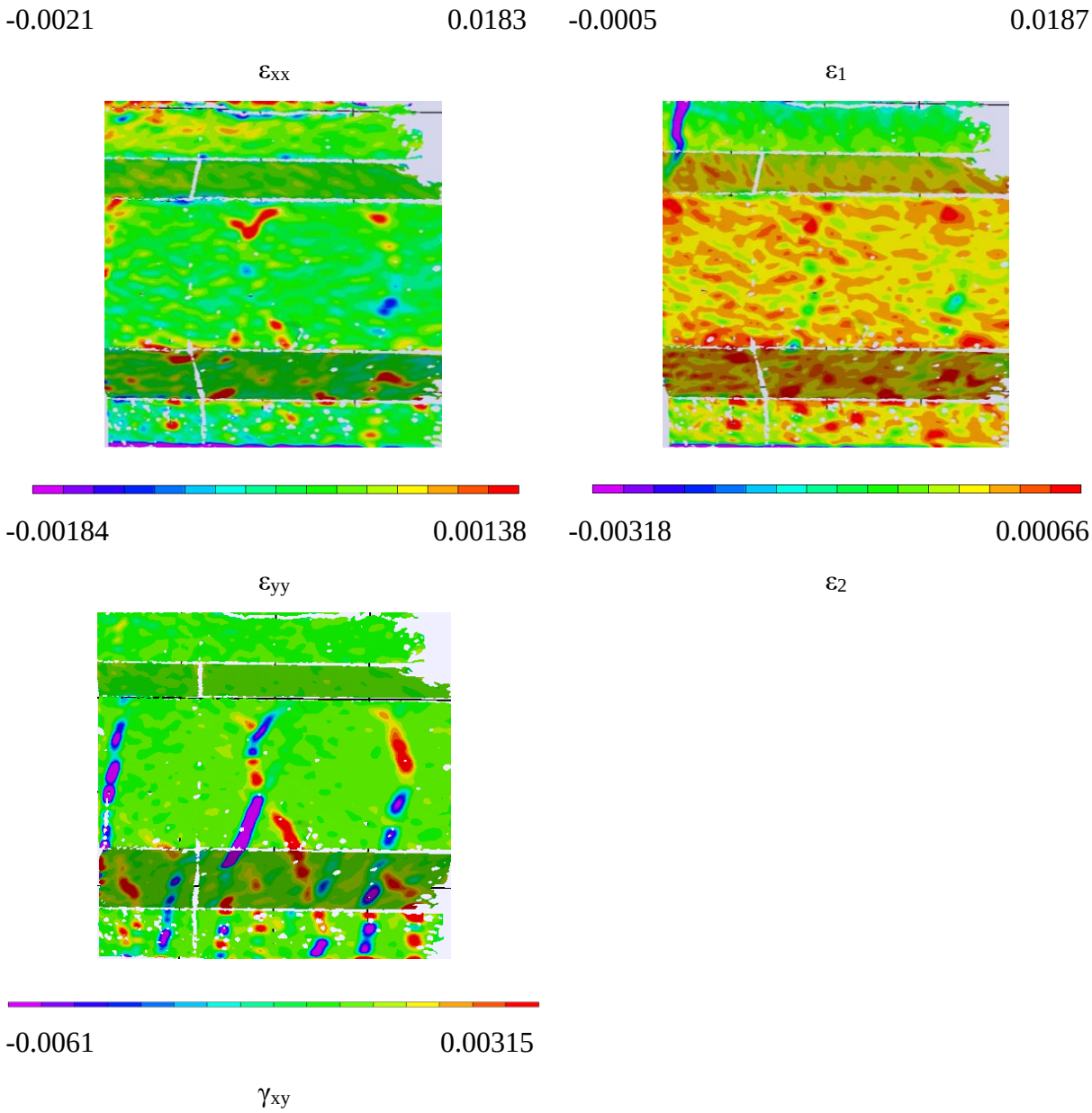

Figure C.57: BTE3 peak load strain maps.

C.4 BTE4 Flexural Testing

The experimental testing of BTE4 began on November 5th, 2021 with load cycles to determine cracking and crack reopening moments. Like BTE2, the first load level for the load cycle reached 75 kips of actuator load corresponding to 37.5 kips of applied shear and an applied moment of approximately 985 k-ft. Consistent with previous tests, the trough of the linear ramp cycles

maintained at least 5 kips of actuator load to ensure no movement in the test apparatus occurred from spreader beam liftoff. During the three cycles up to 75 kips, there was no audible or visible cracking of the girder. The next load level was 95 kips of actuator load corresponding to 47.5 kips of shear and an applied moment of approximately 1250 k-ft. As with the 75 kip load level, there was no audible or visible events observed up to the 95 kip load level cycles. From 95 kips the load level was increased to 115 kips of actuator load corresponding to 57.5 kips of applied shear and an applied moment of 1510 k-ft. During the three cycles to 115 kips, flexural cracking on the beam began and crack opening and closing was observed. Finally, the load level reached 130 kips of actuator load corresponding to 65 kips of applied shear and an applied moment of 1710 k-ft. Flexural cracks became visible from a distance, and crack propagation into the web was observed. Flexure shear cracking started to become visible in the web on either side of the load plates outside the flexural region.

After the load cycles, the specimen was monotonically loaded with several load stages. The first load stage was taken at 100 kips of actuator load. During this load stage, cracks were marked and measured with a crack comparator and photos were taken of the specimen. Monotonic loading of the specimen was resumed until the next load stage at 120 kips occurred. Both the 100 kip and 120 kip load stages were lower load than the highest load level that occurred during load cycles, and so no additional cracking was observed during these load stages. The next load stage occurred at 140 kips of actuator load, and while loading to 140 kips, additional crack opening was observed, and flexure shear cracking continued to propagate into the shear spans. The final load stage occurred at 160 kips of actuator load. While loading to the 160 kip load stage, crack opening was observed and flexure-shear cracks continued to widen and propagate. Consistent with BTE2, load staging was stopped after the 160 kip load stage, and the specimen was then monotonically loaded to peak. Prior to the test, it was decided to stop loading of BTE4 at 184 kips of actuator load to keep the entire span of BTE4 intact for future end region testing. The 184 kips of actuator load corresponds to 95% of the lowest peak moment attained by the previous two girders. The monotonic loading was stopped prior to flexural failure at 184 kips of actuator load corresponding to 2420 k-ft of applied moment. A summary of the cracks marked and measured at the load stages is provided in Figure C.58.

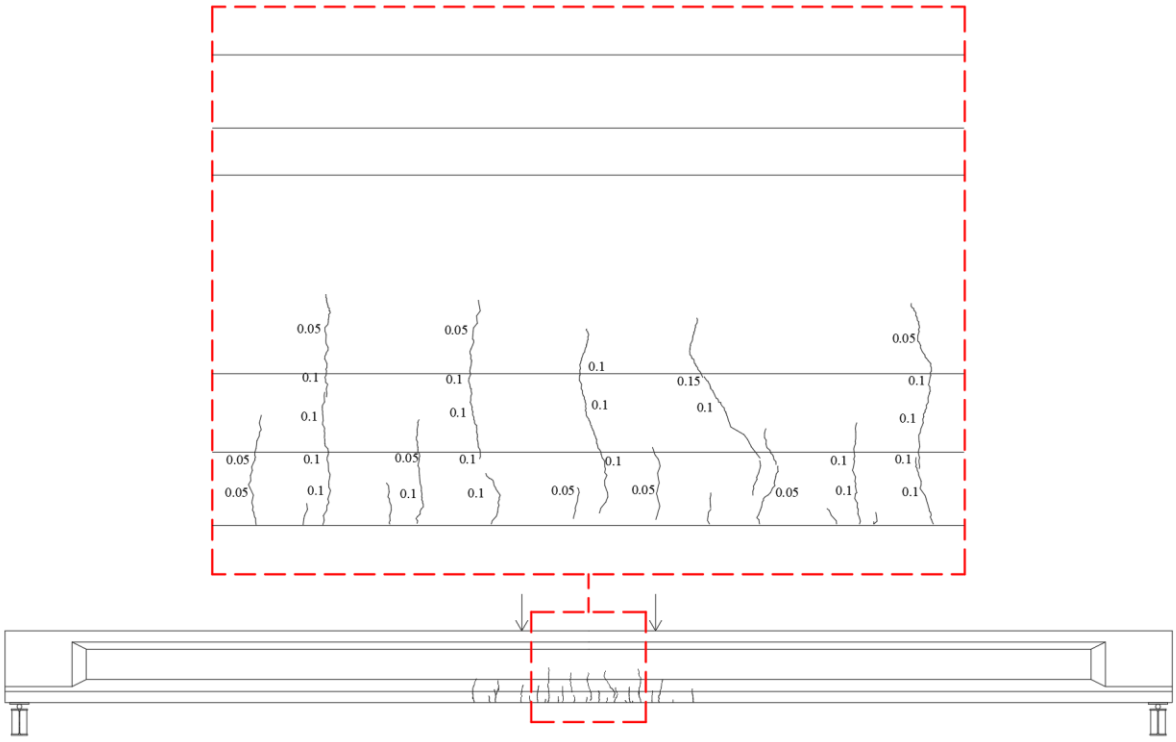

BTE4 Load Stage 1

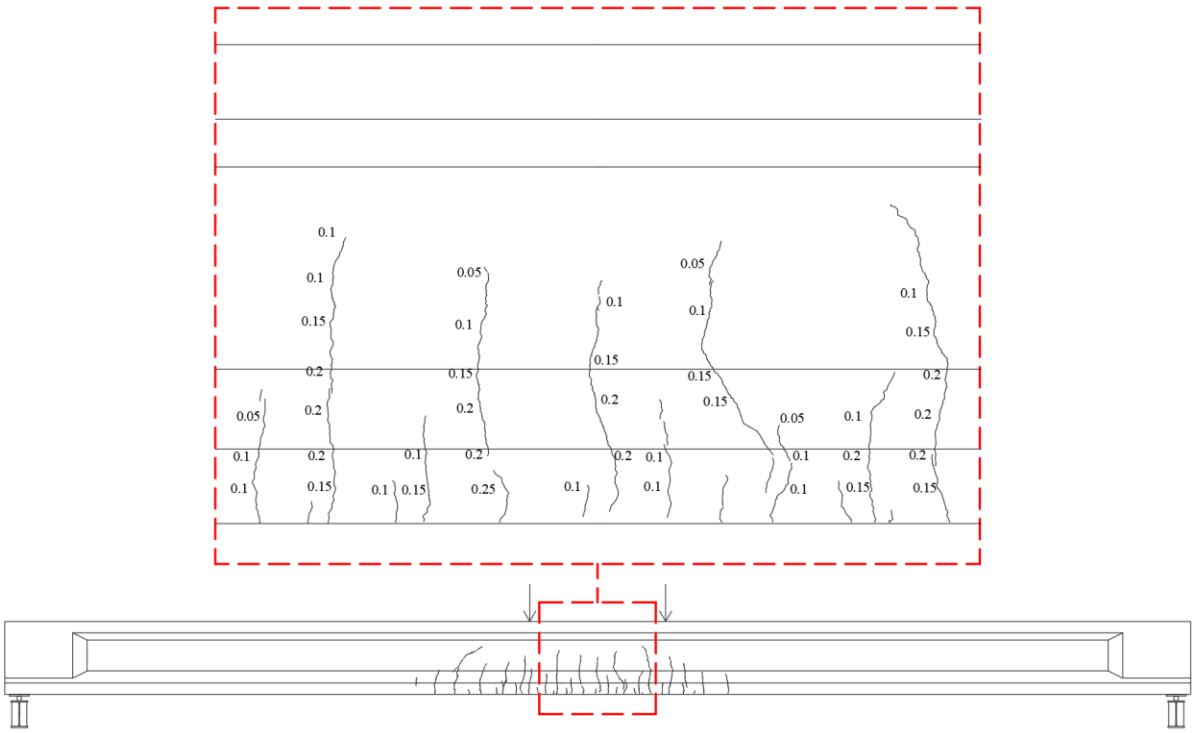

BTE4 Load Stage 2

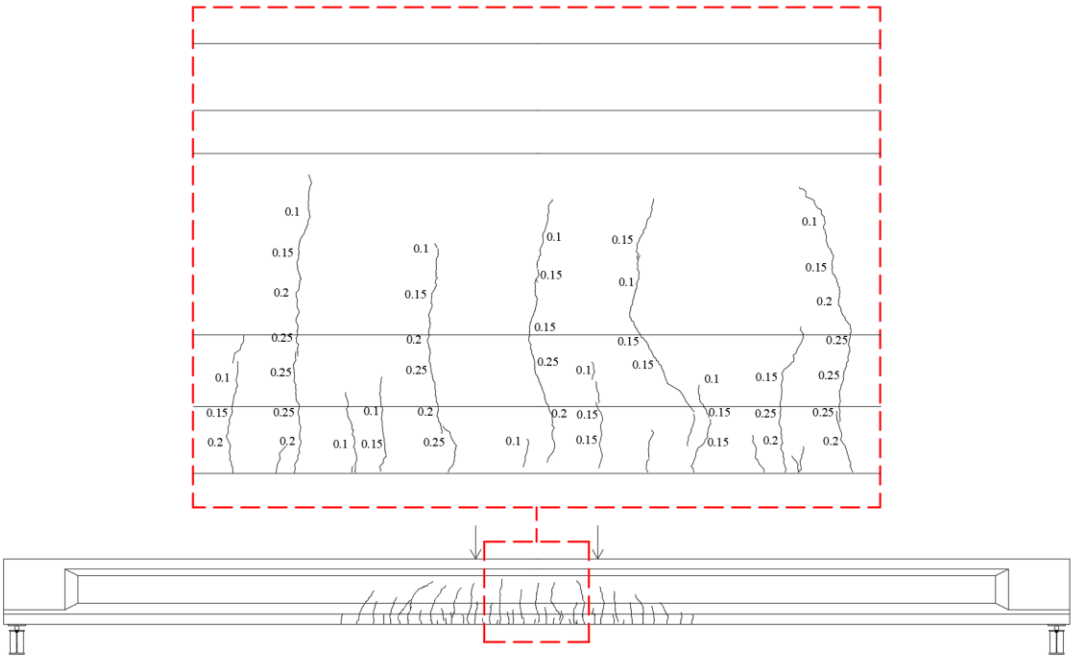

BTE4 Load Stage 3

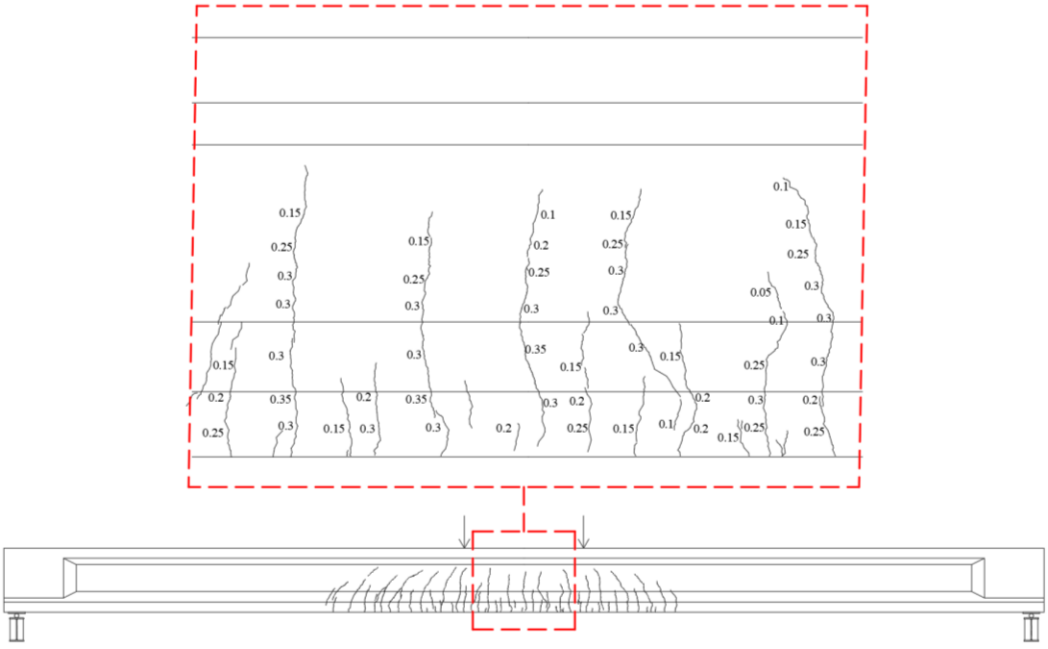

BTE4 Load Stage 4

Figure C.58: BTE4 load stage crack diagrams (Crack widths are in mm).

The load versus midspan displacement curves for the initial load cycles and monotonic loading to peak can be seen in Figure C.59. The maximum deflection of the girder was 5.64 in. at the peak applied load of 184 kips.

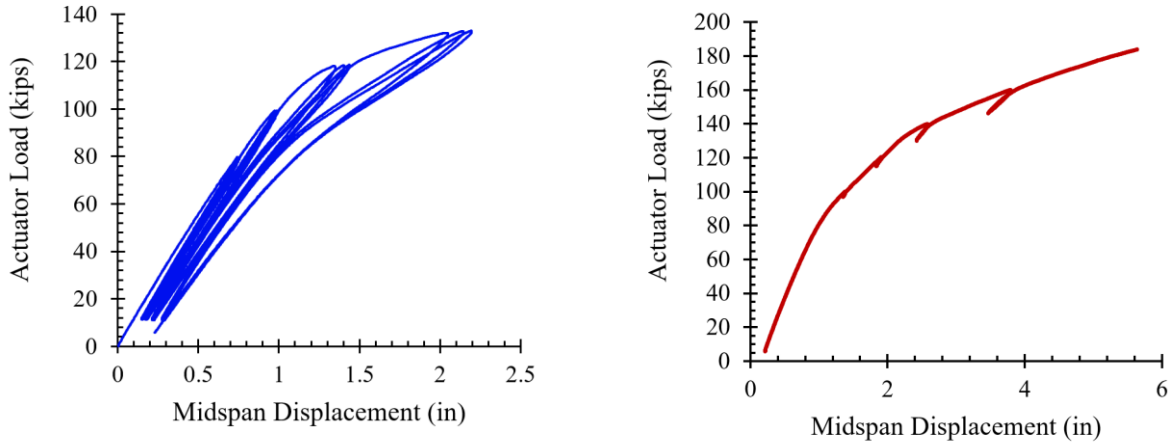

Load Cycles

Monotonic Loading

Figure C.59: BTE4 load versus midspan displacement for load cycles at each load level and monotonic loading to peak.

The girder displacement at each of the five string potentiometers along the span for the monotonic loading can be seen in Figure C.60. The string potentiometers show symmetric distribution along the length of girder.

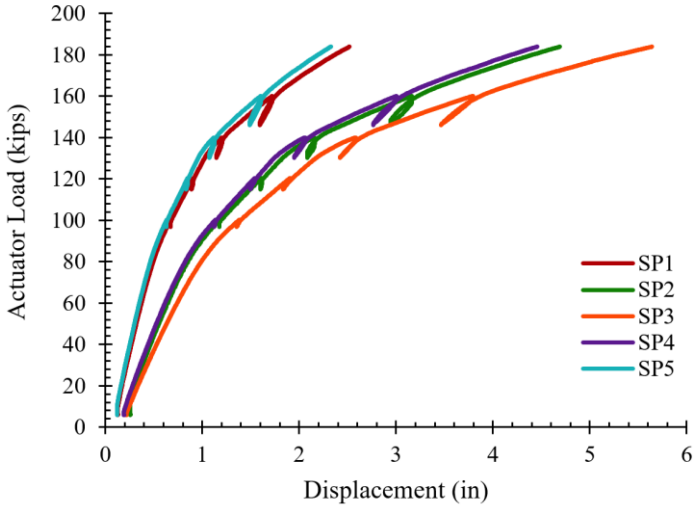

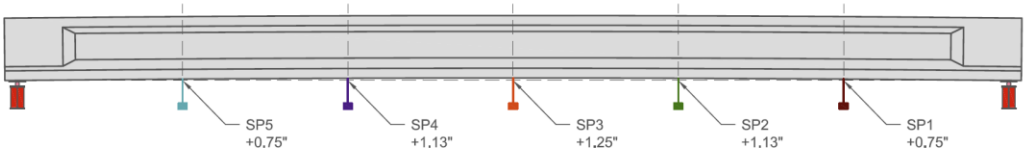

Initial Displacement

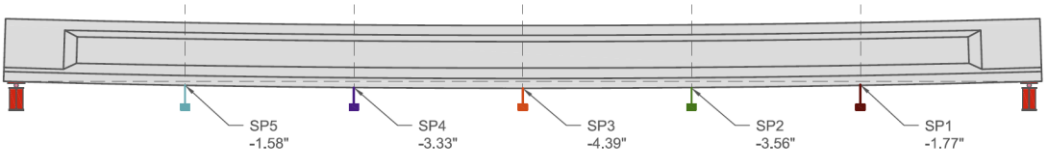

Displacement at Peak Load

Figure C.60: BTE4 displacement along the length.

In addition to load deflection data, the strains through the depth of the member were determined using both strain gauges and DIC data. Figure C.61 shows the top and bottom strains from each set of gauges throughout the load cycles.

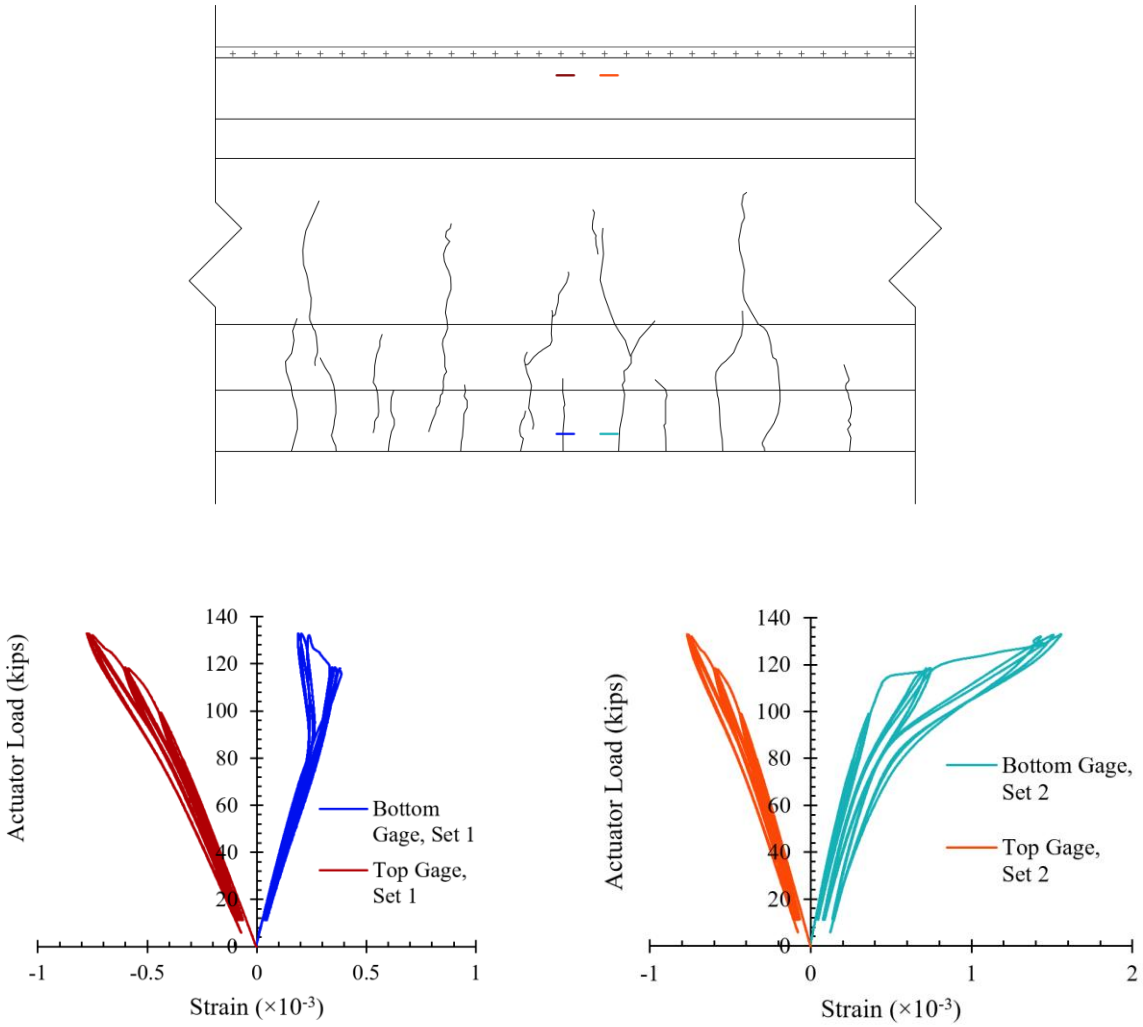

Figure C.61: BTE4 strain gauge data through load cycles. Bottom gauge, set 1 (blue), top gauge, set 1 (red), bottom gauge, set 2 (teal), top gauge, set 2 (orange).

As can be seen in Figure C.61, the top strains remain elastic throughout the load cycles, and the bottom gauges indicate cracking of the girder. The bottom gauge on the second set crossed a crack and shows dramatic increases in strain post cracking. To compare DIC results to the strain gauge data, points were used at the same location as the first set of strain gauges corresponding to the girder's midspan. The results from the DIC points can be seen in Figure C.62.

As with the strain gauges, DIC shows the top strains remain elastic throughout the load cycles. The strains from DIC point near the bottom flange is compared to the average bottom strain gauge behavior for the cracking cycle in Figure C.63. The response agrees reasonably well.

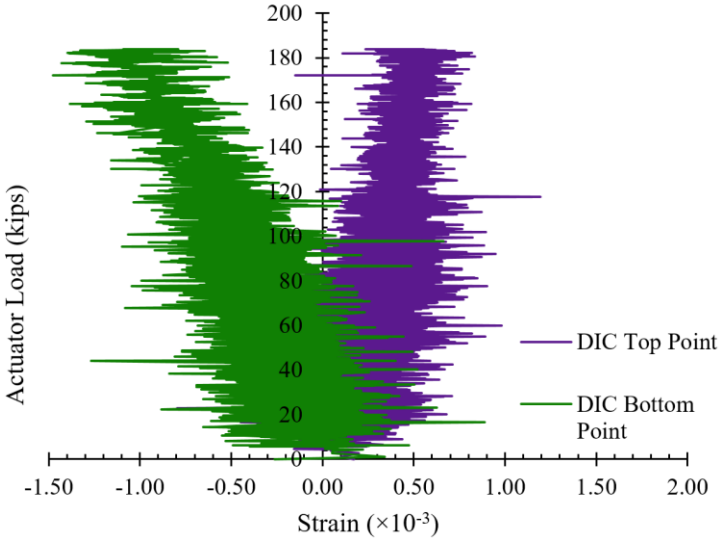

Figure C.62: BTE4 DIC point strains at girder midspan through load cycles.

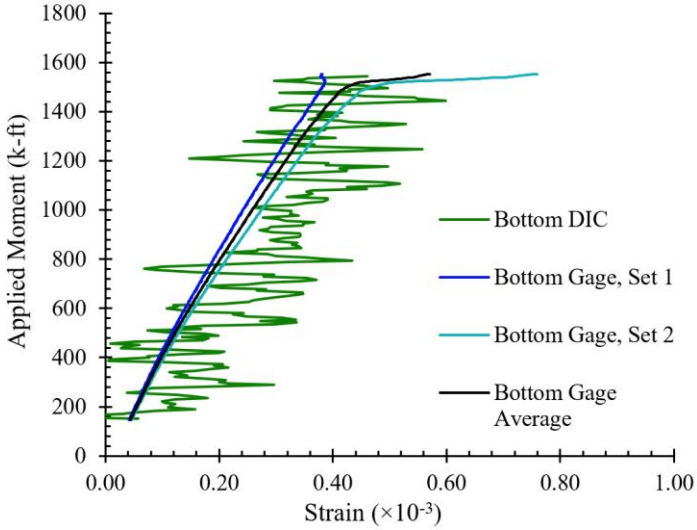

Figure C.63: BTE4 strain comparison between DIC point and strain gauge for first cycle to 115 kips actuator load.

To further understand strains through the depth during loading, horizontal extensometers were used in DIC post-processing at four locations through the depth near midspan. These extensometers provide longitudinal strains through the depth for each image taken during the test.

The strains through the depth can be seen for each of the four load steps during load cycles, the four load stages of monotonic loading, and the ultimate load for the girder in Figure C.64.

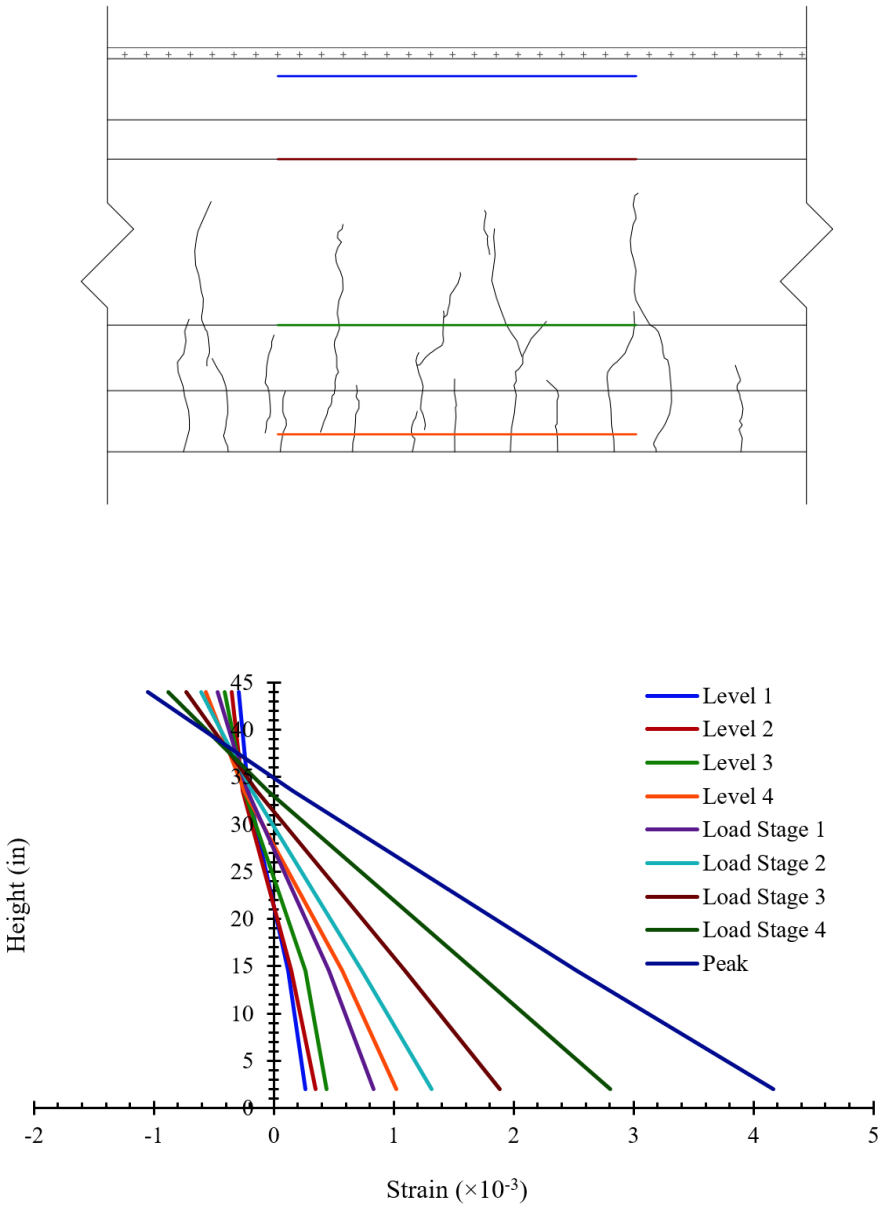

Figure C.64: BTE4 DIC horizontal extensometer strain profile.

Virtual extensometers in DIC post-processing were also used to determine the elongation across cracks during the initial load cycles to determine when crack first opens, when the crack closed and when the crack re-opened. Before cracking of the specimen, the virtual extensometer reads elastic elongation of the girder, but at cracking the extensometer elongation increases

suddenly. Upon unloading, extensometer elongation decreases rapidly until the crack is closed. Then, the slope of the applied moment-extensometer elongation curve becomes similar to that of the uncracked section. The virtual extensometer was placed over the first crack that occurred on the girder, and the location and elongation of the extensometer can be seen in Figure C.65. The extensometer elongation is a five point moving average to of the DIC data.

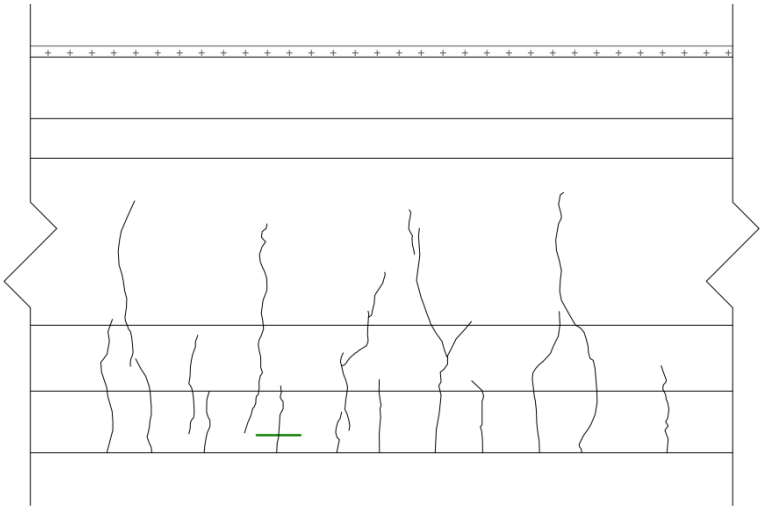

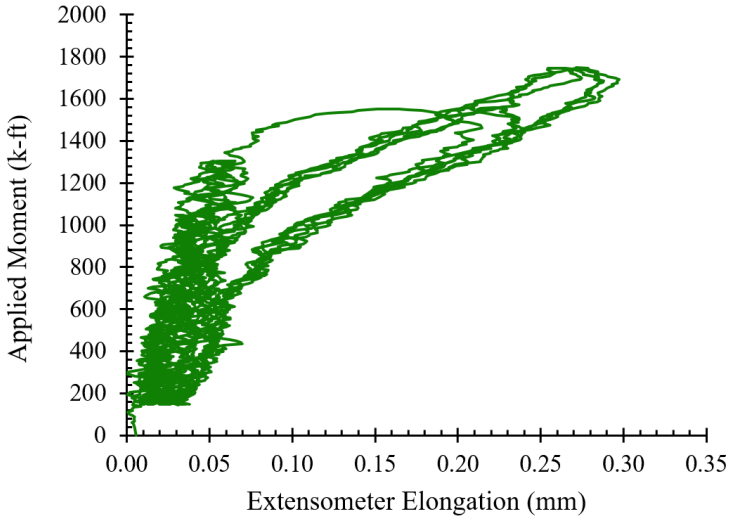

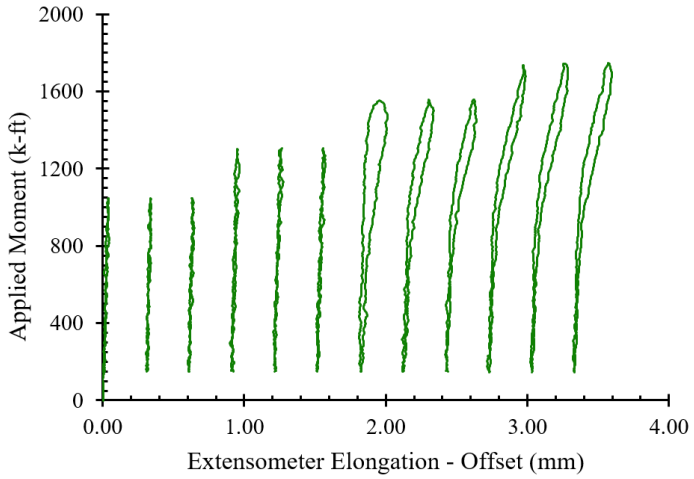

Figure C.65: BTE4 first crack virtual extensometer.

From Figure C.65 with elongation offset for each cycle, the three cycles for load steps of 75 and 95 kips of actuator load are only producing elastic strains in the girder because the lines are a constant slope. The first cycle up to 115 kips of actuator load is the first instance of cracking in the girder because there is a sudden increase in the extensometer's elongation at the peak load for that cycle. Figure C.66 highlights on the first cycle up to 115 kips of actuator load, and the transition from uncracked extensometer elongation to cracked elongation can clearly be seen. However, identifying the exact point of stiffness change requires careful investigation.

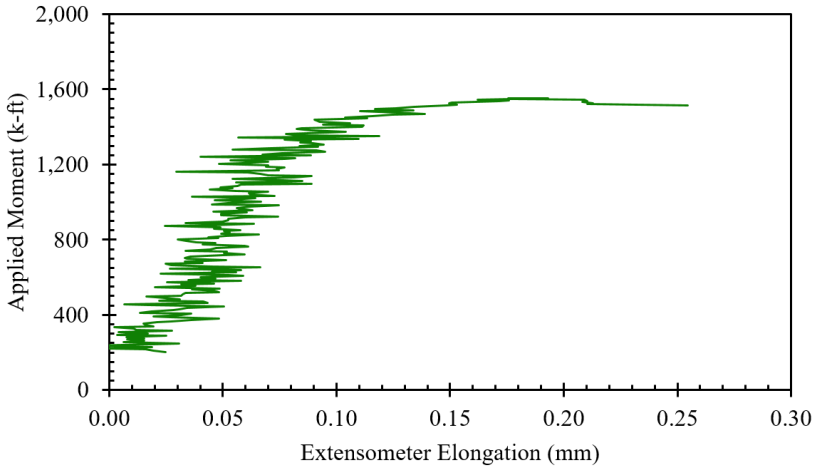

Figure C.66: BTE4 applied moment versus extensometer elongation showing stiffness change during cracking.

The cracking moment and crack reopening moment was found using the two-fold approach outlined before for previous BTE specimens. DIC strain map at the instant when the crack first appeared was captured and a pair of extensometers were placed, one at the crack (E0) and the other right beside it (E1). This was done to compare how the behavior of extensometer elongation changes with and without crack. Both the extensometers were at a depth of 1.75 in from the bottom fiber of the girder. The E0 and E1 extensometer elongation was plotted against load. The extensometer placed between the cracks provide measurements of the elastic elongation throughout the loading and the extensometer placed over the crack provides more detailed crack opening and closing data. A sharp change in extensometer elongation of E0 was observed at a load of 101.7 kips (Figure C.67). This sudden change in elongation occurs when the crack forms. Both the extensometer elongations agree up to first cracking. After this point they diverge and this can be used to determine the first instance of cracking. The DIC strain map shows high strains around the region indicating, either the crack has formed or is on the verge of propagating (Figure C.68a). A 20 point moving average of the extensometer elongation vs load was then plotted against the midspan displacement. This filtering approach helps make clear when the section transitions from uncracked to a cracked section. The average slope starts to increase at an applied moment of 1338 k-ft corresponding to a displacement of 25.0 mm (23.8 mm in Figure C.67 indicates the moving average value and is lower than the actual displacement) which matches with the corresponding DIC strain map. Thus, the cracking moment for BTE4 is 1338 k-ft.

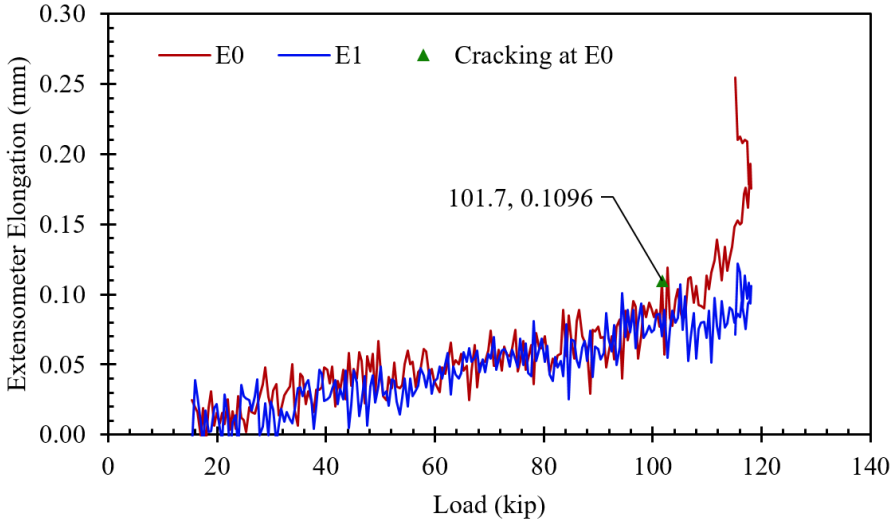

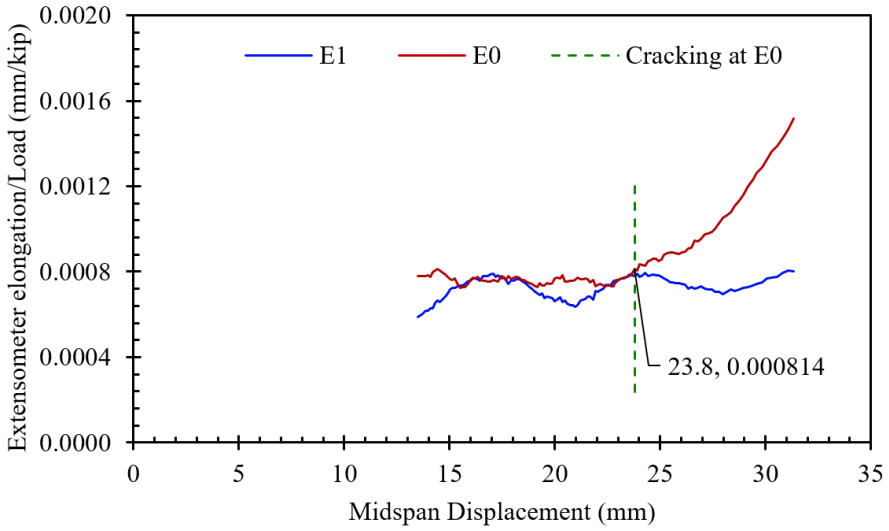

Figure C.67: Identifying first instance of cracking of BTE4.

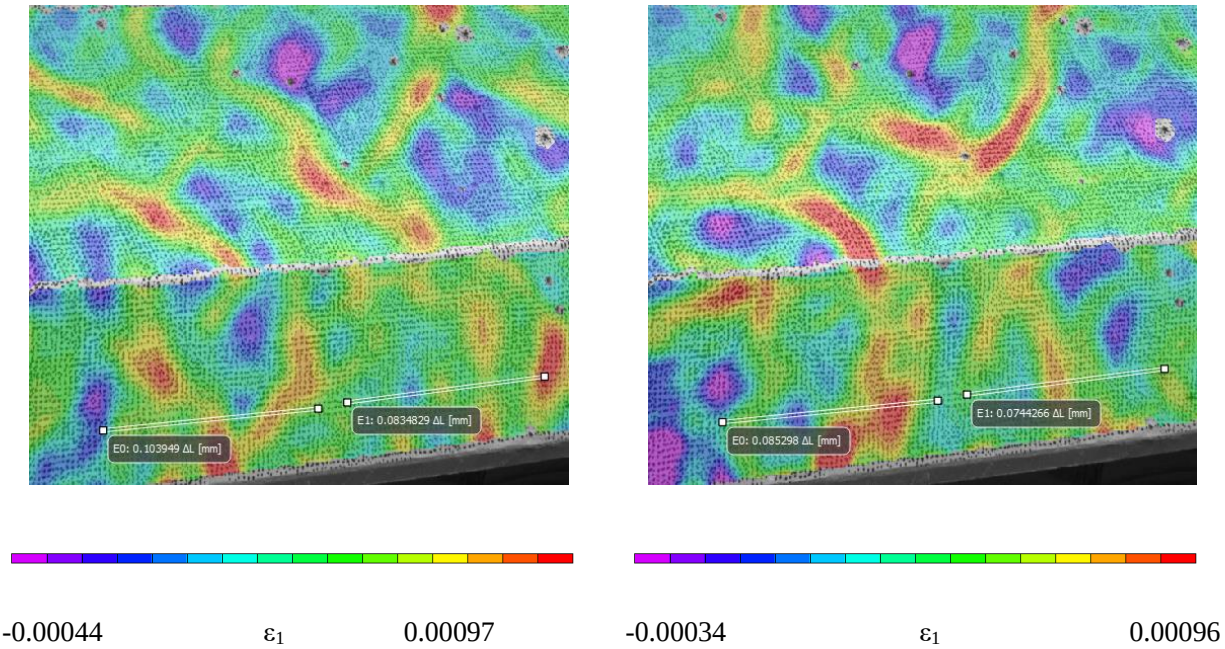

(a) Cracking: M=1338 k-ft

(b) Crack Reopening: M = 995 k-ft

Figure C.68: Principal strain (ε_1) map at the cracking and crack reopening moment.

The crack reopening moment was determined in a similar way by placing the extensometer E0 near the location where the crack would reopen and the extensometer E1 was placed between

cracks and then finally verifying with DIC principal strain map (Figure C.68b). The crack reopening moment was found to be 995 k-ft (Figure C.69).

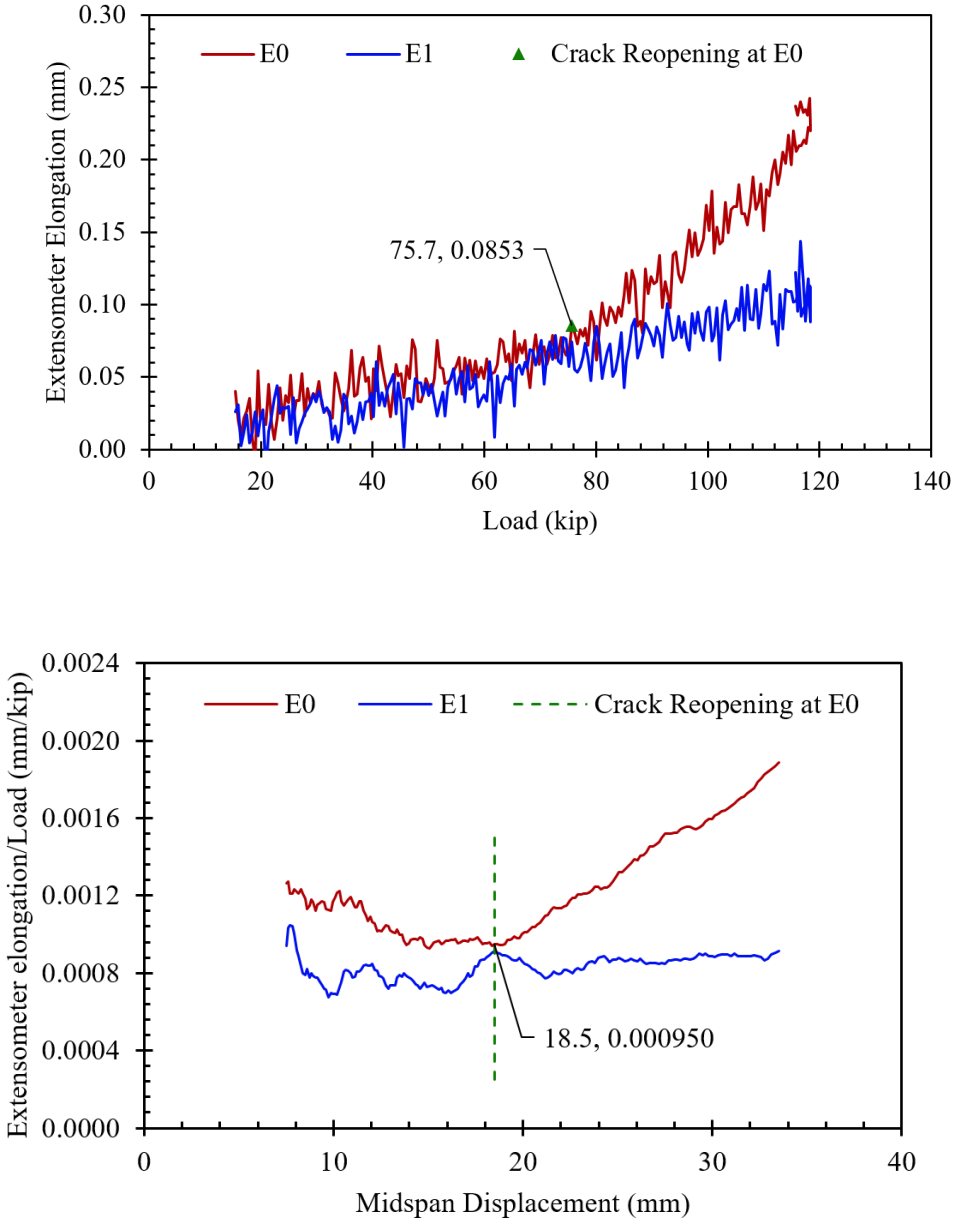

Figure C.69: Identifying first instance of crack reopening of BTE4.

The cracking moment and crack reopening moment also agrees with the applied moment versus extensometer elongation plot as shown in Figure C.70.

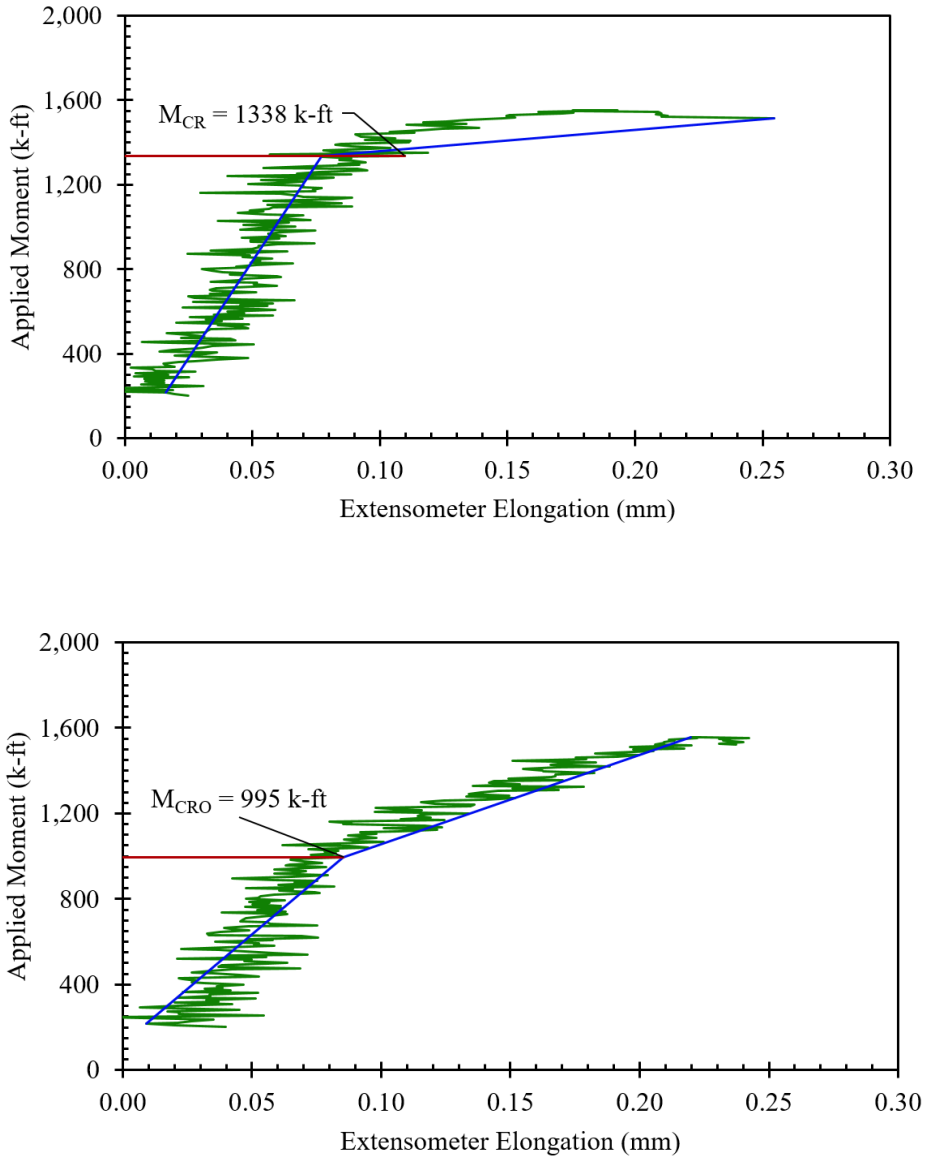

Figure C.70: BTE4 applied moment versus extensometer elongation with bi-linear approach to find (a) Cracking Moment (b) Crack Reopening Moment.

As shown for other BTE specimens, the first cracking and crack reopening moments found above require careful observation of strain maps generated in DIC post-processing of the principal strain, ε_1. The strain maps show when the crack first forms, when the crack is closed and when the crack reopens. It also specifies the location and depth of crack which is used to determine the cracking and crack reopening moment. Figure C.71 and Figure C.72 show the initial cracking of the girder and the reopening of the crack, respectively.

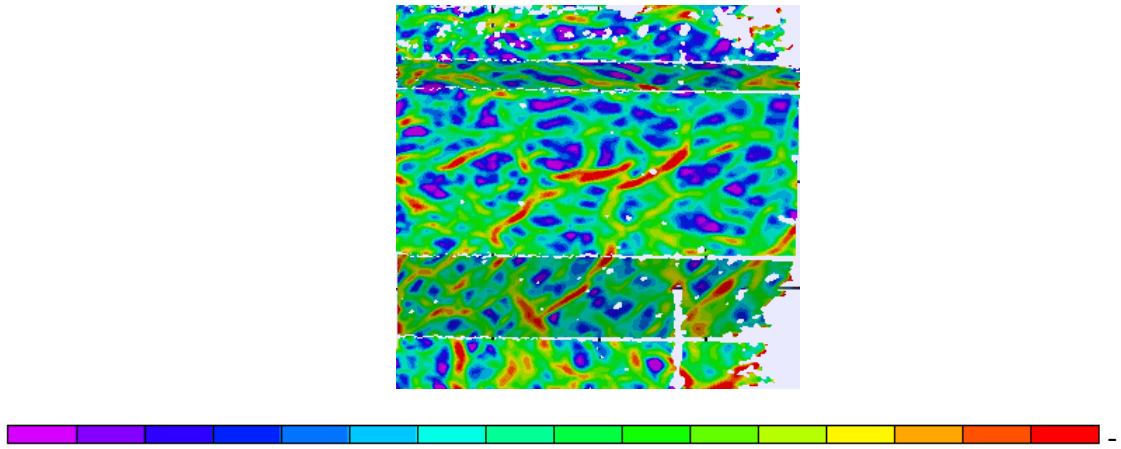

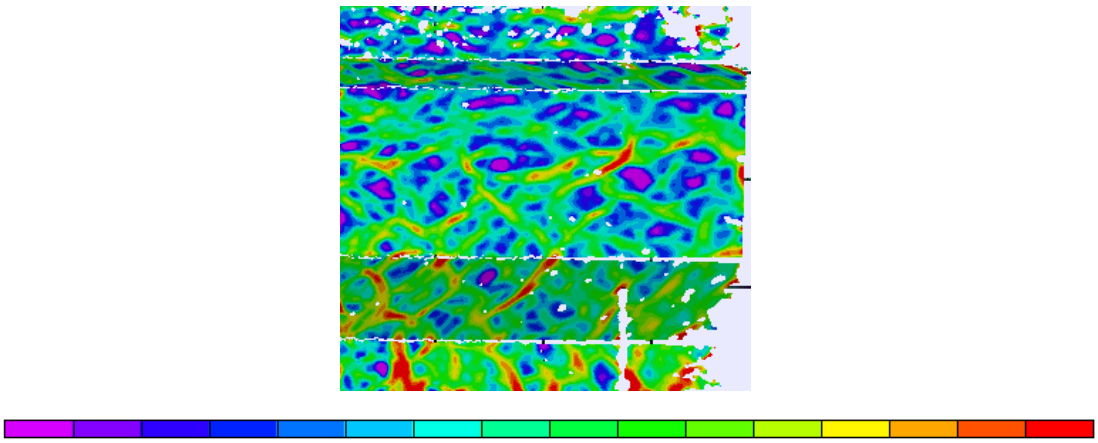

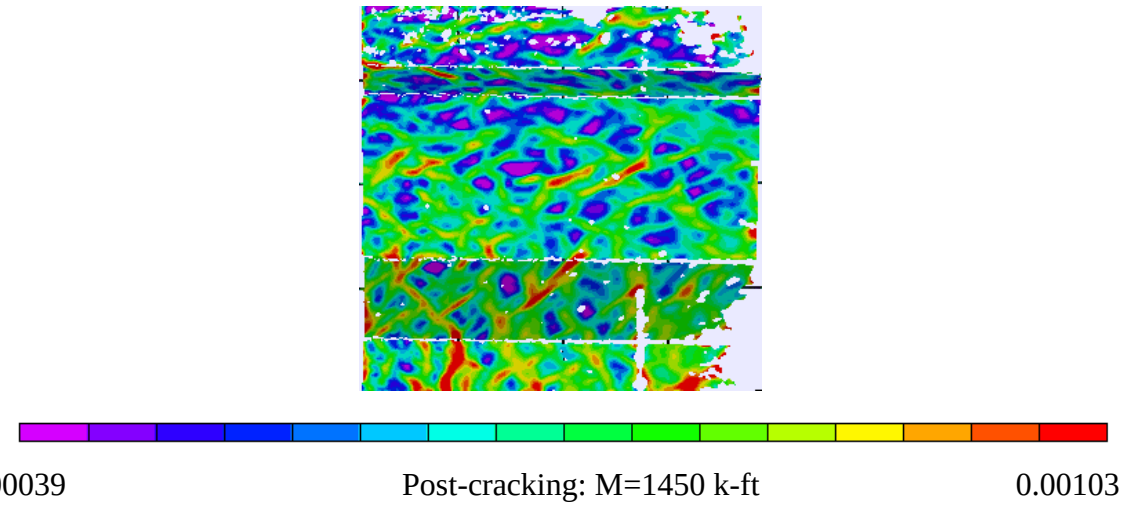

Figure C.71: BTE4 crack opening principal strain maps (ε_1).

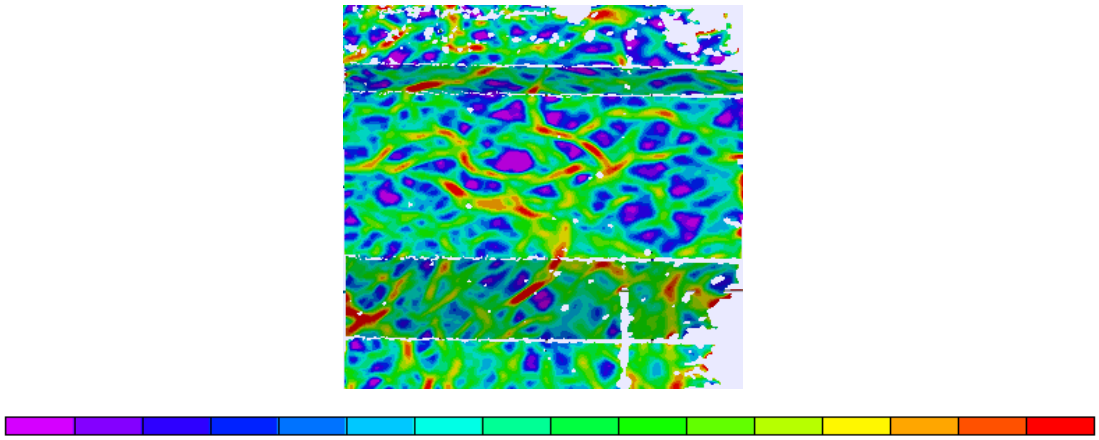

-0.00043 Prior to -reopening: M=800 k-ft 0.00108

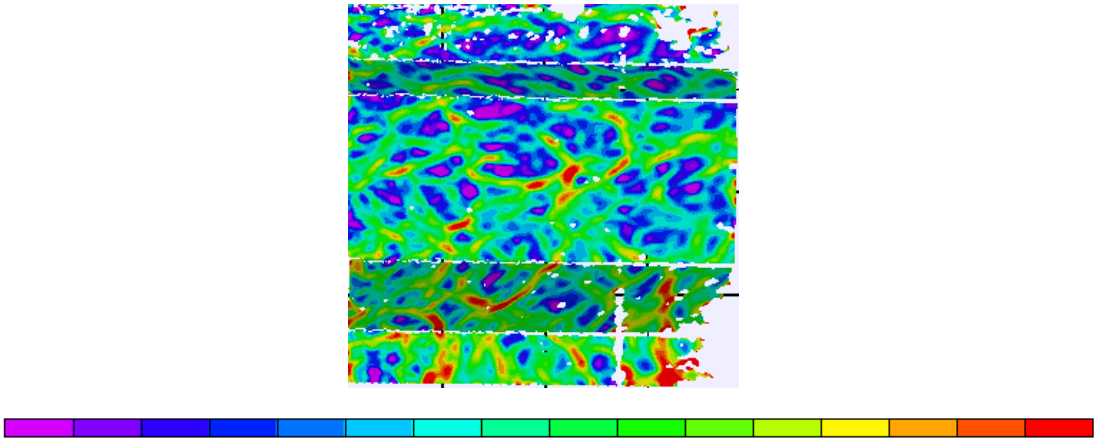

-0.00034 Crack reopening: M=995 k-ft 0.00096

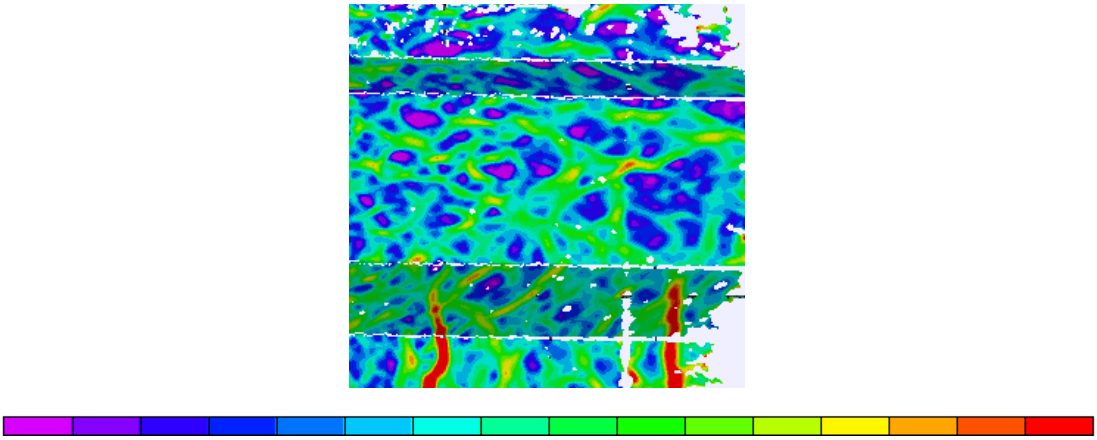

-0.00045 Post reopening: M=1200 k-ft 0.00143

Figure C.72: BTE4 principal strain maps (ε_1) indicating crack reopening.

Strain maps for the full DIC field of view between the load plates are provided below. The principal strain, ε_1, maps for each of the four load steps during load cycles, the four load stages of monotonic loading, and the ultimate load are provided in Figure C.73. These maps show tensile strains with strain concentrations around the flexural cracks. Figure C.74 shows the peak load strain maps for axial strains, ε_x and ε_y, shear strain, γ_{xy}, and principal strains, ε_1 and ε_2.

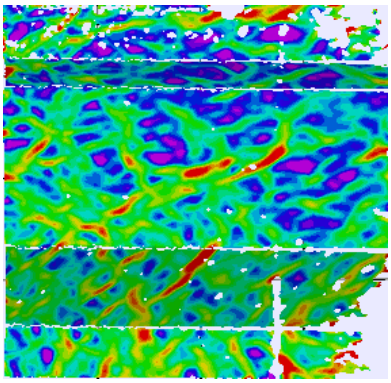

-0.000365 0.00085

Load Step 1: 75k actuator load

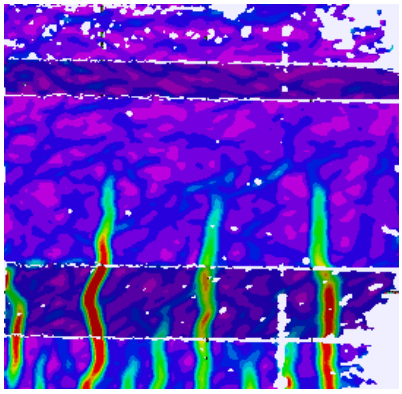

-0.00032 0.0045

Load Stage 1: 100k actuator load

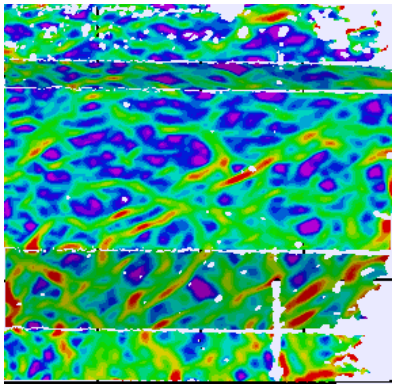

-0.00037 0.00096

Load Step 2: 95k actuator load

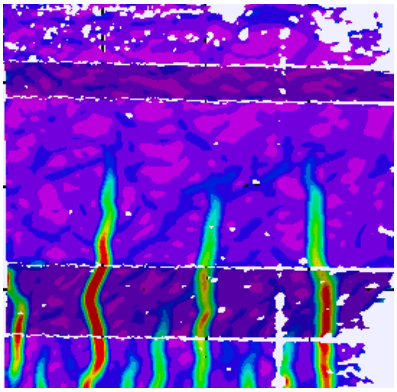

-0.00035 0.00625

Load Stage 2: 120k actuator load

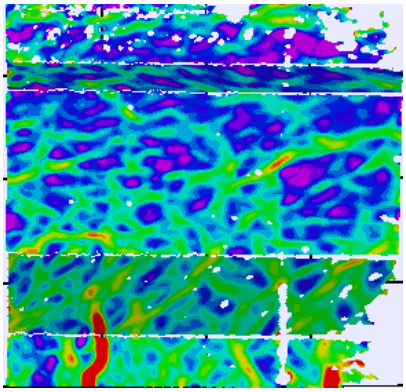

-0.00037 0.00139

Load Step 3: 115k actuator load

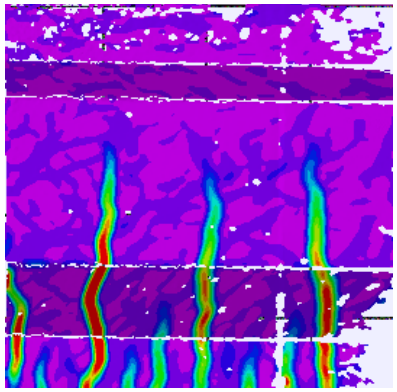

-0.0003 0.0093

Load Stage 3: 140k actuator load

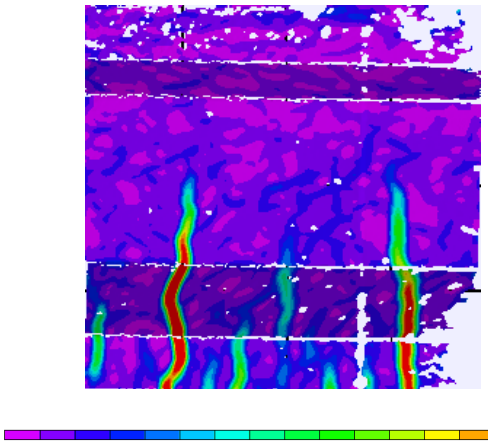

-0.00035 0.00635

Load Step 4: 130k actuator load

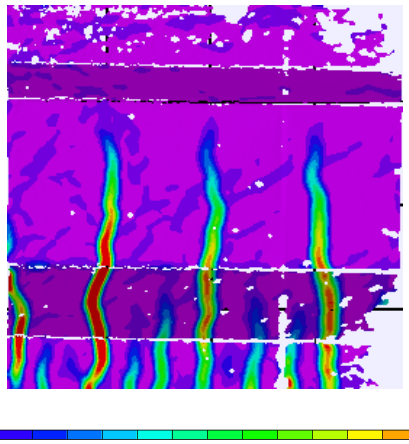

-0.0004 0.0137

Load Stage 4: 160k actuator load

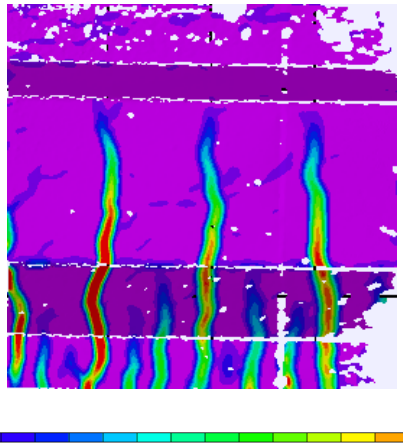

-0.0004 0.0179

Peak Load: 184k actuator load

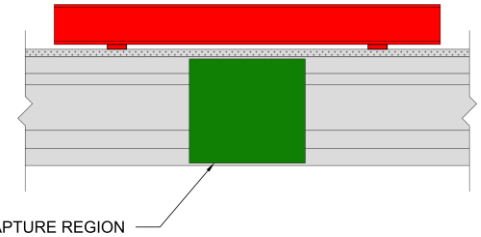

Figure C.73: Principal strain, ε_1, maps for BTE4.

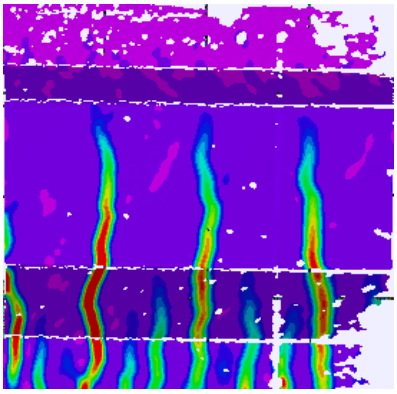

-0.0015 ε_{xx} 0.0175

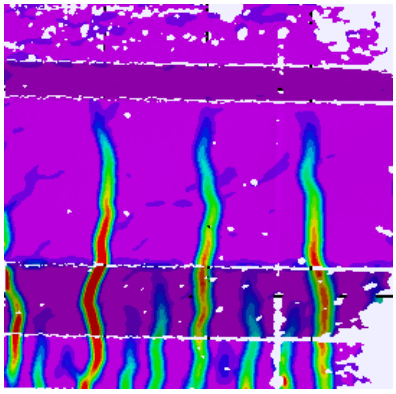

-0.0004 ε_1 0.0179

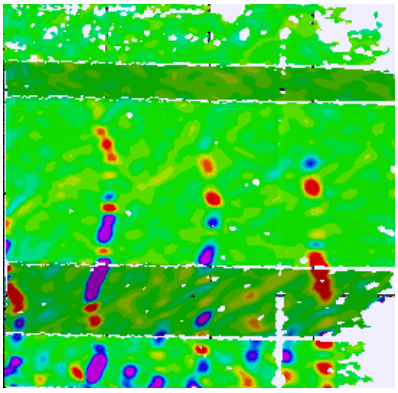

-0.0046 ε_{yy} 0.00295

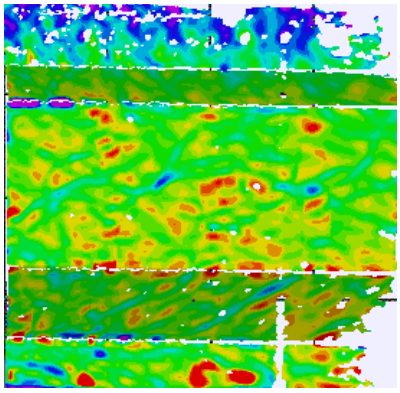

-0.00174 ε_2 0.00074

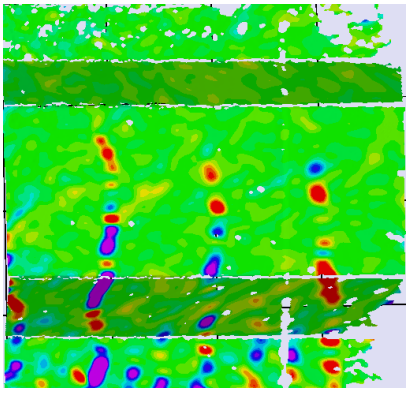

-0.0044 γ_{xy} 0.00275

Figure C.74: BTE4 peak load strain maps.

C.5 Prestress Loss Measurement by Strand Cutting

In addition to assessing prestress loss through flexural testing, several strands in the bottom flange of the girders were also cut to measure the losses. This test was performed by exposing strands by removal of cover concrete, applying two strain gauges to one wire of the seven-wire strand, and severing the strand between the strain gauges with a parting wheel to record the compressive strain to either side of the cut location. The recorded compressive strain after strand cutting is taken as a measure of the strand tensile strain prior to cutting for the determination of residual strand stress and prestress loss. This test was performed near the quarter points on BTE1 and BTE2 because this location incurred no damage from the flexural testing of the specimens and is at a sufficient distance from the end to ensure full strand development. The end regions of BTE3 and BTE4, however, were tested to assess the shear capacity, and it was not possible to do the strand cutting test after flexural testing of these specimens. The compressive strains taken from the average of the two strain gauges on each of the three severed strands in BTE1 were: 3.14×10^{-3}, 2.62×10^{-3}, and 3.15×10^{-3}. For BTE2 the compressive strains for three severed strands were: 4.58×10^{-3}, 3.48×10^{-3}, and 3.06×10^{-3}. Using the average compressive strain from three severed strands on BTE1 the prestress loss was found to be 48.3% and using the average compressive strain from three severed strands on BTE2 the prestress loss was found to be 41%. Halsey and Miller (1996) performed a similar assessment of prestress loss through strand cutting and found the method produced a higher estimate of prestress loss than the flexural test method. The underestimate of the residual strand stress from this method is likely due to residual strains in the strand after cutting. Strain was measured on one of the six wires wound around the king wire, and these wires tend to unwind after severance, but they retain their spiral shape. This indicates that inelastic strains remain in the wire which could contribute to the low measured compressive strain in the strain gauges. The prestress loss found from the strand cutting method is later found to be considerably higher than the losses determined from the flexural testing. The assessment of prestress loss in each of the girders from the flexural testing is covered in detail in Chapter 5 of this report.

APPENDIX D – MAPPING DEFORMATION USING OPTOTRAK DATA

Appendix D shows the displaced shapes from the BTE series of tests using Optotrak data.

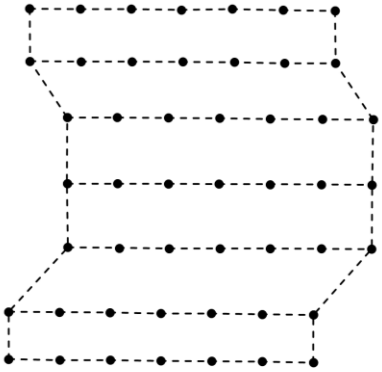

BTE1 Undeformed

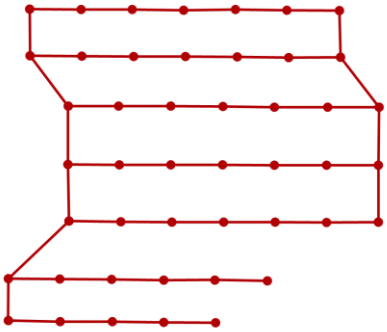

BTE1 Deformed

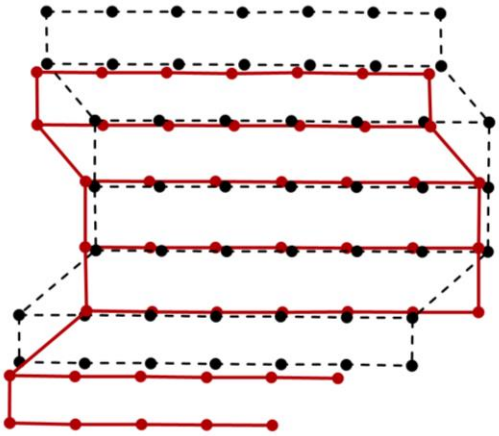

BTE1 Undeformed and Deformed Shape Overlay

Figure D.1: BTE1 undeformed and deformed shape generated from Optotrak data.

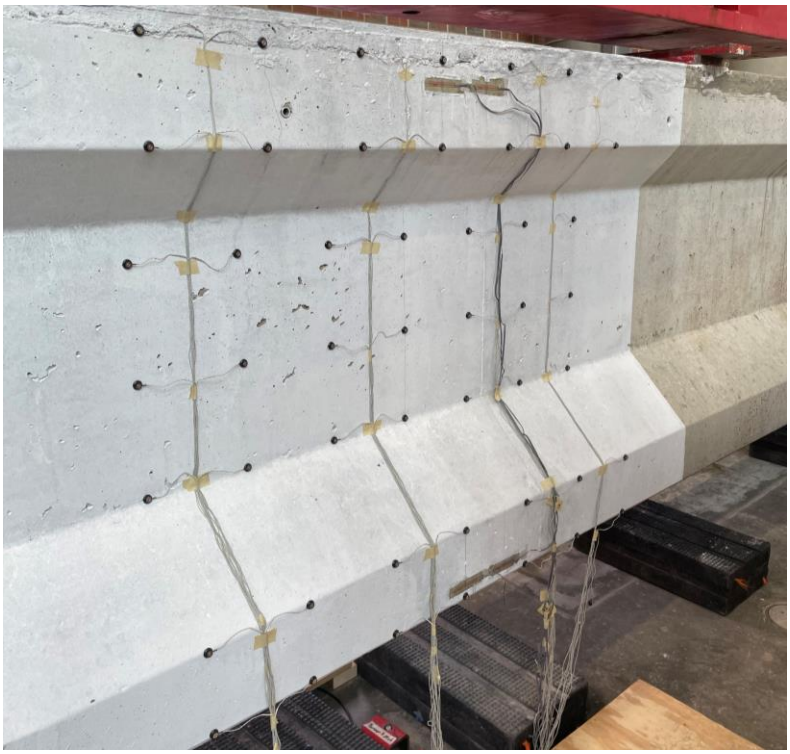

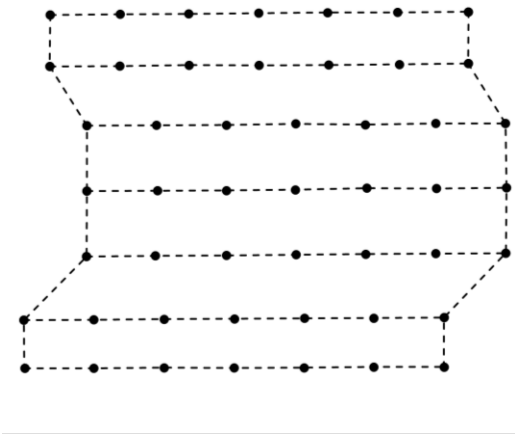

BTE2 Undeformed

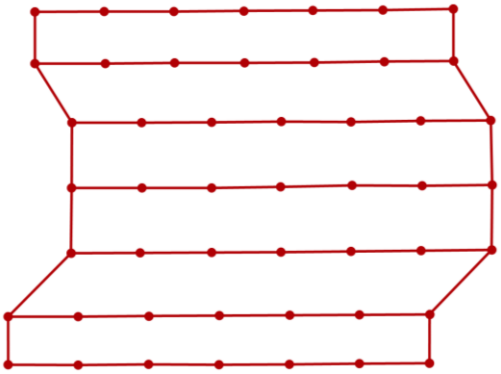

BTE2 Deformed

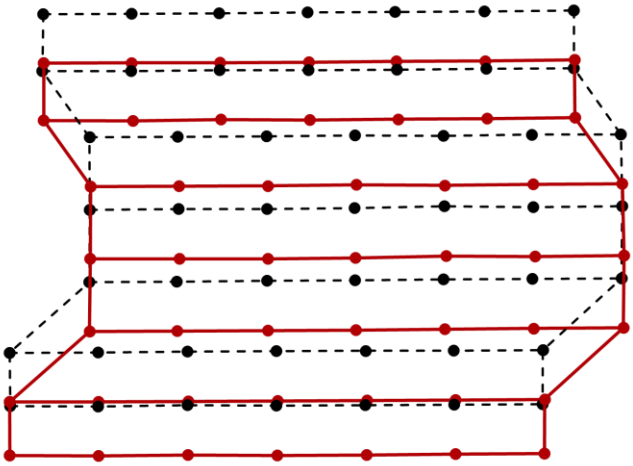

BTE2 Undeformed and Deformed Shape Overlay

Figure D.2: BTE2 undeformed and deformed shape generated from Optotrak data.

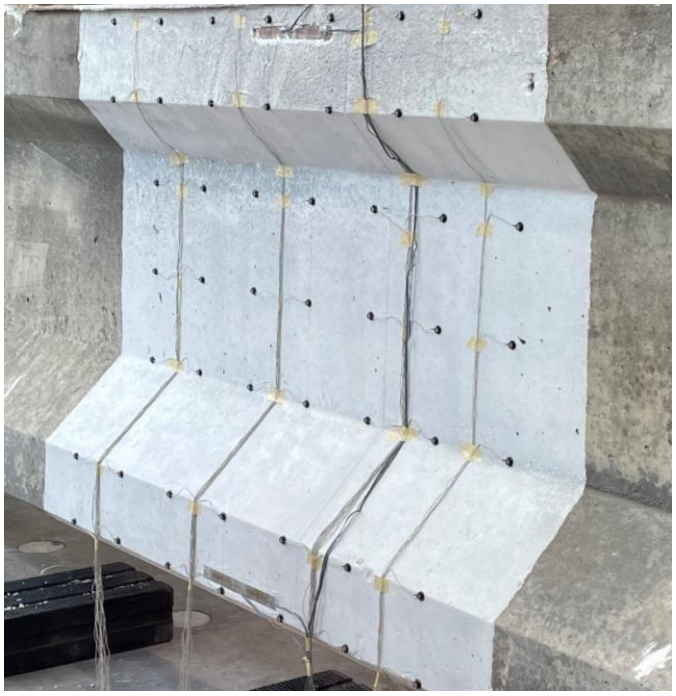

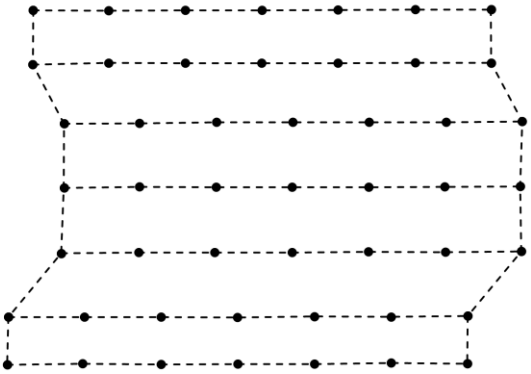

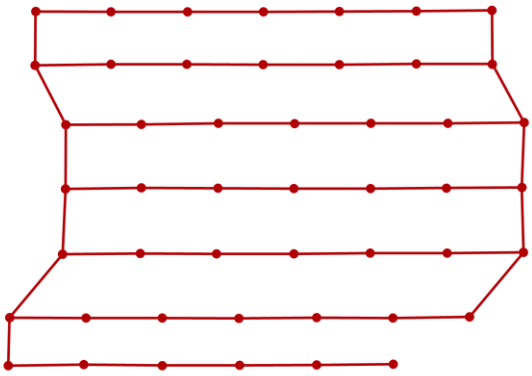

BTE3 Undeformed

BTE3 Deformed

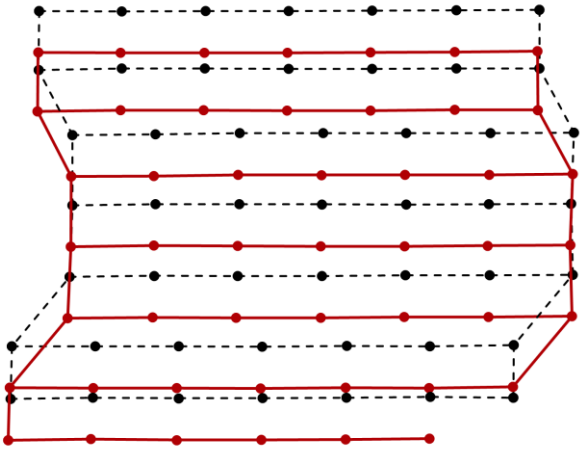

Figure D.3: BTE3 undeformed and deformed shape generated from Optotrak data.

APPENDIX E

E.1 Prestress Losses according to AASHTO LRFD following Refined Method for Long-Term Losses

Girder Properties				Reference/ Note
Gross area of section	A_g=	559.5	in^2	From response drawing - Bonner Bridge midspan cross-section, Pg-53
Girder volume (including ends)	V=	430160	in^3	
Girder surface area	S=	100555	in^2	
Centroid of gross area from bottom (mid - section)	y_g=	20.3	in	
Steel centroid dist. to bottom	e_m=	6.68	in	36 strands at bottom and 2 at top - see strain profile
Eccentricity of strand	e_{pg}=	13.6	in	y_g- e_m
Area of prestressing steel	A_{ps}=	4.1	in^2	*38, 7/16" strand
Modulus of elasticity for prestressing steel	E_p=	28500	ksi	AASHTO LRFD 5.4.4.2, Pg-33
Specified tensile strength of prestressing steel	f_{pu}=	250	ksi	Bonner drawings, Back calculate from prestressing force in each strand, AASHTO LRFD 5.4.4.1, Pg- 33
Moment of inertia of gross concrete secction about centroidal axis neglecting the reinforcement	I_g=	125390	in^4	
Design concrete strength of girder	f'_c=	5	ksi	From NCDOT load rating file
Design concrete compressive strength at time of prestressing for pretensioned members and at time of initial loading for nonprestressed members. If concrete age at time of initial loading is unknown at design time, f ′ci may be taken as 0.80 f ′c (ksi).	f'_{ci}=	4	ksi	AASHTO LRFD 5.4.2.3.2, Pg -28
Unit weight of concrete	w_c=	0.145	kcf	AASHTO LRFD 5.4.2.4 & C5.4.2.4, Pg-30
Modulus of Elasticity for normal weight concrete (girder)	E_c=	4291	ksi	AASHTO LRFD 5.4.2.4, Pg-30
Modulus of elasticity of concrete at transfer (girder)	E_{ci}=	3987	ksi	AASHTO LRFD (C5.9.3.2.3a)

Deck Properties				
Girder Deck Cross -section	A_d=	672	in^2	Girder to girder spacing - 96", Strucural Slab thickness - 7 in , Pg -51 of Bonner Drawing
Area of Haunch	A_h=	24	in^2	Thickness - 1.5"
Volume of Deck + Haunch	V=	510864	in^3	
Deck Surface Area excluding girder and diaphragm contact area	S=	139299	in^2	
Deck centroid dist. to bottom	y_d=	50	in	
Compressive strength of deck	$f'_{c\ deck}$=	3	ksi	From NCDOT load rating file; AASHTO 8.15.2.1.1
Compressive strength of deck at transfer	$f'_{ci\ deck}$=	2.4	ksi	Taken as: $0.8f'_c$; AASHTO LRFD 5.4.2.3.2, Pg -28
Unit weight of concrete	$w_{c\ deck}$=	0.145	kcf	5.4.2.4 & C5.4.2.4, Pg-30
Modulus of Elasticity for normal weight concrete (deck/haunch)	$E_{c\ deck}$=	3625	ksi	AASHTO LRFD 5.4.2.4, Pg-30
Eccentricity of deck with respect to the gross composite section	e_d=	14.6	in	AASHTO LRFD 5.9.3.4.3d, Pg-150;

Composite Section Properties				
Total area of the composite section	A_c=	1148	in^2	
Composite section volume	V=	861774	in^3	Use modular ratio due to difference in concrete deck and girder strength to calculate composite volume;
Composite section surface area	S=	218716	in^2	Use modular ratio due to difference in concrete deck and girder strength to calculate composite volume;
Centroid of composite section	y_c=	35.4	in	Use gross area of girder and use gross area of deck multiplied by modular ratio;
Distance between centroid of bottom steel and centroid of composite section	e_{pc}=	28.8	in	
Moment of inertia of the composite section	I_c=	378476	in^4	

Elastic Losses				
	$\Delta F_{pES}=(E_p/E_{ct})*f_{cgp}$			Eq. 5.9.3.2.3a-1
	$f_{cgp}=f_{pi}A_p[(1/A_g)+(e_p^2/I_g)]-(M_{sw}e_p/I_g)$			*iterate
Prestressing steel stress immediately prior to transfer	f_{pi}=	175	ksi	
Moment due to self-weight (girder only)	M_g=	276	k-ft	
Concrete stress at the center of gravity of prestressing tendons due to the prestressing force immediately after transfer and the selfweight of the member at the section of maximum moment	f_{cgp}=	1.81	ksi	NCDOT uses the full jacking stress as the initial strand stress and use it to calculate initial value of f_{cgp}. According to NCSU Final Report - Predicting Camber, If composite section properties are used iteration is not necessary but if gross cross section properties are used, iteration is necessary. Ref for calculation procedure: ASSHTO LRFD 5.9.3.2.3a , Pg-142; AASHTO Evaluation example, Pg-110; PCI Bridge Design Manual Pg -580,581; NCSU Final Report - Page -129
	f_{pn}=	162	ksi	*for iterating on f_{cgp}, us goal seek to set Δ to zero by changing f_{pn} (avg. strand tensile stress).
	f_{pn+1}=	162	ksi	
	Δ=	0	ksi	
Modulus of elasticity of concrete at transfer (girder)	$E_{ct}=E_{ci}$=	3987	ksi	5.9.3.2.3a , Pg-142
Loss due to elastic shortening in pretensioned members	**ΔF_{pES}=**	**12.96**	**ksi**	5.9.3.2.3a , Pg-142, Alternate equation, 5.9.3.2.3b, Pg-143.

Long-term Loss				
	$\Delta F_{pLT}=(\Delta f_{pSR}+\Delta f_{pCR}+\Delta f_{pR1})_{id}+(\Delta f_{pSD}+\Delta f_{pCD}+\Delta f_{pR2}-\Delta f_{pSS})_{df}$			Eq. 5.9.3.4.1-1
	$\Delta f_{pSR}=\varepsilon_{bid}E_pK_{id}$			Eq. 5.9.3.4.2a-1
Average annual ambient relative humidity	H=	75	% Humidity	Figure 5.4.2.3.3-1—Average Annual Ambient Relative Humidity, in Percent, Pg-29
Age of concrete at time of load application	t_i=	0.75	days	AASHTO LRFD C5.9.3.4.2c, Pg-148
Age of concrete at deck placement	t_d=	120	days	AASHTO LRFD C5.9.3.4.2c, Pg-148
Final age of concrete	t_f=	20440	days	Built in 1963, demolished in 2019, Lifetime 56 years
Factor for the effect of volume-to-surface ratio	k_s=	1.00		Value = 0.89 <1; So take 1.00, AASHTO LRFD 5.4.2.3.2-2, Pg-28
Humidity factor for shrinkage	k_{hs}=	0.95		AASTHO LRFD 5.4.2.3.3-2, Pg-29
Factor for the effect of concrete strength	k_f=	1.00		AASHTO LRFD 5.4.2.3.2-4, Pg-28
Time development factor at deck placement	k_{tdd}=	0.74		5.4.2.3.2-5, Pg-28; for t, use difference between time of deck placement and time of transfer
Concrete shrinkage strain of girder between the time of transfer and deck placement	ε_{bid}=	0.000337		AASHTO LRFD 5.4.2.3.3-1, Pg-29
Humidity factor for creep	k_{hc}=	0.96		AASHTO LRFD 5.4.2.3.2-3, Pg -28
Time Development Factor at final age of concrete	k_{tdf}=	1.00		"*to final time, use with $\Psi_b(t_f,t_i)$"; AASHTO LRFD 5.4.2.3.2-5, Pg-28
Girder Creep Coefficient at final time due to loading introduced at transfer	$\Psi_b(t_f,t_i)$=	1.88		AASHTO LRFD 5.4.2.3.2-1, Pg-27
Transformed section coefficient that accounts for time-dependent interaction between concrete and bonded steel in the section being considered for time period between transfer and deck placement	K_{id}=	0.82		AASHTO LRFD 5.9.3.4.2a-2, Pg-147
Prestress loss due to shrinkage of girder concrete between time of transfer and deck placement	**Δf_{pSR}=**	**7.9**	**ksi**	AASHTO LRFD 5.9.3.4.2;

	$\Delta f_{pCR}=(E_p/E_{ci})f_{cgp}\Psi_b(t_d,t_i)K_{id}$			Eq. 5.9.3.4.2b-1
Concrete stress at the center of gravity of prestressing tendons due to the prestressing force immediately after transfer and the selfweight of the member at the section of maximum moment	f_{cgp}=	1.81	ksi	
Girder creep coefficient at time of deck placement due to loading introduced at transfer	$\Psi_b(t_d,t_i)$=	1.395		AASHTO LRFD 5.4.2.3.2-1, Pg-28; k_{td} should be time between deck placement and loading;
Transformed section coefficient that accounts for time-dependent interaction between concrete and bonded steel in the section being considered for time period between transfer and deck placement	K_{id}=	0.82		AASHTO LRFD 5.9.3.4.2a-2, Pg-147
Prestress loss due to creep of girder concrete between transfer and deck placement	**Δf_{pCR}=**	**14.8**	**ksi**	AASHTO LRFD 5.9.3.4.2b-1, Pg - 148
	$\Delta f_{pR1}=(f_{pt}/K_L)[(f_{pt}/f_{py})-0.55]$			Eq. 5.9.3.4.2c-1
Yield strength of prestressing steel	f_{py}=	212.5		Table 5.4.4.1-1 AASHTO LRFD
Stress in prestressing strands immediately after transfer, taken not less than 0.55fpy	f_{pt}=	162.0	ksi	"*see f_{pn} above in f_{cgp} calculation"
Factor accounting for type of steel taken as 30 for low relaxation strands and 7.0 for other prestressing steel	K_L=	7.0		AASHTO LRFD 5.9.3.4.2c Pg-148, stress-relieved strands
Prestress loss due to relaxation of prestressing strands between time of transfer and deck placement	**Δf_{pR1}=**	**4.9**	**ksi**	AASHTO LRFD 5.9.3.4.2c, Pg-148
	$\Delta f_{pSD}=\varepsilon_{bdf}E_pK_{df}$			Eq. 5.9.3.4.3a-1
Factor for the effect of volume-to-surface ratio	k_s=	1.00		Calculation used girder volume and surface area, Value = 0.89 <1; So take 1.00
Humidity factor for shrinkage	k_{hs}=	0.95		AASTHO LRFD 5.4.2.3.3-2, Pg-29
Factor for the effect of concrete strength	k_f=	1.00		AASHTO LRFD 5.4.2.3.2-4, Pg-28
Time development factor between deck placement and final age	k_{tddf}=	1.00		AASHTO LRFD 5.4.2.3.2-5, Pg-28, use difference between final age and age at deck placement; or use difference between final age and initial to find e_{bid} and then determine e_{bdf}; k_{tddf} = 1.00; k_{tdf} = 1.00
Shrinkage strain of girder between the time of transfer and final time	ε_{bif}=	0.000455		
Shrinkage strain of girder between time of deck placement and final time	ε_{bdf}=	0.000118		AASHTO LRFD 5.4.2.3.3-1, Pg-29; for e_{bif} use k_{td} at final age of concrete, PCI Bridge Design Manual Pg-639
Transformed section coefficient that accounts for time-dependent interaction between concrete and bonded steel in the section being considered for time period between deck placement and final time	K_{df}=	0.83		AASHTO LRFD 5.9.3.4.3a-2, Pg -149
Prestress loss due to shrinkage of girder concrete between time of deck placement and	**Δf_{pSD}=**	**2.8**	**ksi**	AASHTO LRFD 5.9.3.4.3a-1, Pg-149

	$\Delta f_{pCD}=(E_p/E_{ci})f_{cgp}[\Psi_b(t_f,t_i)-\Psi_b(t_d,t_i)]K_{df}+(E_p/E_c)\Delta f_{cd}\Psi_b(t_f,t_d)K_{df}$			Eq. 5.9.3.4.3b-1
	$\Delta f_{cd}= (\Delta P/A_g)+(\Delta P e_{pg}^{\ 2}/I_g)-(M_{sd}e_{pc}/I_c)$			
Girder Creep Coefficient at final time due to loading introduced at transfer	$\Psi_b(t_f,t_i)=$	1.88		t_f = 20440, t_i = 0.75; AASHTO LRFD 5.4.2.3.2-1, Pg-27
Girder creep coefficient at time of deck placement due to loading introduced at transfer	$\Psi_b(t_d,t_i)=$	1.40		t_d = 120, t_i =0.75; AASHTO LRFD 5.4.2.3.2-1, Pg-27
Girder creep coefficient at final time due to loading at deck placement	$\Psi_b(t_f,t_d)=$	1.03		t_f = 20440, t_d =120; AASHTO LRFD 5.4.2.3.2-1, Pg-27
Transformed section coefficient that accounts for time-dependent interaction between concrete and bonded steel in the section being considered for time period between deck placement and final time	$K_{df}=$	0.83		AASHTO LRFD 5.9.3.4.2a-2, Pg-147
Prestress loss to deck laying	$\Delta P=$	-113.2	kips	
Moment from Deck self weight + Haunch	$M_{sd}=$	362	k-ft	
Moment due to Haunch	$M_h=$	11.3	k-ft	
Moment due to Diaphragm	$M_d=$	39.8	k-ft	
Moment due to Barrier Weight	$M_b=$	53.2	k-ft	
Moment due to Future Wearing Course	$M_{ws}=$	79	k-ft	
Change in concrete stress at centroid of prestressing strands due to long-term losses between transfer and deck placement, combined with deck weight and superimposed loads	$\Delta f_{cd}=$	-0.98		Pg -680, PCI Design Manual
Change in prestress (loss is positive, gain is negative) due to creep of girder concrete between time of deck placement and final time	**$\Delta f_{pCD}=$**	**-0.32**	**ksi**	AASHTO LRFD 5.9.3.4.3b, Pg-149

Prestress loss due to relaxation of prestressing strands in composite section between time of deck placement and final time	**$\Delta f_{pR2}=$**	**4.9**	**ksi**	Eq. 5.9.3.4.3c-1, Pg-150
	$\Delta f_{pSS}=(E_p/E_c)\Delta f_{cdf}K_{df}[1+0.7\Psi_b(t_f,t_d)]$			Eq. 5.9.3.4.3d-1
	$\Delta f_{cdf}=\{(\varepsilon_{ddf}A_dE_{c\,deck})/[1+0.7\Psi_d(t_f,t_d)]\}*[(1/A_c)-(e_{pc}e_d/I_c)]$			Eq. 5.9.3.4.3d-2
Factor for the effect of volume-to-surface ratio (Deck)	$k_s=$	1.00		Value = 0.975 <1; So take 1.00, AASHTO LRFD 5.4.2.3.2-2, Pg-28
Humidity factor for shrinkage	$k_{hs}=$	0.95		AASTHO LRFD 5.4.2.3.3-2, Pg-29
Factor for the effect of concrete strength	$k_f=$	1.47		AASHTO LRFD 5.4.2.3.2-4, Pg-28
Time development factor between deck placement and time at transfer	$k_{tdd}=$	0.71		AASHTO LRFD 5.4.2.3.2-5, Pg-28, use difference between age at deck placement and time at transfer
Time development factor between final age and time at transfer	$k_{tdf}=$	1.00		AASHTO LRFD 5.4.2.3.2-5, Pg-28, use difference between final age and time at transfer
Time development factor between deck placement and final age	$k_{tddf}=$	1.00		AASHTO LRFD 5.4.2.3.2-5, Pg-28, use difference between final age and age at deck placement
Shrinkage strain of deck between time of deck placement and final age	$\varepsilon_{ddf}=$	0.000669		AASHTO LRFD 5.9.3.4.3d, Pg-150;
Shrinkage strain of girder between time of deck placement and time at transfer	$\varepsilon_{did}=$	0.000477		AASHTO LRFD 5.9.3.4.3d, Pg-150;
Shrinkage strain of girder between final age and time at transfer	$\varepsilon_{dif}=$	0.000669		AASHTO LRFD 5.9.3.4.3d, Pg-150;
Shrinkage strain of deck between time of deck placement and final age^2	$\varepsilon_{ddf}=$	0.000192		AASHTO LRFD 5.9.3.4.3d, Pg-150;
Humidity factor for creep	$k_{hc}=$	0.96		
Creep coefficient of deck concrete at final time due to loading introduced shortly after deck placement (i.e. overlays, barriers, etc.) per Eq. 5.4.2.3.2-1	$\Psi_d(t_f,t_d)=$	1.52		t_f = 20440, t_d =120; AASHTO LRFD 5.4.2.3.2-1, Pg-27
Change in concrete stress at centroid of prestressing strands due to shrinkage of deck concrete	$\Delta f_{cdf}=$	-0.19	ksi	AASHTO LRFD 5.9.3.4.3d-2, Pg-150
Prestress gain due to shrinkage of deck in composite section	**$\Delta f_{pSS}=$**	**-1.8**	**ksi**	AASHTO LRFD 5.9.3.4.3d-1, Pg-150
Refined Estimates of Time-Dependent Losses	**$\Delta F_{pLT}=$**	**33.2**	**ksi**	AASHTO LRFD Eq. 5.9.3.4.1-1
Total Prestress Loss	**$\Delta F_{pT}=$**	**46.2**	**ksi**	AASHTO LRFD Eq. 5.9.3.1-1

Total Losses at Service Loads				
Elastic gain due to deck weight, superimposed dead load and live load (Service III)				
Elastic gain due to deck weight, superimposed dead load		**3.3**	**ksi**	Article 9.1b.6.6, PCI Bridge Design Manual
Elastic gain due to live load (Service III)		**5.4**	**ksi**	Article 9.1b.6.6, PCI Bridge Design Manual
Elastic gain		**8.7**	**ksi**	
Effective stress in strands after all losses and gains	$\mathbf{f_{pe}}$	**137.6**	**ksi**	
Prestressing stress limit at service limit state	$\mathbf{0.8f_{py}}$	**170.0**	**ksi**	$f_{pe} < 0.8f_{py;}$ ok
Effective stress in strands after all losses and permanent gains	$\mathbf{f_{pe}}$	**132.1**		
Force per strand without live load gains		**14.3**	**kips**	
Total prestressing force after all losses		**542.3**	**kips**	
Final loss percentage		**21.4**	**%**	total losses and gains/ f_{pi}
Final loss percentage without prestressing gains at deck placeemnent		**26.4**	**%**	total losses/ f_{pi}
Final loss percentage without live load gains		**23.3**		

E.2 Prestress Losses according to AASHTO LRFD, following Refined Method for Long - Term Losses and using NCDOT Assumptions

Girder Properties				Reference/ Note
Gross area of section	A_g=	559.5	in^2	From response drawing - Bonner Bridge midspan cross-section, Pg-53
Girder volume (including ends)	V=	430160	in^3	
Girder surface area	S=	100555	in^2	
Centroid of gross area from bottom (mid -section)	y_g=	20.3	in	
Steel centroid dist. to bottom	e_m=	6.68	in	36 strands at bottom and 2 at top - see strain profile
Eccentricity of strand	e_{pg}=	13.6	in	y_g- y_p
Area of prestressing steel	A_{ps}=	4.1	in^2	*38, 7/16" strand
Modulus of elasticity for prestressing steel	E_p=	28500	ksi	AASHTO LRFD 5.4.4.2, Pg-33
Specified tensile strength of prestressing steel	f_{pu}=	250	ksi	Bonner drawings, Back calculate from prestressing force in each strand, AASHTO LRFD 5.4.4.1, Pg- 33
Moment of inertia of gross concrete secction about centroidal axis neglecting the reinforcement	I_g=	125390	in^4	
Design concrete strength of girder	f'_c=	5	ksi	From NCDOT load rating file
Design concrete compressive strength at time of prestressing for pretensioned members and at time of initial loading for nonprestressed members. If concrete age at time of initial loading is unknown at design time, f ′ci may be taken as 0.80 f ′c (ksi).	f'_{ci}=	4	ksi	AASHTO LRFD 5.4.2.3.2, Pg -28
Unit weight of concrete	w_c=	0.145	kcf	AASHTO LRFD 5.4.2.4 & C5.4.2.4, Pg-30
Modulus of Elasticity for normal weight concrete (girder)	E_c=	4291	ksi	AASHTO LRFD 5.4.2.4, Pg-30
Modulus of elasticity of concrete at transfer (girder)	E_{ci}=	3987	ksi	AASHTO LRFD (C5.9.3.2.3a)

Deck Properties				
Girder Deck Cross -section	A_d=	672	in^2	Girder to girder spacing - 96", Slab thickness - 7.25 in which includes 0.25 in wearing course, Pg -51 of Bonner Drawing
Area of Haunch	A_h=	24	in^2	Thickness - 1.5"
Volume of Deck + Haunch	V=	510864	in^3	
Deck Surface Area excluding girder and diaphragm contact area	S=	139299	in^2	
Deck centroid dist. to bottom	y_d=	50	in	
Compressive strength of deck	$f'_{c\ deck}$=	3	ksi	From NCDOT load rating file; AASHTO 8.15.2.1.1
Compressive strength of deck at transfer	$f'_{ci\ deck}$=	2.4	ksi	Taken as: $0.8f'_c$; AASHTO LRFD 5.4.2.3.2, Pg -28
Unit weight of concrete	$w_{c\ deck}$=	0.145	kcf	5.4.2.4 & C5.4.2.4, Pg-30
Modulus of Elasticity for normal weight concrete (deck)	$E_{c\ deck}$=	3625	ksi	AASHTO LRFD 5.4.2.4, Pg-30
Eccentricity of deck with respect to the gross composite section	e_d=	14.6	in	AASHTO LRFD 5.9.3.4.3d, Pg-150;

Composite Section Properties				
Total area of the composite section	A_c=	1148	in^2	
Composite section volume	V=	861774	in^3	Use modular ratio due to difference in concrete deck and girder strength to calculate composite volume;
Composite section surface area	S=	218716	in^2	Use modular ratio due to difference in concrete deck and girder strength to calculate composite volume;
Centroid of composite section	y_c=	35.4	in	Use gross area of girder and use gross area of deck multiplied by modular ratio;
Distance between centroid of bottom steel and centroid of composite section	e_{pc}=	28.8	in	
Moment of inertia of the composite section	I_c=	378476	in^4	
Elastic Losses				
	$\Delta F_{pES}=(E_p/E_{ci})*f_{cgp}$			Eq. 5.9.3.2.3a-1
	$f_{cgp}=f_{pi}A_{ps}[(1/A_g)+(e_p^2/I_g)]-(M_{sw}e_p/I_g)$			*iterate
Prestressing steel stress immediately prior to transfer	f_{pi}=	175	ksi	
Moment due to self-weight (girder only)	M_g=	275.98	k-ft	
Concrete stress at the center of gravity of prestressing tendons due to the prestressing force immediately after transfer and the selfweight of the member at the section of maximum moment	f_{cgp}=	1.81	ksi	NCDOT uses the full jacking stress as the initial strand stress and use it to calculate initial value of f_{cgp}. According to NCSU Final Report - Predicting Camber, If composite section properties are used iteration is not necessary but if gross cross section properties are used, iteration is necessary. Ref for calculation procedure: ASSHTO LRFD 5.9.3.2.3a , Pg-142; AASHTO Evaluation example, Pg-110; PCI Bridge Design Manual Pg -580,581; NCSU Final Report - Page -129
	f_{pn}=	162	ksi	*for iterating on f_{cgp}, us goal seek to set Δ to zero by changing f_{pn} (avg. strand tensile stress).
	f_{pn+1}=	162	ksi	
	Δ=	0	ksi	
Modulus of elasticity of concrete at transfer (girder)	$E_{ct}=E_{ci}$=	3987	ksi	5.9.3.2.3a , Pg-142
Loss due to elastic shortening in pretensioned members	**ΔF_{pES}=**	**12.96**	**ksi**	5.9.3.2.3a , Pg-142, Alternate equation, 5.9.3.2.3b, Pg-143.

Long-term Loss				
	$\Delta F_{pLT}=(\Delta f_{pSR}+\Delta f_{pCR}+\Delta f_{pR1})_{id}+(\Delta f_{pSD}+\Delta f_{pCD}+\Delta f_{pR2}-\Delta f_{pSS})_{df}$			Eq. 5.9.3.4.1-1
	$\Delta f_{pSR}=\varepsilon_{bid}E_pK_{id}$			Eq. 5.9.3.4.2a-1
Average annual ambient relative humidity	H=	75	% Humidity	Figure 5.4.2.3.3-1—Average Annual Ambient Relative Humidity, in Percent, Pg-29
Age of concrete at time of load application	t_i=	1	days	AASHTO LRFD C5.9.3.4.2c, Pg-148
Age of concrete at deck placement	t_d=	90	days	AASHTO LRFD C5.9.3.4.2c, Pg-148
Final age of concrete	t_f=	20000	days	Built in 1963, demolished in 2019, Lifetime 56 years
Factor for the effect of volume-to-surface ratio	k_s=	1.00		Value = 0.89 <1; So take 1.00, AASHTO LRFD 5.4.2.3.2-2, Pg-28
Humidity factor for shrinkage	k_{hs}=	0.95		AASTHO LRFD 5.4.2.3.3-2, Pg-29
Factor for the effect of concrete strength	k_f=	1.00		AASHTO LRFD 5.4.2.3.2-4, Pg-28
Time development factor at deck placement	k_{tdd}=	0.68		5.4.2.3.2-5, Pg-28; for t, use difference between time of deck placement and time of transfer
Concrete shrinkage strain of girder between the time of transfer and deck placement	ε_{bid}=	0.000310		AASHTO LRFD 5.4.2.3.3-1, Pg-29
Humidity factor for creep	k_{hc}=	0.96		AASHTO LRFD 5.4.2.3.2-3, Pg -28
Time Development Factor at final age of concrete	k_{tdf}=	1.00		"*to final time, use with $\Psi_b(t_f,t_i)$"; AASHTO LRFD 5.4.2.3.2-5, Pg-28
Girder Creep Coefficient at final time due to loading introduced at transfer	$\Psi_b(t_f,t_i)$=	1.82		AASHTO LRFD 5.4.2.3.2-1, Pg-27
Transformed section coefficient that accounts for time-dependent interaction between concrete and bonded steel in the section being considered for time period between transfer and deck placement	K_{id}=	0.82		AASHTO LRFD 5.9.3.4.2a-2, Pg-147
Prestress loss due to shrinkage of girder concrete between time of transfer and deck placement	**Δf_{pSR}=**	**7.2**	**ksi**	AASHTO LRFD 5.9.3.4.2;
	$\Delta f_{pCR}=(E_p/E_{ci})f_{cgp}\Psi_b(t_d,t_i)K_{id}$			Eq. 5.9.3.4.2b-1
Concrete stress at the center of gravity of prestressing tendons due to the prestressing force immediately after transfer and the selfweight of the member at the section of maximum moment	f_{cgp}=	1.81	ksi	
Girder creep coefficient at time of deck placement due to loading introduced at transfer	$\Psi_b(t_d,t_i)$=	1.239		AASHTO LRFD 5.4.2.3.2-1, Pg-28; k_{td} should be time between deck placement and loading;
Transformed section coefficient that accounts for time-dependent interaction between concrete and bonded steel in the section being considered for time period between transfer and deck placement	K_{id}=	0.82		AASHTO LRFD 5.9.3.4.2a-2, Pg-147
Prestress loss due to creep of girder concrete between transfer and deck placement	**Δf_{pCR}=**	**13.2**	**ksi**	AASHTO LRFD 5.9.3.4.2b-1, Pg - 148
	$\Delta f_{pR1}=(f_{pt}/K_L)[(f_{pt}/f_{py})-0.55]$			Eq. 5.9.3.4.2c-1
Yield strength of prestressing steel	f_{py}=	212.5		Table 5.4.4.1-1 AASHTO LRFD
Stress in prestressing strands immediately after transfer, taken not less than 0.55fpy	f_{pt}=	162.0	ksi	"*see f_{pn} above in f_{cgp} calculation"
Factor accounting for type of steel taken as 30 for low relaxation strands and 7.0 for other prestressing steel	K_L=	7.0		AASHTO LRFD 5.9.3.4.2c Pg-148, stress-relieved strands
Prestress loss due to relaxation of prestressing strands between time of transfer and deck placement	**Δf_{pR1}=**	**4.9**	**ksi**	AASHTO LRFD 5.9.3.4.2c, Pg-148

	$\Delta f_{pSD}=\varepsilon_{bdf}E_p K_{df}$			Eq. 5.9.3.4.3a-1
Factor for the effect of volume-to-surface ratio	$k_s=$	1.00		Calculation used girder volume and surface area, Value = 0.89 <1; So take 1.00
Humidity factor for shrinkage	$k_{hs}=$	0.95		AASTHO LRFD 5.4.2.3.3-2, Pg-29
Factor for the effect of concrete strength	$k_f=$	1.00		AASHTO LRFD 5.4.2.3.2-4, Pg-28
Time development factor between deck placement and final age	$k_{tddf}=$	1.00		AASHTO LRFD 5.4.2.3.2-5, Pg-28, use difference between final age and age at deck placement; or use difference between final age and initial to find e_{bid} and then determine e_{bdf}; k_{tddf} = 1.00; k_{tdf} = 1.00
Shrinkage strain of girder between the time of transfer and final time	$\varepsilon_{bif}=$	0.000455		
Shrinkage strain of girder between time of deck placement and final time	$\varepsilon_{bdf}=$	0.000145		AASHTO LRFD 5.4.2.3.3-1, Pg-29; for e_{bif} use k_{td} at final age of concrete, PCI Bridge Design Manual Pg-639
Transformed section coefficient that accounts for time-dependent interaction between concrete and bonded steel in the section being considered for time period between deck placement and final time	$K_{df}=$	0.83		AASHTO LRFD 5.9.3.4.3a-2, Pg -149
Prestress loss due to shrinkage of girder concrete between time of deck placement and final time,	$\mathbf{\Delta f_{pSD}=}$	**3.4**	**ksi**	AASHTO LRFD 5.9.3.4.3a-1, Pg-149

	$\Delta f_{pCD}=(E_p/E_{ci})f_{cgp}[\Psi_b(t_f,t_i)-\Psi_b(t_d,t_i)]K_{df}+(E_p/E_c)\Delta f_{cd}\Psi_b(t_f,t_d)K_{df}$			Eq. 5.9.3.4.3b-1
	$\Delta f_{cd}=(\Delta P/A_g)+(\Delta P e_{pg}^2/I_g)-(M_{sd}e_{pc}/I_c)$			
Girder Creep Coefficient at final time due to loading introduced at transfer	$\Psi_b(t_f,t_i)=$	1.82		t_f = 20440, t_i = 0.75; AASHTO LRFD 5.4.2.3.2-1, Pg-27
Girder creep coefficient at time of deck placement due to loading introduced at transfer	$\Psi_b(t_d,t_i)=$	1.24		t_d = 120, t_i =0.75; AASHTO LRFD 5.4.2.3.2-1, Pg-27
Girder creep coefficient at final time due to loading at deck placement	$\Psi_b(t_f,t_d)=$	1.07		t_f = 20440, t_d =120; AASHTO LRFD 5.4.2.3.2-1, Pg-27
Transformed section coefficient that accounts for time-dependent interaction between concrete and bonded steel in the section being considered for time period between deck placement and final time	$K_{df}=$	0.83		AASHTO LRFD 5.9.3.4.2a-2, Pg-147
Prestress loss to deck laying	$\Delta P=$	-104.1	kips	
Moment from deck self weight	$M_{sd}=$	362	k-ft	
Moment due to Haunch	$M_h=$	11.3	k-ft	
Moment due to Diaphragm	$M_d=$	39.8	k-ft	
Moment due to Barrier Weight	$M_b=$	53.2	k-ft	
Moment due to Wearing Course	$M_{ws}=$	79	k-ft	
Change in concrete stress at centroid of prestressing strands due to long-term losses between transfer and deck placement, combined with deck weight and superimposed loads	$\Delta f_{cd}=$	-1.00		Pg -680, PCI Design Manual
Change in prestress (loss is positive, gain is negative) due to creep of girder concrete between time of deck placement and final time	$\mathbf{\Delta f_{pCD}=}$	**0.4**	**ksi**	AASHTO LRFD 5.9.3.4.3b, Pg-149
	$\Delta f'_{pR2}=\Delta f_{pR1}$			
Prestress loss due to relaxation of prestressing strands in composite section between time of deck placement and final time	$\mathbf{\Delta f_{pR2}=}$	**4.9**	**ksi**	Eq. 5.9.3.4.3c-1, Pg-150

	$\Delta f_{pSS}=(E_p/E_c)\Delta f_{cdf}K_{df}[1+0.7\Psi_b(t_f,t_d)]$			Eq. 5.9.3.4.3d-1
	$\Delta f_{cdf}=\{(\varepsilon_{ddf}A_d E_{c\,deck})/[1+0.7\Psi_d(t_f,t_d)]\}*[(1/A_c)-(e_{pc}e_d/I_c)]$			Eq. 5.9.3.4.3d-2
Factor for the effect of volume-to-surface ratio (Deck)	$k_s=$	1.00		Value = 0.975 <1; So take 1.00, AASHTO LRFD 5.4.2.3.2-2, Pg-28
Humidity factor for shrinkage	$k_{hs}=$	0.95		AASTHO LRFD 5.4.2.3.3-2, Pg-29
Factor for the effect of concrete strength	$k_f=$	1.47		AASHTO LRFD 5.4.2.3.2-4, Pg-28
Time development factor between deck placement and time at transfer	$k_{tdd}=$	0.65		AASHTO LRFD 5.4.2.3.2-5, Pg-28, use difference between age at deck placement and time at transfer
Time development factor between final age and time at transfer	$k_{tdf}=$	1.00		AASHTO LRFD 5.4.2.3.2-5, Pg-28, use difference between final age and time at transfer
Time development factor between deck placement and final age	$k_{tddf}=$	1.00		AASHTO LRFD 5.4.2.3.2-5, Pg-28, use difference between final age and age at deck placement
Shrinkage strain of deck between time of deck placement and final age	$\varepsilon_{ddf}=$	0.000669		AASHTO LRFD 5.9.3.4.3d, Pg-150;
Shrinkage strain of girder between time of deck placement and time at transfer	$\varepsilon_{did}=$	0.000434		AASHTO LRFD 5.9.3.4.3d, Pg-150;
Shrinkage strain of girder between final age and time at transfer	$\varepsilon_{dif}=$	0.000669		AASHTO LRFD 5.9.3.4.3d, Pg-150;
Shrinkage strain of deck between time of deck placement and final age[2]	$\varepsilon_{ddf}=$	0.000235		AASHTO LRFD 5.9.3.4.3d, Pg-150;
Humidity factor for creep	$k_{hc}=$	0.96		
Creep coefficient of deck concrete at final time due to loading introduced shortly after deck placement (i.e. overlays, barriers, etc.) per Eq. 5.4.2.3.2-1	$\Psi_d(t_f,t_d)=$	1.57		t_f = 20440, t_d =120; AASHTO LRFD 5.4.2.3.2-1, Pg-27
Change in concrete stress at centroid of prestressing strands due to shrinkage of deck concrete	$\Delta f_{cdf}=$	-0.18	ksi	AASHTO LRFD 5.9.3.4.3d-2, Pg-150
Prestress gain due to shrinkage of deck in composite section	$\mathbf{\Delta f_{pSS}=}$	**-1.8**	**ksi**	AASHTO LRFD 5.9.3.4.3d-1, Pg-150
Refined Estimates of Time-Dependent Losses	$\mathbf{\Delta F_{pLT}=}$	**32.3**	**ksi**	AASHTO LRFD Eq. 5.9.3.4.1-1
Total Prestress Loss	$\mathbf{\Delta F_{pT}=}$	**45.3**	**ksi**	AASHTO LRFD Eq. 5.9.3.1-1

Total Losses at Service Loads				
Elastic gain due to deck weight, superimposed dead load and live load (Service III)				
Elastic gain due to deck weight, superimposed dead load		**3.3**	**ksi**	Article 9.1b.6.6, PCI Bridge Design Manual
Elastic gain due to live load (Service III)		**5.4**	**ksi**	Article 9.1b.6.6, PCI Bridge Design Manual
Elastic gain		**8.7**	**ksi**	
Effective stress in strands after all losses and gains	$\mathbf{f_{pe}}$	**138.5**	**ksi**	
Prestressing stress limit at service limit state	$0.8f_{py}$	**170.0**	**ksi**	$f_{pe} < 0.8f_{py;}$ ok
Effective stress in strands after all losses and permanent gains	$\mathbf{f_{pe}}$	**133.0**		
Force per strand without live load gains		**14.4**	**kips**	
Total prestressing force after all losses		**545.9**	**kips**	
Final loss percentage		**20.9**	**%**	total losses and gains/ f_{pi}
Final loss percentage without prestressing gains at deck placeemnent		**25.9**	**%**	total losses/ f_{pi}
Final loss percentage without live load gains		**22.8**		

Prestress losses specifically calculated for BTE1, BTE2, BTE3 and BTE4 using measured material properties follows the exact method except the design values are replaced with the former.

E.3 Prestress losses following AASHTO LRFD Lum Sump Method

Lump Sum Estimate of Losses (4th Edition of AASHTO LRFD)						
Losses due to Elastic Shortening						
Item	Notation	Value	Unit			Reference/Note
Area of prestressing steel	A_{ps}=	4.1	in^2	2648	mm^2	*38, 7/16" strand
Prestressing steel stress immediately prior to transfer	f_{pbt}=	187.5	ksi	1293	MPa	
Gross area of section	A_g=	559.5	in^2	360967	mm^2	From response drawing - Bonner Bridge midspan cross-section, Pg-53
Centroid of gross area from bottom (mid -section)	y_g=	20.3	in	516	mm	
Steel centroid dist. to bottom	y_p=	6.68	in	170	mm	36 strands at bottom and 2 at top - see strain profile
Eccentricity of strand	e_m=	13.6	in	346	mm	
Design concrete strength of girder	f'_c=	5	ksi	34	MPa	From NCDOT load rating file
Design concrete compressive strength at time of prestressing for pretensioned members and at time of initial loading for nonprestressed members. If concrete age at time of initial loading is unknown at design time, f ′ci may be taken as 0.80 f ′c (ksi).	f'_{ci}=	4	ksi	28	MPa	AASHTO LRFD 5.4.2.3.2, Pg -28
Unit weight of concrete	w_c=	0.145	kcf			AASHTO LRFD 5.4.2.4 & C5.4.2.4, Pg-30
Modulus of Elasticity for normal weight concrete (girder)	E_c=	4291	ksi	29587	MPa	AASHTO LRFD 5.4.2.4, Pg-30
Modulus of elasticity of concrete at transfer (girder)	E_{ci}=	3987	ksi	27486	MPa	AASHTO LRFD (C5.9.3.2.3a)
Modulus of elasticity for prestressing steel	E_p=	28500	ksi	196501	MPa	AASHTO LRFD 5.4.4.2, Pg-33
Moment of inertia of gross concrete secction about centroidal axis neglecting the reinforcement	I_g=	125390	in^4	5.22E+10	mm^4	
Girder volume (including ends)	V=	430160	in^3	7.05E+09	mm^3	
Moment due to self-weight (girder only)	M_g=	276	k-ft	3.74E+08	N-mm	
Loss due to elastic shortening in pretensioned members	$\mathbf{\Delta F_{pES}}$=	**16.20**	**ksi**	**112**	MPa	Alternate equation, 5.9.3.2.3b, Pg-143.
Approximate Estimate of Time-Dependent Losses						
Average annual ambient relative humidity (percent)	H=			75	%	
Correction factor for relative humidity of the ambient air	γ_h=			0.95		AASHTO LRFD 5.9.3.3, Eq- 5.9.3.3-2, Pg-145
Correction factor for specified concrete strength at time of prestress transfer to the concrete member	γ_{st}=			1.012		AASHTO LRFD 5.9.3.3, Eq- 5.9.3.3-3, Pg-145
Relaxation Loss	Δf_{pR}=	10.15	ksi	70	MPa	AASHTO LRFD 5.9.3.3, Pg-145
Long-Term Prestress Loss	$\mathbf{\Delta f_{pLT}}$=	**35.0**	ksi	241	MPa	AASHTO LRFD 5.9.3.3, Eq- 5.9.3.3-1, Pg-145
Total Prestress Loss	$\mathbf{\Delta F_{pT}}$=	**51.2**	**ksi**	**353**	MPa	AASHTO LRFD Eq. 5.9.3.1-1

Lump Sum Estimate of Losses (9th Edition of AASHTO LRFD)				
Losses due to Elastic Shortening				
Item	Notation	Value	Unit	Reference/Note
Area of prestressing steel	A_{ps}=	4.1	in^2	*38, 7/16" strand
Prestressing steel stress immediately prior to transfer	f_{pbt}=	175	ksi	
Gross area of section	A_g=	559.5	in^2	From response drawing - Bonner Bridge midspan cross-section, Pg-53
Centroid of gross area from bottom (mid -section)	y_g=	20.3	in	
Steel centroid dist. to bottom	y_p=	6.68	in	36 strands at bottom and 2 at top - see strain profile
Eccentricity of strand	e_m=	13.6	in	
Design concrete strength of girder	f'_c=	5	ksi	From NCDOT load rating file
Design concrete compressive strength at time of prestressing for pretensioned members and at time of initial loading for nonprestressed members. If concrete age at time of initial loading is unknown at design time, f ′ci may be taken as 0.80 f ′c (ksi).	f'_{ci}=	4	ksi	AASHTO LRFD 5.4.2.3.2, Pg -28
Unit weight of concrete	w_c=	0.145	kcf	AASHTO LRFD 5.4.2.4 & C5.4.2.4, Pg-30
Modulus of Elasticity for normal weight concrete (girder)	E_c=	4291	ksi	AASHTO LRFD 5.4.2.4, Pg-30
Modulus of elasticity of concrete at transfer (girder)	E_{ci}=	3987	ksi	AASHTO LRFD (C5.9.3.2.3a)
Modulus of elasticity for prestressing steel	E_p=	28500	ksi	AASHTO LRFD 5.4.4.2, Pg-33
Moment of inertia of gross concrete secction about centroidal axis neglecting the reinforcement	I_g=	125390	in^4	
Girder volume (including ends)	V=	430160	in^3	
Moment due to self-weight (girder only)	M_g=	276	k-ft	
Loss due to elastic shortening in pretensioned members	**ΔF_{pES}=**	**15.11**	**ksi**	Alternate equation, 5.9.3.2.3b, Pg-143.
Approximate Estimate of Time-Dependent Losses				
Average annual ambient relative humidity (percent)	H=	75	%	
Correction factor for relative humidity of the ambient air	γ_h=	0.95		AASHTO LRFD 5.9.3.3, Eq- 5.9.3.3-2, Pg-145
Correction factor for specified concrete strength at time of prestress transfer to the concrete member	γ_{st}=	1.220		AASHTO LRFD 5.9.3.3, Eq- 5.9.3.3-3, Pg-145
Relaxation Loss	Δf_{pR}=	2.4	ksi	AASHTO LRFD 5.9.3.3, Pg-145
Long-Term Prestress Loss	**Δf_{pLT}=**	31.2	ksi	AASHTO LRFD 5.9.3.3, Eq- 5.9.3.3-1, Pg-145
Total Prestress Loss	**ΔF_{pT}=**	**46.3**	**ksi**	AASHTO LRFD Eq. 5.9.3.1-1

APPENDIX F – LIVE LOAD MOMENT

Live load moments on longitudinal girders (adapted from AASHTO Manual for Bridge Evaluation, 2019)

Live Load Moments in ft-kips per Wheel Line										
Type of Loading (without Impact)					Span, ft c/c	Type of Loading (with Impact)				
H-15	**HS-20**	3	3S2	3-3		H-15	**HS-20**	3	3S2	3-3
15.0	20.0	10.6	9.7	10.0	5	19.5	26.0	13.8	12.6	13.0
18.0	24.0	12.8	11.6	12.0	6	23.4	31.2	16.6	15.1	15.6
21.0	28.0	15.2	13.8	14.0	7	27.3	36.4	19.7	18.0	18.2
24.0	32.0	19.1	17.4	16.0	8	31.2	41.6	24.9	22.7	20.8
27.0	36.0	23.1	21.1	19.1	9	35.1	46.8	30.1	27.4	24.8
30.0	40.0	27.2	24.8	22.4	10	39.0	52.0	35.4	32.2	29.1
33.0	44.0	31.3	28.5	25.8	11	42.9	57.2	40.7	37.1	33.5
36.0	48.0	35.4	32.2	29.2	12	46.8	62.4	46.0	42.0	37.9
39.0	52.0	39.6	36.1	32.6	13	50.7	67.6	51.4	46.9	42.3
42.0	56.0	43.7	39.9	36.0	14	54.6	72.8	56.8	51.8	46.8
45.0	60.0	47.9	43.7	39.4	15	58.5	78.0	62.2	56.8	51.3
48.0	64.0	52.1	47.5	42.9	16	62.4	83.2	67.7	61.7	55.7
51.0	68.0	56.3	51.3	46.3	17	66.3	88.4	73.1	66.7	60.2
54.0	72.0	60.4	55.1	49.8	18	70.2	93.6	78.6	71.6	64.7
57.0	76.0	64.6	58.9	53.2	19	74.1	98.8	84.0	76.6	69.2
60.0	80.0	68.9	62.8	56.7	20	78.0	104.0	89.5	81.6	73.7
63.0	84.0	73.1	66.6	60.2	21	81.9	109.2	95.0	86.6	78.2
66.0	88.0	77.3	70.5	63.6	22	85.8	114.4	100.5	91.6	82.7
69.0	92.0	81.5	75.2	67.1	23	89.7	119.6	105.9	97.7	87.2
72.0	96.3	85.7	80.3	70.6	24	93.6	125.2	111.4	104.4	91.8
75.0	103.7	89.9	85.4	74.1	25	97.5	134.8	116.9	111.0	96.3
78.0	111.1	94.2	90.5	77.5	26	101.4	144.4	122.4	117.7	100.8
81.3	118.5	98.4	95.6	81.0	27	105.7	154.1	127.9	124.3	105.3
85.1	126.0	102.6	100.7	84.5	28	110.6	163.8	133.4	131.0	109.8
88.8	133.5	106.8	105.9	88.0	29	115.4	173.6	138.9	137.6	114.4
92.5	141.0	112.9	111.0	91.5	30	120.2	183.3	146.8	144.3	118.9
99.8	156.2	125.3	121.2	101.5	32	130.0	203.1	162.9	157.6	132.0
107.4	171.8	137.6	131.5	112.3	34	139.6	223.3	178.9	170.9	146.0
114.8	189.4	150.0	141.7	123.1	36	149.2	246.2	195.0	184.2	160.1
122.3	207.1	162.4	151.9	134.0	38	159.0	269.2	211.1	197.5	174.1
129.7	224.9	174.8	162.2	144.8	40	168.6	292.4	227.3	210.8	188.3
137.2	242.7	187.2	172.4	155.7	42	178.3	315.3	243.3	224.0	202.3
144.7	260.4	199.7	182.7	166.6	44	187.5	337.5	258.7	236.7	215.8
152.1	278.3	212.1	192.9	177.4	46	196.6	359.6	274.1	249.3	229.3
159.6	296.1	224.5	203.2	188.3	48	205.7	381.7	289.4	261.9	242.8

167.1	314.0	237.0	220.8	199.3	50	214.8	403.8	304.7	283.9	256.2
174.6	331.8	249.4	238.4	214.3	52	223.9	425.5	319.9	305.8	274.8
182.0	349.7	261.8	256.1	231.3	54	232.8	447.3	335.0	327.6	295.9
189.5	367.6	274.3	273.8	248.3	56	241.8	469.1	350.1	349.4	316.9
198.8	385.4	286.8	291.4	265.3	58	253.1	490.6	365.1	371.1	337.7
209.2*	403.3	299.2	309.2	282.3	60	265.8*	**512.2**	380.1	392.7	358.5
265.1*	492.8	361.5	398.0	372.2	70	333.1*	619.0	454.2	500.1	467.6
327.0*	582.4	423.9	487.1	471.9	80	406.8*	724.5	527.3	605.9	587.0
394.9*	672.2	486.3	576.4	571.7	90	486.7*	828.8	599.4	710.5	704.6
468.8*	762.0	548.7	665.9	671.5	100	572.9*	931.2	670.7	813.9	820.7
634.5*	941.6	673.6	845.1	871.3	120	764.0*	1,133.7	811.1	1,017.5	1,049.1
824.2*	1,121.4	798.5	1,024.5	1,071.1	140	979.8*	1,333.3	949.2	1,217.8	1,273.2
1,038.0*	1,384.0*	923.5	1,204.1	1,270.9	160	1,220.1*	1,626.2*	1,085.5	1,415.3	1,493.9
1,275.8*	1,701.0*	1,048.4	1,383.7	1,470.8	180	1,484.9*	1,980.0*	1,222.3	1,610.6	1,712.0
1,537.5*	2,050.0*	1,173.4	1,563.5	1,670.8	200	1,774.0*	2,365.7*	1,353.9	1,804.0	1,927.8
2,296.9*	3,062.5*	1,485.8	2,013.0	2,170.6	250	2,603.1*	3,469.8*	1,683.9	2,281.4	2,460.0
3,206.2*	4,275.0*	1,798.2	2,462.6	2,670.5	300	3,583.5*	4,779.4*	2,009.8	2,752.4	2,984.7

* Based on standard lane loading. All other values are based on standard truck loading. HS-20 Truck has the same loading configuration as HL-93 Truck which will be used in load rating calculations.

APPENDIX G – LOAD RATING SAMPLE CALCULATION AND LITERATURE REVIEW

G.1 Bridge Load Rating According to AASHTO LRFD and AASHTO Standard Specifications

Materials and other Information	Notation	Value	Units	Notes/ Ref.
Span length	L	61.2	ft	
Depth of girder	h	45.0	in	
Structural slab thickness	t_s	7.0	in	
Thickness of haunch	t_h	1.5	in	
Bridge width (clear roadway)	w	28.0	ft	
Total bridge width (including barrier)		33.5	ft	
Total slab thickness	t_S	7.25	in	
NuManual for Bridge Engineeringr of traffic lanes		2.0	nos.	Integer value of w/12
Future wearing surface	t_w	2.0	in	
Barrier weight	w_B	455	lb/ft	
Concrete strength (girder)	f'_c=	5.00	ksi	From NCDOT load rating file
Concrete strength at release (girder)	f'_{ci}	4.00	ksi	AASHTO LRFD 5.4.2.3.2, Pg -28
Concrete strength (deck)	$f'_{c\ deck}$	3.00	ksi	From NCDOT load rating file; AASHTO 8.15.2.1.1
Compressive strength of deck at transfer	$f'_{ci\ deck}$	2.40	ksi	Taken as: $0.8f'_c$; AASHTO LRFD 5.4.2.3.2, Pg -28
Unit weight of concrete	w_c	0.145	kcf	AASHTO LRFD 5.4.2.4 & C5.4.2.4, Pg-30
Modulus of Elasticity for normal weight concrete (girder)	E_c	4291	ksi	AASHTO LRFD 5.4.2.4, Pg-30
Modulus of elasticity of concrete at transfer (girder)	E_{ci}	3987	ksi	AASHTO LRFD (C5.9.3.2.3a)
Modulus of Elasticity for normal weight concrete (deck)	$E_{c\ deck}$	3625	ksi	AASHTO LRFD 5.4.2.4, Pg-30
Modulus of elasticity of prestressing steel	E_s	28000	ksi	
Allowable tensile stress at service (midspan, Inventory)		0.424	ksi	$6\sqrt{f'_c}$
Allowable tensile stress at service (midspan, Operating)		0.530	ksi	$7.5\sqrt{f'_c}$
Specified tensile strength of prestressing steel	f_{pu}	250	ksi	Bonner drawings, Back calculate from prestressing force in each strand, AASHTO LRFD 5.4.4.1, Pg- 33
Area of prestressing strand	A_{ps}	4.1	in^2	*37, 7/16" strand
Rating vehicle (Design)				HS20 for rating based on the Strandard Specifications
				HL-93 for rating based on the LRFD Specifications
AADT				>5000

Section Properties				
Distance from centroid to the extreme top fiber of the non-composite girder	y_{gt}	24.7	in	
Distance from centroid to the extreme bottom fiber of the non-composite girder	y_{gb}	20.3	in	
Moment of inertia of gross concrete secction about centroidal axis	I_g=	125390	in^4	
Area of cross section of the noncomposite section	A_g=	559.5	in^2	
Distance between the centers of gravity of the girder and the deck	e_g	29.7	in	
Distance from the center of gravity of composite section to the top fiber of the deck	y_{ct}	18.1	in	
Distrance from the center of gravity of composite section to the top fiber of girder	y_{cg}			
Distance from the center of gravity of composite section to the bottom fiber of the girder	y_{cb}	35.4	in	
Composite moment of inertia	I_c	378476	in^4	
Area of cross section of the composite section	A_c	1148	in^2	
Steel centroid dist. to bottom	e_m	6.68	in	36 strands at bottom and 2 at top - see strain profile
Eccentricity of prestressing strand	e_{pg}	13.6	in	

Dead Load Calculations				
Girder moment	M_g	276	k-ft	
Slab moment	M_{sd}	362	k-ft	
Barrier moment	M_b	53.2	k-ft	
Future wearing course	M_{ws}	79.1	k-ft	
Moment due to diaphragm	M_d	39.8	k-ft	
Moment due to haunch	M_h	11.3	k-ft	
Total dead load moment	M_D	821	k-ft	

Stresses and Strength (at midspan and bottom of girder)				
Total Prestress Loss (Refined Method)	ΔF_{pT}	46.2	ksi	
Prestressing steel stress immediately prior to transfer	f_{pi}	175	ksi	$0.7*f_{pu}$; $(18900/A_p/1000)$
Effective final stress	f_{se}	128.8	ksi	
Effective final prestress force	P_{se}	529	kips	
Dead load stress on non-composite section	f_{Nb}	-1.34	ksi	
Dead load stress on composite section	f_{CD}	-0.149	ksi	
Stress from prestress force	f_{pr}	2.11	ksi	Compression
Flexural Strength				
Average stress in prestressing strand	f_{ps}	240	ksi	PCI Bridge Design Manual, Article 9.1a.9
	k	0.38		PCI Bridge Design Manual, Article 9.1a.9
Yield strength of prestressing strand	f_{py}	212.5	ksi	$0.85f_{pu}$
Distance from extreme compression fiber to centroid of prestressing strands	d_p	46.8	in	$h - y_p$
Stress factor of compression block	$\beta 1$	0.85		0.85 for $f'_c \leq 4.0$ ksi
Effective width of compression flange	b	96.0	in	
Distance from the extreme compression fiber to the neutral axis	c	4.74	in	PCI Bridge Design Manual, Article 9.1a.9
Depth of equivalent stress block	a	4.03	in	
Nominal flexural resistance	M_n	3683	k-ft	PCI Bridge Design Manual, Article 9.1a.9
Factored flexural resistance	M_r	3683	k-ft	PCI Bridge Design Manual, Article 9.1a.9
Live Load				
Girder spacing	S	8	ft	
Distribution factor for bending moment				Table 4.6.2.2.2b-1, AASHTO LRFD
Multi-lane loading	LDF	0.596		$0.075 + (S/9.5)^{0.6} (S/L)^{0.2} (K_g/[12.0Lt_s^3])^{0.1}$
Single-lane loading	LDF	0.437		$0.06 + (S/14)^{0.4} (S/L)^{0.3} (K_g/[12.0Lt_s^3])^{0.1}$
	K_g	732562		$n(I_g + A_g e_g^2)$
Governing distribution factor		0.596	lanes/girder	
for x/L = 0 - 0.333	$M_{HL\text{-}93\ Design\ Truck}$	NA	k-ft	Table 8.11.1-1, PCI Bridge Design Manual
for x/L = 0.333 - 0.500	$M_{HL\text{-}93\ Design\ Truck}$	821	k-ft	Table 8.11.1-1, PCI Bridge Design Manual
Design Lane Load 0.640 kips/ft				
Maximum bending moment at midspan	$M_{HL\text{-}93\ Design\ Lane\ Load}$	299	k-ft	Table 8.11.2, PCI Bridge Design Manual
Dynamic allowance	IM	33.0	%	Table 18.1.3.2.3-1, PCI Bridge Design Manual
Live load moment	M_{LL+I}	829	k-ft	18.6.7.1.3, PCI Bridge Design Manual
Live load stress	f_{LL+I}	-0.932	ksi	18.6.7.1.3, PCI Bridge Design Manual

Load Rating				
Strength I				
Inventory Rating	**RF_{IN}**	**1.82**		Table B6A-1, Manual for Bridge Engineering
Operating Rating	**RF_{OP}**	**2.36**		Table B6A-1, Manual for Bridge Engineering
Service III				
Allowable tensile stress				$6\sqrt{f'_c}$
Inventory Rating	**RF_{IN}**	**1.12**		Table B6A-1, Manual for Bridge Engineering

Service I				
Compression stress limit state	Article 6A, Manual for Bridge Engineering; Article 18.6.7.3, PCI Bridge Design Manual			
Case I: The stress at the top of girder under 0.5 (permanent + transient loads)				
Dead load stress on non-composite section	f_{Nt}	1.63	ksi	
Dead load stress on composite section	f_{Ct}	0.04	ksi	
Stress from prestress force	f_{prt}	-0.47	ksi	
Stress from live load	f_{CLL}	0.25	ksi	
Allowable stress	f_{allow}	2.00	ksi	$0.4f'_c$
Load rating	RF	5.58		
Case II: The stress at the top of girder under permanent + transient loads				
Allowable stress	f_{allow}	3.00	ksi	$0.4f'_c$
Load rating	RF	7.18		
Case III: The stress at the top of slab under 0.5 (permanent + transient loads)				
Dead load stress on composite section	f_{Ct}	0.08	ksi	
Stress from live load	f_{CLL}	0.47	ksi	
Allowable stress	f_{allow}	1.20	ksi	$0.4f'_{c,deck}$
Load Rating	**RF**	**2.45**		
Case IV: The stress at the top of slab under permanent + transient loads				
Allowable stress	f_{allow}	1.80	ksi	$0.6f'_{c,deck}$
Load rating	RF	3.63		
Service III (Changing allowable tensile stress)				
Allowable tensile stress		0.212		$3\sqrt{f'_c}$
Inventory Rating	$\mathbf{RF_{IN}}$	**0.90**		Table B6A-1, Manual for Bridge Engineering
Service III (Changing allowable tensile stress)				
Allowable tensile stress		0.00		0
Inventory Rating	$\mathbf{RF_{IN}}$	**0.67**		Table B6A-1, Manual for Bridge Engineering

Rating for Design Loading Based on Standard Specifications				
Prestress Losses				
Initial prestressing force/strand		17.01	kips	
Effective pretension force after allowing for the initial losses	P_{si}	646	kips	Article 18.6.5, PCI Bridge Design Manual
Ecentricity of prestress force	e_{pg}	13.62	in	Article 18.6.5, PCI Bridge Design Manual
Average concrete stress at the center of gravity of the pretensioning steel due to pretensioning force and dead load of girder immediately after transfer	f_{cir}	1.752	ksi	Article 18.6.5, PCI Bridge Design Manual
Concrete stress at the center of gravity of the pretensioning steel due to all dead loads except the dead load present at the time the pretensioning force is applied	f_{cds}	0.659	ksi	Article 18.6.5, PCI Bridge Design Manual
Elastic shortening loss	ES	12.30	ksi	Article 9.16.2, AASHTO Standard Specifications
Shrinkage loss (assume RH = 70%)	SH	6.50	ksi	Article 9.16.2, AASHTO Standard Specifications
Creep loss	CR_c	16.41	ksi	Article 9.16.2, AASHTO Standard Specifications
Relaxation loss	CR_s	2.62	ksi	Article 9.16.2, AASHTO Standard Specifications
Total prestress losses		37.8	ksi	Article 9.16.2, AASHTO Standard Specifications
Effective final stress	f_{se}	137.2	ksi	f_{pi} - Total Loss
Effective final prestress force	P_{se}	563	kips	
Flexural Strength				
Average stress in prestressing strand at the time when nominal resistance is required	f_{ps}	239	ksi	Article 9.17.4.1, AASHTO Standard Specifications
Depth of equivalent stress block	a	4.75	in	
Nominal flexural resistance	M_n	3639	k-ft	Article 9.17, AASHTO Standard Specifications
Live Load (Take max of wheel/lane/tandem load)				
Girder spacing	S	8	ft	
Distribution factor for bending moment (WSD/LFD)				
Multi-lane loading	WDF	1.455		Article 3.23.2, AASHTO Standard Specifications
Governing distribution factor		1.455	lanes/girder	
Maximum wheel-load moment from chart (including impact factor)	$M_{WL-HS20}$	525	k-ft	APPENDIX C6B, Manual for Bridge Engineering
Live load moment/girder	M_{LL+I}	763	k-ft	
Live load stress	f_{LL+I}	-0.858	ksi	18.6.7.1.3, PCI Bridge Design Manual
Stress from prestress force	f_{pr}	2.25	ksi	Compression
Total tensile stress at service	f_{total}	-0.10	ksi	less than f_{allow} allowable stress, -0.424 ksi
Load Ratings				
Inventory rating with AASHTO factored load method	**RF_{IN}**	**1.55**		18.6.6.2, PCI Bridge Design Manual
Operating rating with AASHTO factored load method	**RF_{OP}**	**2.59**		18.6.6.2, PCI Bridge Design Manual
Inventory rating with AASHTO allowable stress method, $6\sqrt{f'c}$	**RF_{IN}**	**1.38**		18.6.6.2, PCI Bridge Design Manual
Inventory rating with AASHTO allowable stress method, $3\sqrt{f'c}$	**RF_{IN}**	**1.13**		Allowable stress - $3\sqrt{f'_c}$
Inventory rating with AASHTO allowable stress method, 0	**RF_{IN}**	**0.89**		Allowable stress - 0

Similar calculations were performed when finding rating using NCDOT assumptions. The only change was the prestress losses used in the calculation. For the load rating calculation specific to each girder, the same procedure was followed except the flexural strength, prestress losses used were obtained from laboratory measured values as well as Response 2000. Girder specific calculations also used measure material properties instead of design values. To avoid repetition, the detailed calculations were excluded since the procedure and equations are essentially the same except for the change of the aforementioned input parameters.

G.2 Purpose of Load Rating of Aged Bridges

Aging, environmental conditions, damage due to vehicular impact, and increased gross vehicle weights result in structural deterioration that affects the load carrying capacity of bridges (PCI BDM, 2014). The capacity of the bridge needs to be periodically reevaluated due to these changes and the Manual for Bridge Engineering (MBE) requires to specify which vehicles can use the bridge or if any level of restriction (posting) has to be imposed. This procedure is called load rating. Around 10.0% of the nation's bridges are structurally deficient and 14.0% are considered functionally obsolete according to a statistics given by U.S. Government Accountability Office in 2014. Many bridges still in the use in the United States were built in the 1970s and have exceeded their 50 year design life. There are only limited financial resources available to maintain this infrastructure (Sanayei et al., 2012) and it needs to be properly allocated for rehabilitation and replacement of these aged bridges. Truck miles travelled over bridges in 2008 were recorded to have almost doubled over the previous 20 years and are expected to grow steadily (AASHTO, 2008). These additional traffic loading can contribute to deterioration of bridge infrastructure. Other forms of deterioration such as prestress losses, deterioration of the concrete matrix, corrosion, cracks, degradation in bond between reinforcing steel, etc. also can reduce the structural capacity of member. A study of the literature indicates, most of the research conducted previously used only non-destructive test data to obtain strain information, or is used to calibrate finite element models that are then used to conduct load rating calculations. (Brena et al., 2013, Schiebel et al., 2002; Chajes et al., 1997; Yost et al., 2005). Some studies have indicated that calculated load-carrying capacities tend to be underestimated (Bakht and Jaeger, 1990; Goble et al., 1992; NCHRP 1998; Chajes et al. 2000). However, limited research has been conducted to perform destructive tests of actual aged bridge girder specimens to determine their flexural capacity, shear capacity and cracking stresses and in turn inform the load rating. Discussions from previous chapters has shown that prestress losses have an impact on the cracking moment, first tensile stress and ultimate capacity of these aged girders. Thus, accurate load ratings are critical for effective bridge management and this study provides a unique opportunity to conduct load rating calculations for four prestressed concrete girders after 56 years of service.

G.3 Assumptions

Current practices uses 2D girder-by-girder analysis for rating bridges and typically do not model the 3D behavior of bridge as factors such as deck continuity, diaphragms, and parapet stiffness. Load rating is based on existing structural conditions, material properties. Field inspections can be used to inform load rating. Rating factors determined at the end of service life can take into account the compressive strength of cores extracted from the girders, current modulus of elasticity of the prestressing strands, etc. It is assumed that any form of deterioration are usually accounted for by reducing the cross-sectional area of concrete section or area of steel so that their effect can be evaluated. The effective section properties are used to determine the resistance or strength of section.

G.4 Methods of Load Rating according to AASHTO

Bridges are load rated for service and strength limit states. While the strength limit states allow for the maximum permissible loads and is concerned about the nominal strength of the structure, service limit states avoid cracking under routine service loads under current practices. Some DOTs limit the tensile stress in the girders to zero.

The Manual for Bridge Engineering describes the following rating methods:

1. Load and Resistance Factor Rating (LRFR) method consistent with AASHTO LRFD Bridge Design Specifications.
2. Load Factor Rating (LFR) in accordance with Allowable Stress Design and Load Factor Design of AASHTO Standard Specifications.

The generalized expression of load rating in LRFR method is as follows:

$$RF = \frac{C-(\gamma_{DC})(DC)-(\gamma_{DW})(DW)\pm(\gamma_P)(P)}{(\gamma_{LL})(LL+IM)} \quad (76)$$

For the strength limit states,

$$C = \varphi_c \varphi_S \varphi R_n \quad (77)$$

Where

$$\varphi_c \varphi_S > 0.85 \quad (78)$$

For the service limit states,

$$C = f_R$$

Where

RF = Rating factor

C = Capacity

f_R = Allowable stress specified in the LRFD code

R_n = Nominal member resistance (as inspected)

DC = Dead load effect due to structural components and attachments

DW = Dead load effect due to wearing surface and utilities

P = Permanent loads other than dead loads

LL = Live load effect

IM = Dynamic load allowance

γ_{DC} = LRFD load factor for structural components and attachments

γ_{DW} = LRFD load factor for wearing surfaces and utilities

γ_P = LRFD load factor for permanent loads other than dead loads = 1.0

φ_C = Condition factor

φ_S = System factor

φ= Condition factor

Aged prestressed concrete bridges have undergone deterioration over their service life. This can potentially increase the rate of future deterioration. To account for this uncertainty, the condition factor is used. The system factor is taken as 1.00 for prestressed concrete bridges.

The general expression used in Load Factor Rating is as follows:

$$RF = \frac{C - A_1 D}{A_2 L(1+I)} \tag{79}$$

Where

RF = Rating factor for the live load carrying capacity. The rating factor multiplied by the rating vehicle in tons gives the rating of the structure

C = Capacity of member

D = Dead load effect on the member.

L = Live load effect on the member

I = Impact factor to be used with the live load effect

A_1 = Factor for dead loads

A_2 = Factor for live load

The Rating Factor (RF) obtained may be used to determine the safe load capacity of the bridge in tons as follows:

$$RT = RF \times W \tag{80}$$

Where

RT = Rating in tons for truck used in computing live load effect

W = Weight in tons of truck used in computing live load effect

G.5 Rating of Prestressed Concrete Bridges

The choice of method, either working stress or factored load method for rating of prestressed concrete bridges depends on the bridge owner's policy. Moreover, the bridge may be posted for operating or inventory or an intermediate condition. For this study, the bridge is load rated by both the methods and the safe load capacity of the Bonner Bridge girders are assessed. The rating equations used for both LRFR and LFR method are listed below:

G.5.1 LRFR rating equations for different limit states

Strength I:

$$\text{Inventory Rating, } RF_{IN} = \frac{\phi M_n - 1.25\,(M_G + M_S + M_B + M_{DP} + M_H) - 1.5M_{WS}}{(M_{LL+I})(1.75)} \tag{81}$$

$$\text{Operating Rating, } RF_{OP} = \frac{\phi M_n - 1.25\,(M_G + M_S + M_B + M_{DP} + M_H) - 1.5M_{WS}}{(M_{LL+I})(1.35)} \tag{82}$$

Where

$$M_{LL+I} = \text{Live load moment} = LDF\{M_{lane-HS\,20\,(Lane)} + MAX(M_{lane-HS\,20\,(Truck)}, M_{lane-HS\,20\,(Tandem)})(1 + IM)\} \tag{83}$$

Service III

$$\text{Inventory Rating, } RF_{IN} = \frac{f_{allow} - (f_{pe} + f_{DL})}{0.8 f_{LL+I}} \tag{84}$$

Where

$$f_{allow} = \text{Allowable tensile stress} = 6\sqrt{f_c'} \tag{85}$$

$$f_{pe} = \text{Stress from prestress force} = \frac{P_{se}}{A_g} + \frac{P_{se} e_{pg} y_{gb}}{I_g} \tag{86}$$

$$f_{DL} = \text{Dead load stress on composite and non-composite section} = f_{Nb} + f_{CD} \tag{87}$$

$$f_{Nb} = \text{Dead load stress on non-composite section} = -\frac{(M_g + M_{sd} + M_d + M_h) y_{gb}}{I_g} \tag{88}$$

$$f_{CD} = \text{Dead load stress on composite section} = -\frac{(M_b+M_{ws})y_{cb}}{I_c} \quad (89)$$

$$f_{LL+I} = \text{Live load stress} = \frac{M_{LL+I}y_{Cb}}{I_c} \quad (90)$$

Service I

Case I: Stress at the top of girder under 0.5 (permanent + transient loads)

$$RF = \frac{f_{allow}-0.5\,(f_{Nt}+f_{Ct}+f_{prt})}{f_{CLL}} \quad (91)$$

Where

$$f_{allow} = 0.4f_c' \quad (92)$$

$$f_{Nt} = \text{Dead load stress on non-composite section} = \frac{(M_g+M_{sd}+M_d+M_h)y_{gt}}{I_g} \quad (93)$$

$$f_{Ct} = \text{Dead load stress on non-composite section} = \frac{(M_b+M_{ws})y_{cgt}}{I_c} \quad (94)$$

$$f_{prt} = \text{Stress from prestress force} = \frac{P_{se}}{A_g} - \frac{P_{se}e_{pg}y_{gt}}{I_g} \quad (95)$$

$$f_{CLL} = \text{Live load stress} = \frac{M_{LL+I}y_{cgt}}{I_c} \quad (96)$$

y_{cgt} = distance from the center of gravity of composite section to the top fiber of the girder

Case II: The stress at the top of girder under permanent + transient loads

$$RF = \frac{f_{allow}-(f_{Nt}+f_{Ct}+f_{prt})}{f_{CLL}} \quad (97)$$

Case III: The stress at the top of slab under 0.5 (permanent + transient loads)

$$RF = \frac{f_{allow}-0.5\,f_{Ct}}{f_{CLL}} \quad (98)$$

Where

$$f_{Ct} = \frac{(M_b + M_{ws})y_{ct}}{I_c} \quad (99)$$

$$f_{CLL} = \text{Live load stress} = \frac{M_{LL+I}y_{ct}}{I_c} \quad (100)$$

$$f_{allow} = \text{Allowable tensile stress} = 0.4f'_{c,deck} \quad (101)$$

Case IV: The stress at the top of slab under permanent + transient loads

$$RF = \frac{f_{allow} - f_{Ct}}{f_{CLL}} \quad (102)$$

$$f_{allow} = \text{Allowable tensile stress} = 0.6f'_{c,deck} \quad (103)$$

Description of sectional property notations are appended at the end.

G.5.2 LFR Rating Equations

Inventory rating with AASHTO factored load method

$$RF_{IN} = \frac{\phi M_n - 1.3M_D}{2.17M_{LL+I}} \quad (104)$$

Inventory rating with AASHTO factored load method

$$RF_{OP} = \frac{\phi M_n - 1.3M_D}{1.3M_{LL+I}} \quad (105)$$

Inventory rating with AASHTO allowable stress method, $6\sqrt{f'c}$

$$RF_{IN} = \frac{f_{allow} - (f_{pe} + f_{DL})}{f_{LL+I}} \quad (106)$$

Where

$$M_{LL+I} = -\frac{M_{LL+I}y_{cb}}{I_c} \quad (107)$$

APPENDIX H - SHEAR CAPACITY OF BONNER BRIDGE GIRDERS

Prestress losses and flexural capacity of Bonner Bridge have already been discussed in great detail. The research program provided the unique opportunity to also determine the shear capacity of recovered bridge girders through testing the ends of the members. In order to test the ends of the girders, BTE3 and BTE4 were brought very near to their peak flexural capacity but did not catastrophically fail the members so the ends could be tested in shear. The girders were tested in three point bending test so that the shear capacity in certain load configurations could be determined. BTE3 was tested on both ends while it was possible to test only one end of BTE4. This chapter outlines the experimental program, instrumentation, and behavior of prestressed concrete girders in shear.

H.1 Girder Experimental Setup

The arrangement of the load was determined so that shear failures rather than flexural failures were predicted. Also, it was determined that the shear span to depth ratio should be as large as possible while avoiding flexural failures. The first test was conducted on the south end of BTE3. The south end refers to the geographical south of BTE3 which had a shorter shear span. The shear span to depth (a/d) ratio for the shorter span was 2.05. The supports were placed at 9 in inward from the girder ends. A point load was applied at 8 feet 9 inches from the girder end in the shorter shear span. The shear force and moment diagram from the applied load is shown in Figure H.1. Support configurations and actuators used were the same as in flexural test. The side and end view of the test setup can be seen in Figure H.2.

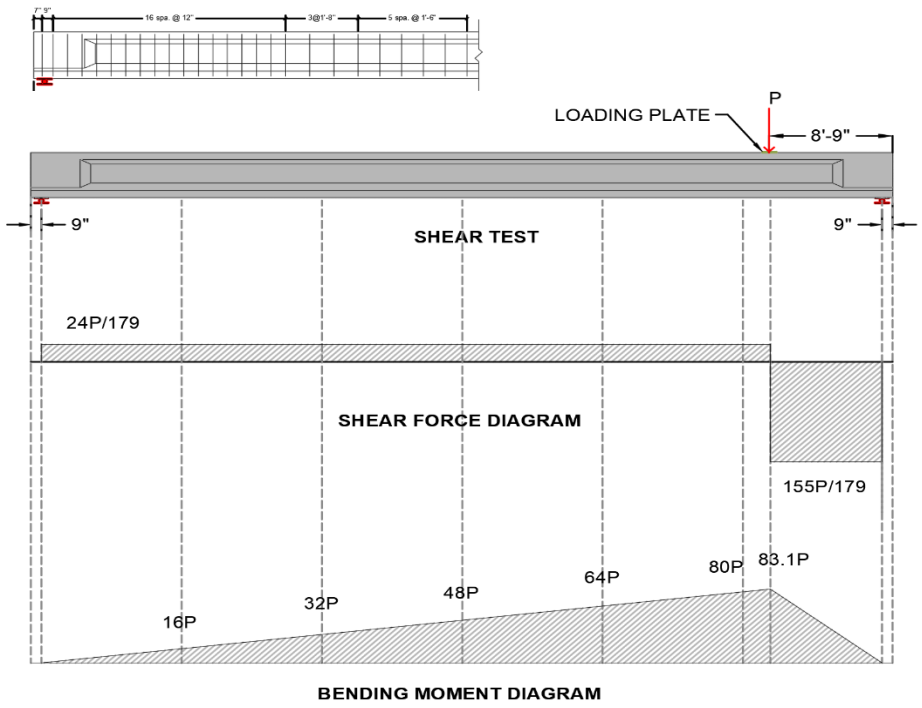

Figure H.1: Applied shear and moment due to applied load in BTE3 South (Shear is in kips, moment is in kips-in).

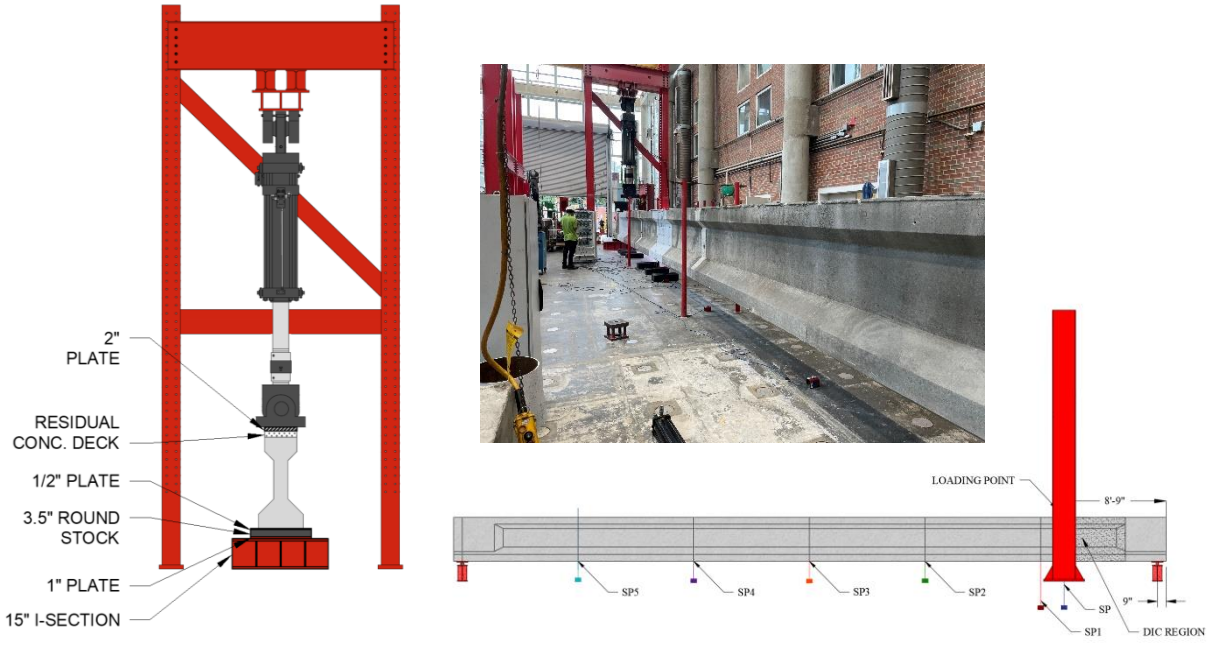

Figure H.2: Experimental setup for BTE3 - South End

The second and third test, north end of BTE3 and south end of BTE4 were tested in different load configuration. The load plate was placed at 15 feet from one end of the girder. The support near the load plate was placed at 6 feet from the end and the other support at 9 in from the far end. The shear span to depth ratio for the shorter shear span was 2.31. The setup and the corresponding shear force and bending moment diagram due to applied load is shown in Figure H.3. Figure H.4 shows the side and end view of the test setup.

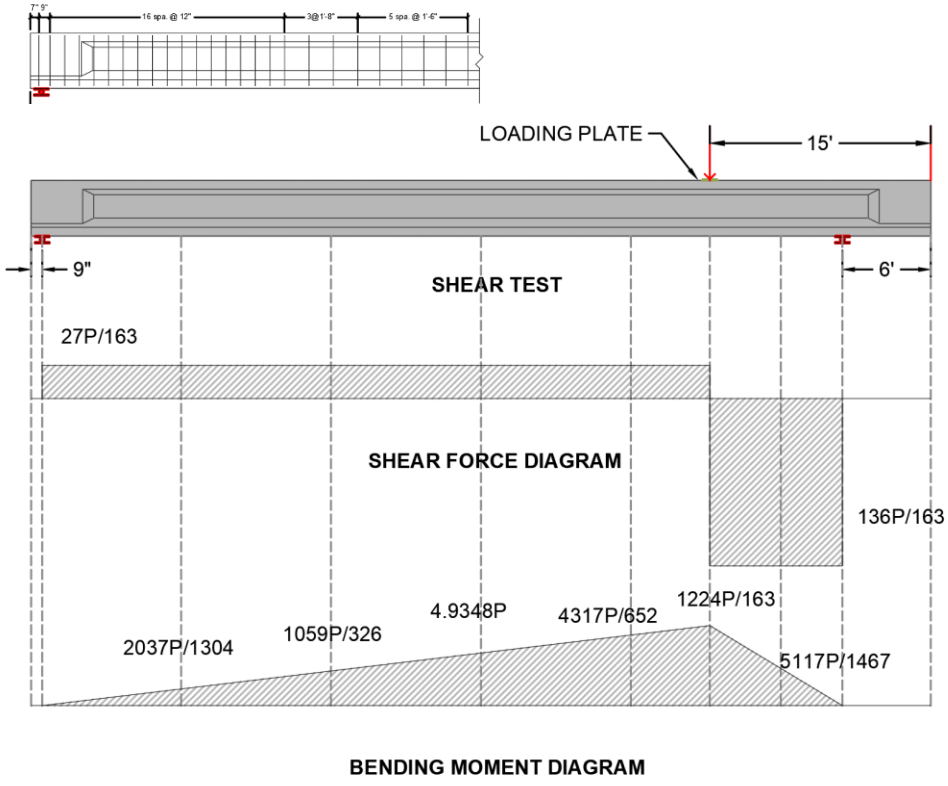

Figure H.3: Applied shear and moment due to applied load in BTE3 North and BTE4 South (Shear is in kips, moment is in kips-in).

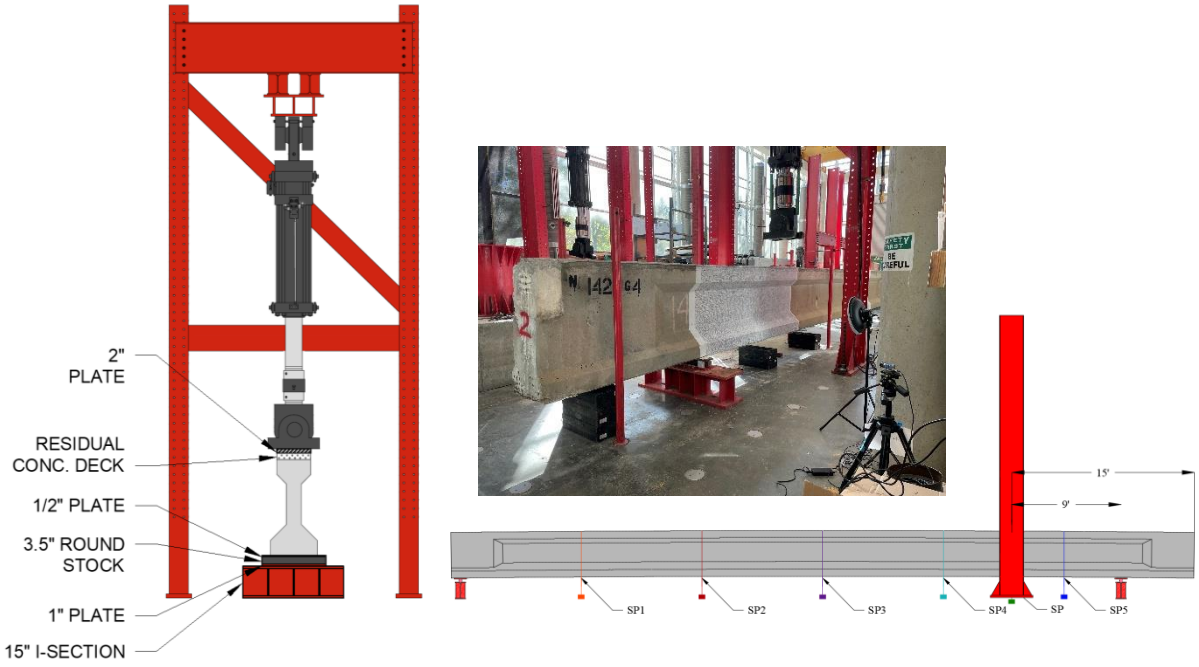

Figure H.4: Experimental setup for shear test of BTE3 North.

The first test was conducted to have a reaction to very much represent how the structure would behave under a very large concentrated load near the support. In subsequent tests, the focus was to understand how the web transmitted shear without the beneficial effects of the widened end region near the support. This could provide additional information on the capacity of the girders. The a/d ratio for all the three tests were less than 2.50. It is well known members with a/d ratio less than 2.50 do not adhere to the classical plane-sections remain-plane hypothesis, and the response likely corresponds to that of a disturbed region.

H.2 Instrumentation

All the girders were instrumented to obtain load, vertical displacement and deformation data along the length of beam. Load was applied through a hydraulic actuator and measured using a load cell. The hydraulic actuator was also instrumented with a displacement transducer that recorded the displacement as load increased. Deformation of the girder between the loading point and the support in the shorter shear span was measured using Digital Image Correlation (DIC). The instrumentation was placed on the west face of BTE3 South and BTE3 North and east face of

BTE4 South. In addition to full field deformation data, string potentiometers were used to collect vertical displacement at different location along the length of the girder.

H.2.1 Digital Image Correlation

Data on crack widths, their location and full field of deformation data was obtained with Digital Image Correlation (DIC). DIC instrumentation is used to study the shear cracking behavior along with flexural cracks that appear throughout the loading protocol. Images from the cameras were taken at 2 Hz. The process of DIC instrumentation is the same as in flexural test and can be found in section A2.2.4. Figure H.5 shows the speckle pattern and camera setup for shear test. The speckled region for DIC data collection is shown in Figure H.6.

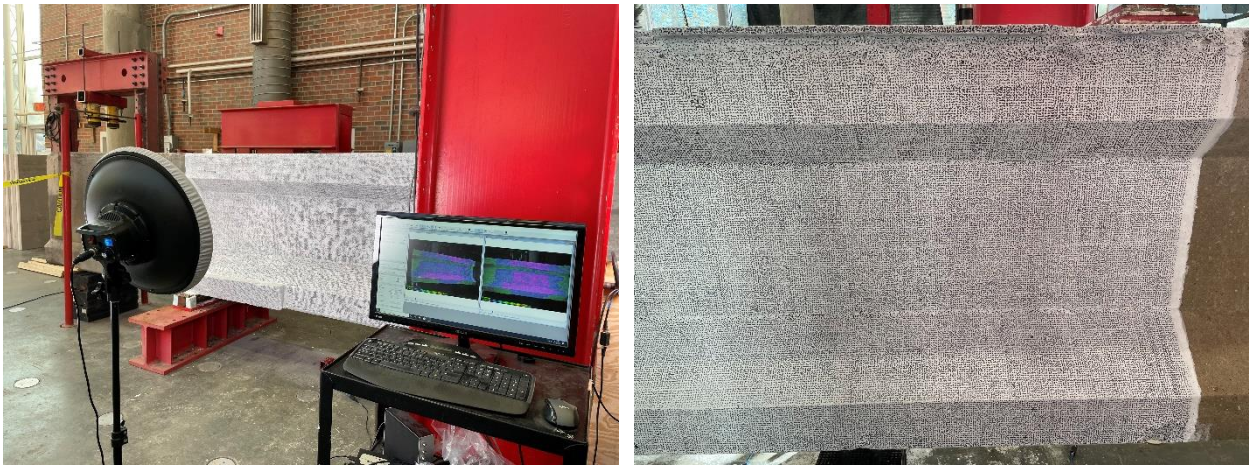

Figure H.5: DIC instrumentation and speckle pattern.

H.2.2 String Potentiometer

Five string potentiometers were placed underneath the beam at a spacing of 119 in. to measure the vertical displacement of the beam throughout loading along with one additional string potentiometer located at the loading point. The string potentiometer layout for BTE3 South and that for BTE3 North and BTE4 South is shown in Figure H.6. The string potentiometer displacements include the vertical displacement of the strong floor during loading, but the stiffness

of the strong floor is much higher than that of the girder and does not contribute significantly to the total deflection.

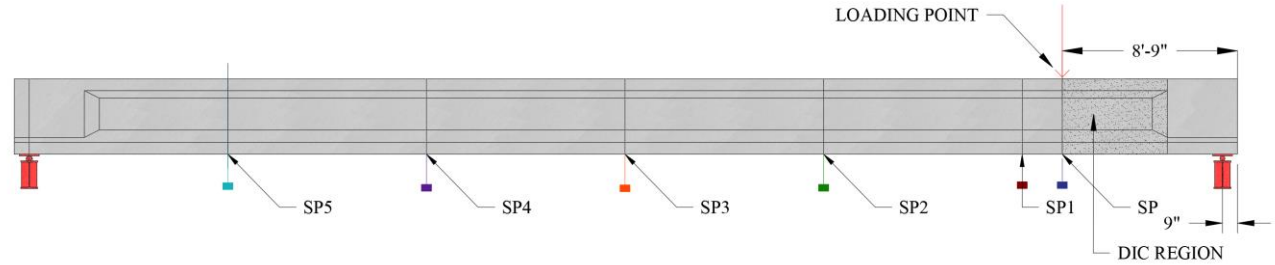

(a)

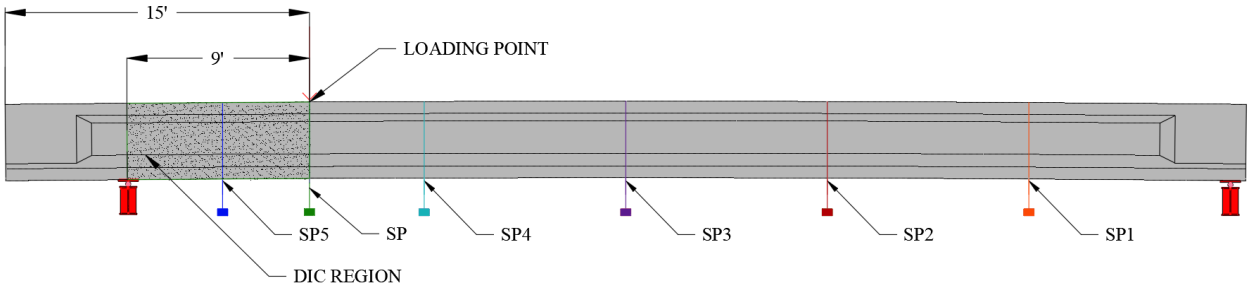

(b)

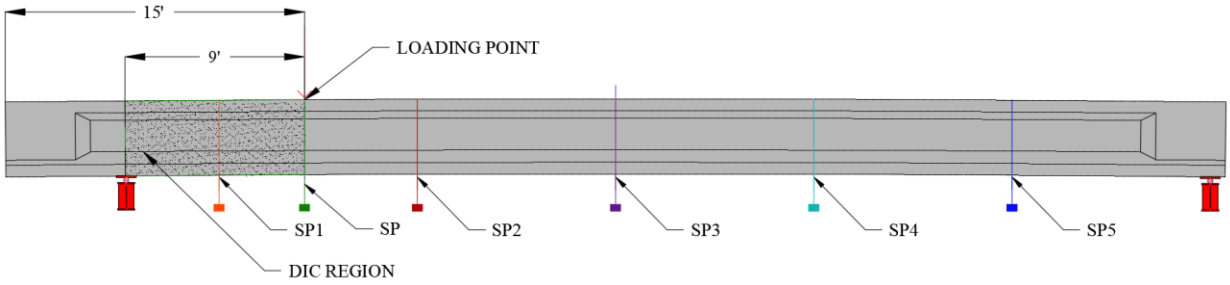

(c)

Figure H.6: String Potentiometer and DIC Region (a) BTE3 – South End (b) BTE3 – North End (c) BTE4 – South End

H.3 Loading Protocol

Shear testing of the girder involved monotonic loading to failure in displacement control. During the test, load stages were performed where loading was stopped so that the specimen could be approacched. For BTE3-South, the load stages were performed at 80 kips, 220 kips, 230 kips, 250 kips, 270 kips, 290 kips and 310 kips. For BTE3-North and BTE4-South, the load stages were performed at 210 kips, 230 kips, 250 kips, 270 kips, 290 kips and the final load stage occurred at 310 kips. At each load stage, the load was reduced by at least 10% for safety concerns as a sudden failure of concrete due to shear or cocnrete crushing may be catastrophic when the girder is approached for crack measurements. Cracks were marked, photographed and their widths measured using a crack comparator.

H.4 Experimental Observation

The results of the shear test of BTE series is outlined in this chapter. This includes the shear capacity, load-deformation, longitudinal, principal and shear strain variation in the web, strains maps from DIC and photographs from the experimental program. A summary of the speimen properties, peak loads and crack widths is listed in Table H.1. The maximum actuator capacity was reached prior to failing BTE3 at the South end. So, the strength is higher than that reported in Table H.1.

Table H.1: Summary of shear test results

Specimen	$f'_{c,girder}$ (psi)	$E_{c,girder}$ (ksi)	$\varepsilon'_{c,girder}$ ($\times 10^{-3}$)	$f'_{c,deck}$ (psi)	$E_{c,deck}$ (ksi)	$\varepsilon'_{c,deck}$ ($\times 10^{-3}$)	a/d	Max. Applied Shear (kips)	Max. Applied Moment (kips-ft)	Max. Crack Width (mm)
BTE3 North	7270	5870	1.70	5550	3950	2.08	2.31	287	2585	1.80
BTE3 South							2.05	276	2447	2.00
BTE4 South	7974	5051	2.09				2.31	274	2394	2.50

H.4.1 BTE3 North

The girder failed in shear at a peak applied load of 344 kips and the corresponding applied moment is 2585 k-ft. Figure H.7 shows a photo of the specimen at the last load stage and at the peak applied load. At the final load stage both the critical shear crack and flexural shear cracks can be seen. The critical shear crack extended from the loading point to the support traversing across the entire depth of web. A summary of the cracks marked and measured at the final load stage is provided in Figure H.8. The maximum crack width observed at 310 kips of actuator load was 1.8 mm.

a) Final Load Stage : 310 kips b) Peak Load: 344 kips

Figure H.7: BTE3 North (a) Cracks at final load stage (b) Failure photo at peak applied load

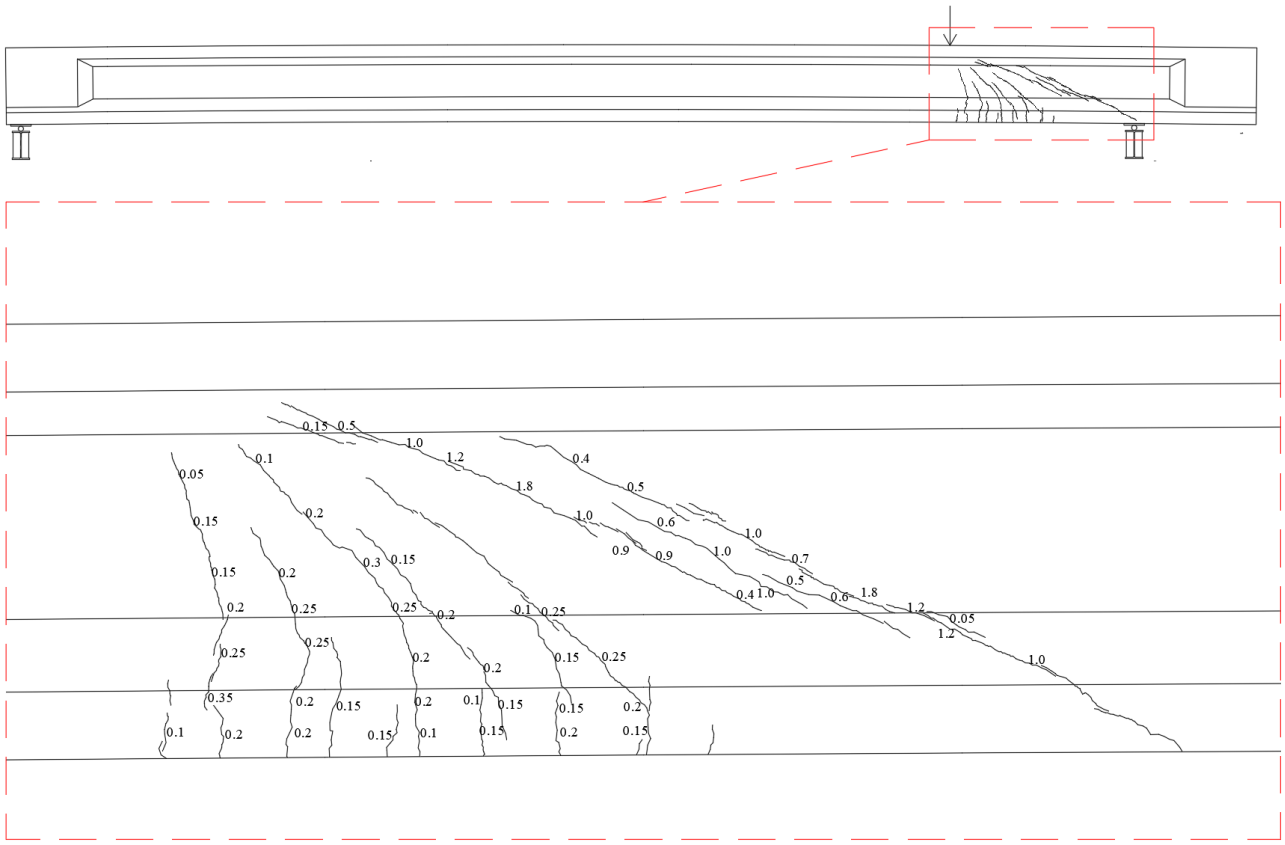

Figure H.8: BTE3 North Final Load Stage Crack Diagram (crack widths are in mm)

The vertical deflection of the girder was measured on the bottom of the beam at the loading point using the DIC system. The deflection at peak load was 1.72 in. The load-displacement plot is shown in Figure H.9. The girder displacement was also recorded by the string potentiometers along the span for the monotonic loading can be seen in Figure H.10. The string potentiometer at the loading point shows a deflection of 2.56 in. at peak load. The string potentiometer displacements include the vertical displacement of the strong floor during loading and also support displacements and could be the reason behind the difference between the maximum deflection obtained from the DIC and the string potentiometer.

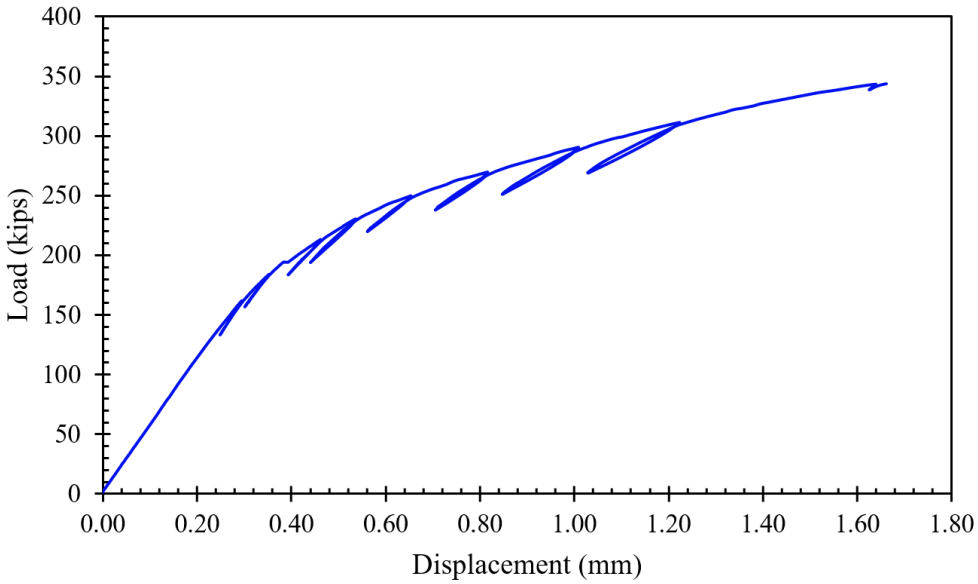

Figure H.9: Load-displacement plot using DIC system

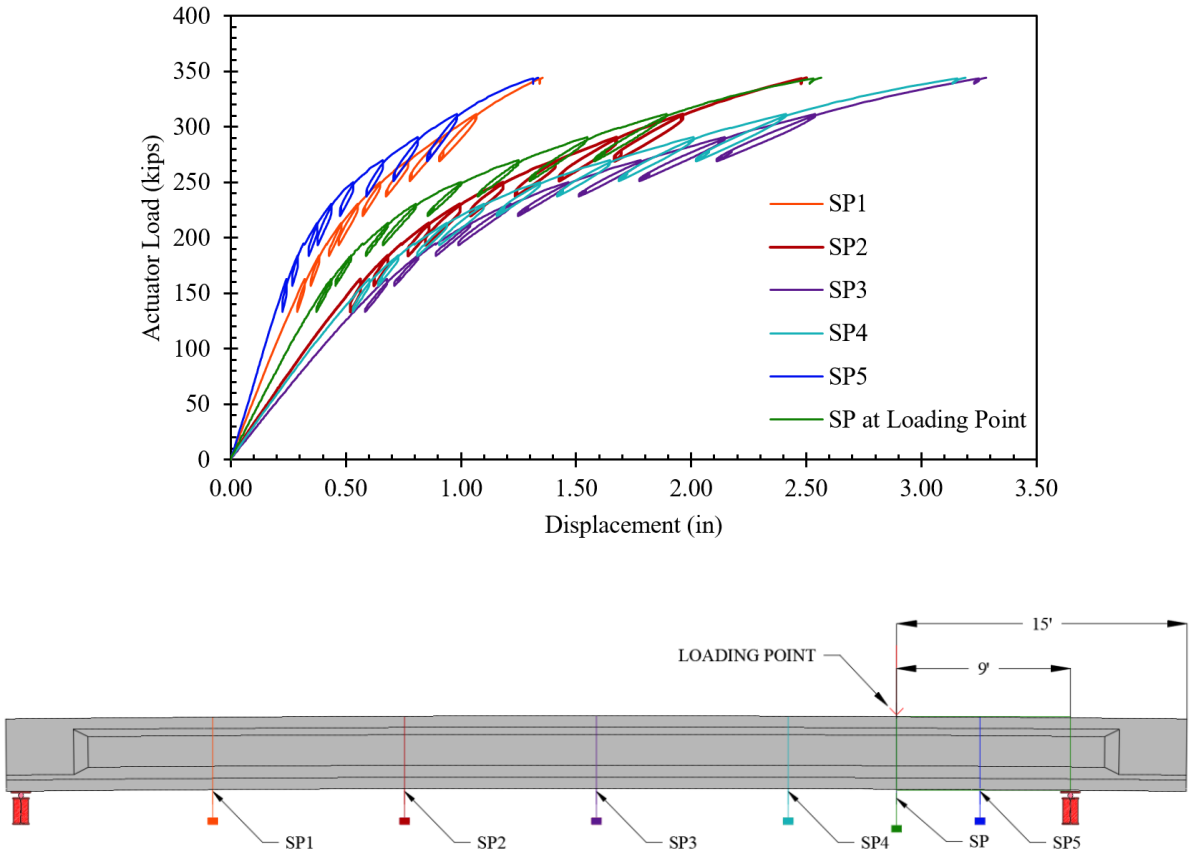

Figure H.10: BTE3 North displacement along length

DIC is used to measure the 3D deformation field of the specimen surfce. In order to study the deformation and strains which leads to formation of cracks, the entire region from the loading point to the support were speckled and the speckle images were analyzed. Additionally, horizontal, vertical and inclined extensometers were placed in the test region to measure average strains in the member. The virtual extensometers were used to determine the average horizontal strain, average vertical strain, shear and principal strains across the web of the girder. Extensometers were placed in the form of a strain rosette over the web region of the girder as illustrated in Figure H.11.

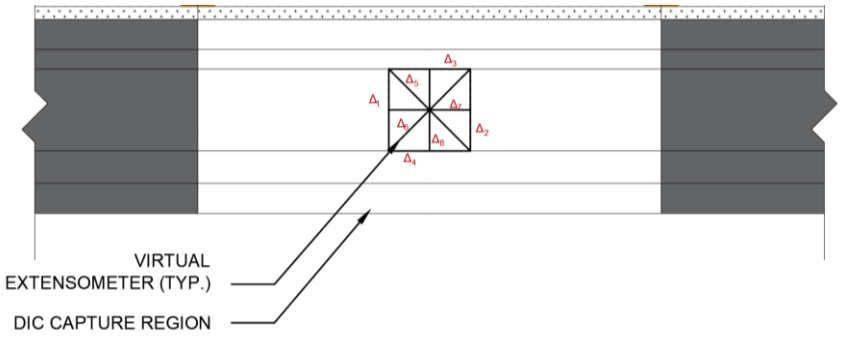

Figure H.11: Strain rosette in the DIC region

Two sets of extensometer rosettes were used. The first one was located in the middle of the DIC region (Δ_M) and the other one was near the loading point (Δ_p). The set of extensometers in the middle of DIC zone (Δ_M) is divided by the critical shear crack whereas the set near the loading point (Δ_P) remains entirely below the critical diagonal crack. Figure H.12 shows the strains from the extensometer rosette E_M plotted against the applied moment due to actuator. It also shows the DIC principal strain map at the peak load in the web region over which the extensometer rosette was placed.

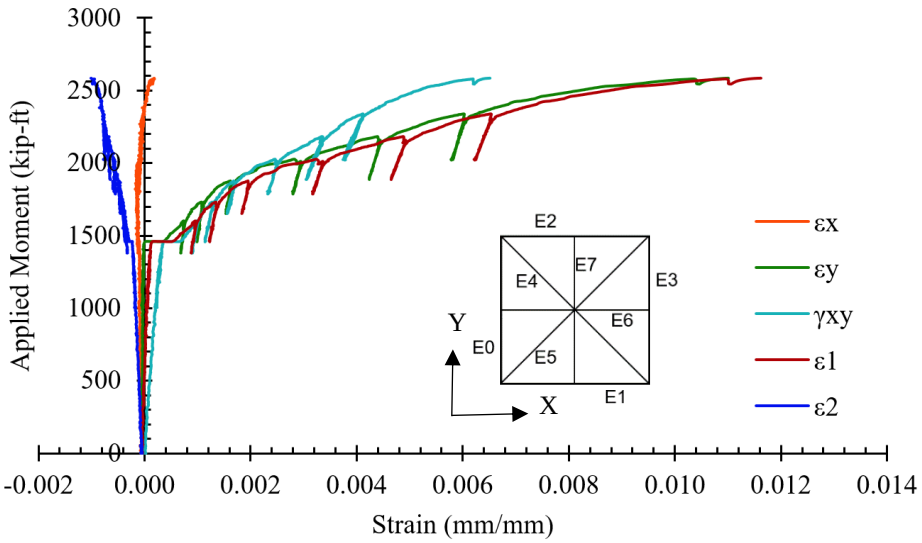

(a)

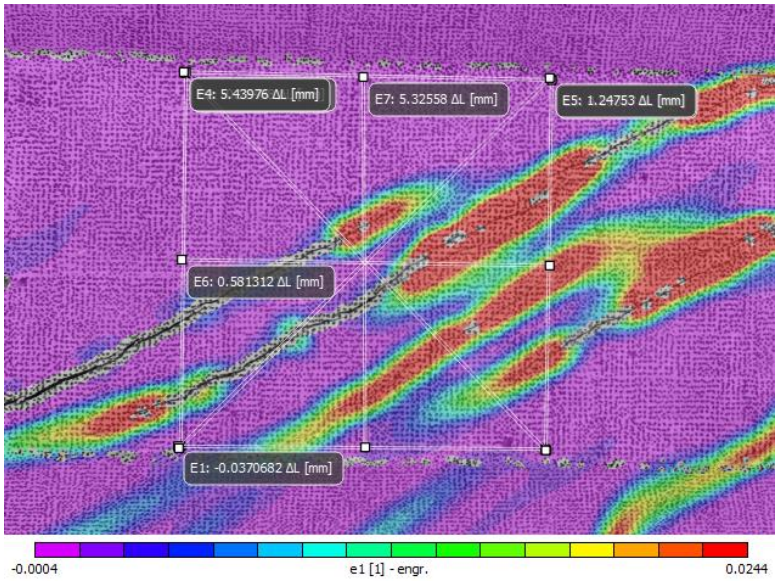

(b)

Figure H.12: (a) Applied moment versus strain obtained from extensometer rosette Δ_M (b) DIC principal strain map at peak load with Δ_M

The shear strain and principal strains are determined from the extensometer rosette by fitting a Mohr's circle of "best-fit" using a procedure that has been developed by Ruggiero (2015). The maximum horizontal, vertical, principal tensile, principal compressive and shear strains

observed at peak load are 0.443×10^{-3}, 12.93×10^{-3}, 13.65×10^{-3}, 1.184×10^{-3} and 8.02×10^{-3}. respectively. All strains are elastic until the shear crack forms at around an applied moment of 1463 k-ft. The principal tensile strain occurs perpendicular to the critical shear crack and with the increase in crack width, principal tensile strain increases rapidly. The variation of strain with applied moment given by the extensometer rosette Δ_p placed near the loading point is shown in Figure H.13. The maximum horizontal, vertical, principal tensile, principal compressive and shear strains at peak load are 0.223×10^{-3}, 5.96×10^{-3}, 7.31×10^{-3}, 0.975×10^{-3} and 6.12×10^{-3} respectively.

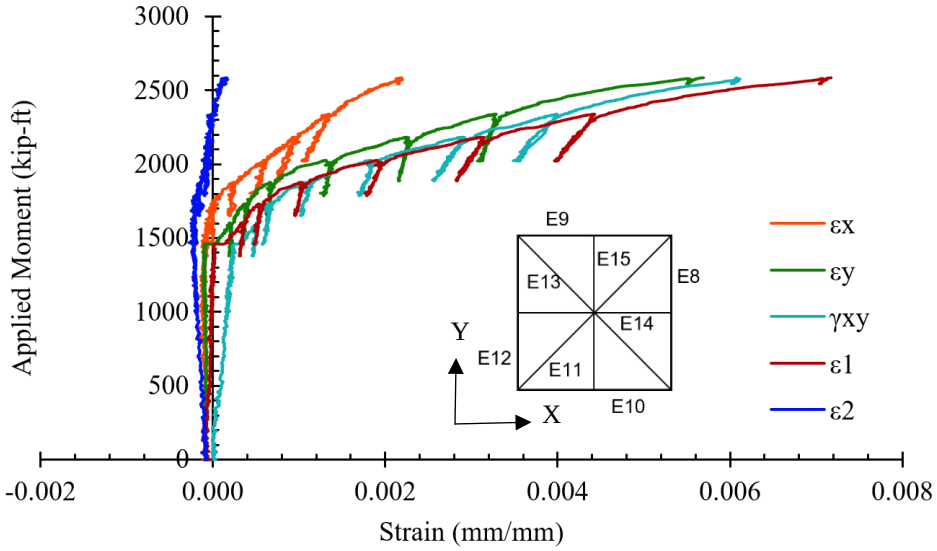

(a)

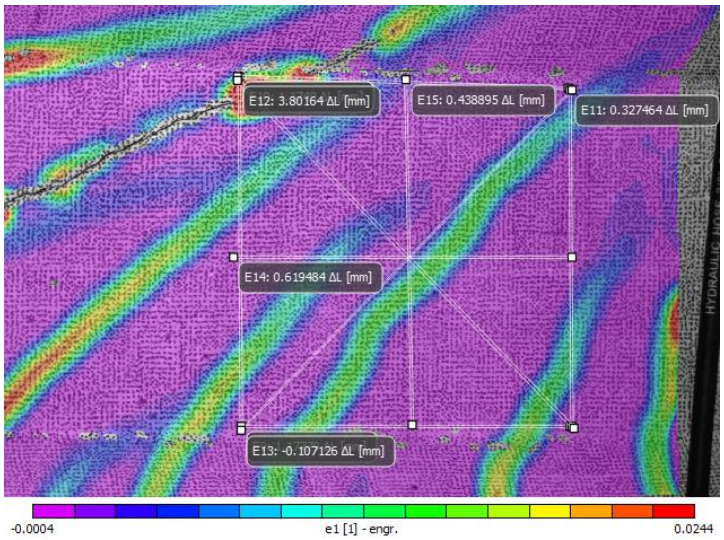

(b)

Figure H.13: (a) Applied moment versus strain obtained from extensometer rosette Δ_P (b) DIC principal strain map at peak load with Δ_P.

The maximum principal tensile strain at peak load in Δ_M is 1.87 times of that in Δ_P. This is because the shear crack never crosses any extensometer in Δ_P at the current location of rosette although there are flexure and flexural shear cracks which have relatively smaller crack widths. The principal tensile strain at the peak load clearly depends on the number of the cracks it crosses and the orientation of the extensometer. The DIC strain map shows the concrete above the critical shear crack remains almost undeformed in comparison to the concrete section below.

The principal strain, ε_1, maps for 100 kips, 150 kips, the four load stages of monotonic loading, and the ultimate load are provided in Figure H.14. These maps show the formation of strain concentrations near the shear crack which begins at mid depth of the girder and slowly progress towards the support and loading plate. Flexural cracks can also be seen forming at the bottom of girder near the loading point. One interesting observation is that its possible for the shear cracks to occur before the appearance of flexural cracks.

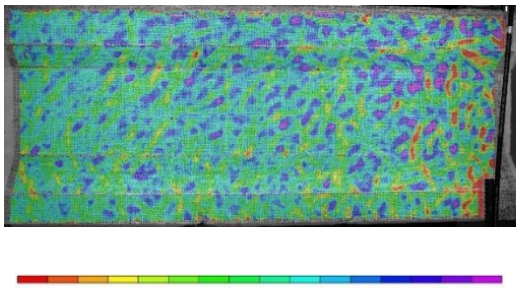

0.000645 100 kips -0.00032

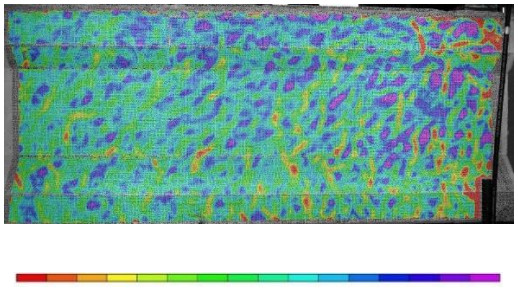

0.00069 150 kips -0.000305

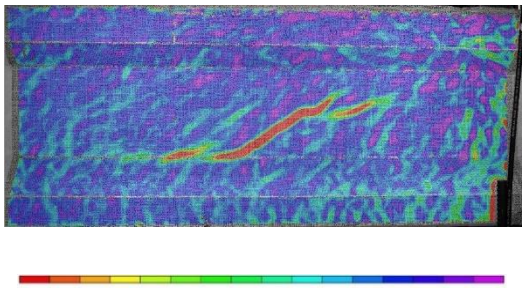

0.00165 195 kips -0.00032

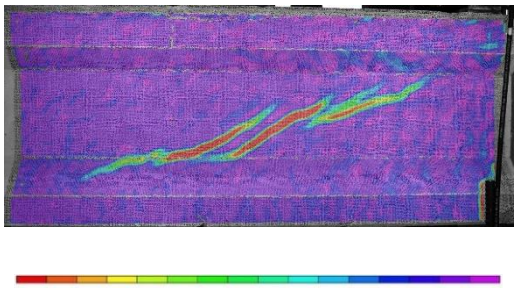

0.00905 210 kips -0.0004

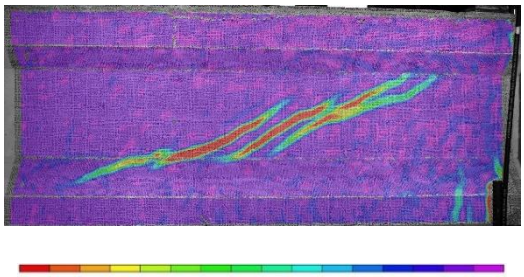

0.00645 230 kips -0.00045

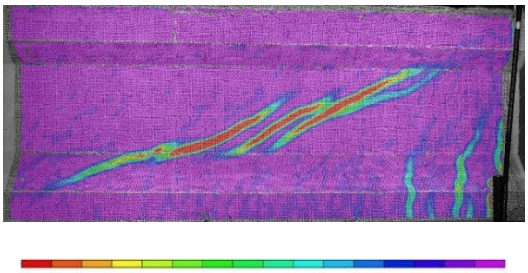

0.0101 250 kips -0.00035

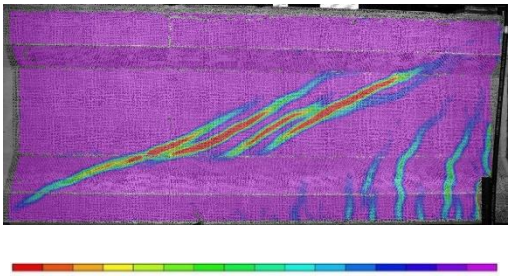

0.0155 270 kips -0.0004

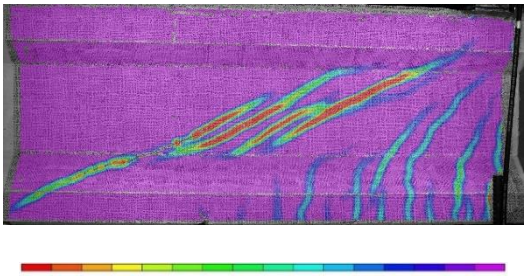

0.0207 290 kips -0.0004

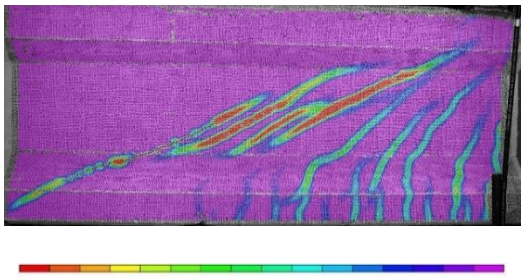

0.0225 310 kips -0.0004

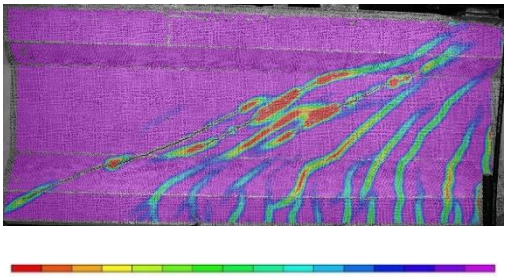

0.0244 344 kips -0.0004

Figure H.14: Principal strain (ε_1) maps at different stages of loading in BTE3 North.

The ultimate load strain maps for axial strains, ε_x and ε_y, shear strain, ε_{xy} and γ_{xy}, and principal strains, ε_1 and ε_2 are shown in Figure H.15.

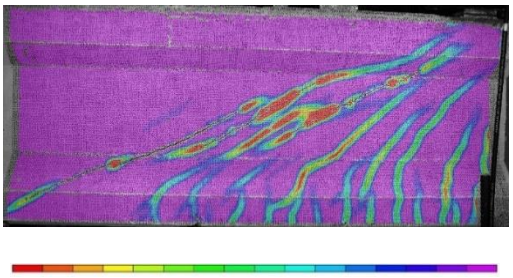

0.024 ε_1 -0.0005

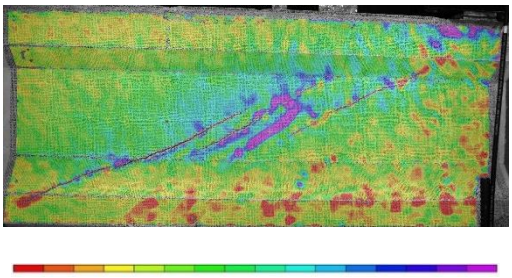

0.00058 ε_2 -0.0021

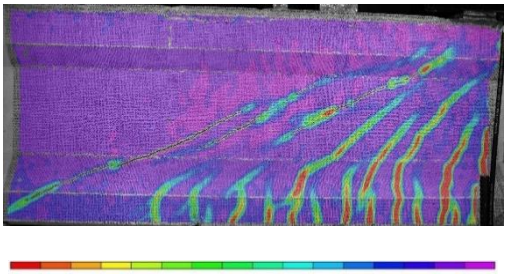

0.0113 ε_{xx} -0.0014

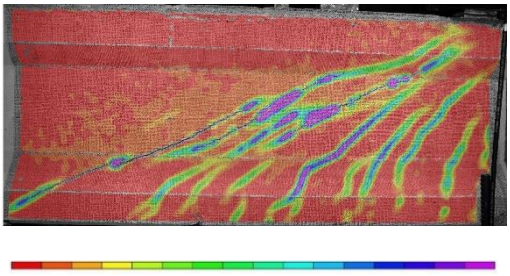

0.0007 ε_{xy} -0.0208

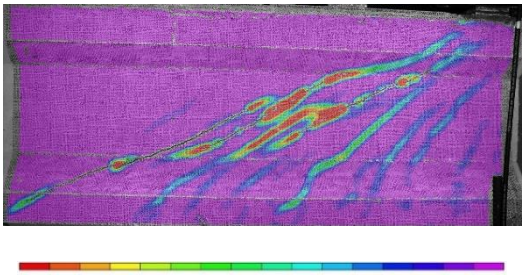

0.0211 ε_{yy} -0.0008

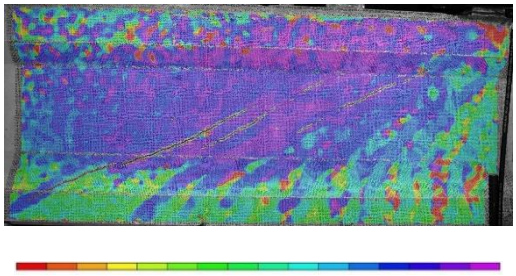

1.42 γ_{xy} -1.52

Figure H.15: Strain maps at peak load in BTE3 North.

H.4.2 BTE4 South

The girder failed in shear at a peak applied load of 319 kips and the corresponding applied moment is 2394 k-ft. The specimen at load stages of 210 kips, 270 kips and at failure can be seen in Figure H.16. Both the critical shear crack and flexural shear cracks can be seen at a load stage of 270 kips.

(a)

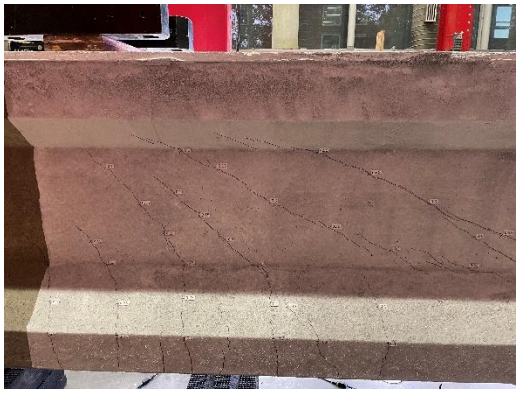

(b)

(c)

Figure H.16: BTE4 South (a) Cracks at a load stage at 210 kips (b) Cracks at a load stage of 270 kips (c) Failure photo at peak applied load.

A summary of the cracks marked and measured at the final load stage is provided in Figure H.17. The maximum crack width observed at 310 kips of actuator load was 2.5 mm.

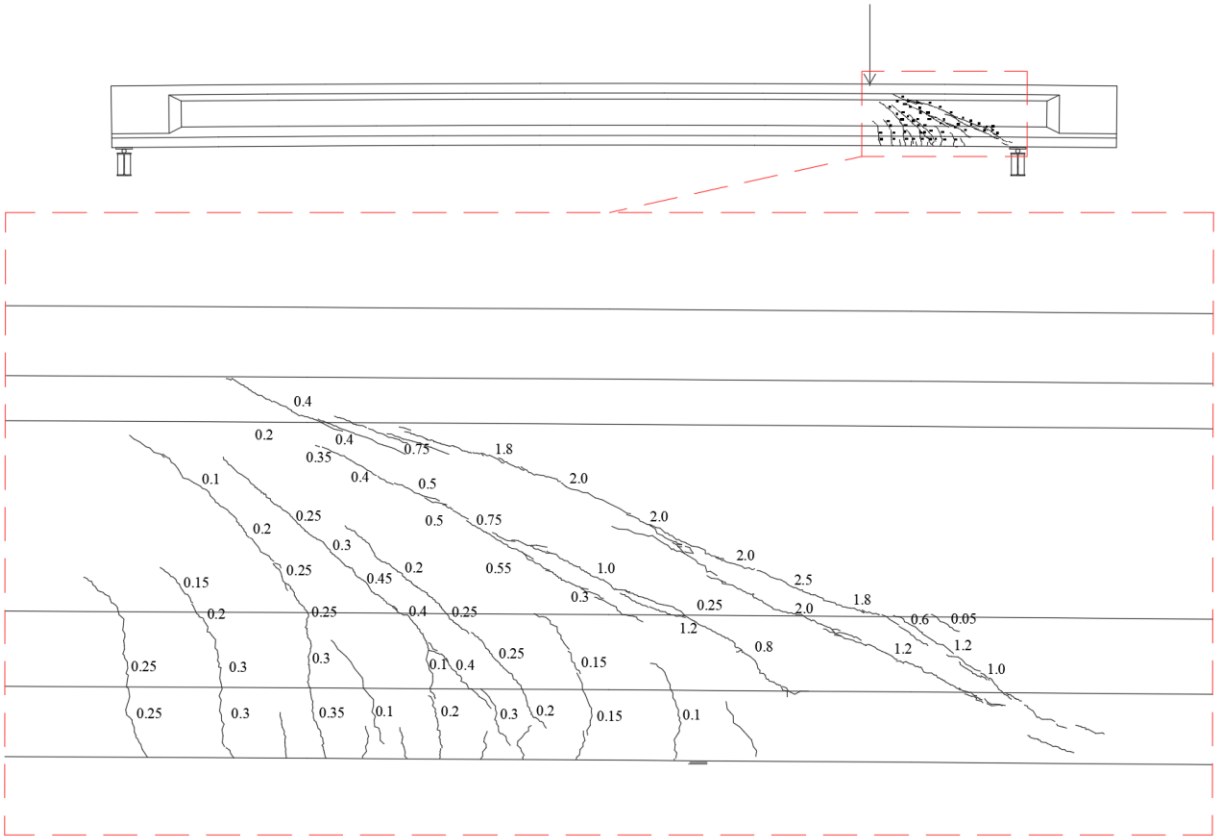

Figure H.17: BTE4 South Final Load Stage Crack Diagram

Similar to BTE3 North, the vertical deflection of the girder was measured on the bottom of the beam at the loading point using the DIC system. The deflection at peak load was 2.44 in. The load-displacement plot is shown in Figure H.18. The girder displacement was also recorded by the string potentiometers along the span for the monotonic loading can be seen in Figure H.19. The string potentiometer at the loading point shows a deflection of 2.56 in at peak load.

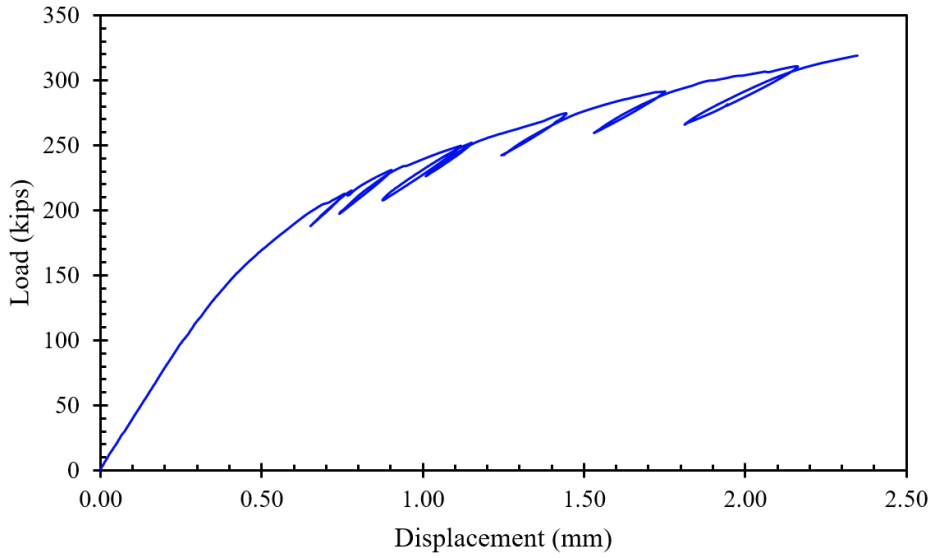

Figure H.18: BTE4 South load-displacement plot using DIC system

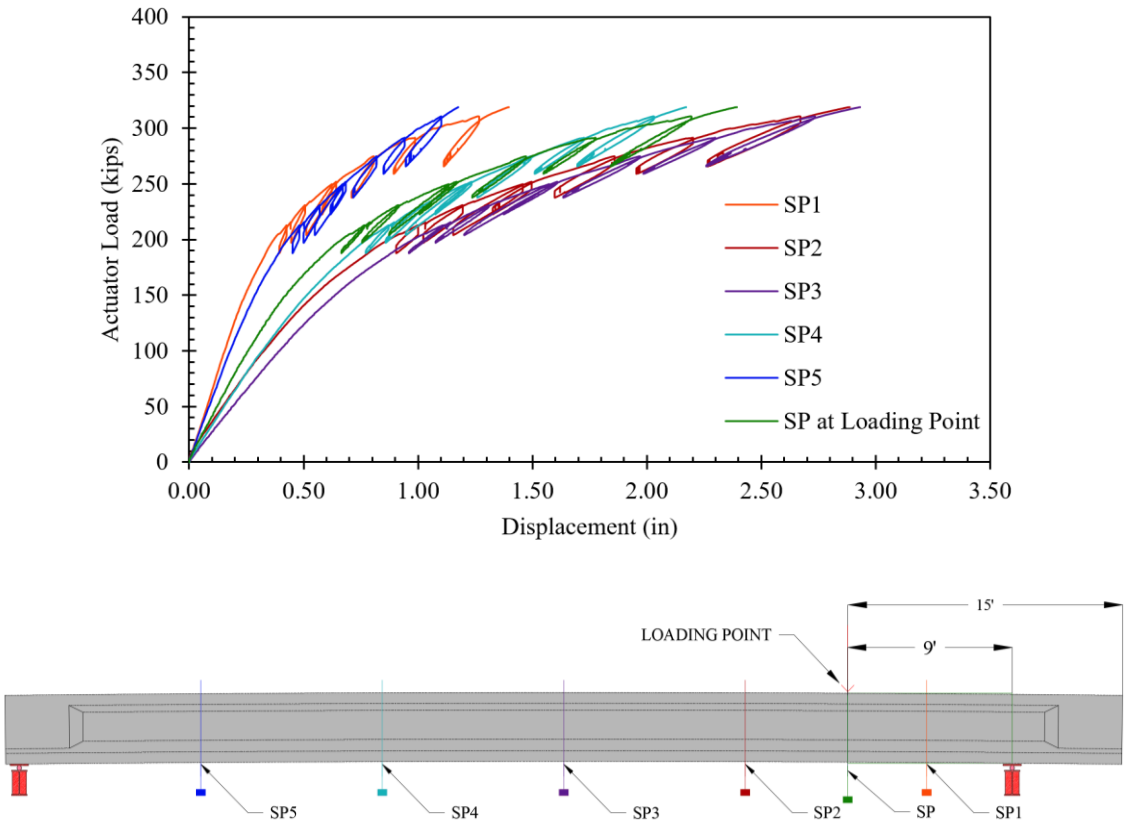

Figure H.19: BTE4 South displacement along length

Extensometer rosettes were placed over the web region to observe variation of strain with applied moment. Figure H.20 shows the variation of strain over the web region with increase in applied moment. At the peak load, the maximum horizontal, vertical, principal tensile, principal compressive and shear strains at peak load are 0.933×10^{-3}, 15.78×10^{-3}, 17.07×10^{-3}, 0.493×10^{-3} and 8.10×10^{-3} respectively.

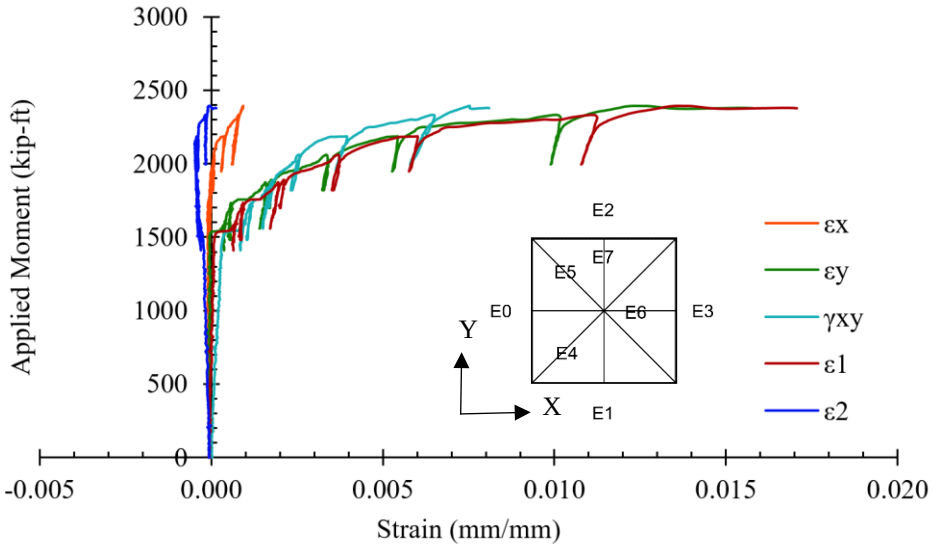

(a)

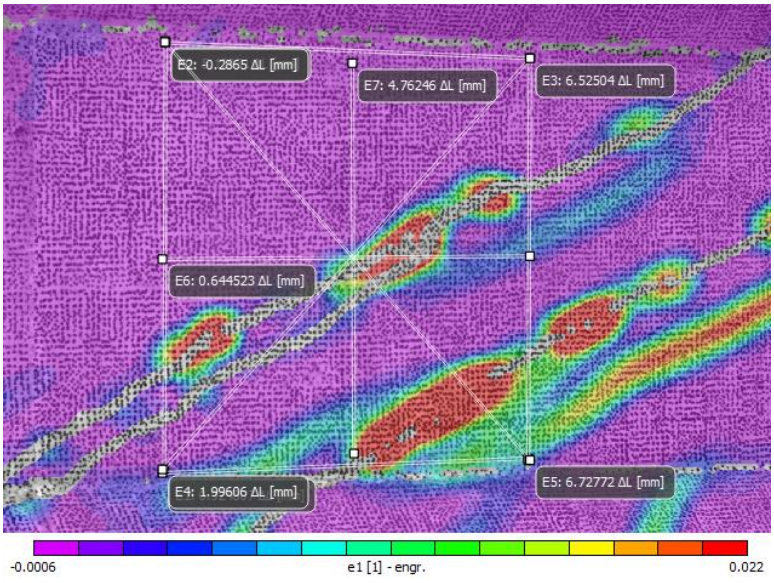

(b)

Figure H.20: BTE4 South (a) Applied moment versus strain given by extensometer rosette Δ_M (b) DIC principal strain map at peak load with Δ_M.

The variation of strain near the loading point with applied moment is shown in Figure H.21 along with the DIC principal strain map at peak load. At the peak load, the maximum horizontal, vertical, principal tensile, principal compressive and shear strains at peak load are 0.855×10^{-3},

1.461×10^{-3}, 3.06×10^{-3}, 0.888×10^{-3} and 3.87×10^{-3} respectively. The strains near the loading point are significantly less compared to the strains observed in the middle of DIC region.

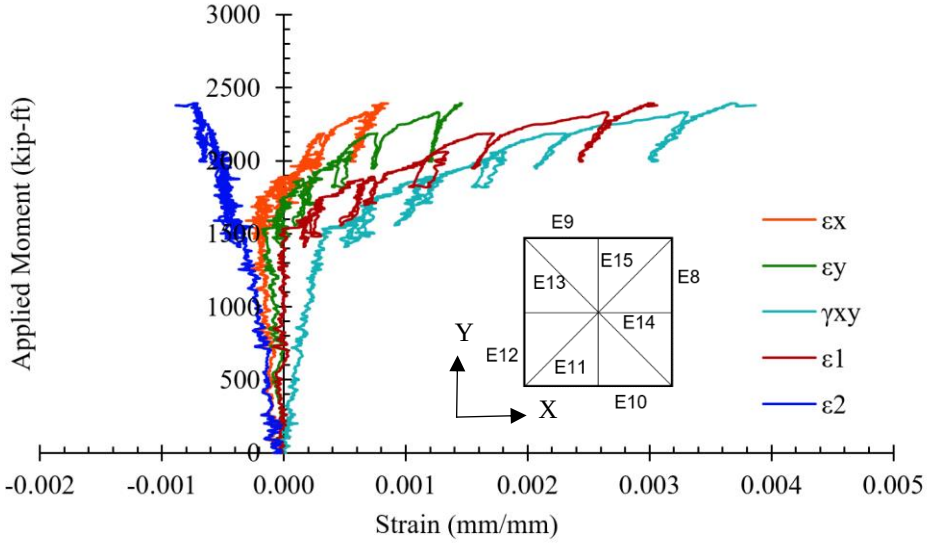

(a)

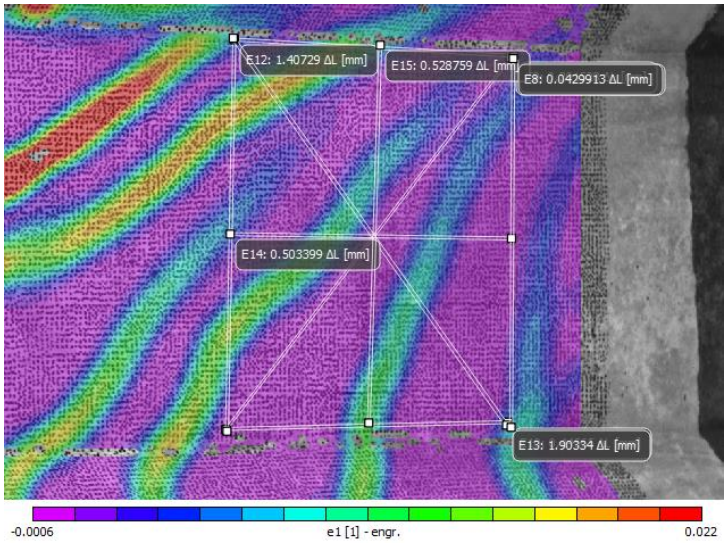

(b)

Figure H.21: (a) Applied moment vs strain near loading point of BTE4 South (b) DIC principal strain map at peak load with Δ_p

The applied moment versus strain is fairly linear until cracks start to appear when there is a signficant increase in the principal tensile strain, shear strain and vertical strain. The largest principal tensile strain occurs in extensometers placed in vertical and perpendicular to the shear crack. This is because of the elongation of cracks and also due to the curvature of the girder. Concrete above the shear crack is relatively undeformed but flexural cracks can be seen underneath.

Strain maps for the full DIC field of view between the load plate and support are provided below. The principal strain, ε1, maps for 100 kips, 150 kips, the four load stages of monotonic loading, and the ultimate load are provided in Figure H.22. The ultimate load strain maps for axial strains, ε_x and ε_y, shear strain, γ_{xy}, and principal strains, ε_1 and ε_2 are shown in Figure H.23.

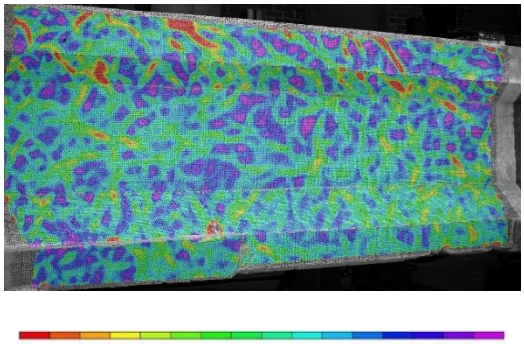

0.00095 100 kips -0.00031

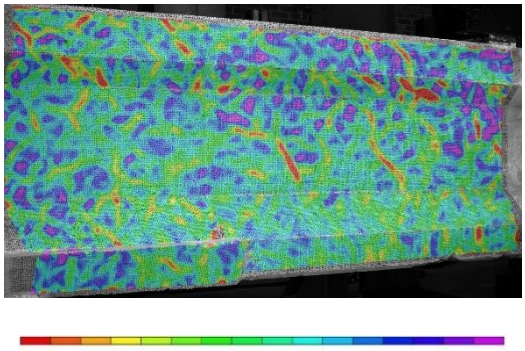

0.00099 150 kips -0.0004

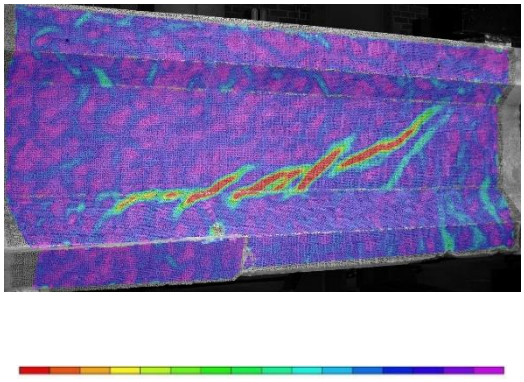

0.0036 210 kips -0.00036

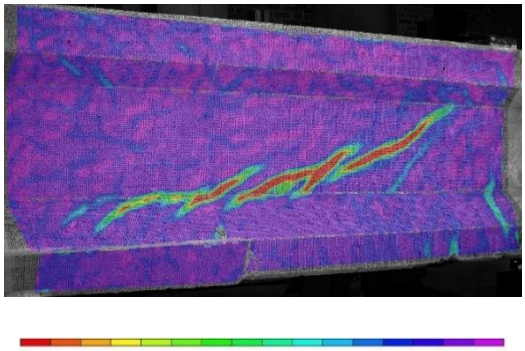

0.00555 230 kips -0.00045

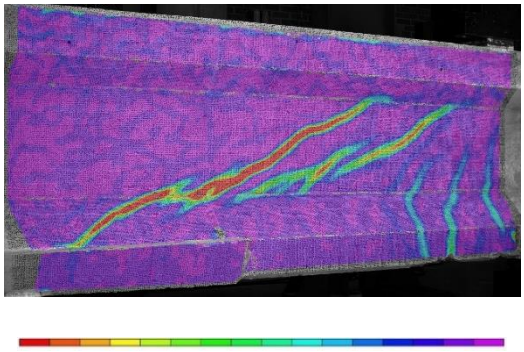

0.01045 250 kips -0.00055

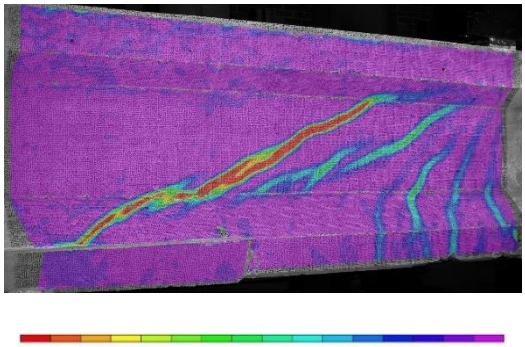

0.0183 270 kips -0.0007

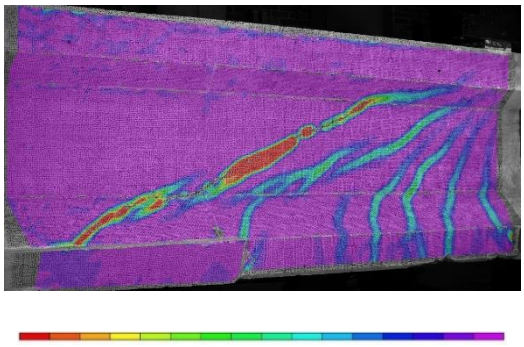

0.0209 290 kips -0.0007

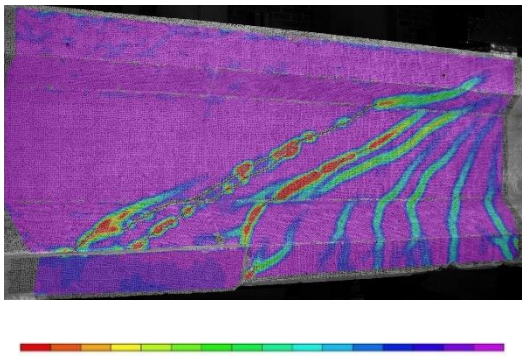

0.024 310 kips -0.0008

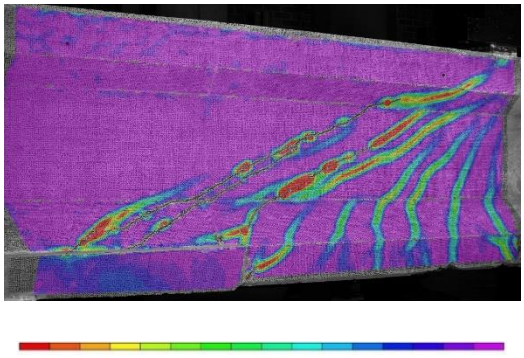

0.022 319 kips -0.0006

Figure H.22: Principal strain (ε_1) maps at different stages of loading in BTE4 South.

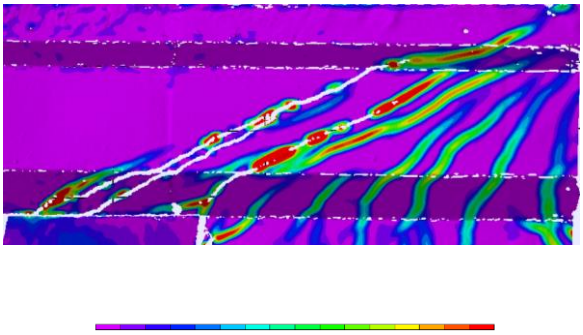

-0.0006 ε_1 0.022

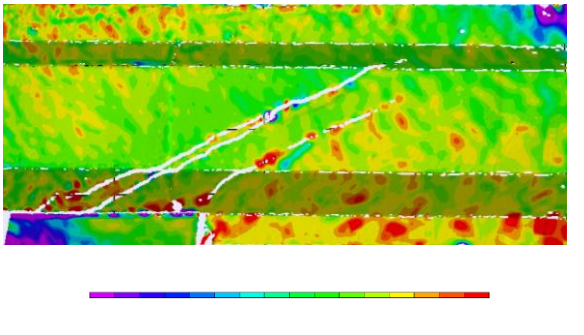

-0.00435 ε_2 0.00105

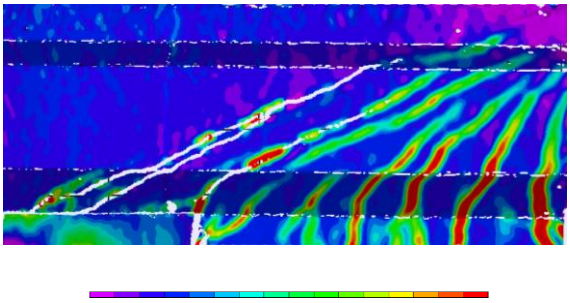

-0.0021 ε_{xx} 0.00785

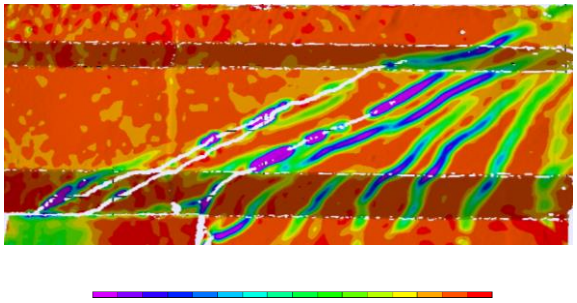

-0.0176 ε_{xy} 0.0016

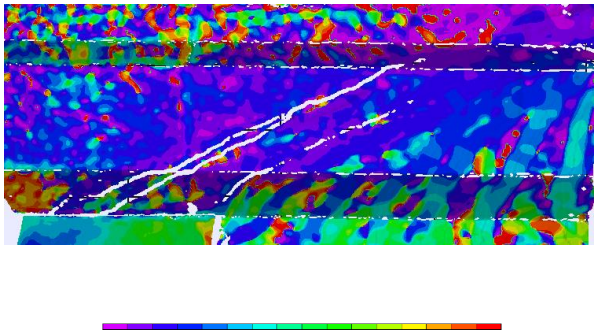

-1.56 γ_{xy} 1.54

Figure H.23: Strain maps at peak load in BTE4 South.

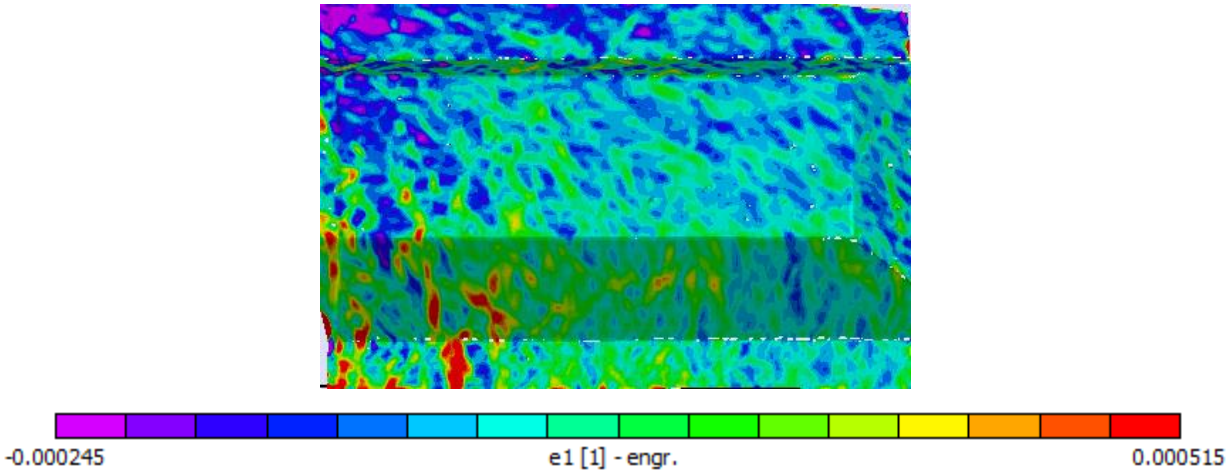

100 kips

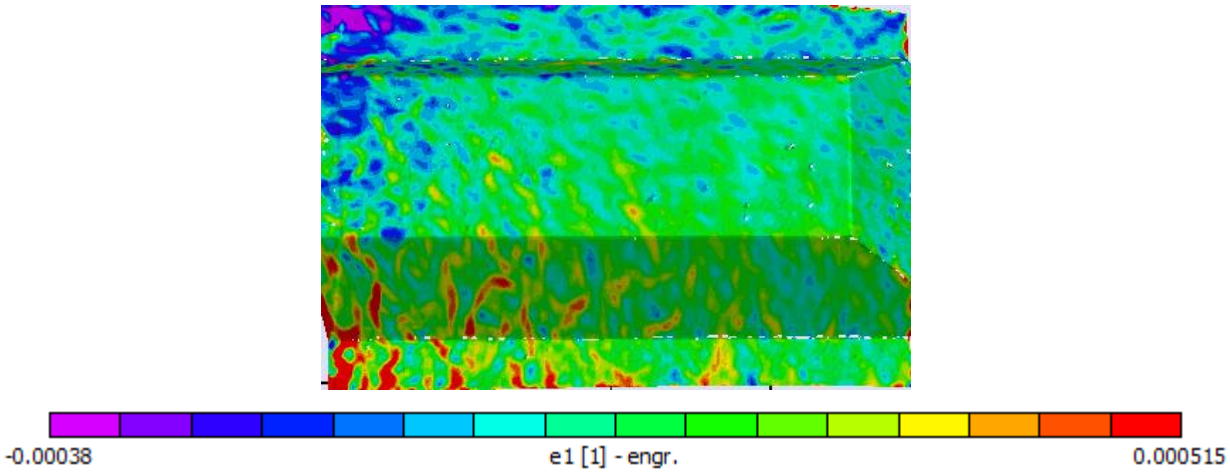

150 kips

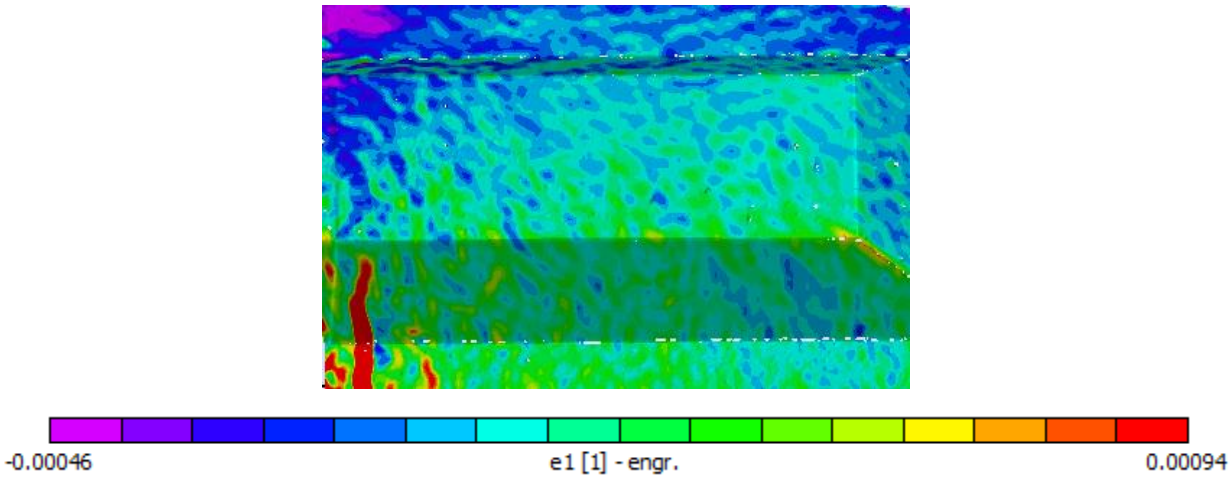

210 kips

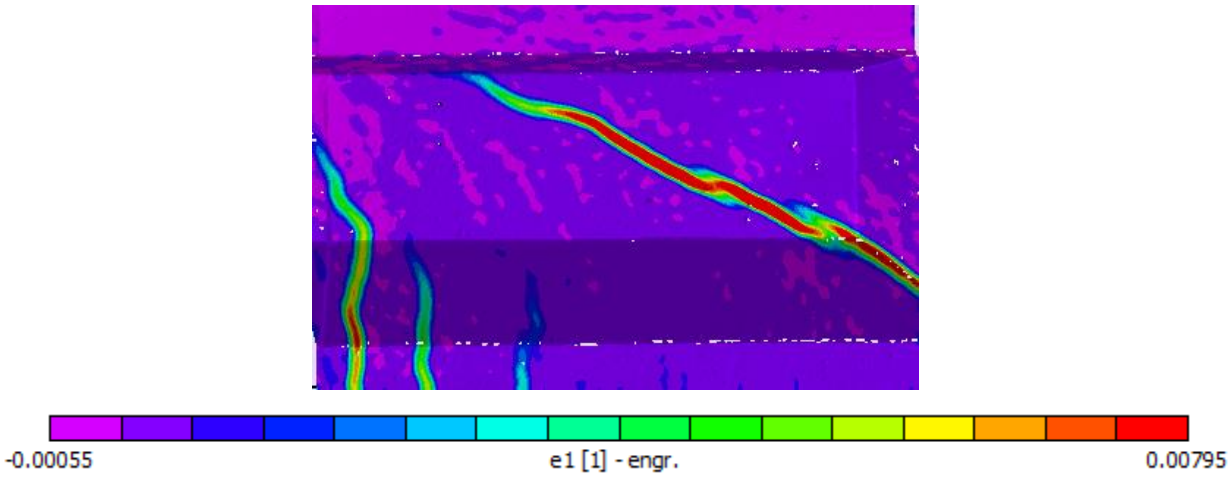

230 kips

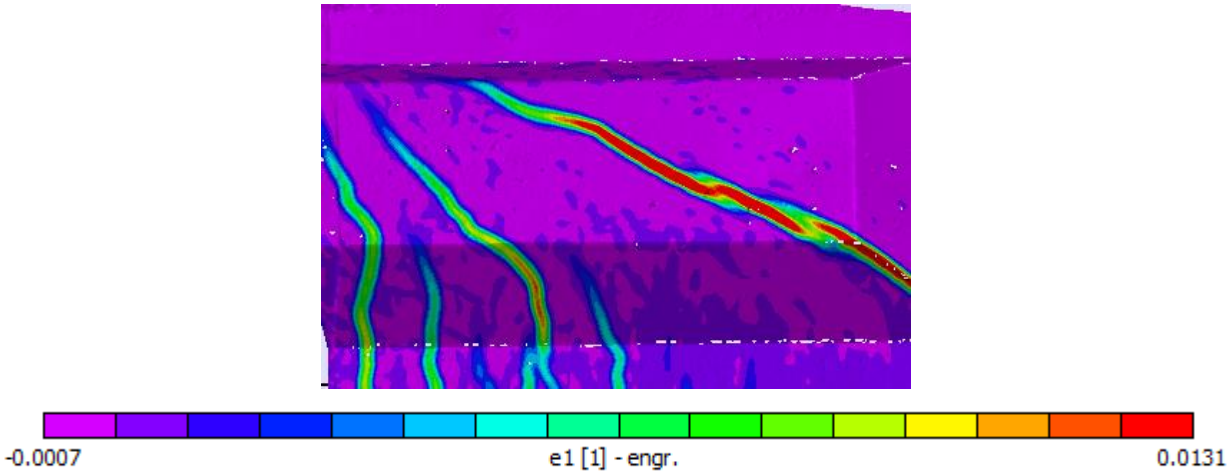

250 kips

Figure H.24: Principal strain map of BTE3 South at load stages.